



HAL
open science

A contribution to rainfall observation in Africa from polarimetric weather radar and commercial micro-wave links

Matías Alcoba Kait

► **To cite this version:**

Matías Alcoba Kait. A contribution to rainfall observation in Africa from polarimetric weather radar and commercial micro-wave links. Climatology. Université Paul Sabatier - Toulouse III, 2019. English. NNT : 2019TOU30238 . tel-02955598

HAL Id: tel-02955598

<https://theses.hal.science/tel-02955598>

Submitted on 2 Oct 2020

HAL is a multi-disciplinary open access archive for the deposit and dissemination of scientific research documents, whether they are published or not. The documents may come from teaching and research institutions in France or abroad, or from public or private research centers.

L'archive ouverte pluridisciplinaire **HAL**, est destinée au dépôt et à la diffusion de documents scientifiques de niveau recherche, publiés ou non, émanant des établissements d'enseignement et de recherche français ou étrangers, des laboratoires publics ou privés.



THÈSE

**En vue de l'obtention du
DOCTORAT DE L'UNIVERSITÉ DE TOULOUSE
Délivré par l'Université Toulouse 3 - Paul Sabatier**

**Présentée et soutenue par
Matías ALCOBA KAIT**

Le 16 décembre 2019

**Contribution à l'observation des précipitations en Afrique avec un
radar polarimétrique et des liens microondes commerciaux.**

Ecole doctorale : **SDU2E - Sciences de l'Univers, de l'Environnement et de
l'Espace**

Spécialité : **Océan, Atmosphère, Climat**

Unité de recherche :
GET - Geosciences Environnement Toulouse

Thèse dirigée par
Eric MOUGIN et Marielle GOSSET

Jury

M. Hidde LEIJNSE, Rapporteur
M. Brice BOUDEVILLAIN, Rapporteur
M. Roger Moussa, Examineur
M. Frank Roux, Examineur
M. Eric MOUGIN, Directeur de thèse
Mme Marielle GOSSET, Co-directrice de thèse

RÉSUMÉ

Le climat ouest africain est gouverné par un régime de mousson, les précipitations, souvent intenses, y sont principalement associées à des systèmes convectifs de méso-échelle. Dans un contexte de risques hydrométéorologiques, caractériser ces précipitations jusqu'aux plus fines échelles est important. Deux types d'observation des précipitations par télédétection active, au sol, dans le domaine des micro-ondes, sont explorés : un radar météorologique polarimétrique et des liens micro-ondes commerciaux.

La première partie de la thèse est dédiée à la caractérisation des hydrométéores à partir d'un radar polarimétrique opérant en bande X. Le lien entre les observations et les caractéristiques des hydrométéores peut se faire à partir de modèles physiques. L'inversion de ces modèles permet de retrouver les caractéristiques des hydrométéores à partir des observations. On présente une première méthode d'inversion permettant d'obtenir la densité des hydrométéores au-dessus de la couche de fusion grâce à la modélisation simple du profil vertical de réflectivité radar. La deuxième méthode d'inversion vise à créer des cartes horizontales de la distribution de taille de gouttes de pluie à partir des mesurables radar polarimétrique. La méthode exploite toute l'information d'une radiale pour estimer la distribution de taille de gouttes tout en corrigeant de l'atténuation par la pluie.

La deuxième partie est consacrée à la mesure des précipitations à partir de liens micro-ondes commerciaux, issus des réseaux de téléphonie mobile. Cette méthode prometteuse pour les régions mal couvertes par les mesures météorologiques opérationnelles exploite l'atténuation par la pluie des signaux transmis entre les antennes relais. Les principes de la méthode, les sources d'incertitudes et la validation quantitative sur un jeu de données acquis au Niger sont présentés. Enfin, on analyse différentes méthodes d'interpolation des données de liens pour créer des cartes de pluie.

Mots clefs : Télédétection, microondes, radar polarimétrique, liens microondes commerciaux, précipitations, inversions

ABSTRACT

West Africa climate is driven by a monsoon regime: the precipitations are characterized by heavy rain rates which are organized into mesoscale convective systems. In a context of hydro-meteorological risks, the characterization of such systems at fine scales is important. Two type of ground precipitation observation by active microwave remote sensing are explored: a meteorological polarimetric radar and commercial microwave links.

The first part is dedicated to the characterization of hydrometeors with X-band polarimetric radar data. The link between the observations and the hydrometeor characteristics can be made with physical models. The physical characteristics of hydrometeors can be retrieved with inversion of these physical models. We present a first inversion method permitting the retrieval of the hydrometeors density above the 0°C isotherm, with the simple modelization of the vertical profile of reflectivity. The second inversion method aims to produce maps of rainfall drop size distribution with polarimetric radar observables. In the proposed method we use all the information of a radar radial to estimate the size distribution of drops and, at the same time, correcting the attenuation.

The second part is focused on the precipitation estimation with commercial microwave links from telecommunication companies. This promising method for ill-equipped regions, uses the rain induced attenuation between a pair of antennas composing a link to estimate rainfall. The principle of the method, the sources of uncertainties and the quantitative evaluation of a dataset in Niger are presented. Finally, we analyse different interpolation methods to create rainfall maps from commercial microwave links data.

Keywords: Remote Sensing, Microwaves, Polarimetric Radar, Microwave links, Precipitation, Inversion

ACKNOWLEDGEMENTS

Je voudrais remercier tous ceux qui ont rendu possible ce travail, en France, au Burkina-Faso, au Niger, au Mali et au Cameroun.

Un grand merci à Hervé Andrieu pour ses conseils et son regard sur la méthode d'inversion polarimétrique, mais aussi pour ses commentaires et réflexions sur le reste de mon travail qui m'ont aidé à prendre du recul.

Un grand merci aussi à Frédéric Cazenave pour m'avoir appris à me débrouiller en Afrique de l'Ouest, à faire du terrain et à opérer le radar.

Je voudrais aussi remercier les techniciens de terrain et ingénieurs qui créent des données d'une grande qualité, merci à Guillaume Quantin, Marc Arjounin, Nogmana Soumaguel, Salomon Bouda parmi tant d'autres.

Merci à mes partenaires, collègues et amis africains, Modeste Kacou, Apolline Yapi, Ali Doumounia.

Merci à Emmanuel Fontaine et Duncan Devaux pour leur travail, sans lequel je n'aurais pas pu arriver à certains des résultats présentés.

Merci à mes collègues doctorants passés et présents pour les discussions de sciences et l'ambiance agréable d'équipe, Claire Cassé, Clément Guilloteau, Maxime Turko.

Merci beaucoup à Eric Mougin pour me soutenir dans mon projet de thèse.

Et surtout merci Dieu (aka. Marielle Gosset) pour m'avoir permis de réaliser ce travail et de m'avoir appris le métier depuis ces quelques belles années. Merci pour ton soutien, pour ton attention envers les personnes qui travaillent avec toi, pour ton regard critique, tes conseils et ta bonne humeur.

Merci à Orange-Niger et à ses ingénieurs pour partager les données d'atténuation, essentielles pour toute une partie de ce travail.

Merci beaucoup aux collègues Français et Burkinabés avec lesquels on passe des bons moments de science et d'humour !

Merci à Elo pour les aventures.

Merci à la famille et amis pour supporter mes histoires sur la thèse !

CONTENTS

Introduction.....	1
Chapter 1: Rainfall characteristics and measurement in Africa.....	6
1.1 The organization and structure of rainfall systems in the study region	6
1.2 Ground based measurement of rainfall	9
1.3 Main scientific questions	19
1.4 Data used in the present work.....	19
Part 1: Retrievals of physical characteristics of precipitations with a polarimetric radar	24
Chapter 2: Radar measurement of rainfall	27
2.1 Principle of radar measurement	27
2.2 Hydrometeors characteristics impacting microwave remote sensing	33
2.3 Models representing hydrometeors and EM interaction	39
Chapter 3: A simple bright band method to infer the density of icy hydrometeors	46
Chapter 4: An inverse method for drop size distribution retrieval.....	60
4.1 Introduction.....	61
4.2 Study area and dataset.....	65
4.3 Forward modelling of polarimetric radar observables.....	69
4.4 The inverse problem to retrieve DSD from observation.....	75
4.5 Results.....	79
4.6 Conclusion	90
Part 2: Commercial microwave links for rainfall monitoring.....	97

Chapter 5: Rainfall measurement from microwave links: principle and sources of uncertainty	99
5.1 Measurement principle.....	100
5.2 Sources of uncertainties in CML based rainfall estimation.....	114
Chapter 6: Evaluation of CML rainfall measurements in Niamey	133
6.1 Data	133
6.2 Baseline detection	136
6.3 Rainfall retrieval algorithm: calibration and evaluation against gauges	137
6.4 Conclusions	166
Chapter 7: Mapping algorithms of CML: A new method based on machine learning.....	170
7.1 Introduction	170
7.2 Rain mapping from links: common methods	173
7.3 Synthetic data	180
7.4 Results on synthetic data	184
7.5 Results on real data	192
7.6 Discussion and perspectives.....	196
Conclusion and perspectives	198
Appendix 1: Quasi-Newton algorithm demonstration	206
Appendix 2: Self-consistency correction.....	208
Appendix 3: Data quality control.....	210
Appendix 4: Minimization of parameters of CML-gage dataset in Niamey	213
Appendix 5: Investigation of the bias dependency on links' length using simulations ..	218
Appendix 6: Additional figures of chapter 7.....	225
Bibliography	233

LIST OF TABLES

TABLE 4-1: LIST OF EVENTS RECORDED BY THE DISDROMETER AND THE RADAR, NUMBER OF PPIs WHERE THE INVERSION WAS APPLIED.....	87
TABLE 5-1: K-R LAW COEFFICIENTS FOR 18 AND 23 GHz.....	108
TABLE 5-2: SUMMARY OF THE DIFFERENT SOURCES OF ATMOSPHERIC ATTENUATION ...	117
TABLE 5-3: K-R LAW COEFFICIENTS	122
TABLE 5-4: SUMMARY OF THE DIFFERENT BIAS AND UNCERTAINTIES OF THE DIFFERENT CAUSES	136
TABLE 6-1:PARAMETERS FITTED TO THE OBSERVED ATTENUATION.....	146
TABLE 6-2: TOTAL SEASON BIAS (%) AND DAILY R2 AGAINST RAINGAGE	172
TABLE 6-3: CALIBRATION PARAMETERS RETAINED.....	173
TABLE 7-1: NUMBER OF RAINFALL FIELDS IN THE TRAINING DATASET.....	187
TABLE 7-2: DETECTION SCORES OF THE CROSS-VALIDATION	200
TABLE 7-3: SCORES OF THE DIFFERENT METHODS IN THE CROSS-VALIDATION.....	201
TABLE A 1: CHARACTERISTICS OF THE CML NETWORKS USED FOR THE RAINFALL MAPPING	230

LIST OF FIGURES

FIGURE 1-1: EXAMPLE OF 2-D IMAGES RECORDED BY THE PRECIPITATION IMAGING PROBE	9
FIGURE 1-2: EVOLUTION OF THE NUMBER OF RAIN GAGES	12
FIGURE 1-3: VOLUME RESOLUTION OF RADAR MEASUREMENT	16
FIGURE 1-4: : MEASUREMENT GEOMETRY OF METEOROLOGICAL RADAR DATA	17
FIGURE 1-5: LOCATION OF REPORTED RADARS	17
FIGURE 1-6: X-PORT RADAR LOCATION IN OUAGADOUGOU	21

FIGURE 1-7: DIFFERENT LOCATIONS OF X-PORT RADAR.....	22
FIGURE 1-8: CML ORANGE NETWORK IN NIAMEY	23
FIGURE 2-1: EXAMPLE OF RAW POLARIMETRIC OBSERVABLES	34
FIGURE 2-2: EXAMPLE OF RAW POLARIMETRIC OBSERVABLES	34
FIGURE 2-3: EXAMPLE OF RAIN DROP PHOTOS.....	40
FIGURE 2-4: DIFFERENT RATIO SHAPE LAWS USED IN THIS WORK.....	40
FIGURE 2-5: EXTINCTION CROSS SECTIONS FOR DIFFERENT FREQUENCIES BY DROP DIAMETER FOR MIE AND RAYLEIGH MODELS.	45
FIGURE 2-6: MIE EXTINCTION CROSS SECTIONS FOR DIFFERENT FREQUENCIES AND TEMPERATURES BY DROP DIAMETER.	45
FIGURE 4-1: ONE DROP T-MATRIX OUTPUT	74
FIGURE 4-2: T-MATRIX SIMULATED RADAR VARIABLES	76
FIGURE 4-3: EXAMPLE OF THE OBSERVED, A PRIORI AND RETRIEVED ATTENUATED POLAR VARIABLES AND DSD PARAMETERS FOR A GIVEN RADIAL	83
FIGURE 4-4: RETRIEVED (TOP) AND A PRIORI (BOTTOM) MAPS OF DSD PARAMETERS F ...	85
FIGURE 4-5: RETRIEVED FIELDS OF ATTENUATED RADAR OBSERVABLES.	86
FIGURE 4-6: TIME EVOLUTION OF DM (TOP) AND $LO_{10}[N0^*]$ (BOTTOM)	88
FIGURE 4-7: SENSITIVITY OF THE RETRIEVED DM (TOP) AND $LO_{10}[N0^*]$ (BOTTOM).....	90
FIGURE 4-8: : CONTOUR PLOT ON $N0^*$ -DM SPACE OF DISTRIBUTIONS OF DISDROMETER DSD AND RADAR RETRIEVED DSD.	91
FIGURE 4-9: SCATTERPLOT OF THE RADAR RETRIEVED DSD PARAMETERS.....	92
FIGURE 5-1: SCHEMATIC REPRESENTATION OF A LINE-OF-SIGHT MICROWAVE LINK.....	104
FIGURE 5-2: K-R LAWS RETRIEVED FROM DSD OBSERVATIONS.	107
FIGURE 5-3: COEFFICIENTS OF THE K-R LAW FITTED	108
FIGURE 5-4: RECORDS OF THE BANIZOUMBOU STATION	116
FIGURE 5-5: : RELATIVE DIFFERENCES IN RAINFALL ESTIMATION WITH K-R.....	119
FIGURE 5-6: K-R LAWS CONSIDERING DIFFERENT POLARIZATIONS.	120
FIGURE 5-7: RELATIVE DIFFERENCE ON RAINFALL DUE TO DIFFERENT POLARIZATION ...	121

FIGURE 5-8: RELATIVE DIFFERENCE ON RAINFALL DUE TO DIFFERENT POLARIZATION...	121
FIGURE 5-9: RESIDUALS BETWEEN OBSERVED DSD RAINFALL AND FITTED A-R LAW ...	123
FIGURE 5-10: MINIMAL DETECTABLE RAIN 1DB	126
FIGURE 5-11: MINIMAL DETECTABLE RAIN 0.1DB.	127
FIGURE 5-12: RELATIVE UNCERTAINTY DUE TO QUANTIZATION STEP	128
FIGURE 5-13: RELATIVE ERROR DUE TO A 3DB WET ANTENNA ATTENUATION.....	130
FIGURE 6-1: CML ORANGE NETWORK IN NIAMEY.....	138
FIGURE 6-2: AVAILABLE CML DATA PER DAY FOR 2016-2017 SEASONS IN NIAMEY AND HISTOGRAM OF CML LENGTHS IN THE NIAMEY ORANGE NETWORK.	139
FIGURE 6-3: NUMBER OF COLLOCATED SAMPLES IN THE DATA	139
FIGURE 6-4: : EXAMPLE OF RAW ATTENUATION AND BASELINE DETECTION.....	141
FIGURE 6-5: EXAMPLE ATTENUATION MINIMIZATION FOR CALIBRATION 1	145
FIGURE 6-6: AVERAGE BIAS BY CALIBRATION DEPICTED BY RAINFALL RATE AND CML LENGTH CLASS.	148
FIGURE 6-7: RELAITVE BIAS BY CALIBRATION DEPICTED BY RAINFALL RATE AND CML LENGTH CLASS.	149
FIGURE 6-8: BIAS DECOMPOSITION BY CALIBRATION DEPICTED BY RAINFALL RATE.	149
FIGURE 6-9: BOOTSTRAPPING OF CALIBRATION 1	150
FIGURE 6-10: BOOTSTRAPPING OF CALIBRATION 1 (FILTERED).....	151
FIGURE 6-11: BOOTSTRAPPING OF CALIBRATION 2	152
FIGURE 6-12: BOOTSTRAPPING OF CALIBRATION 2 (FILTERED).....	152
FIGURE 6-13: BOOTSTRAPPING OF CALIBRATION 3	153
FIGURE 6-14: BOOTSTRAPPING OF CALIBRATION 3 (FILTERED).....	154
FIGURE 6-15: RELATIVE BIAS OF RAINFALL FOR CALIBRATION 3.	156
FIGURE 6-16: RELATIVE BIAS OF RAINFALL FOR CALIBRATION 3	157
FIGURE 6-17: : COMPARISON OF THE DIFFERENT CALIBRATIONS OF WET ANTENNA ATTENUATION (FOR BOTH ANTENNAS)	158

FIGURE 6-18: SCATTERPLOTS OF SPECIFIC ATTENUATION K OF CML AFTER WET ANTENNA CORRECTION VERSUS RAIN GAGE RAINFALL FOR CALIBRATION 2	160
FIGURE 6-19: SCATTERPLOTS OF RETRIEVED CML RAINFALL VERSUS RAIN GAGE RAINFALL FOR CALIBRATION 1 (FILTERED)	161
FIGURE 6-20: : SCATTERPLOTS OF RETRIEVED CML RAINFALL VERSUS RAIN GAGE RAINFALL FOR CALIBRATION 2 (FILTERED).....	162
FIGURE 6-21: SCATTERPLOTS OF RETRIEVED CML RAINFALL VERSUS RAIN GAGE RAINFALL FOR CALIBRATION 3 (FILTERED) WITH G=0.65.....	163
FIGURE 6-22: DAILY RAINFALL TIME SERIES FOR RAIN GAGE AND CML BY LENGTH CLASS FOR CALIBRATION 1	165
FIGURE 6-23: DAILY RAINFALL TIME SERIES FOR RAIN GAGE AND CML BY LENGTH CLASS FOR CALIBRATION 2.	165
FIGURE 6-24: DAILY RAINFALL TIME SERIES FOR RAIN GAGE AND CML BY LENGTH CLASS FOR CALIBRATION 3.	167
FIGURE 6-25: DAILY RAINFALL TIME SERIES FOR RAIN GAGE AND CML BY LENGTH CLASS FOR CALIBRATION 3 BIS.....	167
FIGURE 6-26: : RELATIVE BIAS DECOMPOSITION FOR CALIBRATION 1	168
FIGURE 6-27: RELATIVE BIAS DECOMPOSITION FOR CALIBRATION 2	169
FIGURE 6-28: RELATIVE BIAS DECOMPOSITION FOR CALIBRATION 3	169
FIGURE 6-29: RELATIVE BIAS DECOMPOSITION FOR CALIBRATION 3 BIS	170
FIGURE 7-1: ZOOM ON THE NIAMEY CML NETWORK.	178
FIGURE 7-2: EMPIRICAL VARIOGRAM AND FITTED MODEL.	180
FIGURE 7-3: EXAMPLE OF A CML OVER A REGULAR GRID.	182
FIGURE 7-4: ARCHITECTURE OF THE NN USED IN THIS STUDY	184
FIGURE 7-5: EXAMPLE OF A 15MIN RADAR FIELD.....	188
FIGURE 7-6: EXAMPLE OF MAPPINGS FOR THE THREE METHODS.....	190
FIGURE 7-7: R2 MAPS OF THE THREE MAPPING METHODS COMPARED TO THE REFERENCE RADAR RAIN FIELD	193

FIGURE 7-8: BIAS MAPS OF THE THREE MAPPING METHODS COMPARED TO THE REFERENCE RADAR RAIN FIELD	194
FIGURE 7-9: TAYLOR’S DIAGRAMS OF THE THREE METHODS FOR EACH DIFFERENT NETWORK.....	196
FIGURE 7-10: TAYLOR DIAGRAM OF THE THREE METHODS OF INTERPOLATION APPLIED TO REAL DATA FOR NIAMEY	200
FIGURE A 1: CORRELOGRAMS FOR 16 CML IN NIAMEY.	217
FIGURE A 2: EXAMPLE OF ATTENUATION MINIMIZATION FOR MODEL 1	218
FIGURE A 3: EXAMPLE OF ATTENUATION MINIMIZATION FOR MODEL 1 (FILTERED)	219
FIGURE A 4: EXAMPLE ATTENUATION MINIMIZATION FOR MODEL 1 18GHZ.....	219
FIGURE A 5: EXAMPLE ATTENUATION MINIMIZATION FOR MODEL 1 (FILTERED) 18GHZ	220
FIGURE A 6: EXAMPLE ATTENUATION MINIMIZATION FOR MODEL 2	220
FIGURE A 7: EXAMPLE ATTENUATION MINIMIZATION FOR MODEL 2 (FILTERED)	221
FIGURE A 8: EXAMPLE ATTENUATION MINIMIZATION FOR MODEL 2 18GHZ	221
FIGURE A 9: EXAMPLE ATTENUATION MINIMIZATION FOR MODEL 2 (FILTERED) 18GHZ.....	222
FIGURE A 10: RADAR FIELD OF RETRIEVED EQUIVOLUMETRIC MEDIAN DIAMETER DM..	225
FIGURE A 11: SCATTERPLOTS OF SIMULATED CML SAMPLING VERSUS RAINGAGE SAMPLING WITH RADAR DSD FIELDS	229
FIGURE A 12: ADDITIONAL EXAMPLES OF MAPPING TECHNIQUES.....	231
FIGURE A 13:ADDITIONAL EXAMPLES OF MAPPING TECHNIQUES.....	232
FIGURE A 14: ADDITIONAL EXAMPLES OF MAPPING TECHNIQUES.....	233
FIGURE A 15: ADDITIONAL EXAMPLES OF MAPPING TECHNIQUES.....	234
FIGURE A 16: BIAS MAPS BY METHOD AND ATTENUATION QUANTIFICATION FOR DOUALA CML NETWORK.	235
FIGURE A 17: BIAS MAPS BY METHOD AND ATTENUATION QUANTIFICATION FOR NIAMEY CML NETWORK.	235

FIGURE A 18: R2 MAPS BY METHOD AND ATTENUATION QUANTIFICATION FOR DOUALA CML NETWORK.	236
FIGURE A 19: R2 MAPS BY METHOD AND ATTENUATION QUANTIFICATION FOR DOUALA CML NETWORK.	236
FIGURE A 20: R2 MAPS BY METHOD AND ATTENUATION QUANTIFICATION FOR DOUALA CML NETWORK.	237

LIST OF ABBREVIATIONS AND ACRONYMS

ANDS99: Andsanger et al. 1999 aspect ratio law

AMMA-CATCH : Analyse Multidisciplinaire de la Mousson Africaine – Couplage de l'Atmosphère Tropicale et du Cycle Hydrologique

CML: Commercial Microwave Link

DBS: Dual Beam Spectropluviometer

DSD: Drop Size Distribution

EM: Electro-Magnetic waves

GPCC: Global Precipitation Climatology Center

ILLI02: Illingworth et al. 2002 aspect ratio law

IR: Infrared radiation

IRD : Institut de Recherche pour le Développement (French research institution)

LIN1: Aspect ratio law from Gorgucci et al. 2000 with $\beta_e = 0.052$

LIN5: Aspect ratio law from Gorgucci et al. 2000 with $\beta_e = 0.072$

LWC: Liquid Water Content

MCS : Mesoscale Convective Systems

MT : Megha-Tropiques satellite

MP: Marshall-Palmer parameterization of the DSD

MW : Microwaves

PPI : Plan Position Indicator

QPE : Quantitative Precipitation Estimate

RAINCELL: for Rain Measurement from Cellular network ; Name of the Scientific program initiated in Africa by IRD to monitor rainfall with CML

UV: Ultraviolet radiation

WMO: World Meteorological Organization

X-PORT: Name of the X-band doppler dual polarization radar developed by IRD/IGE (F. Cazenave and M. Gosset) that operated in West-Africa

INTRODUCTION

Rainfall is a major variable in the water cycle. Because it is the main entry for fresh water to continental surfaces, it has a great impact on human societies. Hence, it is a key parameter for hydrological forecast, crop modelling and hazard management. The precipitating systems plays a major role in the energy budget of the planet. Due to its spatial and temporal variability and its intermittency, the measurement of rainfall is a challenge. The uncertainties associated with the quantitative estimation of rainfall need to be understood and quantified for several applications.

The West African monsoon season, which lasts from May to October, provides the yearly rainfall accumulation in this region. It is mainly driven by large organized convective storms associated with intense rainfall rates that can lead to flood events. As elsewhere in the tropics, rainfall in West Africa is poorly monitored due to the scarcity of the operational meteorological networks.

Rainfall measurement can be ground or satellite based. Ground based measurements are made with rain gages, disdrometers, radars or commercial microwave links which sample the hydrometeors or the rainfall accumulations from ground level. They can be direct measurements or based on remote sensing. Satellite measurements are based on remote sensing techniques which use the interaction between hydrometeors and electromagnetic radiation to retrieve information about the hydrometeors in the sampled volume. Microwave remote sensing of precipitation can be used to infer the spatial distribution

Introduction

and physical properties of hydrometeors in horizontal and vertical scales. When they grow, the frozen hydrometeors start falling and melting, producing precipitations.

Rain gages are the historical mean to measure rainfall. They are often considered as the ground truth because their measurement principle is simple and quite direct. Rain gauges, however, sample only an area of a few hundred of cm^2 and the spatial representativity of their measurement is therefore limited.

Meteorological radars, developed in the second half of the 20th century, are the main instrument for ground-based active remote sensing of rainfall. An important asset of radars is their resolution which offer a fine horizontal and vertical sampling of precipitating systems. They provide an indirect measurement of precipitation: the main variable measured by a radar is the back-scattered power due to the scattering of microwaves by hydrometeors. The back-scattering is very sensitive to the phase of the hydrometeors: water drops are much more sensitive to microwaves than frozen hydrometeors. Some radar systems can use polarized emitted signals adding a layer of information: they use the differential response in vertical and horizontal polarizations to better characterize the precipitation. Empirical relationships are often used to convert the radar observables into physical quantities leading to estimation uncertainties. Radars are the major instrument for rainfall monitoring, but they are expensive instruments affordable only in rich countries.

In the past ten years, an innovative technique to measure rainfall has emerged based on commercial microwave links (hereafter CML). The method is based on the rainfall induced attenuation of the EM signal between a pair of antennas. The attenuation levels of the CML are monitored by the telecom companies to survey their network. Telecom companies ensure the installation and maintenance costs. They are an alternative to radars and rain gauges in ill-equipped regions but they are unequally distributed over territories with dense networks in highly populated areas.

Satellites provide a global coverage of rainfall but the measurements are indirect. Different types of instruments exist based on infra-red or microwave observations. The microwave-based instruments can be passive or active sensors. Active sensors are radars, based on the same principle as ground based radars. Passive sensors measure the brightness temperature in different wavelengths at the top of the clouds. The retrieval of physical characteristics of rainfall with passive satellites depends on the modeling of the characteristics of the hydrometeors in the atmospheric column. Rainfall estimation with

Introduction

satellites is still subjected to important uncertainties (Gosset et al. 2013; Gosset et al. 2018; Kirstetter, Viltard, and Gosset 2013) and coarse resolutions (~25km for 3h (Guilloteau, Roca, and Gosset 2016)) which are inappropriate for small scale studies (such as flash floods in small catchments).

This thesis is the result of several years of work developed as an engineer. My first mission consisted in the validation of Megha-Tropiques satellite products with ground reference rainfall data. The Megha-Tropiques (*MT*) satellite mission (Roca et al. 2015) is dedicated to monitor the water and energy cycle in the tropical atmosphere with passive microwave radiometry. The original feature of the satellite is its tropical orbit (a low inclination orbit), which decrease the revisiting time span in the tropics, increasing the daily microwave (MW) observations and improving the gridded accumulated rainfall products. The Megha-Tropiques Ground Validation campaign (MTGV) gathered different types of observations of mesoscale convective systems in West Africa. The main goal of the campaign was to evaluate the performance of the satellite rainfall products. It also became an opportunity to combine different types of observations of precipitating systems as airborne observations were supplemented with a ground based dual-polarization radar (X-port). In addition to my duties I was able to carry out research on dual-polarization radar to improve the characterization of the sampled hydrometeors. The first part of this thesis deals with the development of two techniques using meteorological radar data to extract information on hydrometeors.

The first original technique developed consist in the retrieval of the density of the icy hydrometeors above the 0°C isotherm with the modeling of the observation of the melting layer by the radar. The density retrievals were validated with the *in-situ* airborne observations. The density of icy hydrometeors impacts the passive microwave observation from satellites as the hydrometeors have different scattering properties depending on their density. Obtaining information regarding the density of hydrometeors above the melting layer could improve rainfall retrieval from satellites.

The second original technique presented in this thesis is the retrieval of the drop size distribution (DSD) by inversion of polarimetric radar data. The drop size distribution variability is one of the main sources of uncertainty in radar and microwave link rainfall retrievals, as the relations linking radar observables and drops are not constant. Radar polarimetry facilitates accessing information about the differential response of the hydrometeors as seen by the horizontal and vertical channels of the radar. That differential

Introduction

response is linked to the drop size distribution. X-band radars are strongly affected by attenuation. Usually, in literature, a two-step procedure is used to retrieve drop size distributions from polarimetric radar: first an attenuation correction is obtained and later, a retrieval of the DSD with empirical relations. In the proposed inversion of the DSD in this thesis, the retrieval is performed on the uncorrected radar variables, thus avoiding the empirical approximation of the attenuation. The retrieval is not based on empirical relations but in a physical model of scattering.

Both techniques developed have a similar approach: first a model is used to simulate the observations and then an original inversion technique is applied to retrieve the physical characteristics of the hydrometeors in the sampled volume.

My second mission as an engineer was the data processing of commercial microwave links in West-African countries. The RAIN CELL project began as a solution to increase the ground based data for the validation of MEGHA-TROPIQUES satellite products. Beginning in 2012, it was developed in the framework of a collaboration between IRD (Institut de Recherche pour le Développement) and the telecom company Orange.

Later, the objective of the project was to show the potential use of CML to monitor rainfall on real time in small scales (i.e. cities) so that an urban hydrological model could be fed in order to forecast flood episodes. First the validation of the measurement of rainfall with CML needed to be addressed. Two seasons of data (2016-2017) were provided for the CML network in the city of Niamey, Niger from Orange-Niger. The second part of this thesis starts with an introductory chapter on the principle of rainfall measurement with CML followed by the quantitative evaluation of the data set in Niger.

The final objective was to combine CML observations to produce rainfall maps to feed hydrological models. The last chapter of this thesis introduce a prospective method to combine heterogeneous information from dense CML networks to retrieve rainfall maps on a city-scale.

The thesis is organized in two parts introduced by a general chapter (Chap. 1). The first part is dedicated to the retrieval of the physical characteristics of precipitation with polarimetric radar. It is composed by three chapters. Chapter 2 describes the physics of the radar measurement. Chapter 3 describes the ice particles density retrieval by inverting the melting layer observation. Chapter 4 describes the inversion of polarimetric radar variables at attenuating frequencies to retrieve the drop size distribution.

Introduction

The second part of the thesis introduces the commercial microwave links for rainfall monitoring. The first chapter (Chap 5) describes how CML rainfall measurement operates, considering its uncertainties. Chapter 6 describes the assessment of the CML Niamey measurements and analyzes the CML-gage comparison. The concluding chapter 7 introduces an original method to retrieve rainfall maps from a network of CML based on machine learning of radar rainfall maps.

1 RAINFALL

CHARACTERISTICS AND MEASUREMENT IN WEST AFRICA

As in most of the tropics, rainfall in West Africa is driven by convection leading to intense precipitation. The Sahel climate is characterized by a wet season which runs from May to October and a dry season from November to April with almost no rainfall accumulation. During the wet season in the Sahel a small number of strong events account for most of the annual precipitation. Rainfall in such events is characterized by strong horizontal variability and a particular vertical structure.

In the first part of this chapter we describe the organization, structure and composition of rainfall systems in the study region. Later we describe the different ground-based instruments to measure rainfall and their particular benefits. A section is dedicated to raise explicitly the scientific questions addressed in this work. Finally, we describe the context and the data sets used.

1.1 The organization and structure of rainfall systems in the study region

Mesoscale convective systems

Mesoscale convective systems (MCS) accounts for the majority of the rainfall in the tropics and on Earth (Roca et al. 2014). They have a strong impact in water resources in tropical regions and they can also generate floods due the associated violent rainfall rates.

A precipitating system is considered a MCS when it produces a contiguous precipitation area of 100km or more in at least one direction. They are formed by a convective front area of buoyant moist air creating strong precipitation rates and by a stratiform cloud area associated with light and medium rain rates.

In this region the climatic conditions lead to rapidly moving squall lines (~60 km/hr) and a seasonal dependence of precipitations. In the Sahel region 80% of the precipitation comes from convective rainfall cells, in the front of the squall line (Houze 2004).

Microphysics in MCS

Hydrometeors are atmospheric particles formed by water molecules in ice or liquid phase. The condensation of water vapor requires condensation nuclei (aerosols) to start the phase transition. Hydrometeors can be in liquid or ice phase, depending on the temperature of the atmospheric layer and the generation process. Two principal growth mechanisms can initiate the precipitation of hydrometeors: condensation/riming and coalescence with other hydrometeors. By growing, the hydrometeors become heavier and start falling.

Above the freezing level of the atmosphere (0°C isotherm) the hydrometeors are usually in the form of ice particles. The microphysical processes involved in the formation and evolution of the particles are numerous and complex. The dynamical growing processes (aggregation, riming) adds complexity on the resulting geometries and densities of the particles leading to a large fauna of ice crystals. Some atmospheric situation can lead to water drops in super-cooled state (liquid phase with a temperature below freezing point) and the production of graupel.

Under the freezing layer of the atmosphere, precipitating ice particles begin to melt, increasing their density and accelerating their fall, as they become raindrops. The complexity of physical processes involved in hydrometeors generation and evolution in MCS leads to a high spatial variability of the particles quantity and sizes. As we describe later, the particle size distribution (PSD) above the melting layer and the drop size distribution (DSD) of rainfall play an important role in precipitation remote sensing with microwaves.

Figure 1-1 shows images of sampled ice particles from a probe installed in a scientific aircraft during the MTGV validation campaign from (Fontaine et al. 2014).

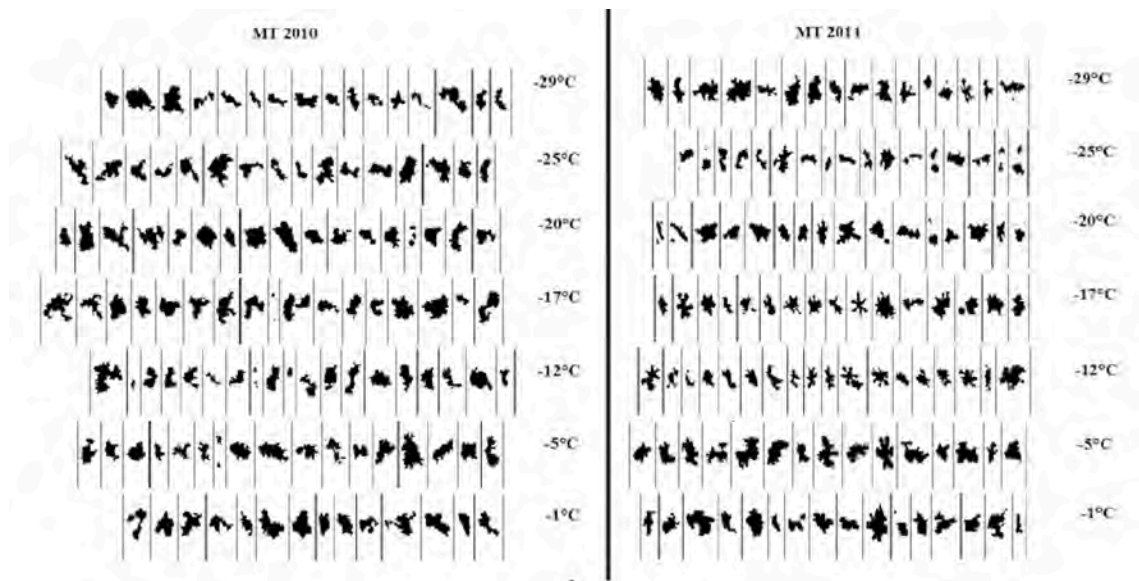


Figure 1-1: Example of 2-D images recorded by the precipitation imaging probe PIP for Megha-Tropiques validation campaigns. Images of hydrometeors presented as a function of temperature. From [Fontaine et al. 2014]

1.2 Ground based measurement of rainfall

In the following section we describe the instruments used to measure rainfall, their assets and limitations are discussed.

1.2.1 Rain gages

Point rain gage measurement

The oldest, simplest and direct method to measure rainfall accumulations is the rain gage. The tipping-bucket gauge is composed by a bucket which swing for a certain volume of water. Each tip time of the bucket is then recorded into an electronic system (or a rolling chart for the old school instruments).

The measurement of rainfall by a rain gage is subjected to different sources of errors. Some common sources of error are the evaporative loss, the instrument calibration, the outsplash of the drops, the levelling of the gage, the instrument sitting and the wind effects. The wind effects are the most important source of error and the more difficult to correct.

(Ciach 2003) used an empirical method using 15 collocated rain gages to derive the errors of local random differences and the effect of bucket sampling when calculating rain rates at different time scales and rain rates: the relative error increase with low rain rates, and increase with shorter time scales. They stated the errors to be 2% for high rain rates (>20mm/h) in 1 hour sampling, 3% for 15 minutes sampling and 6% for 5 minutes sampling.

Rain gages are considered the reference rainfall measurement, but their measurements are associated with a significant uncertainty. The rainfall measurement uncertainty of a raingage should be considered when using it as a reference.

Representativity and interpolation

For many applications there is a need of spatial averages of rainfall instead of local measures as rain gage do. As we pointed out, rainfall is extremely variable and intermittent in space and time. Using a reduced number of rain gages over an area can lead to wrong estimations of the mean areal rainfall. The concept of ‘representativity’ of a rain gage measurement arises: to which extent can a single (or multiple rain gages) account for the mean areal surface rain in a certain spatio-temporal scale?

An example is the impact of the rainfall variability in a hydrology model: the output water flow (for floods or outflow prediction) can be impacted by a wrong estimation of rainfall, leading to a wrong calibration or initialization of the hydrological model (Arnaud et al. 2011; Balme et al. 2006).

Scarcity of measurements

Rain gauges are relatively cheap but dense networks are needed to account for rain variability as discussed. Dense networks require recurrent maintenance to provide reliable data, which represent a cost in human resources. The national meteorological agencies manage synoptic networks of rain gages of variable densities depending on the country wealth. There is a strong inequality on instrument coverage between countries, and regions inside of them. In their work, (Lorenz and Kunstmann 2012) analyze three global atmospheric reanalysis models in terms of precipitation and temperature estimates with independent observations worldwide between 1989 and 2006. They pointed out that the major source of uncertainty in the analysis is the density evolution of the observations through time and space. Figure 1-2 shows decreasing number of rain gauges through 1989-2006 in the global gridded ground rainfall products GPCC (v4.0 v5.0) and CPC (v5.0). The figure shows the small number of reported rain gauges in Africa. Some reasons of the loss reported could be the decrease of investments in meteorology to support the human resources necessary and the instruments substitution, the lack of reliable data filtered by the quality controls procedures or the lack of reporting of the data by the national responsible institutions.

Chapter 1: Rainfall characteristics and measurement in West Africa

In order to have a global perspective about the total number of rain gages reported worldwide, in their recent work (Kidd et al. 2017), estimated the total area of directly measured rainfall compared to a football pitch. They concluded that the actual rainfall surface directly measured worldwide is less than half a football pitch. If we consider near real-time transmitted rain gauges, the surface is equivalent to the center circle of a football field. Even considering that a single rain gauge is representative of an area extended to 5 km from each gage (in daily accumulation), this still only represents about 1% of Earth surface (with a highly inhomogeneous repartition). This statement is even worse if we consider water surfaces (oceans, lakes, seas) where almost no observations exist.

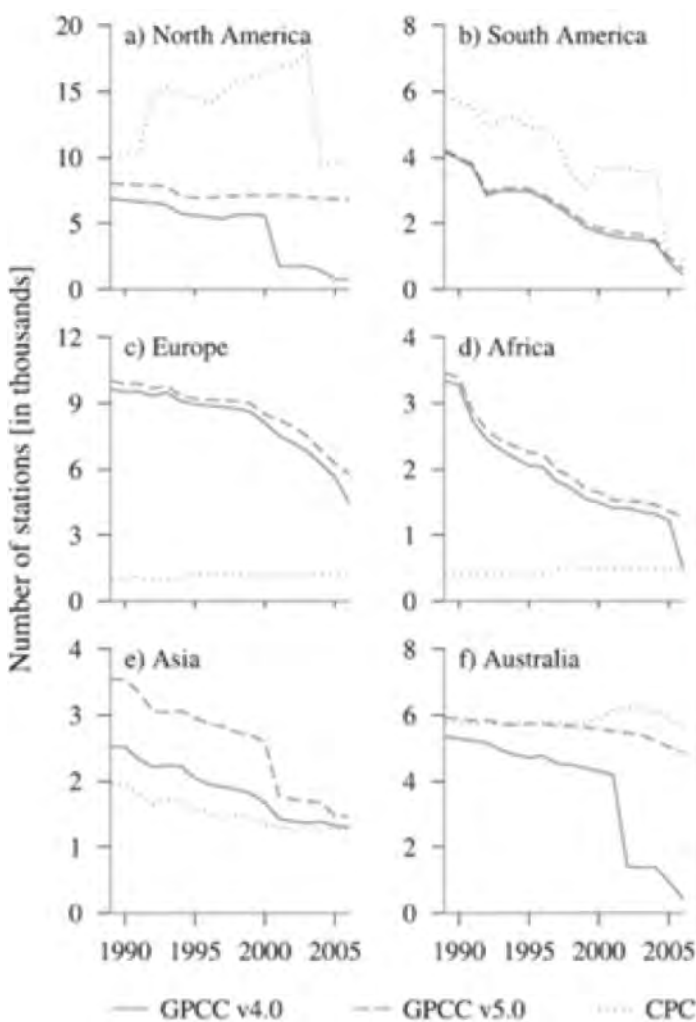


Figure 1-2: Evolutions of the number of rain gages in the GPCP (v4.0 v5.0) and CPC global gridded products per continent. From [Lorenz & Kuntzmann 2012]

1.2.2 Disdrometer

Disdrometers are instruments designed to measure the drop sizes of rainfall. They sample the individual drops deriving into drop size distributions over a time period (ie. the number of drop in several classes of diameter). Disdrometers uses different principles to sample the number of drops and their sizes. Here we describe the Dual Beam Spectropluviometer (DBS) (Delahaye et al. 2006) installed near Djougou, Benin, in 2006 and used in Chapter 4 for validation of the retrieved DSD from polarimetric radar.

The DBS instrument is composed by a double infrared beam and a system of lens which project the IR beam. The sensor measures a signal depending on the quantity of energy received. The amplitude and duration of the signal due to a raindrop transit are a function of the vertical section of the drop and the crossing time in the volume. A correct processing of the signal allows to retrieve the equivalent diameter of the raindrop. The raindrop falling speed is deduced with the crossing time through the IR beam.

Disdrometers have also their sources of errors. Small drops, with diameters smaller than the resolution limit, are not measured. Also the biggest drops, having a strong impact on microwave observation of rainfall, can be under represented for small sampling times. The wind and two simultaneous drops can also be sources of errors.

1.2.3 Meteorological radar

Principle

Radars (for RAdio Detection And Ranging) are composed by a microwave emitter and an antenna which detects the reflected power over time. The localization of the target is based on the antenna direction and the time measurement between the emission and the reception signal, converted into distance with the speed of light in the atmosphere. The maximum available range is limited by the time span between two pulses and by the emission power and the attenuation (which depends on the wavelength). Due to the beam opening angle (given by the antenna characteristics, diagram on figure 1-3) and the pulse duration, the radar resolution volume is a quasi-cone section (neglecting the second lobes

of the antenna emission diagram). The volume resolution size become bigger for increasing ranges.

Hydrometeors reflect the MW radiation: the total reflected power depends on the amount, sizes and phase of the hydrometeors. The frequency of the MW signal has an impact on the amount of reflected energy and the attenuation of the signal along its propagation. The operational radars for weather monitoring are C or S band as the maximal range is high and the attenuation by water drops is low. But higher wavelength (lower frequency) involves big antennas and leads to expensive radars for maintenance and operation. Research radars are often X-band (~10 GHz) as they offer an easier mobility and cost.

Quantitative Precipitation Estimate

The principal objective of operational radars is the quantitative precipitation estimation (QPE). Traditional radars measure the received power converted into reflectivity, a property of the hydrometeors present in the resolution volume. Reflectivity factor is closely linked to the drop size distribution (DSD) of the hydrometeors. The link between reflectivity and rainfall rate is not straightforward: both are moments of different order of the DSD. The precipitation (R) estimation through reflectivity factor (Z) is usually done through Z-R power laws which contains implicit assumptions on the DSD. Z-R laws are empirically calibrated with collocated measures of rain gage and radars, or with disdrometer measurements. Such laws are very noisy due to the DSD variability. The reflectivity is quantitatively more impacted by large drops than the rainfall rate. The variability of the DSD is the main source of uncertainty in the precipitation estimation through radar.

3D scanning geometry

Radars emits a pulse in a certain azimuth and elevation and moves to sample the desired zone. The azimuth $\varphi \in [0,360]$ is the angle with the north direction (clock wise) and the elevation $\theta \in [0,90]$ is the angle with the horizontal. Usually, meteorological radars for rainfall monitoring visit all the azimuths (with a certain angular resolution) and after changes the elevation to revisit the azimuths for different heights over the ranges. A visit over all azimuth for a certain elevation is called PPI (Plan Position Indicator). Figure 1-4 shows the 3D geometry of the radar measurement for 5 PPI at different elevations.

With this particular scanning geometry, radars sample the horizontal spatial variability of precipitation inside the systems. The vertical evolution of precipitation is also observed; radars access the layers of the atmosphere where the frozen hydrometeors are generated. The melting layer of hydrometeors, located at the 0°C isotherm has a particular signature when observed by radars. An artifact of the observation creates a peak of reflectivity on the melting layer (bright band) due to the high reflectivity of melting hydrometeors. Most studies concerning the bright band focus on its correction for QPE, which can create errors. While the bright band artifact depends on the properties of hydrometeors melting, we can use the bright band observation to infer hydrometeors properties.

Polarimetry, adding information

Polarimetric radars emit pulses at horizontal and vertical polarizations (H and V channels) adding information with the differences in the returned echoes. The differences of H and V channels comes from the hydrometeor's anisotropy: horizontal polarization echoes in rainfall are more intense due the oblateness of large raindrops (Chapter 2). Polarimetric radars measure the received power at H and V polarizations, but also the phase shift of the EM wave between the two channels. The differential phase of H and V channels is impacted during the propagation in an anisotropic scattering medium (Bringi and Chandrasekar 2001).

The QPE estimation with polarimetric radar benefits from additional information improving the estimations. For X-band radars the attenuation correction is a crucial step, as the attenuation is high. With polarimetry we can estimate the attenuation with the phase shift propagative variable. The phase shift between H and V channels is also closely linked to rainfall rate. Rainfall estimation with the phase shift usually performs better than the above mentioned Z-R relations based only on reflectivity factor. Though, the phase shift-rainfall relations are also power laws empirically established.

The additional information provided by polarimetry can improve the characterization of the average properties of the hydrometeors in the resolution volume. Polarimetric information can be used to constrain the modelling of the interaction between MW and hydrometeors.

Radars in the tropics

Radars are the reference instrument to measure the spatial variability of precipitation, but they are expensive instruments which require regular maintenance. Operational weather agencies in developed countries have networks of radars which cover the country-wide scale. In developing countries, the access to such instruments is prohibitive. Figure 1-5 from WMO shows the location of reported meteorological radars in the world. We can notice the lack of instruments in Africa.

In West-Africa it does not exist such equipment in an operational framework. Some scientific campaigns installed radars for short time period to measure MCS, in order to better understand the systems composing the monsoon.

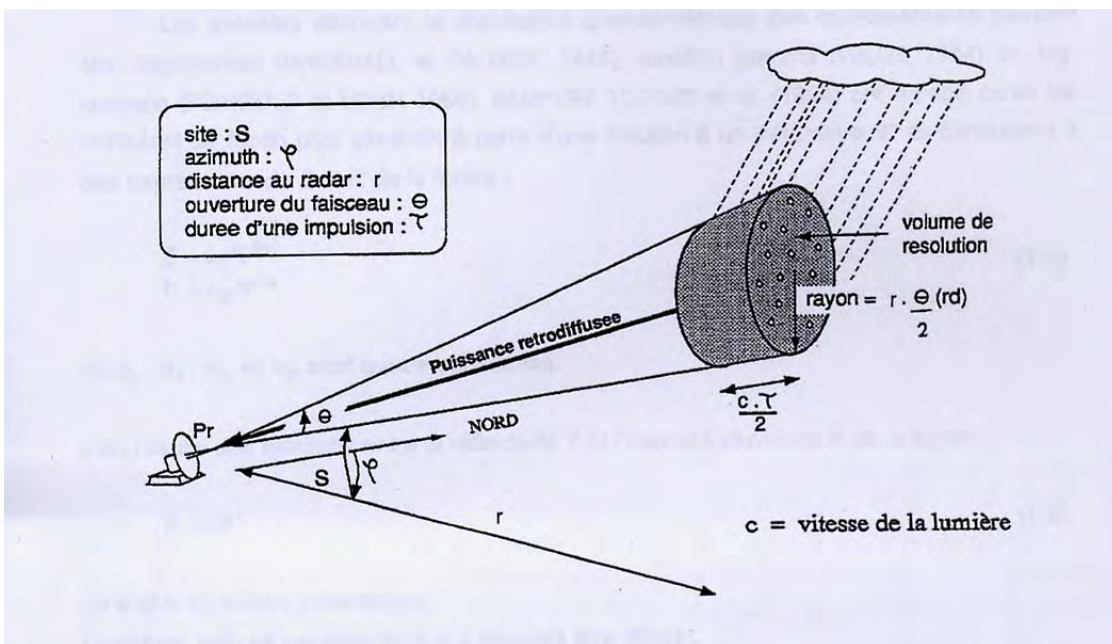


Figure 1-3: Volume resolution of radar measurement

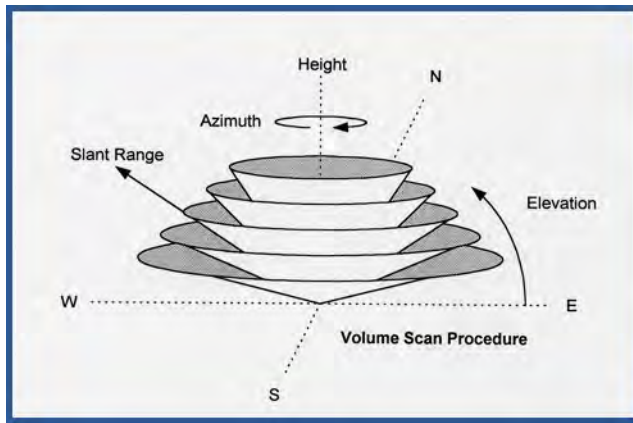


Figure 1-4: : Measurement geometry of meteorological radar

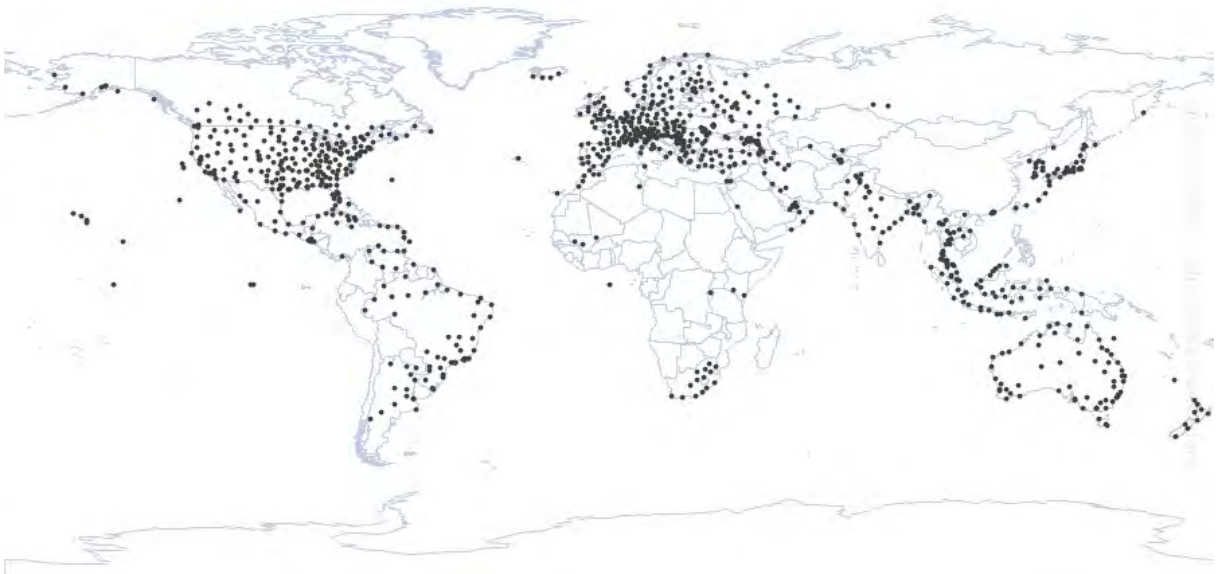


Figure 1-5: Location of reported radars (all bands and dual-single polarizations) from WMO radar database (2019).

1.2.4 Commercial microwave links

Origin

Since the early development of microwave telecommunication networks in the 70', engineers considered the microwave signals attenuation due to rainfall to avoid signal extinctions. Some early works made the first quantification on the signal's attenuation due to rainfall in order to prevent signal loss (Atlas and Ulbrich 1977; Semplak and Turrin 1969; Olsen, Rogers, and Hodge 1978).

The utilization of CML for rainfall observation was developed in the last decade as an opportunistic measure using operational equipment of telecommunication companies, benefitting from their maintenance. (Messer 2006; Overeem, Leijnse, and Uijlenhoet 2013; Doumounia et al. 2014). The rainfall estimation is based on the measuring of the rainfall induced attenuation. The attenuation of CML is usually monitored by the telecom companies to evaluate their network.

CML in Africa

In developing countries, the operational meteorological observation networks are scarce while the mobile telephony is growing rapidly. A technological jump occurred in such countries: the line telephony was not developed, especially in rural areas, while today the mobile telephony is widely spread, even in villages with no power connection.

The increasing demography and the economic development are boosting the development of the backhaul networks. Also the evolution of protocols, 3G/4G/5G will impact the networks. Today the smartphone penetration and internet accessibility are low in West-Africa. But we can expect an evolution in the next years due to the emergence of low cost smartphones and the future development of 5G technology, which can increase the number of CML and the range of used microwave frequencies.

CML for precipitation monitoring is an interesting solution to complement ground observation in under equipped countries. As the networks are constantly monitored by the telecom companies, the observation can be done potentially in real time frameworks.

Geographical distribution

Telecommunication companies use the backhaul microwave network of antennas to transmit their information in a country wide scale. The density of CML is closely related to the population density. In cities, dense networks are used to collect signals from all the neighborhoods. The number of CML in a city exceed several hundreds of CML. For example, the city of Bamako, Mali has 700 CML, Yaounde in Cameroon around 200 CML, Douala, Cameroon, 300 and Niamey 100 for the Orange network. Such density of ground measurement of rainfall is unique, even for developed countries. Outside cities, longer CML interconnects villages with central nodes of the telecom company. The country wide coverage of CML and the high densities in cities offers new perspectives on rainfall monitoring. The combination of such rich densities of heterogeneous measurements and the merging with classical observation are open questions.

Indirect measurement

However, the rainfall observation with commercial microwave links is not straightforward. CML are not optimized for rainfall measuring. The sampling is controlled by the equipment of the telecom company. As we use information of a private company, we do not have access to the instrument setup. Sometimes the collected information is not the optimal information which we would collect in a scientific dedicated experiment.

Integrated measurement

The CML attenuation due to rainfall is linked to the average rainfall rate in the CML path. It is a 'lineal' integrated measurement. Integrated measurements are interesting for hydrology due to the poor spatial representativity of a raingage as discussed. Usually hydrological models need the integrated rainfall over an area (watershed) instead of ponctual measurements.

The attenuation-rainfall relation is almost linear (depending on the signal frequency) which reduces the impact of the rainfall variability inside the CML. The microwave attenuation is closer to the rainfall rate than the radar reflectivity factor (Z). The rainfall estimation by attenuation measurement is an effective technique as we will see in part 2 of this thesis.

1.3 Main scientific questions

This section points out the main scientific questions that we will try to develop in this work.

Radar to characterize precipitation

The first part of this thesis concerns the retrieval of the precipitation characteristics with polarimetric radar.

- Can a radar observational artifact be used to characterize physical properties of the scatters?
- At which level can a simple modelization of the melting layer observation bring information?
- Can we derive drop size distribution constraining an observational model with polarimetric information?
- Can we avoid using empirical relations, using a physical model of the observation to derive DSD parameters?

Commercial Microwave Links to measure precipitation

The second part of the thesis concerns the use of CML to measure precipitation

- Can we evaluate the uncertainties related to precipitation monitoring with CML?
- How can we calibrate CML observation with a reference observation?
- How can we combine dense network of CML to produce rainfall maps?

1.4 Data used in the present work

In this section we present the different datasets used to address the presented scientific questions. We present the X-port polarimetric radar and their different locations in West-Africa. Later we present the CML dataset provided by Orange in Niamey, and the rain gages used to evaluate the rainfall retrieval with CML.

1.4.1 X-Port radar



Figure 1-6: X-port radar location in Ouagadougou, Burkina-Faso in 2012 with a squall line front and the associated dust cloud due to high speed winds.

X-port is an X-band Doppler polarimetric research radar developed by the IRD (Institut de Recherche pour le Développement) to increase the observations in the tropics. X-port was located in 2006 and 2007 in Djougou, Benin, in the framework of the AMMA-CATCH project. AMMA-CATCH is a long term observatory which aims to document the climatic, hydrological and ecological evolutions in West-Africa in a changing climate and increasing demographic pressure.

X-port was moved to Niamey, Niger, in 2010 in the framework of MEGHA-TROPIQUES ground validation campaign. MEGHA-TROPIQUES, a French-Indian satellite mission, was designed to sample the rainfall in the tropics with a frequent revisit. X-port was planned as the ground reference to validate the rainfall satellite products of MEGHA-TROPIQUES. The security situation in Niamey deteriorated in 2011, and the radar was moved to Ouagadougou, Burkina-Faso, for the years 2012-2013 to continue the validation campaign. Figure 1-6 shows X-port radar at its location in Ouagadougou during the rainy season of 2012, in the background we observe the approximation of the convective front of an MCS. Figure 1-7 shows the different location of X-port and the years of the data used in this work.

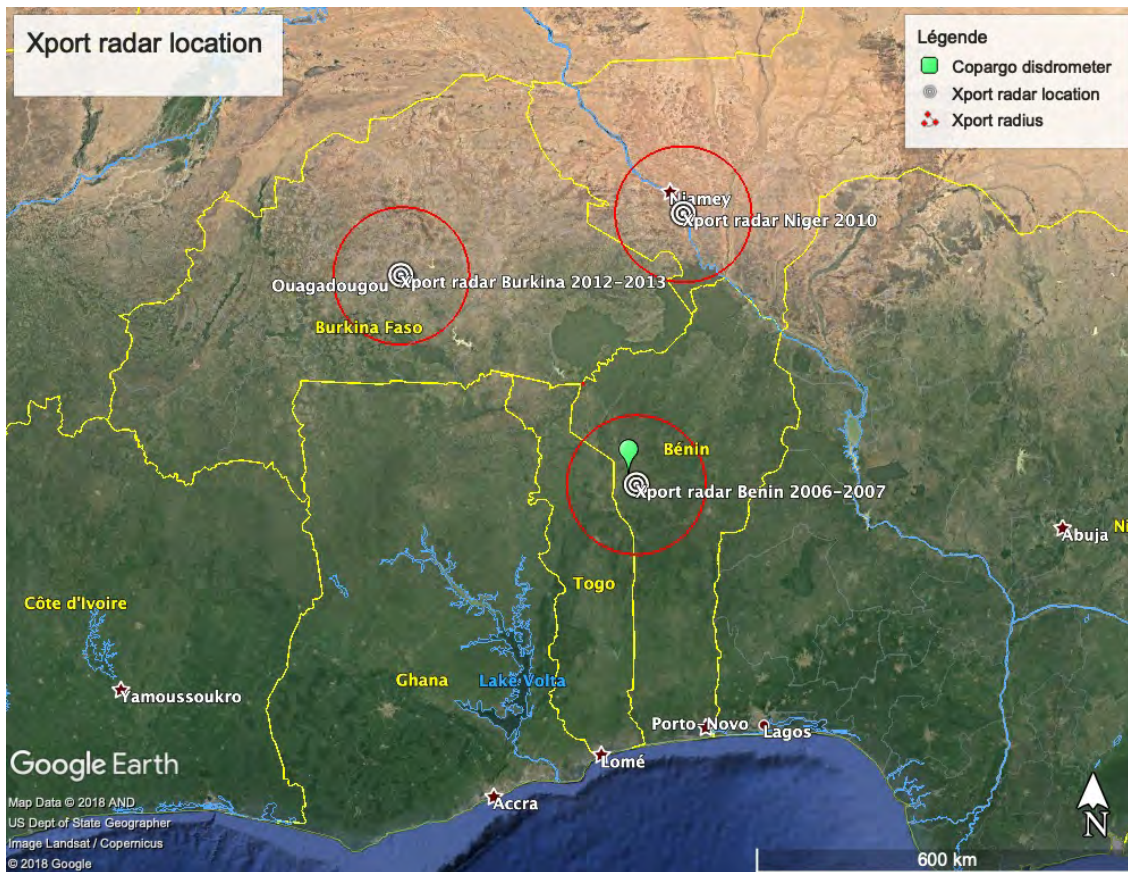


Figure 1-7: Different locations of X-port radar.

1.4.2 Microwave links

During the MEGHA-TROPIQUES ground validation campaign emerged the idea of complementing the X-port and gauges observation with CML data for the validation of satellite rainfall products due to the lack of measures in the tropics, and the Sahel in particular. Contacts with local and international telecom companies began in order to access the data. Telecel-Faso, a Burkina-Faso telecom company acceded to share data from some long CML in the field of view of X-port radar in 2012. The result of the rainfall retrieval was published in (Doumounia et al. 2014). This was a premiere for rainfall observation in Africa with CML.

Later Orange provided two complete rainy seasons (MJJASO) of CML data in Niger for the years 2016 and 2017. The CML are situated in the four mains cities of the country: Niamey, Maradi, Tahoua and Agadez. The total number of links provided by Orange for the best day is 494 (some of them doubled) for the whole country. The number of link's

Chapter 1: Rainfall characteristics and measurement in West Africa

data provided vary for each day due to problems in the operational network and transmission of the data.

In this work we have focused on the CML network of Niamey, the capital of Niger, as the network has the higher density of links and the IRD operates three rain gages in the city from the cited AMMA-CATCH observatory. Figure 1-8 show the location of the 92 CML of the city of Niamey used in the study and the location of three rain gages.

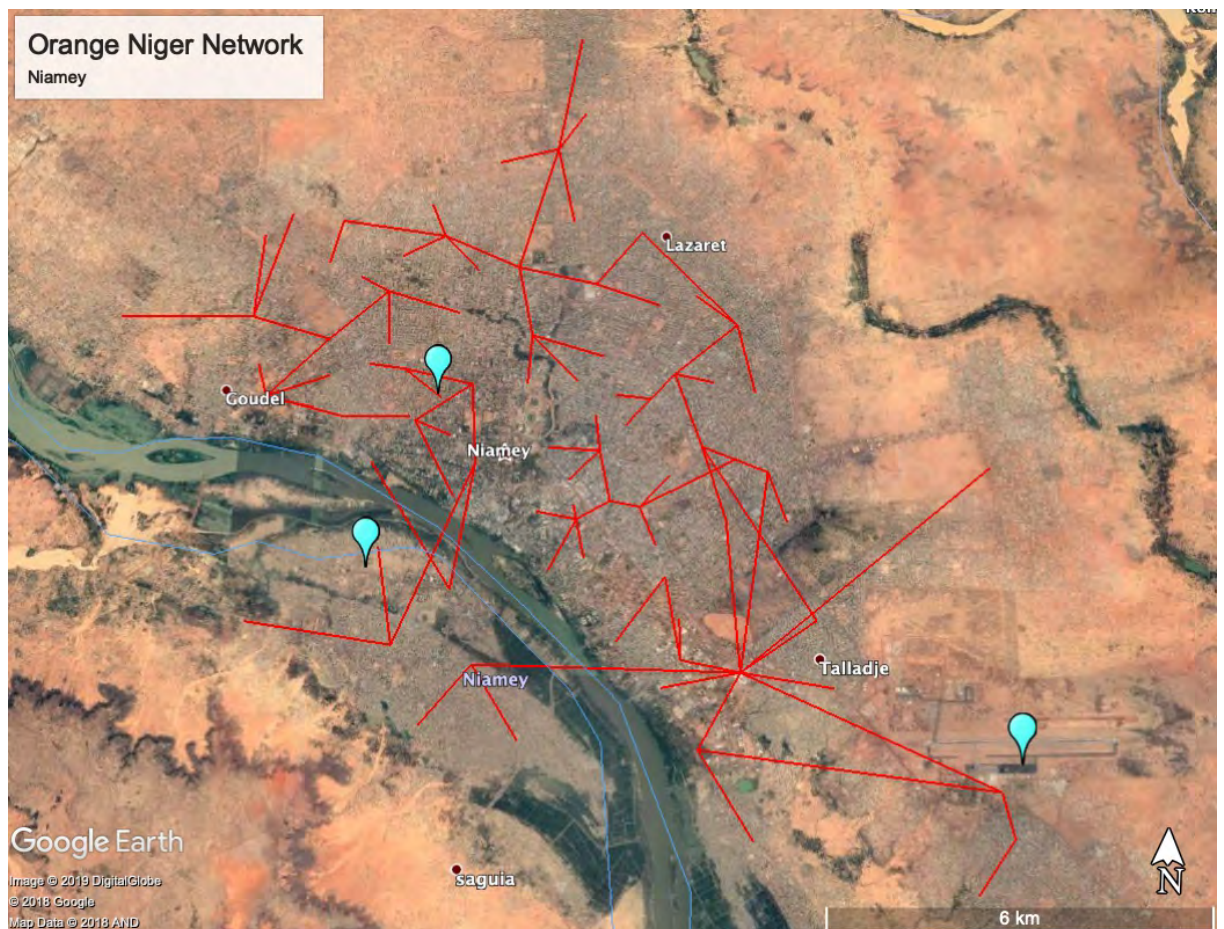


Figure 1-8: CML Orange network in Niamey. Blue dots represent the location of the AMMA-CATCH rain gages

1.4.3 AMMA-CATCH network in Niamey

The AMMA-CATCH observatory presented in the previous section has a long term component in Niger. The Niger rain gage network is composed of 40 to 50 tipping bucket rain gages (depending on the year) in an area of $100 \times 100 \text{ km}^2$. The network was installed in the late 90' and is operational since then. Figure 1-8 shows the location of the gages in the area of Niamey (blue points).

The gages are equipped with 0.5 mm tipping buckets and a collection surface of 400 cm^2 . The maintenance protocol of the instruments includes a GPS time pick up by the technicians at each visit to correct from possible temporal drift of the electronic device. A rainfall accumulator is buried next to each raingage in order to correct the tipping bucket calibration errors. The technicians revisit period is two weeks during the rainy season to ensure the quality of the raingage data.

PART 1

RETRIEVALS OF PHYSICAL CHARACTERISTICS OF PRECIPITATIONS WITH A POLARIMETRIC RADAR

Meteorological radars are a powerful instrument to study hydrometeors. By their particular configuration they can access the lower and upper layers of the precipitating systems, where direct measurements are expensive (flights), difficult to do and risky. Polarimetric radar measures magnitudes (power and differential phase) which are linked to the average characteristics of the hydrometeors in the sampled resolution volume. The sizes, phase and types of the hydrometeors impacts the polarimetric radar measurements.

Compared to conventional radars, polarimetric radar adds information which can improve the quantitative precipitation estimate at ground level. But also, they can be used to identify the frozen hydrometeors above the freezing level to understand the microphysical processes forming such particles.

The hydrometeors classification by type, by their characteristics (density, shape), and by their variability inside a system are essential elements to improve the radiative transfer models in the atmospheric column, which are the basis of passive microwave satellite rainfall retrieval algorithms. Passive microwave sensors in satellites measures brightness temperatures at the top of the clouds which are the result of the radiative processes along the atmosphere. Ice crystals variability have a strong impact on the observed brightness temperatures (Kummerow, Olson, and Giglio 1996; Bennartz and Petty 2001).

Different methods are found in the literature to classify hydrometeors with polarimetric radar measurements. One method is based on fuzzy logic algorithms (Liu and Chandrasekar 2000; Cazenave et al. 2016). In chapter 3 we present a published paper describing an original method to infer the density of the hydrometeors above the bright band of reflectivity (related to the melting layer of frozen particles). The idea is to exploit the shape and size of the bright band to retrieve a density law of the frozen hydrometeors. Previous studies showed the link between the properties of the bright band and microphysical processes aloft (Uijlenhoet, Steiner, and Smith 2003; Fabry and Szyrmer 1999). In this study we present a simple model describing the melting layer: the model do not describe the thermodynamics of the melting layer unlike (Fabry and Zawadzki 1995). The idea is to reproduce the main characteristics of the melting layer, to derive the density of crystals above with an inversion method.

Melted ice crystals become water drops. Their sizes depend on the particle size distribution above the melting layer, and the break-up and coalescence mechanisms during the fall. The first objective of drop size distribution (DSD) retrieval with polarimetric radar is to improve the quantitative precipitation estimates at the ground level, as the DSD is the main source or uncertainty in rainfall retrievals.

DSD retrievals in the literature are often based on empirical relations linking polarimetric radar observables and the DSD parameters. The β -method by (Gorgucci et al. 2002) is based on the derivation of a β parameter of the drop shape law (from radar observables) to later express the parameters of the DSD by β and the observables. Another example is the constrained gamma-method which uses empirical relation between the slope and shape of the DSD from which are derived the relation expressing DSD parameters to radar polarimetric variables.

The majority of the studies are made with C-band radars, associated with a low attenuation of the MW signal by the rainfall. The studies with X-band radar (high MW signal attenuation by rainfall) correct first the attenuation empirically to later derive DSD parameters. (Yoshikawa, Chandrasekar, and Ushio 2014) notice that the 2-step empirical procedure (correction and DSD parameter retrieval) can lead to errors. In the third chapter we present a submitted article describing an inversion method of DSD parameters. The inversion is done on the uncorrected polarimetric variables in a context of high attenuation. The inversion of the whole radar tilt using all the polarimetric information

Chapter 1: Rainfall characteristics and measurement in West Africa

brings coherence to the solution and avoid the 2-steps procedure and the use of empirical relationships.

The two algorithms presented in this section aims to retrieve characteristics of the precipitation with the inversion of radar observations.

2 RADAR MEASUREMENT OF RAINFALL

This chapter introduces the principle of meteorological radar observation. First the radar observables are described. Then the main hydrometeors characteristics impacting the microwave radiation emitted by radars are detailed in order to introduce the techniques developed in chapters 3 and 4. It starts with a description of the usual parameterizations used to describe the water drops and ice hydrometeors. The models to represent the interaction between hydrometeors and microwaves are described at the end.

2.1 Principle of radar measurement

Radars are composed by an active emitter and an antenna emitting pulses of microwaves and measuring the received power back-scattered by the targets. The precipitating systems are scanned in 3 dimensions with the particular geometry of radar measurements (chapter 1). Conventional radars measure the backscattered power. Polarimetric radars emit pulses in horizontal and vertical polarizations. They measure received power from the back-scattered microwave radiation and have also access to the phase of the horizontal and vertical polarizations. The anisotropy of rain drops create different signal in horizontal and vertical polarizations in terms of back-scattered power and phase shift.

The Radar equation

The radar equation links the received power P_r [W] to the emitted power P_e [W] with the reflectivity factor Z of the hydrometeors in a volume V at a distance r by:

$$P_r = P_e C \frac{\pi^5}{\lambda^4} |K|^2 \frac{Z}{r^2} \quad (\text{eq. 2.1})$$

Chapter 2: Radar measurement of rainfall

With C a constant depending on the radar characteristics. K is defined in equation 2.34 from the complex refractive index of the target and λ is the wavelength of the signal. The reflectivity factor Z [mm^6m^{-3}] can be defined in the Rayleigh approximation (section 2.3) as the sum of the sixth power of drop sizes in the volume V :

$$Z = \sum_i D_i^6 \quad (eq. 2.2)$$

The reflectivity factor is an average characteristic of the scatters in the volume resolution, independent from the wavelength λ in the Rayleigh approximation. It is the moment of order 6 of the DSD. Z is usually expressed in [mm^6m^{-3}] but can be expressed in decibels [dB]:

$$Z[dB] = 10\log_{10}(Z[mm^6m^{-3}]) \quad (eq. 2.3)$$

Attenuation through the atmosphere and rainfall

The propagation of the EM wave in a scattering medium leads to progressive attenuation of the signal by diffusion and absorption. The attenuation depends on the frequency of the microwave signal, and on the composition of the propagation medium.

We can define the attenuation of an EM radiation by a medium filled with scatters by the power loss dP as a function of the propagated distance dr , the transmitted power P_e and the extinction cross section of the scatters σ_{ext} by :

$$dP = -(\Sigma \sigma_{ext})P_e dr \quad (eq. 2.4)$$

Then by integrating (eq. 2.4):

$$\frac{P}{P_0} = \exp\left(-\int_0^r \Sigma \sigma_{ext} dr\right) \quad (eq. 2.5)$$

The path integrated attenuation A_t is usually expressed in dB due to its exponential character, thus:

$$A_t[dB] = 10\log_{10}\left(\frac{P}{P_0}\right) = \frac{10}{\ln(10)} \ln\left(\frac{P}{P_0}\right) = -4.343 \int_0^r \Sigma \sigma_{ext} dr \quad (eq. 2.6)$$

$$A_t[dB] = \frac{10}{\ln(10)} \ln\left(\frac{P}{P_0}\right) = -4.343 \int_0^r \Sigma \sigma_{ext} dr \quad (eq. 2.7)$$

Chapter 2: Radar measurement of rainfall

With A_t [dB] the path integrated attenuation. The specific attenuation K_t is defined by unit of length [dB/km]:

$$A_t(r) = \int_0^r K_t dr \quad (eq. 2.8)$$

Considering that $\Sigma \sigma_{ext}$ is the contribution of all the drops in a unity volume of air then equation 2.25 and 2.23 lead to:

$$K_t = 0.4343 \sum_i \sigma_{ext}(i) \quad (eq. 2.9)$$

With K_t in [dB.km⁻¹] and σ_{ext} in [cm²].

For radar observation the attenuation must be corrected to have reliable variables, especially at high frequencies (> 5 GHz) where the effects of attenuation become important for high rainfall rates, associated with convective rainfall (common in the tropics).

Thus the observed uncorrected reflectivity Z^{obs} can be expressed with the integrated attenuation over the path:

$$Z^{obs}(r)[dB] = Z^{corr}(r) - 2 * A_t(r) \quad (eq. 2.10)$$

Where r is the range of the radar observation.

Polarimetric radar observables

Polarimetric radars exploit the asymmetrical shapes of raindrops and ice crystals to obtain integrated information about the observed hydrometeors. The differences on the H and V signals are related to the rainfall drops sizes as the drops flattening depend on their sizes. Big drops have a low axis ratio, i.e. the drops are horizontally flattened, and thus the horizontal polarization signal is more impacted by the drop than the vertical polarization. For ice crystals the polarimetric response is very dependent on the type of crystal as their scattering properties (composition and shape) are very variable.

The horizontal and vertical reflectivity factor $Z_{H,V}$ from the radar received power is:

$$Z_{H,V} = 10 \log_{10} z_{H,V}$$

With $z_{H,V}$ [mm⁶m⁻³] the reflectivity factor deduced from the incoming power for each polarization.

Chapter 2: Radar measurement of rainfall

The differential reflectivity factor Z_{DR} (dB) is defined as:

$$Z_{DR} = Z_H - Z_V = 10 \log \left(\frac{Z_H}{Z_V} \right) \quad (\text{eq. 2.11})$$

Z_{DR} is stronger for bigger drops, as the flattening is higher. For water rain drops $Z_{DR} > 0$, as the drops are larger in the horizontal direction and $Z_H > Z_V$. In some systems needle-shaped crystals can become vertical orientated in the presence of a strong vertical electrostatic field (before a lighting) resulting in a $Z_{DR} < 0$.

The Z_{DR} variable is function of:

- the incidence angle of the incoming EM field (elevation)
- the particle orientation angles
- dielectric constant (or relative permittivity) of the particle
- Aspect ratio of the particle.

The particle orientation and the elevation of the radar (incidence angle) have a strong impact on Z_{DR} measurement. As the water drops have a symmetrical revolution axis vertically oriented (on average), i.e. horizontal flattening, the greater the elevation, the lower Z_{DR} for the same ensemble of drops. For a 90° elevation the drops look symmetrical (circles) and $Z_{DR} = 0$. This property is used to calibrate the Z_{DR} variable on polarimetric radars by observing clouds or light rain at vertical incidence.

The resulting Z_{DR} is weighted by the dielectric constant of hydrometeors ϵ (see section 2.3). For low density snow (dry snowflakes) ϵ is low and $Z_{DR} \rightarrow 1$ even for strongly flattened particles.

The propagation of the MW signal in a scatter medium has two consequences:

- 1/ The attenuation of the signal
- 2/ The progressive phase shift between H and V channels.

The phase shift between H and V channels is due to the propagation of the MW in different volumes of scatters. H polarization crosses more water in his path compare to V polarization

The propagative variables in radar polarimetry are $A_{H,V}, A_{DP}, K_{DP}$ namely, specific attenuation, differential attenuation and specific differential phase shift respectively.

Chapter 2: Radar measurement of rainfall

The specific attenuation (detailed in the previous section) is the basis of rainfall estimation using CML. For radar observation, the polarimetric variables must be corrected from attenuation, especially at X-band frequencies and high rainfall rates when the effects are stronger.

Thus the observed uncorrected variables can be expressed with the integrated attenuation A_H^{tot} over the path:

$$Z_H^{obs}(r) = Z_h(r) - 2A_H^{tot}(r) \quad (eq. 2.12)$$

$$Z_{DR}^{obs}(r) = Z_{DR}^{corr}(r) - 2A_{DP}(r) \quad (eq. 2.13)$$

With A_H^{tot} being the integrative of specific attenuation K_H

$$A_H^{tot} = 2 \int K_H dr \quad (eq. 2.14)$$

And $A_{DP} = K_H - K_V$.

The radar can measure the differential phase shift ϕ_{DP} between H and V channels, which is a cyclic variable and varies in the $[0, 2\pi]$ interval. Considering that the phase shifts in a continuous way during the propagation, the signal is unwrapped to follow a continuous variation. Then we can express the measured phase shift ϕ_{DP} with K_{DP} and δ_{HV} , the back scatter differential phase:

$$\phi_{DP}(i) = 2 \int_0^i K_{DP} dr + \delta_{HV}(i) \quad (eq. 2.15)$$

In Rayleigh regime $\delta_{HV} \approx 0^\circ$ while non zero values of δ_{HV} are indicative of Mie scattering effects [Hubbert and Bringi 1994]. If we consider small or constant δ_{HV} , ϕ_{DP} become the simple integral K_{DP} . Thus we can estimate K_{DP} by filtering ϕ_{DP} (as it is a very noisy variable) and deriving it for each range interval (see chapter 4).

Figures 2-1 and 2-2 shows two examples of radar observables PPI for an MCS system (Chapter 1) from the polarimetric radar X-port installed in north Benin in 2008. The MCS is moving westwards. In the first image at 06h30 UTC the convective front is clearly visible in the horizontal reflectivity peaks of about 60 dBZ related to strong showers. ϕ_{DP} shows also high values in the convective zone. Uncorrected Z_{DR} shows values around $\sim 3dB$ associated with big flattened drops. Behind the convective front the signal is loss due to extinction: the power is absorbed and scattered and the incoming signal is only

noise. The second image at 07h37, once the MCS passed over the radar (at the center) shows the stratiform part of the system hidden in the previous image. The convective front is no longer distinguishable with Z_H due to strong attenuation, but the strong signal in ϕ_{DP} suggests the convective front.

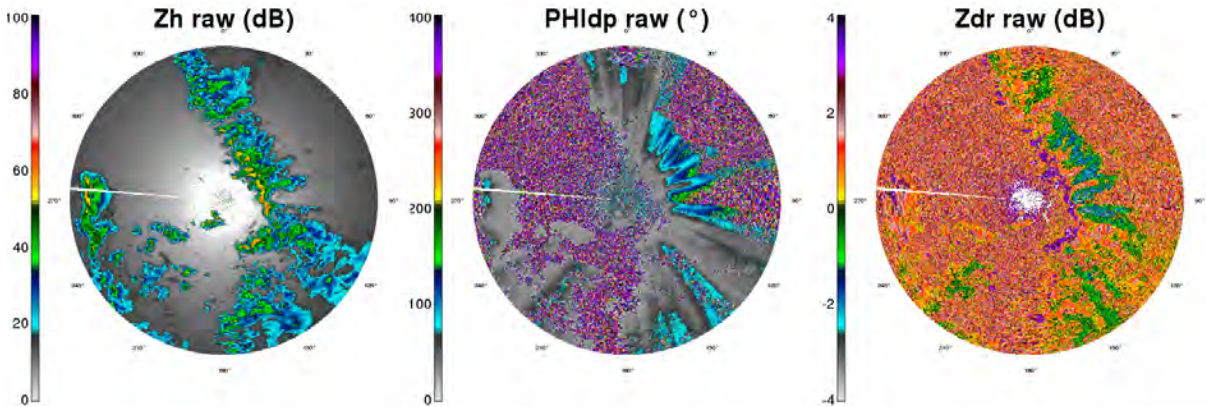


Figure 2-1: Example of raw polarimetric observables (not corrected from attenuation) for the 28/07/2006 06h30 UTC in north Benin with the X-port X-band radar (9.4 GHz). Worth noting the extinction of the signal due to strong attenuation in the convective front.

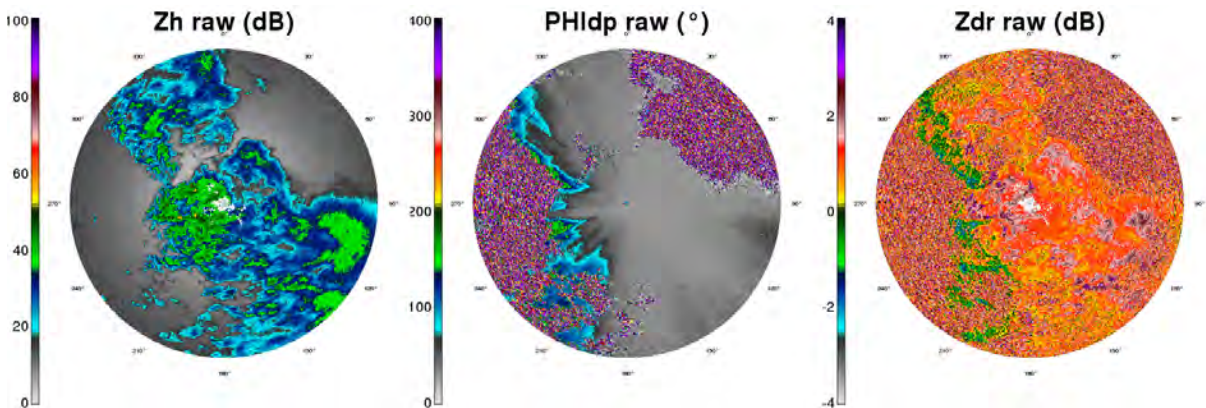


Figure 2-2: Example of raw polarimetric observables (not corrected from attenuation) for the 28/07/2006 07h37 UTC in north Benin. Note the difference of values in the front compared to figure 2-4 due to the attenuation of the signal.

2.2 Hydrometeors characteristics impacting microwave remote sensing

This section details the common parameterizations used to describe the hydrometeors properties.

Fall speed of rain drops

The terminal fall speed V of rain drops subjected to gravity is reached soon as they start falling caused by the air friction. The terminal speed increases with the particle diameter and decreases as the drops falls and encounter denser air. Atlas and Ulbrich with laboratory measurements establish an empirical power law between the terminal velocity $V(D)$ at ground level depending on the drop diameter D which is widely used in the literature (Atlas and Ulbrich 1977) :

$$V(D) = 3.78D^{0.67} \quad (\text{eq. 2.16})$$

With V in $[m \cdot s^{-1}]$ and D in $[mm]$. This power law is widely used due to its simple expression, but other laws exists.

DSD definition and moments

The size distribution of raindrops is the result of the condensation, growth, break-up and coalescence processes during the fall. After reaching a certain size, drops become unstable and break-up into smaller drops during the fall. Drop Size Distribution (DSD) and its variability are key factors in rainfall observation: in remote sensing we do not have direct access to the amount of rainfall but to information related to the drop size distribution. Due to non-linear laws in the absorption and diffusion of microwaves by water droplets, the DSD assumptions impacts the retrieval of rainfall from radar, satellite or microwave links.

The drop size distribution $N(D)$ in $[m^{-3}mm^{-1}]$ is defined as the number of rain drops by volume unit and by diameter D .

The rainfall rate R In $[mm \cdot h^{-1}]$ can be defined as the volume of water crossing a surface in a unit of time, we can write it in function of the DSD $N(D)$:

$$R = \int CN(D)V(D)D^3 \frac{\pi}{6} dD \quad (eq. 2.17)$$

Where C is the scale factor to convert units, $N(D)$ in $[m^{-3}mm^{-1}]$ is the number of rain drops per volume unit by diameter, $V(D)$ in $[ms^{-1}]$ the fall speed of drops at i^{th} bin, and $D^3 \frac{\pi}{6}$ the volume of the drop with diameter D in $[mm]$. Considering the fall speed in equation 2.16, then:

$$R = C \int V(D)D^3 N(D) dD = C_R M_{3.67} \quad (eq. 2.18)$$

Where $C_R = 22.68\pi 10^{-4}$ and $M_{3.67}$ is the moment of order 3.67 of the drop size distribution $N(D)$.

A moment of order n of a distribution $N(D)$ can be defined as:

$$M_n = \int_0^{\infty} D^n N(D) dD \quad (eq. 2.19)$$

The rainfall is proportional to the 3.67 moment of the DSD (using eq. 2.16 and eq. 2.18). The characterization of the DSD with its moments is a useful tool as the usual information that we get when doing remote sensing are integrated variables depending on the DSD moments. The radar reflectivity factor Z $[dBZ]$ is proportional to the 6th moment of the DSD in Rayleigh approximation (when the droplet radius are much smaller than the radar wavelength).

$$Z \propto M_6 \quad (eq. 2.20)$$

The other polarimetric radar variables are linked to integrated moments of the DSD.

DSD double moment normalization M3, M4

In this work we adopted the (Testud et al. 2001) DSD parameterization. The authors have a physical approach considering that the goal of a DSD parameterization is to derive the rain intensity (or liquid water content LWC). The scaling parameters of the DSD are defined with the moments of the DSD. Thus, they are related to the bulk polarimetric variables. The intrinsic normalized shape function of the DSD is independent from the scaling parameters.

For its normalization the authors chose two scaling parameters $[N_0^*; D_m]$ and is as follows:

$$N(D) = N_0^* F(D/D_m) \quad (eq. 2.21)$$

Chapter 2: Radar measurement of rainfall

Where $F(X)$ is the normalized shape of the DSD. The normalization diameter is the equivolumetric median volume D_m , defined as:

$$D_m = \frac{\int_0^{\infty} D^4 N(D) dD}{\int_0^{\infty} D^3 N(D) dD} = \frac{M_4}{M_3} \quad (\text{eq. 2.22})$$

The liquid water content (LWC) in a volume of air can be written with the third moment of the DSD:

$$LWC = \frac{\pi \rho_w}{6} M_3 \quad (\text{eq. 2.23})$$

With ρ_w the density of water and M_3 the third moment of the DSD.

It follows from the definition of LWC and eq. 2.21, that:

$$LWC = \frac{\pi \rho_w}{6} \int_0^{\infty} N_0^* F(D/D_m) D^3 dD = \frac{D_m^4 N_0^* \pi \rho_w}{6} \int_0^{\infty} F(X) X^3 dX \quad (\text{eq. 2.24})$$

For the normalized function $F(X)$ to be independent of LWC and D_m it is required that :

$$\int_0^{\infty} F(X) X^3 dX = C_0 \quad (\text{eq. 2.25})$$

Where C_0 is a constant, thus:

$$N_0^* = \frac{6}{C_0 \pi \rho_w} \frac{LWC}{D_m^4} \quad (\text{eq. 2.26})$$

The second scaling parameter N_0^* is proportional to M_3^5 and M_4^{-4} . If we choose the C_0 constant to be $C_0 = \Gamma(4)/4^4$, the N_0^* parameter can be interpreted as the intercept parameter of the exponential DSD with an equivalent LWC and D_m .

In their work, they applied the new parametrization to airborne microphysical observations of DSD and conclude that the average normalized shape is remarkably stable for all rain categories and independent of the parameters (they chose a normalized gamma distribution for $F(X)$).

The DSD, as rainfall, has important spatial and temporal variability. The different physics of precipitation impacts the resulting DSD. The convective front in a MCS has different DSD characteristics compared to the stratiform region in the resulting DSD fields retrieved in chapter 4. The DSD can also vary from climatic regions, over the sea versus land and for different seasons. A usual solution is to parameterize the DSD parameters ($[N_0^*; D_m]$ in the Testud et al 2001 work) with one moment of the DSD, rainfall being a

common choice. (Moumouni, Gosset, and Houngninou 2008) after extensive analysis of Benin disdrometer data (2006-2007) parameterized the DSD for MCS in West-Africa. In the submitted paper presented in chapter 4 we present an inversion of the polarimetric radar variables to retrieve the parameters of the Testud DSD parametrization. In chapter 5 we quantify the uncertainty related to different parameterization of the DSD in the retrieval of rainfall rates with microwave links.

Water drop shapes

When raindrops fall they are subjected to the air resistance increasing with speed. The air drag force modifies the shape of the water drops by flattening it. The resulting shape of the drops are an equilibrium between drag forces which depends on terminal velocity (thus diameter) and drop surface tension resulting in a obloid. In figure 2-3 from (Pruppacher and Beard 1970) we show an image of falling drops for different diameters.

The turbulent air flow around the drop leads to its oscillation which can be described theoretically by spherical harmonics oscillation modes, or in a pragmatic way, by a mean canting angle.

The flattening of the drops depending on its sizes is the cause of differential signals of horizontal and vertical polarimetric signals. The flattening parameterization is a strong assumption in remote sensing retrievals with polarimetry. Many studies focus on the rain drop shape laws, their variability, and the canting angle of drops in natural conditions with two different group of methods: experimental and theoretical. Three recent reviews summarize the literature on rain drop shapes (Beard, Bringi, and Thurai 2010; Szakáll et al. 2010; Gorgucci, Baldini, and Chandrasekar 2006). The experimental methods involve imaging techniques as high-speed video cameras (Thurai et al. 2009) or two dimensional video disdrometers (2DVD) for in-situ measurements (Tokay and Beard 1996). Other technique aiming the simulation of real conditions (like drop terminal velocity), is to use a long shaft (Andsager, Beard, and Laird 1999) or wind tunnels (Pruppacher and Beard 1970) to control the observation setup.

There is a large spectrum of laws describing the falling drop shapes depending on the conditions of the experiment or assumptions. In addition, the presence of a canting angle of the droplet main axis due to particle oscillation (apparently due to resonance with eddy shedding (Beard, Bringi, and Thurai 2010)) can lead to a high variability of ratio laws for

Chapter 2: Radar measurement of rainfall

a particular diameter. In this work we have consider three laws describing the axis ratio $r_a = a_D/b_D$ where a_D is the minimum diameter and b_D the maximum diameter of a flattened drop.

The linear expression proposed by (Pruppacher and Beard 1970) has been modified by (Gorgucci et al. 2000; Matrosov et al. 2002) with a varying parameter β_e which account for the variations of the canting angle and thus the distribution of axis ratios, the law is:

$$r_a = \begin{cases} 1.03 - \beta_e D_e & \text{for } D_e \geq 0.5mm \\ 1.0 & \text{for } 0 \leq D_e < 0.5mm \end{cases} \quad (eq. 2.27)$$

With r_a the axis ratio, D_e equivalent spherical diameter in [mm] and $\beta_e = [0.052, 0.072]$ [mm^{-1}], slope parameter (hereafter LIN1 and LIN5 respectively).

We also have considered the ((Andsager, Beard, and Laird 1999) hereafter ANDS99) accounting for large drop canting angles and (Illingworth and Blackman 2002) ILLI02 law derived from disdrometers DSD compared to radar data.

The ANDS99 relation is as follows (D_e in cm) :

$$r_a = \begin{cases} 1.012 - 0.1445D_e - 1.028D_e^2 & \text{for } 1.1 \leq D_e \leq 4.4mm \\ 1.0048 - 0.0057D_e - 2.628D_e^2 + 3.682D_e^3 - 1.677D_e^4 & \text{for } D_e < 1.1 \cup D_e > 4.4mm \end{cases} \quad (eq. 2.28)$$

And the ILLI02 relation (D_e in mm):

$$r_a = 1.075 - 0.065D_e - 0.003D_e^2 + 0.0004D_e^4 \quad (eq. 2.29)$$

The figure 2-4 shows the four axis ratio laws used in this work.



Figure 2-3: Example of rain drop photos having spherical equivalent diameters of $D_e=[8.00,7.35,5.80,5.30,3.45,2.70$ mm] by Pruppacher and Beard (1970)

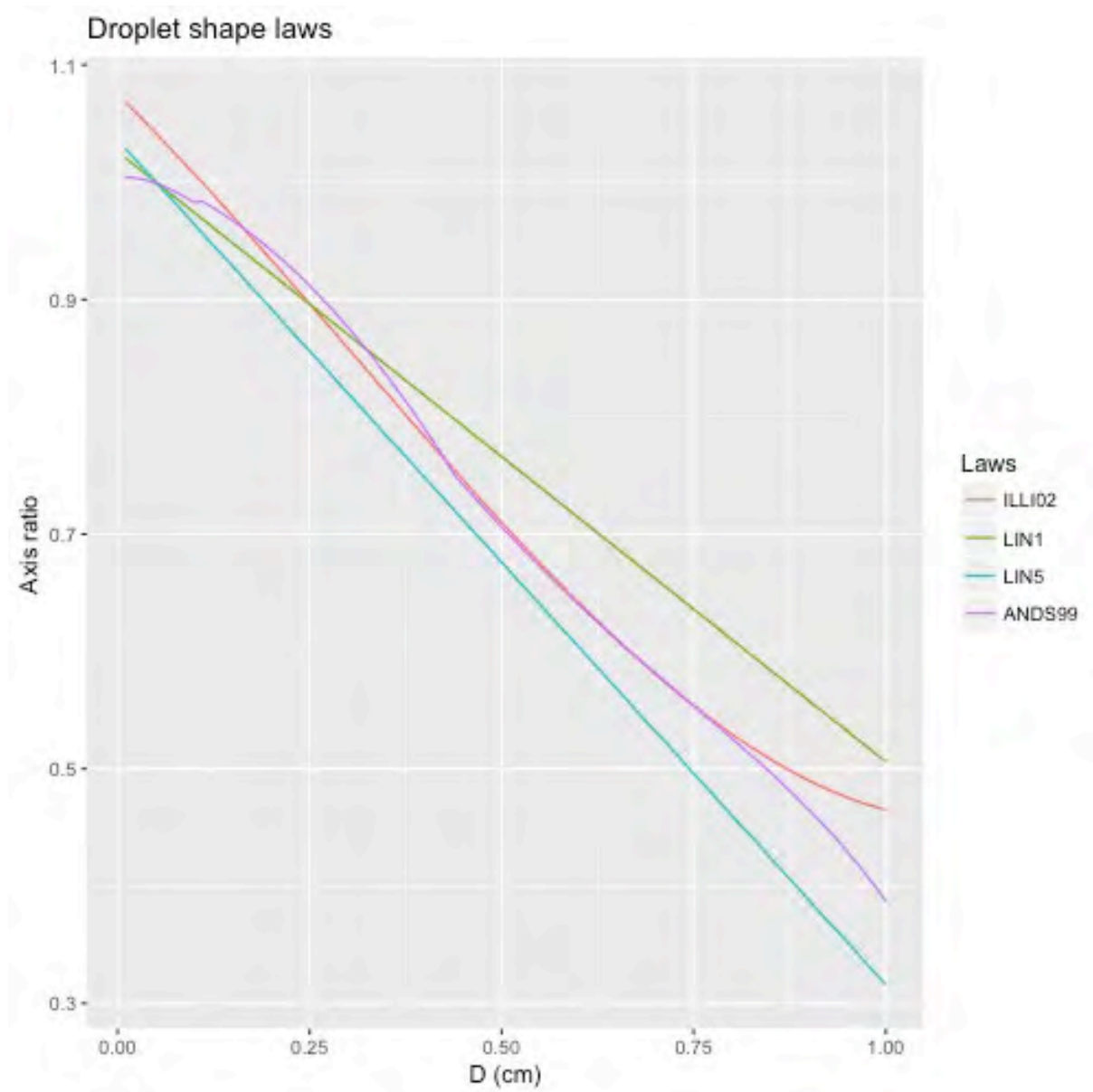


Figure 2-4: Different ratio shape laws used in this work.

Ice particles parameterization

The average properties of icy hydrometeors are often parameterized by power laws derived from observed data (Fontaine et al. 2014). The diameter of an icy hydrometeor is ill defined, usually the maximum diameter of the particle is used, D_{max} , or the melted equivalent spherical diameter $D_{eq,w}$. Related to the hydrometeor density, the mass can be parameterized by a power law:

$$m_h = \alpha_m D_{max}^{\beta_m} \quad (eq. 2.30)$$

With α_m and β_m the mass-diameter law coefficients.

Similarly, another usual parameterization is the density-diameter relationship:

$$\rho_h = \alpha_d D_{eq,w}^{\beta_d} \quad (eq. 2.31)$$

Where ρ_h is the density.

Many other parameterizations exist to describe the fauna of icy crystals. The radiative properties of crystals can be extremely different depending on their shapes. This variety on the response of crystals to the IR and MW radiation has an incidence on the remote sensing by radar and satellite (reflectivity and polar. variables for radar, brightness temperatures for passive satellites). Ice crystals add a layer of uncertainty, compared to melted rainfall, when modelling the interaction between EM waves and hydrometeors.

2.3 Models representing hydrometeors and EM interaction

In this section we describe the main dielectric properties of hydrometeors used to describe their interaction with EM radiation. Then we describe the usual theories for hydrometeors microwave scattering calculation.

Dielectric properties of hydrometeors

The dielectric constant ϵ of the hydrometeors varies with the wavelength of the EM field λ , the temperature and the phase of the scatter (ice, water or mix).

The complex refractive index m is defined with the dielectric constant ϵ :

$$m = \sqrt{\varepsilon} = n - ik_a \quad (\text{eq. 2.32})$$

With n the ordinary refractive index and k_a the absorption coefficient of the scatter material.

The refraction index impacts the scattering properties of the hydrometeors and thus the received signal on the radars. The model of (Liebe, Hufford, and Manabe 1991) is commonly used to calculate the refraction index of water at microwave frequencies.

For solid and melting hydrometeors the refraction index depends on the relative fraction of the different phases constituting the particle: during melting the particles are constituted of a mix of air, ice and water. The solid hydrometeors are constituted by ice or ice and air. Different models exist to calculate the refractive index of a melting particle. In chapter 3 we detail the models and use the radar observation of the melting layer to derive their density using such models.

Two simplifying theories: Rayleigh and Mie scattering

The theory of scattering of EM waves by particles was developed in the 19th and early 20th century. A general solution was given by Mie (Mie 1908). It is based on the application of the Maxwell's equations in the scatter and the propagation medium and applying the limit conditions at the border of the scatter by considering the continuity of the tangential component of the electromagnetic field.

The resulting scattered field depends on the following basic parameters:

- The scattering direction
- the dielectric constant ε of the scatter which varies with the wavelength of the EM field λ and the temperature T . The complex refractive index m defined by $m = \sqrt{\varepsilon} = n - ik_a$ with n the ordinary refractive index and k_a the absorption coefficient of the scatter material
- The size parameter $\alpha = \pi D / \lambda$ with D the diameter of the scatter and λ the wavelength of the EM field.

Chapter 2: Radar measurement of rainfall

When the size parameter $\alpha \ll 1$, the scatter size is small with respect to the wavelength, the approximation of Rayleigh is satisfied.

The scattering cross section multiplied by the power density of the incident wave is equivalent to the total amount of energy removed from the electromagnetic wave due to scattering in all directions. A certain amount of energy is absorbed by heating by the particle: this amount is equal to the absorption cross section multiplied by the power density of the incident wave. The backscattering cross section is related to the quantity of power scattered by the particle in the same direction than the incident wave.

The backscattering cross section, absorption cross section and the scattering cross section can be expressed with the diameter D and by K being:

$$K = \frac{m^2 - 1}{m^2 + 2} \quad (eq. 2.33)$$

In Rayleigh approximation we can express σ_{bs} the backscattering cross-section, σ_a the absorption cross section of the scatter, σ_s the scattering cross section, and σ_{ext} the extinction cross section:

$$\sigma_{bs} = \frac{\pi^5}{\lambda^4} D^6 |K|^2 \quad (eq. 2.34)$$

$$\sigma_a = \frac{\pi^2}{\lambda} D^3 \text{Im}(-K) \quad (eq. 2.35)$$

$$\sigma_s = \frac{2\pi^5}{3\lambda^4} D^6 |K|^2 \quad (eq. 2.36)$$

$$\sigma_{ext} = \sigma_a + \sigma_s \quad (eq. 2.37)$$

If the MW signal is at 3 GHz ($\lambda \sim 10\text{cm}$) all rain drop sizes verify the Rayleigh approximation.

For higher frequencies the Rayleigh approximation is no longer valid and we shall use the Mie's theory.

Then if the size parameter $\alpha \sim 1$, the Mie's theory shows that the scattering and total absorption cross sections are given by:

$$\sigma_{bs} = \frac{\lambda^2}{4\pi} \left| \sum_{n=1}^{\infty} (2n+1)(-1)^n (|a_n|^2 + |b_n|^2) \right|^2 \quad (eq. 2.38)$$

$$\sigma_s = \frac{\lambda^2}{2\pi} \sum_{n=1}^{\infty} (2n + 1)(|a_n|^2 + |b_n|^2) \quad (eq. 2.39)$$

$$\sigma_{ext} = \frac{-\lambda^2}{2\pi} \text{Real} \left(\sum_{n=1}^{\infty} (2n + 1)(|a_n|^2 + |b_n|^2) \right) \quad (eq. 2.40)$$

Where a_n and b_n are the spherical Bessel functions of order n with arguments α and m . Figures 2-5 and 2-6 shows the Rayleigh and Mie scattering cross sections for different frequencies, at different temperatures for the typical range of water drops. There is a high sensitivity on the frequency with different impacts at different drop sizes. Worth noting the Mie oscillation at 5mm diameter at 7 GHz. The Mie and Rayleigh calculations of the scattering cross sections converge at a certain diameter depending on the frequency. For low frequencies (ie. 7 GHz in the figure), the Mie and Rayleigh cross sections converges at 3.5 mm. For higher frequencies, we move away from Rayleigh regime and the meeting of both curves occur for lower diameters. The dependency on temperature is lower, as we see in figure 2-6. This dependency comes from the evolution of the complex refractive index of water with temperature.

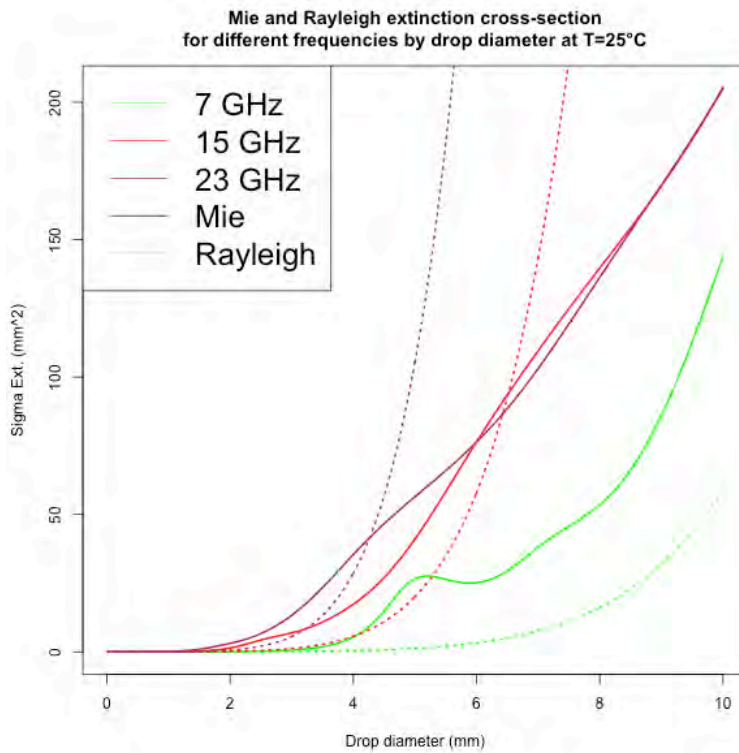


Figure 2-5: Extinction cross sections for different frequencies by drop diameter for Mie and Rayleigh models.

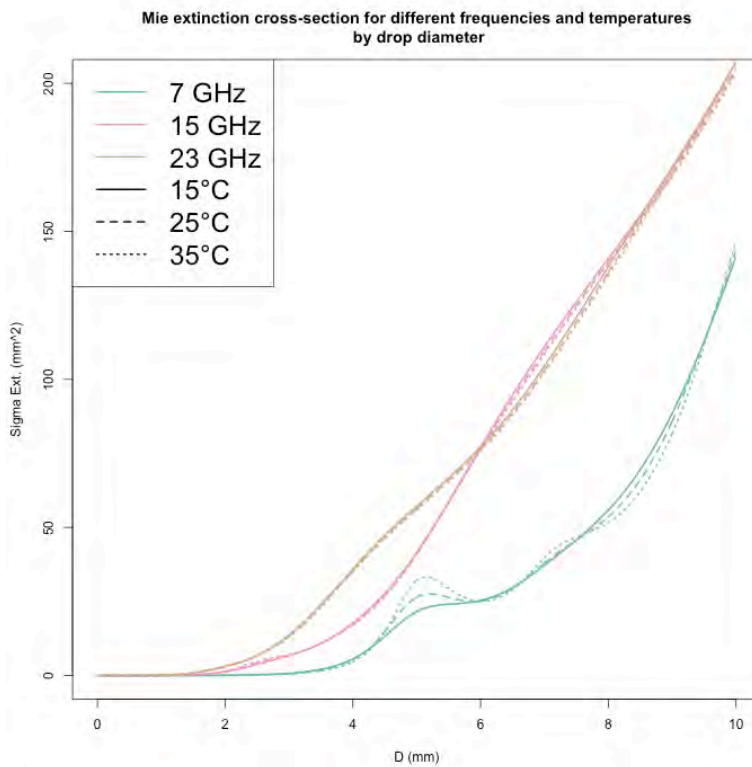


Figure 2-6: Mie extinction cross sections for different frequencies and temperatures by drop diameter.

T-matrix model

The T-matrix approach (Mishchenko, Travis, and Mackowski 1996) was developed to calculate scattering of non-spherical icy and liquid hydrometeors (Barber and Yeh 1975; Vivekanandan, Adams, and Bringi 1991). The scattering calculations for an irregular scatter are made by solving the Maxwell's equations explicitly (more details in the cited articles).

The T-matrix method for EM scattering by non-spherical particles is a reference in weather radar polarimetry and an open source code has generalized its use. The method calculates the propagative and scattering properties of populations of spheroid drops defined by their aspect ratio, their orientation compared to the incident electromagnetic field, their size relative to the wavelength, and their refractive index. In order to account for drop oscillation, a distribution of canting angles can be provided.

The T-matrix solves the scattered electromagnetic field by estimating the scattering matrix components S_{ij} , which is the operator between the incident EM field decomposed into the vertical and horizontal polarizations and the scattered field by a conjunction of asymmetrical spheroids:

$$\begin{pmatrix} E_H^S \\ E_V^S \end{pmatrix} = \frac{e^{-ik_0 r}}{r} \begin{bmatrix} S_{HH} & S_{HV} \\ S_{VH} & S_{VV} \end{bmatrix} \begin{pmatrix} E_H^i \\ E_V^i \end{pmatrix} \quad (eq. 2.41)$$

With k_0 the wave number, $E_{H,V}^S$ the components of the scattered field, and $E_{H,V}^i$ the components of the incident field.

We can define the horizontal and vertical reflectivity factors with the coefficients S_{ij} by:

$$Z_{H,V} = \frac{4\lambda^4}{\pi^5} |K|^2 \int_{D_{\min}}^{D_{\max}} |S_{HH,VV}(D)|^2 (D) N(D) dD \quad (eq. 2.42)$$

The differential reflectivity factor Z_{DR} (dB) is defined as:

$$Z_{DR} = Z_H - Z_V = 10 \log \left(\frac{Z_H}{Z_V} \right) = 10 \log \left(\frac{|S_{HH}|^2}{|S_{VV}|^2} \right) \quad (eq. 2.43)$$

The T-matrix approach estimates the $f_{H,V}$ forward and $s_{HH,VV}$ backward scattering amplitudes (m) at horizontal (H) or vertical (V) polarization respectively, which can be used to derive the propagative variables:

Chapter 2: Radar measurement of rainfall

$$k_{H,V} = 8.68 \lambda \int_{D_{\min}}^{D_{\max}} \text{Im}[f_{H,V}(D)] N(D) dD \quad (\text{eq. 2.44})$$

$$K_{DP} = \frac{180 \pi}{\lambda} \int_{D_{\min}}^{D_{\max}} \text{Re}[f_H(D) - f_V(D)] N(D) dD \quad [^\circ/\text{km}] \quad (\text{eq. 2.45})$$

With λ wavelength (m), Re and Im denoting their real and imaginary parts.

In chapter 4 we use T-matrix calculations for different aspect ratio laws as a forward model to estimate polarimetric variables from the characteristics of the hydrometeors. The model is then inverted to retrieve the characteristics of the hydrometeors from polarimetric radar measurements.

3 A SIMPLE BRIGHT BAND METHOD TO INFER THE DENSITY OF HYDROMETEORS

Characterization of Hydrometeors in Sahelian Convective Systems with an X-Band Radar and Comparison with In Situ Measurements. Part II: A Simple Brightband Method to Infer the Density of Icy Hydrometeors

M. ALCOBA AND M. GOSSET

Geoscience Environnement Toulouse, UMR 5563 CNRS/IRD/UTM, Observatoire Midi-Pyrénées, Toulouse, France

M. KACOU

Geoscience Environnement Toulouse, UMR 5563 CNRS/IRD/UTM, Observatoire Midi-Pyrénées, Toulouse, France, and Laboratoire de Physique de l'Atmosphère et de Mécanique des Fluides, Université Félix Houphouët-Boigny, Abidjan, Ivory Coast

F. CAZENAVE

Laboratoire d'étude des Transferts en Hydrologie et Environnement, IRD/Université Grenoble Alpes/CNRS, Grenoble, France

E. FONTAINE

Laboratoire de Météorologie Physique, Université Blaise Pascal, Aubière, France

(Manuscript received 3 January 2015, in final form 15 July 2015)

ABSTRACT

A simple scheme that is based on the shape and intensity of the radar bright band is used to infer the density of hydrometeors just above the freezing level in Sahelian mesoscale convective systems (MCS). Four MCS jointly observed by a ground-based X-band radar and by an instrumented aircraft as part of the *Megha-Tropiques* algorithm-validation campaign during August 2010 in Niamey, Niger, are analyzed. The instrumented aircraft (with a 94-GHz radar and various optical probes on board) provided mass-diameter laws for the particles sampled during the flights. The mass-diameter laws derived from the ground-radar vertical profile of reflectivity (VPR) for each flight are compared with those derived from the airborne measurements. The density laws derived by both methods are consistent and encourage further use of the simple VPR scheme to quantify hydrometeor density laws and their variability for various analyses (microphysical processes and icy-hydrometeor scattering and radiative properties).

1. Introduction

The physical and scattering properties of icy hydrometeors need to be better characterized to improve precipitation estimation from satellites [see Johnson et al. (2012) and Stephens and Kummerow (2007) for documented reviews]. Over the continental tropics, there is need for better documentation of ice scattering properties as linked with passive microwave satellite rain retrievals (Kummerow et al. 1996; Bennartz and Petty 2001). Over land where the lowest microwave frequencies are affected by the surface emissivity, the estimation of surface rainfall intensities is based on

quantifying the precipitating ice particles aloft. The accuracy of these estimators is strongly dependent on 1) the physical link between the quantity of icy hydrometeors aloft and surface rain (Viltard et al. 2006) and 2) a quantitative knowledge of the icy hydrometeors' scattering properties that need to be represented in radiative transfer models. This was the main motivation for the *Megha-Tropiques* Ground Validation (MTGV) algorithm-validation campaign that took place in Niger, Sahelian Africa, in August 2010.

The *Megha-Tropiques* mission from the French space agency [Centre National d'Etude Spatiales (CNES)] and the Indian Space Research Organization was launched in October 2011 (<http://meghatropiques.ipsl.polytechnique.fr/>). *Megha-Tropiques* is a member of the Global Precipitation Measurement constellation. In preparation for the launch and to improve the Bayesian

Corresponding author address: M. Gosset, GET (UMR 5563 CNRS, IRD, UTM), Observatoire Midi-Pyrénées, 14 Ave. Edouard Belin, 31400 Toulouse, France.
E-mail: marielle.gosset@ird.fr

Rain Retrieval Algorithm including Neural Network (BRAIN; Viltard et al. 2006), a prelaunch campaign dedicated to exploring the microphysics of tropical convective systems was set up in 2010. The specific objectives of the campaign were to document the properties—in particular, the density—of the icy hydrometeors that contribute most to the scattering signal of the 89-GHz radiometer on land. According to the BRAIN developers, the critical region is from 4 to 7 km above the ground or, in other words, just above the freezing level for Sahelian convective systems. During August of 2010, a Falcon research aircraft from the Service des Avions Français Instrumentés pour la Recherche Environnementale (French Service of Instrumented Aircraft for Environmental Research; SAFIRE) that was brought to Niamey, Niger, for the campaign flew inside the stratiform region of 11 convective systems that are representative of the Sahelian region. As during the African Monsoon Multidisciplinary Analyses (AMMA) campaign (Bouniol et al. 2010), the aircraft was equipped with microphysical probes and the Radar Aéroporté et Sol de Télédétection des Propriétés Nuageuses (RASTA; Protat et al. 2009) 94-GHz radar. This combination of instruments allows retrieval of the particle size distribution but also the inference of other properties such as the density of the hydrometeors (Fontaine et al. 2014, hereinafter FO14). A ground-based X-band polarimetric radar was also deployed in Niamey in 2010 for the MTGV campaign. A companion paper (Cazenave et al. 2016, hereinafter Part I) explores the classification of hydrometeors on the basis of the polarimetric variables using a fuzzy-logic algorithm (Dolan and Rutledge 2009). The current paper investigates another method for characterizing the properties of icy hydrometeors just above the freezing level. It is based on exploiting the shape and intensity of the radar bright band (BB). The simple implementation presented here is based solely on the apparent vertical profile of reflectivity (VPR). Three main hypotheses are used to simplify the BB model. First, we consider no aggregation or breakup of particles as they fall; the total number of hydrometeors remains the same during the melting process. We also consider the observed apparent VPR to be the real VPR (no beam-broadening effects). The degree of melting inside the BB is parameterized as a function of height below the 0°C isotherm because this study does not aim to describe the complex thermodynamics processes inside the melting layer, unlike Fabry and Zawadzki (1995).

Many studies (Fabry and Zawadzki 1995; Fabry and Szyrmer 1999; Uijlenhoet et al. 2003) have shown that the properties of the BB are an indicator of the microphysical processes aloft. One salient feature is that when the particles above the 0°C level are dense and rimed then the BB peak is less marked than when large unrimed aggregates are the most common particles. Kirstetter et al. (2013) have used these principles to

propose a “physical” inversion of the VPR. They retrieved the vertical profile of particle size distribution as well as the density of the hydrometeors above the BB. Kirstetter et al. (2013) built on the previous work by Andrieu and Creutin (1995) and proposed a full inversion of the VPR that accounts for radar beam enlargement effects. Our paper uses a simplified version of their model. The focus is on inferring the density law of the hydrometeors just above the BB and not on VPR correction for quantitative precipitation estimation (QPE). The BB properties are analyzed relatively close to the radar so that beam-broadening effects can be neglected and the apparent VPR directly inverted. Following recent findings by FO14, the mass–diameter relationship for icy hydrometeors is modeled as a power law with a fixed exponent. The VPR inversion retrieves the prefactor of the mass–diameter law and its temporal variability as the mesoscale convective system (MCS) crosses over the radar site. The values retrieved by the radar technique are compared with those inferred from in situ measurement using the FO14 technique for four flights for which the aircraft was close enough to the X-band ground radar.

Section 2 presents the radar and inflight-probe data and the MCS case studies. Section 3 presents the BB model and the method used to fit the model to observations. Section 4 provides a quantitative comparison between the radar-retrieved and in situ mass–diameter laws.

2. The *Megha-Tropiques* Niamey 2010 campaign dataset

The *Megha-Tropiques* algorithm-validation campaign was set in Niamey in August 2010. The experimental setup has been described in Part I and in FO14. Eleven flights were scheduled, mostly in MCS. For obvious safety reasons, the flights are restricted to the stratiform region and do not penetrate the intense convective cells. Four of the flight trajectories were close enough to the X-band radar to allow the VPR analysis to be compared with the in situ flight measurements. Figure 1 displays the ground projection of the flight trajectories superimposed on a map of reflectivity at a given time within each of the four flights.

The systems observed on 13 and 18 August 2010 are organized squall lines with a well-defined convective front and a long stratiform region. The 6 and 10 August 2010 systems are less organized and have a scattered and smaller stratiform region.

a. Radar data

“Xport” (Part I) is an X-band (9.4 GHz) polarimetric radar with a 1.4° beamwidth. The resolution of the range bins is 205 m, and the maximum processed range is

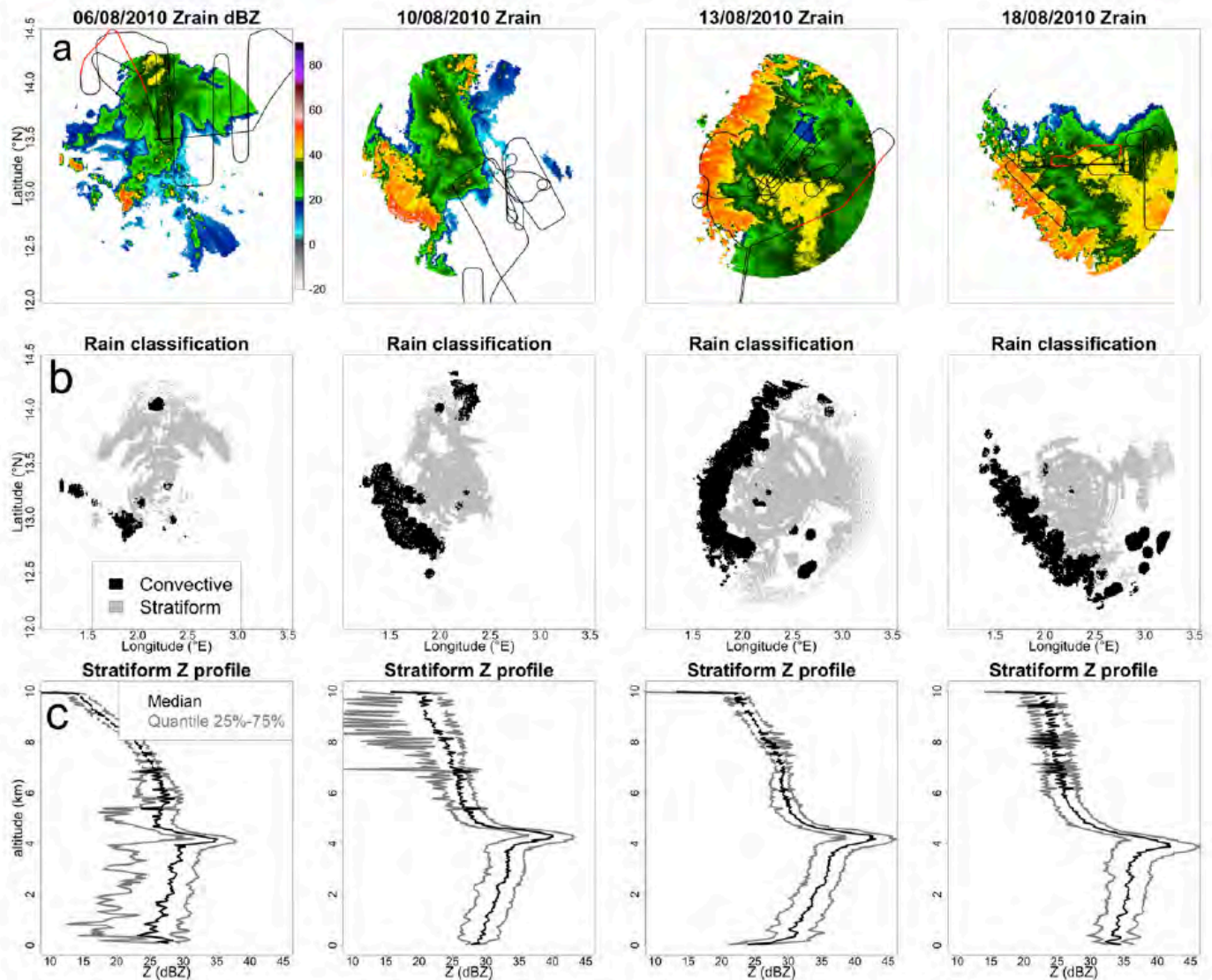


FIG. 1. Example of volume-scan analysis for each of the four MCSs analyzed in 2010. (a) Reflectivity field in the rain (2–3-km height). The black and red lines over the image represent the path of the Falcon plane on the day (typical flight duration: 1–2 h). The red part of the path is for the 12-min duration of the shown PPI sequence. (b) Convective (black)/stratiform (gray) masks. (c) The VPR of the close (<25 km) stratiform region for this particular 12-min scan.

140 km. In 2010, the radar was located in Sadore (13.235°N, 2.285°E), close to Niamey.

The scanning protocol for the 2010 campaign consisted of volume scans with 12 elevation angles (PPI) scanned in 12 min, with a radial recorded every 1° in azimuth. Two sequences of six PPIs are interlaced, resulting in the following order of elevation angles: 1.1°, 2.6°, 5.5°, 9.5°, 15°, 31°, 1.1°, 4°, 7.5°, 12°, 21.7°, and 45°. The interlacing allows a frequent revisit of the lowest angle (1.1°) used for QPE. It also reduces the horizontal shift of the convective system between the lowest and highest scan that results from system displacement. Figure 2a shows the projection of the 12 radar beams in a vertical plan (fixed azimuth), illustrating the vertical distance between scans and the beamwidth, and their range dependence. The horizontal lines at 3.5 and 4.5 km

denote the usual level and extent of the BB in August in Niamey. The height of the 0°C isotherm in the region during the peak of the monsoon season is relatively stable (confirmed by the radiosoundings and radar data acquired during the AMMA campaigns) and is usually located near 4.5–4.7 km.

In this study, the analysis is restricted to distances ranging from 10 to 25 km from the radar to minimize the beam-broadening effect and also to work with a relatively uniform shape and spatial sampling of the BB. Figure 2b shows the number of radar bins per vertical slice of 50-m width and per azimuth direction. This number ranges from above 20 points per height class below 2-km height to about 10 points per height class between 4- and 6-km heights. The number of points available for the VPR analysis depends on the horizontal spread of the system.

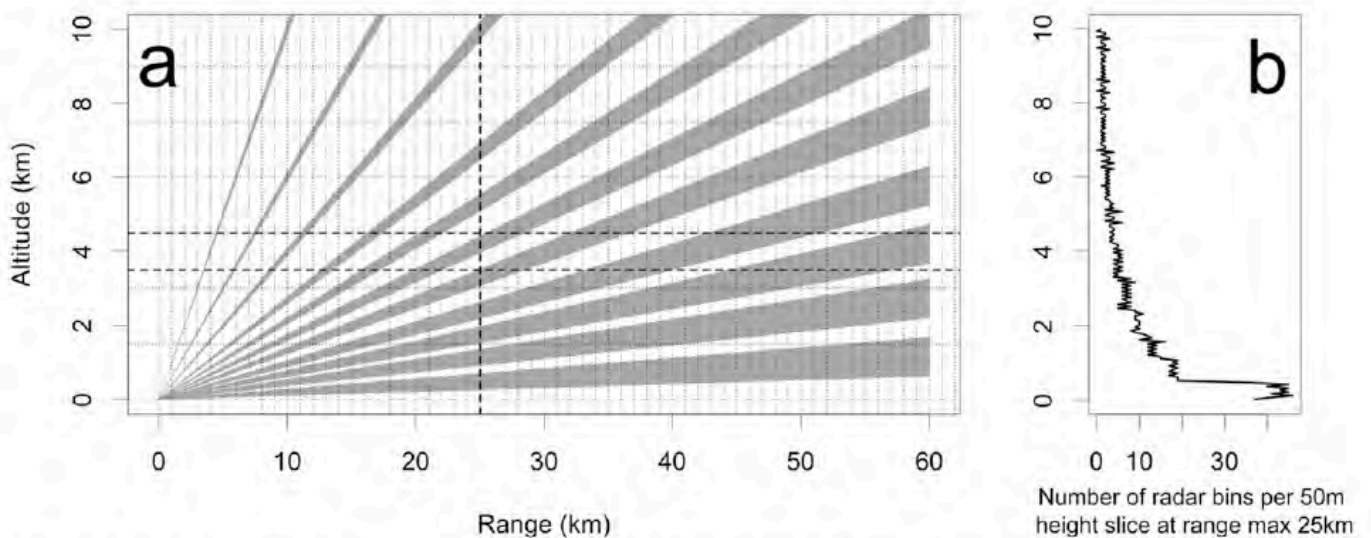


FIG. 2. (a) Projection of the 12 elevations (1.1° , 2.6° , 4° , 5.5° , 7.5° , 9.5° , 12° , 15° , 21.7° , 31° , and 45°) of the radar beams in a vertical plan. The horizontal dotted lines show the typical upper and lower extent of the bright band; the vertical dotted line shows the maximum distance for the quantitative VPR analysis. (b) Number of radar bins per 50-m height slice at range maximum of 25 km.

If the system is spread all around the radar, the numbers in Fig. 2b must be multiplied by 360 (the number of azimuths in a complete scan). For the cases shown in this work, the analysis was performed if the system spread over at least a 45° sector within the 25-km maximum distance. The study focuses on the analysis of the VPR close to the BB region, from 3 to 5.5 km; in this height range and for 45° azimuth or more, the number of points sampled per class of height is more than 400.

At X-band frequencies, the attenuation by rain is strong and must be corrected before analyzing the VPR. Restricting the analysis to a 25-km range limits the effects of attenuation. Because of the strong convection encountered in Niamey, however, attenuation correction is systematically applied. The attenuation correction is based on the differential phase shift between horizontal and vertical polarization ϕ_{DP} as described in Koffi et al. (2014) and Part I.

As stated, the focus is on applying the VPR inversion technique in the stratiform region of the studied MCS where in situ observation is also available. The first stage of the processing is to delineate the convective and stratiform regions within the system on the basis of the 3D reflectivity structure, as described below.

1) DELINEATION OF THE STRATIFORM REGION

The convective/stratiform classification method is similar to Chapon et al. (2008) and builds on the work from Steiner et al. (1995) on the radar signature of the convective region and Sánchez-Diezma et al. (2000) on the BB signature. The convective region is characterized by high values of reflectivity up to relatively high levels within the storm (up to 10 km or above for tropical convection).

It is also characterized by strong horizontal gradients in the reflectivity field (Steiner et al. 1995). In the stratiform region, on the contrary, the horizontal gradients are weaker than the vertical ones and the vertical profile of reflectivity is marked by the BB (Sánchez-Diezma et al. 2000) radar signature of the melting hydrometeors. On this basis, the 3D structure of the reflectivity field can be analyzed to detect convective and stratiform regions.

The classification is performed for each 12-min (and 12 PPIs) volume scan. The data are first converted into a Cartesian grid with 1-km horizontal resolution and vertical bins every 50 m. Each column of $1 \text{ km} \times 1 \text{ km}$ horizontal section is then classified as convective, stratiform, or undetermined. The classification is based on the criteria proposed by Steiner et al. (1995) and Sánchez-Diezma et al. (2000).

The first criterion in Steiner et al. (1995) to classify convective areas is for the reflectivity near the surface (in rain) to be above a given threshold (typically 40 dBZ). In tropical MCSs, some stratiform regions exhibit a high value of reflectivity near the surface associated with old decaying convective cells embedded in the stratiform region [Evaristo et al. 2010; an example of a region of strong reflectivity (40 dBZ or greater) within the stratiform region can be seen in Fig. 4 (which is described in more detail later in the paper) for the PPIs recorded after 1400 UTC]. To avoid erroneous detection of stratiform rain as convective, and given the vertical extension of convection in the Sahelian region, the reflectivity threshold is applied at a higher altitude than in Chapon et al. (2008) above the 0°C isotherm altitude. A 40-dBZ threshold is applied to the reflectivity field between 4.5- and 6.5-km height [whereas a 43-dBZ threshold

is applied near the ground in Chapon et al. (2008) for French Cévennes convection cases].

The second convective classification criterion is the horizontal gradient of the near-surface (between 0 and 3 km) reflectivity. A pixel that has not been classified as convective using the first criterion is convective if its reflectivity exceeds the average reflectivity of its neighbors by a certain amount. This gradient criterion was parameterized by Steiner et al. (1995) with the formula

$$\Delta Z > A - (Z_{bg}^2/B), \quad (1)$$

where Z_{bg} is the mean reflectivity of the pixels within a (horizontal) distance of 10 km. In Steiner et al. (1995), $A = 10$ and $B = 180$; with these values, any area where $Z_{bg} \geq 42.43$ dBZ is classified as convective. The values have been adjusted to $A = 10$ and $B = 234$ to limit the erroneous flagging of stratiform pixels into convective.

The third step in Steiner's scheme is to define a convective *active radius* around the convective pixel. All pixels the centers of which are within the active radius of the center of a convective pixel are flagged as convective. The radius depends on the reflectivity value of the convective center that was defined in the first two steps. We adopted the parameterization of the active convective zone that was proposed by Steiner et al. (1995): a radius of 1 km for convective pixels with a reflectivity lower than 20 dBZ, a 2-km radius for 20–25 dBZ, a 3-km radius for 25–30 dBZ, a 4-km radius for 30–35 dBZ, and a 5-km radius above 35 dBZ.

The classification of stratiform rain (Sánchez-Diezma et al. 2000) is based on the detection of the reflectivity peak associated with the BB in the vertical profile of reflectivity. Given the stable altitude of the 0°C isotherm in Niamey during the monsoon season, the BB signature is sought between 3- and 5-km heights.

As in Sánchez-Diezma et al. (2000), the stratiform classification has two steps: In step 1, for each column (1 km \times 1 km), we look for a maximum of reflectivity within this predetermined range of heights (3–5 km). The maximum should be higher than the reflectivity above and below (in our case, 2–3 and 5–6 km, respectively) by 5 dBZ. This calculation defines the mean BB level. In step 2, vertical reflectivity peaks of at least 2 dBZ must be detected near the mean BB level defined in step 1 to qualify as stratiform.

This method is applied to the measured VPR for each 1-km-resolution column closer than 50 km from the radar. Beyond 50 km, the smoothing of the VPR as a result of beam broadening prohibits direct detection of the peak. In that case, the classification is based on simulating the degradation of the VPR due to beam broadening and finding which among the degraded

stratiform/convective VPR best explains the observed profile [as in Chapon et al. (2008)].

The convective/stratiform classification for one sequence of each observed MCS is illustrated in Fig. 1b. The black region is the convective rain, and the gray region is the stratiform rain. The convective front of the squall lines (in red-orange with reflectivities in the range of 40–50 dBZ in Fig. 1a) is well detected for all of the MCSs as is the stratiform region. Some parts of the stratiform regions were detected as both convective and stratiform. They are excluded from the stratiform mask (in gray) so as not to degrade the composite stratiform VPR used for inversion.

2) VERTICAL PROFILE OF REFLECTIVITY

The reflectivities from all radar bins belonging to the stratiform region (gray mask in Fig. 1b) and located within a 25-km range from the radar are used to analyze the shape of the VPR for each 12-min scan. The VPRs displayed in Fig. 1c are composites built from the distribution of reflectivities of all of the radar bins of each height class (of width 50 m). The median value and the 25th–75th quartiles are plotted. The 25th–75th quartiles illustrate the variability of the VPR within a 25-km range of the radar. These profiles have a different shape than the median profile. In section 4, the VPR inversion is applied to the median VPR and also to the 25th–75th quartiles to provide some insight on the variability of the density law within a 25-km range of the radar. As discussed in section 4, the retrieval is applied only for 12-min sequences when the mean interquartile VPR difference is below 10 dBZ so as to limit the effect of VPR variability. The median profiles for the four presented sequences are representative of a typical stratiform profile inside tropical convective systems (Leary and Houze 1979): a well-defined BB is seen at \sim 4-km height, the ice reflectivity (5 km and more) tends to decrease with height, and the rain reflectivity (3.5 km and below) decreases slightly toward the surface, probably because of rain reevaporation. In the rest of the paper the focus is on using the VPR between 3 and 5.5 km (the BB itself, the ice level just above the BB, 4.7–5.5 km, the rain level just below the BB) to infer the density of the hydrometeors in the altitude 5–6 km. This layer of icy precipitation is important for interpreting the 89-GHz radiometric brightness temperatures and subsequent rain retrieval (Viltard et al. 2006).

b. *In situ* information from the instrumented aircraft

Detailed information on the airborne microphysical probes and the 94-GHz RASTA (Protat et al. 2009) on board as well as on the method used to combine all of the information can be found in F014 and references within.

A Falcon 20 research aircraft was used during the *Megha-Tropiques* validation campaign in Niamey in 2010. Eleven flights were conducted to sample microphysical characteristics in the West African MCSs. The flights were performed in the stratiform part of these MCSs for safety reasons. The aircraft was equipped with a 94-GHz Doppler cloud radar (RASTA; Protat et al. 2009) and with a new generation of optical probes to make in situ hydrometeor measurements: the 2D stereo probe (2D-S) from Stratton Park Engineering Company, Inc., which acquires 2D images of hydrometeors in the size range of 10–1280 μm , and the Precipitation Imaging Probe from Droplet Measurement Technologies, Inc., which allows measurements in the range of 100–6400 μm . The probes record 2D images of hydrometeors sampled with a time resolution of 1 s. The images are analyzed to derive particle size distributions and aspect ratios of particles over a time period of 5 s. The basic principle is to combine the particle size distribution (PSD) provided by the probes and the reflectivity measured simultaneously by the airborne radar to infer the mass–diameter relationship of the hydrometeors. The method is based on simulating 94-GHz reflectivities from the observed PSD and a scattering model (Mie or **T** matrix) and finding the mass–diameter relationship that provides the best match between the RASTA measurement and the simulations. On the basis of the Niamey 2010 campaign, FO14 have found that the mass–diameter relationship of icy hydrometeors in the precipitating stratiform region of the Sahelian MCS is of the form

$$m_h = \alpha_m D_{\max}^{\beta_m}, \quad (2)$$

where m_h is the mass of the particle in grams and D_{\max} is the maximum dimension of the particle in centimeters (or its diameter if the particle is a sphere). The mean values that were found for parameters α_m and β_m during the Niamey 2010 campaign (all seven flights) are 0.015 and 2.33, respectively (FO14).

For the validation of the VPR inversion below, the aircraft information was processed for each of the four flight cases in Fig. 1. The value of β_m was held constant to the mean value 2.33, and α_m was adjusted (as in FO14) at a time step of 1 min. These in situ values of α_m are to be compared with those retrieved from the X-band ground-radar VPR analysis.

3. The radar brightband model and its inversion

The retrieval of icy-hydrometeor density from the X-band ground radar is based on the inversion of a simplified, yet physical, BB VPR model. The model is

the one introduced by Kirstetter et al. (2013) with some minor adjustments to fit our specific questions.

a. The simplified BB model

The main simplifying assumption in the model is that the only process in the BB is the melting process and that the mass of hydrometeors is conserved. In other words, if the PSD is expressed as a function of the equivalent melted diameter (i.e., the diameter of a water sphere of the same mass) D_{eqw} of the particles, then this PSD is the same just above and just below the BB. No evaporation is assumed in the BB model, but evidence of this phenomenon is observed lower down in the reflectivity rain profile between 3.7 km and the ground level. No aggregation or breakup that would affect the PSD is accounted for; neither is the acceleration of the particle through melting. A version of the model that accounts for the latter impact [following Fabry and Szyrmer (1999)] was tested but did not result in substantially different values of the retrieved mass–diameter relationship and is not reported here.

1) PSD

The PSD is commonly modeled by a gamma function. According to Moumouni et al. (2008), this parameterization is suited for the raindrop size distribution (DSD) in the African MCS. Moumouni et al. (2008) also showed that the DSD observed in organized MCSs in northern Benin were similar to those previously recorded for MCSs in other parts of West Africa (as in Niger and Ivory Coast).

As in Testud et al. (2001), the normalized gamma DSD, with two scaling parameters—the mean volumetric diameter D_m (L) and the volume-normalized intercept parameter N_0^* (L^{-4})—is adopted:

$$n(D_{\text{eqw}}) = N_0^* F(D_{\text{eqw}}/D_m), \quad (3)$$

with

$$F(X) = \frac{\Gamma(4)(\mu + 4)^{\mu+4}}{4^4 \Gamma(\mu + 4)} X^\mu e^{-X(\mu+4)}. \quad (4)$$

Moumouni et al. (2008) found that the parameter μ of the gamma DSD is relatively stable and is close to 2 for African MCSs. The impact on the density-law retrieval of assuming a fixed μ value has been analyzed. We found (not shown) that changing the value of μ —and, for instance, allowing μ to vary with D_m —changes considerably the retrieved values of N_0^* and D_m but has little quantitative impact on the retrieved prefactor of the density law. As illustrated in Fig. 3, the main factor affecting the VPR shape is indeed the density law. For the sake of simplicity, and because the focus is on retrieving

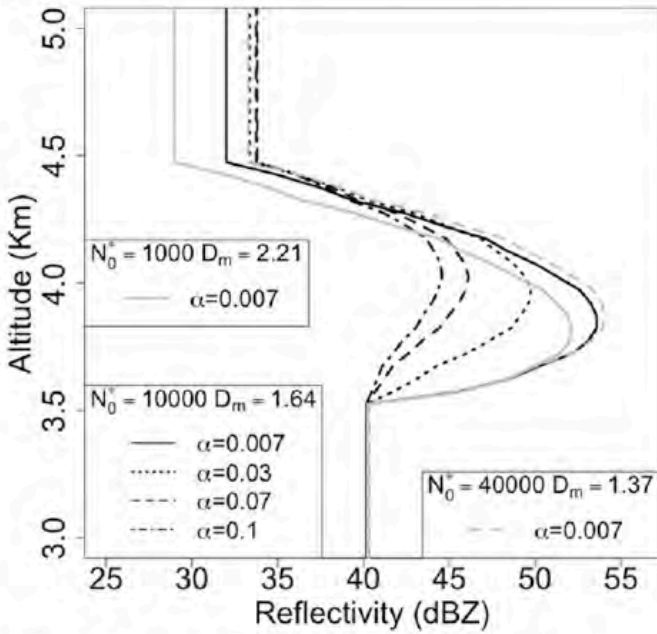


FIG. 3. Sensitivity of the BB model to the prefactor α_d of the density-diameter law and the DSD parameters.

the density law and not on the PSD, a fixed value of $\mu = 2$ was therefore adopted for the PSD.

2) DENSITY LAW

Following the findings of FO14 and Eq. (2), the icy hydrometeors (above the freezing level) have a diameter-dependent density of the form

$$\rho_h = \alpha_d D_{\text{eqw}}^{\beta_d}, \quad (5)$$

where ρ_h is in grams per centimeters cubed and D_{eqw} is the equivalent melted diameter (here in centimeters). The relationship between the prefactor and exponent (α_d and β_d) in Eq. (5) and the α_m and β_m in Eq. (2) is formally established in the appendix for the case in which the hydrometeors are oblate, as suggested by FO14. For $\beta_m = 2.33$, $\beta_d = -0.86$; this negative value means that the small particles are denser than the larger ones (like aggregates). The range of allowed densities is limited to a minimum value of $5 \times 10^{-3} \text{ g cm}^{-3}$ for pure snowflakes and an upper limit of 0.9 g cm^{-3} for very dense ice particles that are closer to hail. When the particles are entirely melted, their density is that of water, taken as 1 g cm^{-3} . During the melting process and transition through the BB, the hydrometeors become gradually denser as the pure ice becomes water and less and less air is trapped in the lattice.

3) DIELECTRIC PROPERTIES

As discussed by previous authors, the dielectric properties of hydrometeors can be modeled as a function of

the relative proportion of pure ice, air, and water that they contain and also depending on their internal structure (Fabry and Szyrmer 1999; Johnson et al. 2012). Following Boudevillain and Andrieu (2003) and after several sensitivity tests, the “ice in air in a lattice of water,” or “ia_w,” concept is adopted.

The dielectric constant of the mixture can be written as (Klaassen 1988)

$$\varepsilon = \frac{(1 - F_{\text{inc}})\varepsilon_{\text{mat}} + BF_{\text{inc}}\varepsilon_{\text{inc}}}{1 - F_{\text{inc}} + BF_{\text{inc}}}, \quad (6)$$

where F_{inc} is the volumetric fraction of the inclusions, ε_{mat} is the dielectric constant of the matrix, ε_{inc} is the dielectric constant of the inclusion, and B is defined as

$$B = \frac{2\varepsilon_{\text{mat}}}{\varepsilon_{\text{inc}} - \varepsilon_{\text{mat}}} \left[\frac{\varepsilon_{\text{inc}}}{\varepsilon_{\text{inc}} - \varepsilon_{\text{mat}}} \log\left(\frac{\varepsilon_{\text{inc}}}{\varepsilon_{\text{mat}}}\right) - 1 \right]. \quad (7)$$

The dielectric constant of the inclusions or the matrix can also be a mix. In the present case of ia_w, the dielectric constant of the air-ice mixture “ice inclusions in air matrix” is first calculated using Eq. (7) with $\varepsilon_{\text{inc}} = \varepsilon_{\text{ice}}$ and $\varepsilon_{\text{mat}} = \varepsilon_{\text{air}}$. Then Eq. (7) is applied again with the inclusion being the air-ice mixture and the matrix being the water.

The volumetric fraction of the water F_{water} can be written as a function of the melted fraction of the particle f_m and the density of water ρ_l , and the density of the ice particle ρ_s (smaller than pure ice density in general):

$$F_{\text{water}} = f_m \frac{\rho_s}{\rho_l \left[1 - f_m \left(1 - \frac{\rho_s}{\rho_l} \right) \right]}. \quad (8)$$

The volumetric fraction of the ice-air mixture is

$$F_{\text{inc_ice-air}} = 1 - F_{\text{water}}. \quad (9)$$

4) MELTING FRACTION AND ALTITUDE DEPENDENCE

The evolution of melting with height is modeled analytically as in Boudevillain and Andrieu (2003). No attempt was made to model the real thermodynamics of the melting particle as in Klaassen (1988), Szyrmer and Zawadzki (1999), or Zawadzki et al. (2005). The objective is to have a simple parameterization for the BB shape and its relationship with what we seek: an indicator of hydrometeor density. Following Boudevillain and Andrieu (2003), a symmetric melting profile approximated by a sine function is applied. The melted fraction at a height h between the upper and lower boundary of the BB is given by

$$f_m(h) = \frac{1}{2} \left[\sin \left(\pi \frac{h_{\text{iso}0} - h}{h_{\text{iso}0} - h_{\text{min}}} - \frac{\pi}{2} \right) + 1 \right]. \quad (10)$$

It depends only on the relative position to the BB top and bottom. The top of the BB, the 0°C isotherm level $h_{\text{iso}0}$, and the bottom h_{min} are set. In section 3b we explain how the positions $h_{\text{iso}0}$ and h_{min} are constrained by observations.

5) RESULTING REFLECTIVITY PROFILE

Once the PSD and the dielectric properties are set, the vertical profile of reflectivity can be calculated. In this version, the X-band reflectivity is calculated on the basis of Mie theory.

The simulated VPR for different assumptions on the two PSD parameters N_0^* and D_m and the prefactor α_d of the density law are shown in Fig. 3. In Fig. 3, the reflectivity at the bottom of the BB (in rain) has been imposed and set to 40 dBZ, which constrains the allowed domain of variation for N_0^* and D_m . The proposed example illustrates the effects of the parameters on the VPR shape: for a given reflectivity at the bottom of the BB, the size and position of the BB peak and the reflectivity at the BB top depend strongly on the density prefactor α_d and mildly on the choice of N_0^* and D_m . The lighter the particles are, the more marked is the BB peak and also the lower is the altitude of the peak within the simulated BB.

b. Fitting the model to observed VPR

The model parameters that are held constant are the type of PSD [gamma, with parameter $m = 2$; see section 3a(1)], the dielectric model [section 3a(3)], the sinus shape of the melting profile [section 3a(4)], and the β_d exponent of the density law [The β_d is set to -0.86 . It corresponds to the mean value of β_m (2.33) found by FO14 for the Niamey 2010 campaign. For this work, the airborne dataset (probes and RASTA) was processed so that a mean value of the in situ-based α_m (with β_m set to 2.33) is produced every minute along each flight. The comparisons in section 4 are based on these in situ values of α_m (and the corresponding α_d). The parameters that are constrained by the radar or auxiliary observations for each 12-min sequence are the height of 0°C isotherm, the bottom of the BB, and the value of reflectivity in the rain below, as follows. In the current implementation, the 0°C level was set by the aircraft temperature profile. In the future, it is planned to test the use of the cross-polarization correlation RHO_{HV} to detect the 0°C isotherm using radar data only (Kalogiros et al. 2013). The BB bottom is derived from the shape of the median VPR (i.e., for each 50-m height slice, the median of the

reflectivity distribution is taken). A brutal inflexion in the VPR is sought within the altitude range 3–4 km (i.e., 0.5–1.5 km below the usual level of the 0°C isotherm). The reflectivity in rain Z_{rain} is the median of the reflectivity distribution for the height level at 2–3 km. The three parameters that are retrieved through optimization (by minimizing the distance between the simulated and observed VPR) are the two PSD parameters N_0^* and D_m and the density prefactor α_d . Note that once Z_{rain} is set then N_0^* and D_m are linked and only two independent parameters are retrieved: one PSD parameter and α_d . As explained in section 3a(5), the parameter with most sensitivity is α_d .

The next step is to find the profile in the space of parameters that minimizes the distance to the observed VPR. The minimization criterion is the root-mean-square error (RMSE) between the observed and simulated profiles at heights going from the BB bottom to the BB top (in practice, 3–4.7 km). The minimization technique is the simplex method with two parameters (Nelder and Mead 1965).

4. Results

Examples of the observed and best-fit VPR model for three volume scans within the 13 August 2010 case are shown in Fig. 4. The top panels of Fig. 4 display the radar reflectivity in rain (average value over 0–3-km height) at 1336, 1411, and 1435 UTC as the convective front is gradually moving westward. The bottom panels of Fig. 4 show the observed median VPR (solid curve) and the best-fit VPR (dotted curve). The observed profiles are for the stratiform region within a 25-km radius from the radar. The convective pixels are eliminated as a result of the stratiform/convective classification [section 2a(1)]. The solid horizontal line represents the 0°C isotherm (BB top) given by the aircraft observation.

The modeled VPR are consistent in shape and BB peak value with the observed VPR. The boundaries of the observed profiles are smoothed relative to the modeled VPR. This effect is probably caused by the vertical resolution of the radar and also by the simplicity of the model.

Figure 5 and Table 1 summarize the density prefactor retrieval for the four case studies. The duration of the transit of the systems over the radar ranges from 5 to 14 h (see Table 1), but the VPR is analyzed only when the region within a 25-km radius of the radar is mostly stratiform, after the convective front has gone west of the radar. To limit uncertainties due to VPR variability within the 25-km range, the profiles that are too “noisy” are excluded from the

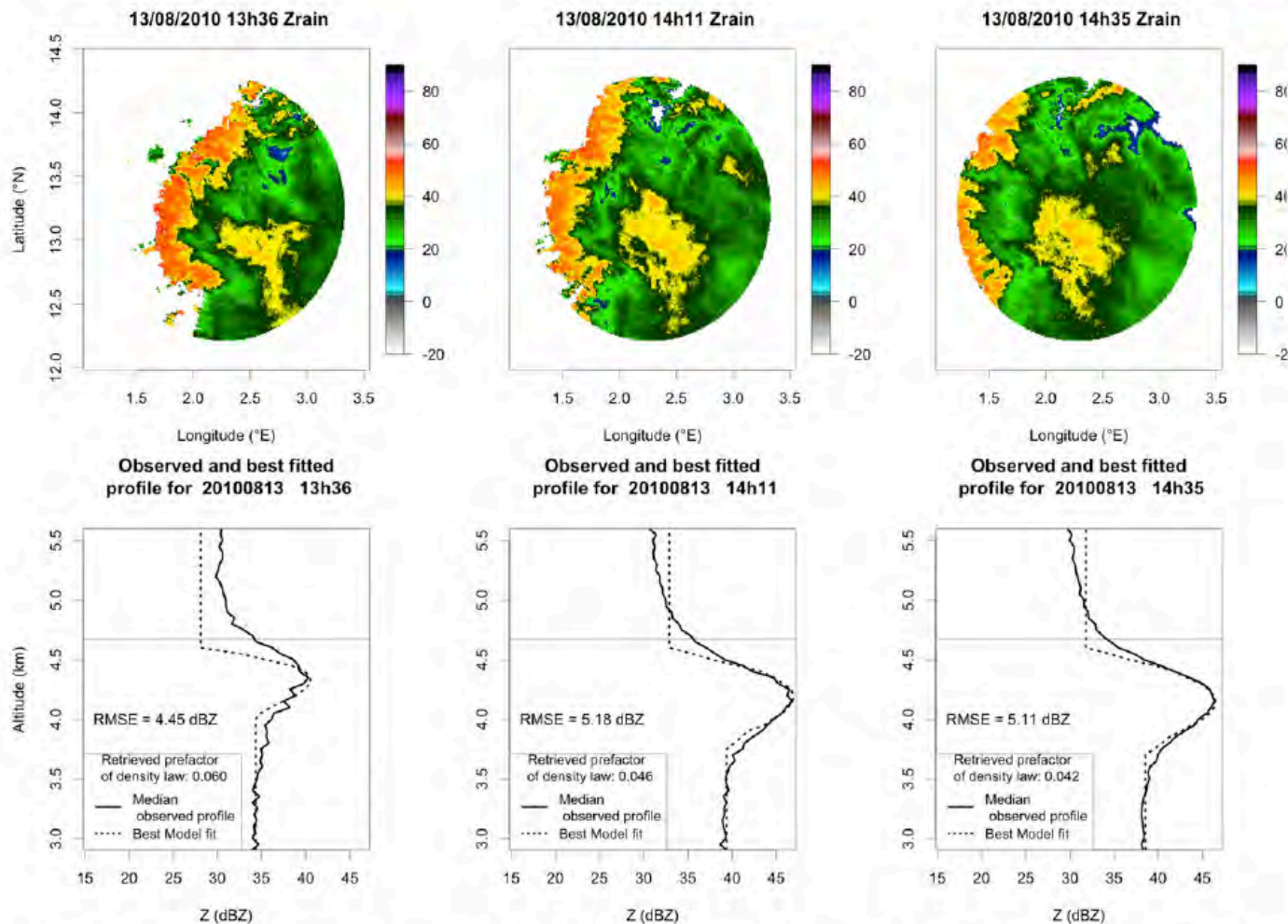


FIG. 4. (top) The 2–3-km-height mean reflectivity field for three volume scans of the 13 Aug 2010 case study. (bottom) Observed (solid curves) and fitted (dotted curves) stratiform VPR. The retrieved prefactor α_d of the density law and the RMSE between the observed and fit VPR are indicated on the plots.

inversion: only profiles with a mean interquartile difference of less than 10 dBZ are kept.

Figure 5 shows the time evolution of the retrieved prefactor for each case study; the time line is in minutes after the convective front has gone through. The inversion based on the median profile (black squares) and the inversion based on the 25th and 75th quartiles (gray symbols) are shown to illustrate VPR variability. The dashed curve is the RMSE between the fitted and observed (median) VPR. It is an indicator of the fit quality. For example, the three last profiles of the 6 August 2010 case have a high RMSE (3 dBZ and more) in comparison with the profiles from previous volumes scans and in comparison with the other days. The VPR from this event are less defined (more spread between the 25th and 75th quartiles) than for the other days, as seen in Fig. 1c. The event of 6 August 2010 had a scattered stratiform part, and the stratiform area observed within 25 km is less extended than for the three other events. These conditions lead to a noisy VPR.

The horizontal lines in Fig. 5 represent the mean and mean plus/minus the standard deviation of the in situ-derived prefactor α_d for all measurements of the day when the aircraft altitude was between 5 and 7 km (just above the BB). Note that, unlike in Part I, the radar pixels and the aircraft trajectory are not matched in space or in time. The objective here is a statistical comparison of two distributions of the prefactor α_d retrieved within the same stratiform region by two different and totally independent methods: in situ measurement all along the flight trajectory and VPR analysis within 25 km of the radar.

The agreement between the in situ and ground-radar-derived values is very good for the 6, 10, and 13 August cases. The radar retrieved values are within the standard deviation of the in situ observation, even when the interquartile spread is considered. The agreement is not as good for the 18 August case. As we can see, the densities retrieved by the 25th–75th quartiles are much more spread for the 18 August case than

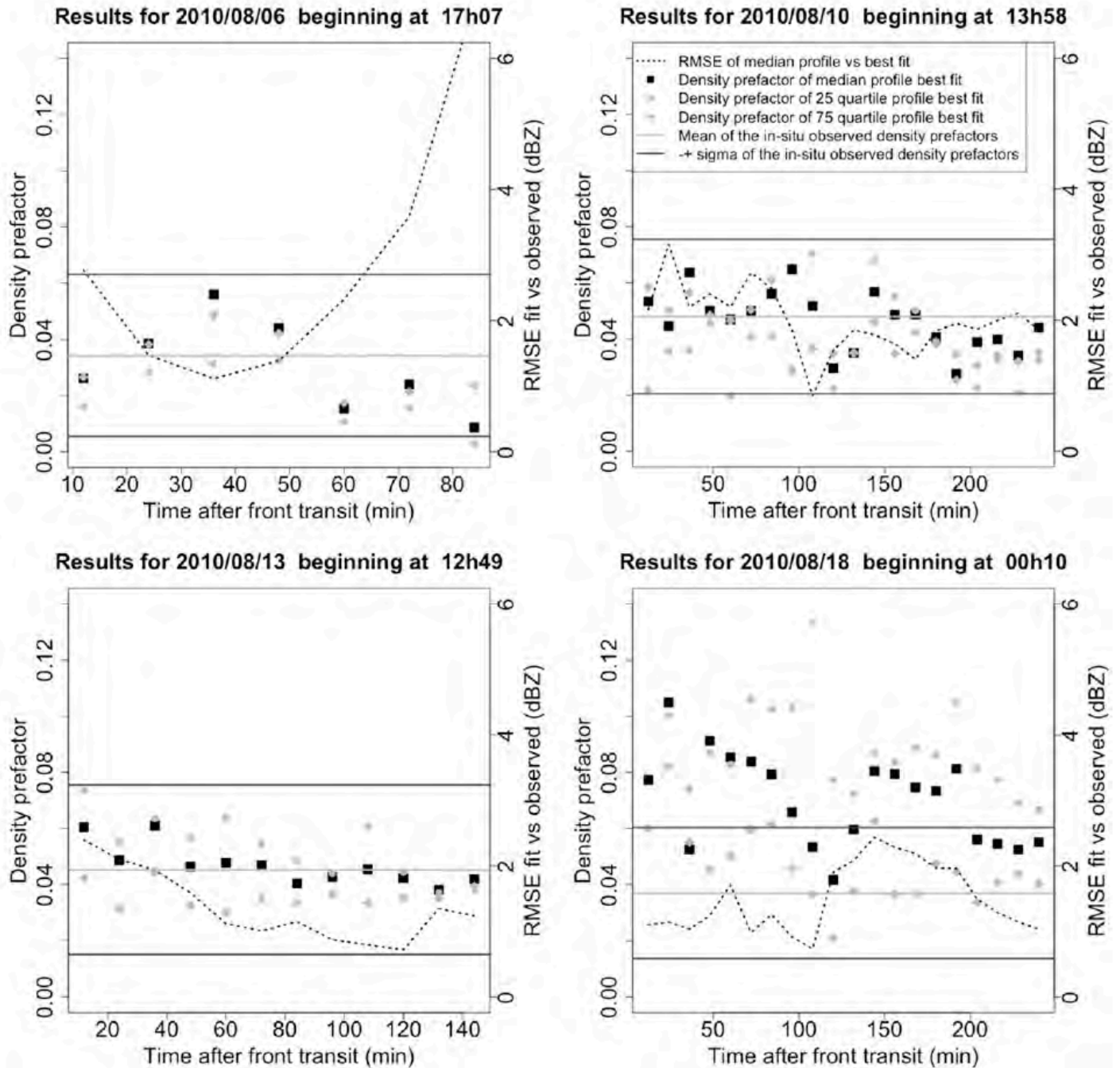


FIG. 5. Density prefactor retrieval for each studied system. The time line is given in minutes from the instant that the convective front was on the radar. The black squares are the radar retrieved density prefactors α_d for the median VPR, with gray dots and diamonds representing the 25th and 75th VPR quartiles, respectively. The dotted lines represent the RMSE of the retrieval (dBZ; right axis), and the solid lines represent the mean, maxima, and minima of the in situ density prefactor.

for the other cases. In Fig. 1c, the differences in the BB height and shape between the 25th and 75th quartiles are also quite marked. Further analysis of the time evolution of the VPR on that day reveals that the BB level changes over time and drops during the day. Also, the 0°C isotherm as recorded by the aircraft was higher than what can be seen on the VPR profile: the BB is also thicker than for the other cases. The differences could also be related to the mismatch in the sampling volumes between aircraft and radar. These

differences are not greater on 18 August than for the other cases, but the BB seems to show more space–time variability on that day. Further analysis would be needed to understand why the radar-retrieved prefactor is globally higher on 18 August than for the other cases: for instance, comparing the VPR analysis with the polarimetry-based particle identification method presented in Part I and also analyzing the processed 94-GHz airborne radar profiles when they will be available.

TABLE 1. Summary of the VPR-retrieved and in situ–derived density prefactor α for each case study, with their starting times and durations.

	6 Aug 2010		10 Aug 2010		13 Aug 2010		18 Aug 2010	
	VPR retrieved	In situ obs						
α mean	0.030	0.034	0.045	0.048	0.046	0.045	0.061	0.037
α max	0.054	0.086	0.064	0.11	0.060	0.094	0.104	0.115
α min	0.008	0.012	0.027	0.009	0.037	0.012	0.039	0.016
α std dev	0.016	0.028	0.009	0.027	0.006	0.030	0.013	0.023
Start time (UTC)	1336		0707		1202		2234	
Inverted/total no. of profiles (duration)	7/7 (84 min)		15/20 (240 min)		12/12 (144 min)		10/20 (240 min)	

Table 1 and Fig. 5 show that the simple BB model inversion provides relevant information about icy particles above. For three of the four cases, the prefactor of density retrieved by the model is in the ± 1 -standard-deviation region of the observed densities.

Note also from Fig. 5 that, for the three cases in which the analysis is done over at least 2 h (10, 13, and 18 August), the density prefactor appears to decrease as the distance from the convective front increases. This feature is consistent with the findings in Part I that the proportion of aggregates increases at the expense of the denser graupels as the convective front goes away.

5. Conclusions

A simple method that is based on the analysis of the vertical profile of reflectivity to infer information on the density of the hydrometeors just above the freezing level has been applied in Sahelian squall lines. From the experimental framework provided in the *Megha-Tropiques* algorithm-validation experiments (FO14; Part I), the radar-derived densities were compared with simultaneous observations from an instrumented aircraft. The results show good consistency between the radar retrieval and the in situ observations in terms of retrieved density. This good agreement between radar observations (both the VPR analysis presented here and the Part I polarimetry results) and the density law proposed by FO14 is an incentive to use the results of the MTGV campaigns in Africa to improve microphysics parameterization in the BRAIN (Viltard et al. 2006) retrieval scheme. A similar effort has been undertaken in the Indian Ocean as part of the Cooperative Indian Ocean Experiment on Intra-seasonal Variability–Dynamics of the Madden–Julian Oscillation (CINDY–DYNAMO) campaigns (Martini et al. 2015). Sensitivity studies are being carried out to test the effect of improved density laws in the radiative transfer model used by BRAIN. In the three cases of the study presented here, when the VPR evolution inside

African MCSs was observed for at least 2 h then the density prefactor decreases as the distance from the convective front increases. This feature is consistent with results from Part I, in which it was found that the proportion of aggregates increases at the expense of the denser graupel as the convective front goes away. Higher densities are expected near the convective front, where the uplift of melted droplets can create high-density ice particles and riming. These results could be used for parameterizing the evolution of particle density within continental MCS. The next step would be to analyze the sensitivity of the rain retrieval to such a parameterization and also to check the final results in terms of rainfall estimation by comparing the satellite estimates with rain fields derived from the Xport radar in Niamey in 2010 and also in Ouagadougou, Burkina Faso, in 2012 and 2013.

One limitation of the current study is that we restricted the domain to a 25-km range from radar to work with the observed (or apparent) VPR. Inversion methods that account for the broadening of the radar beam with distance [Kirstetter et al. (2013) and references within] would allow extension of the study to a wider domain.

In this work, a single value of the mass–diameter-relationship prefactor α_d is calculated for each radar sequence (of 12 PPIs); also, the exponent β is fixed to the value provided by FO14 from the in situ information. In the future, we could allow more degrees of freedom in the exercise and provide an interval of values or a probability density function for α_d (and an uncertainty bar around the output of the model).

A more complicated model with fall speed and an evolution of the PSD above and below the bright band would allow better insight into the microphysics of West African squall lines. Other planned work is to combine the current VPR approach with other information such as the type of hydrometeors as classified with the polarimetric signal (Part I), and/or the type of convective system or the stage of its life cycle

as seen by geostationary imagery (Fiolleau and Roca 2013).

Acknowledgments. This work was financed by the French CNES TOSCA program as part of the MTGV program, with support from the Institut de Recherche pour le Développement (IRD).

APPENDIX

Note on the Conversion from Mass–Diameter Laws to Density–Diameter Laws

The BB model described in section 3 uses a density law given as a function of the hydrometeor equivalent melted diameter D_{eqw} (cm):

$$\rho_h = \alpha_d D_{\text{eqw}}^{\beta_d}. \quad (\text{A1})$$

The equivalent melted diameter is defined as the diameter of a raindrop (density of 1 g cm^{-3}) having the same mass as a considered hydrometeor. It is common for microphysics in situ observations (FO14) to provide a mass–diameter relationship expressed as a function of largest dimension of the particle D_{max} :

$$m_h = \alpha_m D_{\text{max}}^{\beta_m}, \quad (\text{A2})$$

where m_h is the mass of the hydrometeor (g).

Deriving α_d and β_d from α_m and β_m is not trivial unless simplifying assumptions are adopted. Here, we consider that the icy hydrometeors are oblate, as suggested by FO14 from the in situ observations. Given the aspect ratio a/b , the link between the equivalent spherical diameter $D_{\text{eq_ice}}$ (diameter of a sphere of same volume) and the largest dimension is

$$D_{\text{eq_ice}} = D_{\text{max}} (a/b)^{1/3}. \quad (\text{A3})$$

The volume V_h and the mass m_h of the hydrometeor can be written as

$$V_h = \frac{4\pi}{3} \left(\frac{D_{\text{eq_ice}}}{2} \right)^3 = \frac{\pi}{6} D_{\text{max}}^3 \frac{a}{b} \quad \text{and} \quad (\text{A4})$$

$$m_h = \rho_h V_h = \frac{\pi}{6} D_{\text{max}}^3 \frac{a}{b} \rho_h. \quad (\text{A5})$$

The relation between equivalent spherical melt and icy maximum diameter of particles involves the density and the axis ratio a/b of spheroids as follows:

$$D_{\text{eqw}}^3 = D_{\text{eq_ice}}^3 \rho_h = D_{\text{max}}^3 \rho_h (a/b). \quad (\text{A6})$$

The maximal diameter from Eq. (A6) is

$$D_{\text{max}} = \frac{D_{\text{eqw}}}{\rho_h^{1/3}} \left(\frac{a}{b} \right)^{-1/3}. \quad (\text{A7})$$

By using Eq. (A2) to replace m_h in Eq. (A5), we obtain

$$\frac{\pi}{6} D_{\text{max}}^3 \frac{a}{b} \rho_h = \alpha_m D_{\text{max}}^{\beta_m}, \quad (\text{A8})$$

which is equivalent to

$$\rho_h = \frac{6}{\pi} \frac{b}{a} \alpha_m D_{\text{max}}^{\beta_m - 3}. \quad (\text{A9})$$

Then we replace D_{max} in Eq. (A9) with its expression from Eq. (A7):

$$\rho_h = \frac{6}{\pi} \frac{b}{a} \alpha_m \left[\frac{D_{\text{eqw}}}{\rho_h^{1/3}} \left(\frac{a}{b} \right)^{-1/3} \right]^{\beta_m - 3}. \quad (\text{A10})$$

Extracting the density is equivalent to

$$\rho_h^{\beta_m/3} = \frac{6}{\pi} \left(\frac{a}{b} \right)^{\beta_m/3} \alpha_m (D_{\text{eqw}})^{\beta_m - 3}. \quad (\text{A11})$$

We obtain an expression for ρ_h that is equivalent to Eq. (A1):

$$\rho_h = \frac{a}{b} \left(\frac{6}{\pi} \alpha_m \right)^{3/\beta_m} D_{\text{eqw}}^{3 - (9/\beta_m)}. \quad (\text{A12})$$

Through a comparison with Eq. (A1), we can establish the link between the parameters of density law and the parameters of mass law:

$$\alpha_d = \frac{a}{b} \left(\frac{6}{\pi} \alpha_m \right)^{3/\beta_m} \quad \text{and} \quad (\text{A13})$$

$$\beta_d = 3 - (9/\beta_m). \quad (\text{A14})$$

REFERENCES

- Andrieu, H., and J. D. Creutin, 1995: Identification of vertical profiles of radar reflectivity for hydrological applications using an inverse method. Part II: Formulation. *J. Appl. Meteor.*, **34**, 240–259, doi:10.1175/1520-0450(1995)034<0240:IOVPOR>2.0.CO;2.
- Bennartz, R., and G. W. Petty, 2001: The sensitivity of microwave remote sensing observations of precipitation to ice particle size distributions. *J. Appl. Meteor.*, **40**, 345–364, doi:10.1175/1520-0450(2001)040<0345:TSMORS>2.0.CO;2.
- Boudevillain, B., and H. Andrieu, 2003: Assessment of vertically integrated liquid (VIL) water content radar measurement. *J. Atmos. Oceanic Technol.*, **20**, 807–819, doi:10.1175/1520-0426(2003)020<0807:AOVILV>2.0.CO;2.

- Bouniol, D., J. Delanoë, C. Duroure, A. Protat, V. Giraud, and G. Penide, 2010: Microphysical characterisation of West African MCS anvils. *Quart. J. Roy. Meteor. Soc.*, **136**, 323–344, doi:10.1002/qj.557.
- Cazenave, F., M. Gosset, M. Kacou, E. Fontaine, C. Duroure, and B. Dolan, 2016: Characterization of hydrometeors in Sahelian convective systems with an X-band radar and comparison with in situ measurements. Part I: Particle identification from polarimetric data. *J. Appl. Meteor. Climatol.*, **55**, 231–249, doi:10.1175/JAMC-D-15-0013.1.
- Chapon, B., G. Delrieu, M. Gosset, and B. Boudevillain, 2008: Variability of rain drop size distribution and its effect on the Z–R relationship: A case study for intense Mediterranean rainfall. *Atmos. Res.*, **87**, 52–65, doi:10.1016/j.atmosres.2007.07.003.
- Dolan, B., and S. A. Rutledge, 2009: A theory-based hydrometeor identification algorithm for X-band polarimetric radars. *J. Atmos. Oceanic Technol.*, **26**, 2071–2088, doi:10.1175/2009JTECHA1208.1.
- Evaristo, R., G. Scialom, N. Viltard, and Y. Lemaître, 2010: Polarimetric signatures and hydrometeor classification of West African squall lines. *Quart. J. Roy. Meteor. Soc.*, **136**, 272–288, doi:10.1002/qj.561.
- Fabry, F., and I. Zawadzki, 1995: Long-term radar observations of the melting layer of precipitation and their interpretation. *J. Atmos. Sci.*, **52**, 838–851, doi:10.1175/1520-0469(1995)052<0838:LROOT>2.0.CO;2.
- , and W. Szyrmer, 1999: Modeling of the melting layer. Part II: Electromagnetic. *J. Atmos. Sci.*, **56**, 3593–3600, doi:10.1175/1520-0469(1999)056<3593:MOTMLP>2.0.CO;2.
- Fioleau, T., and R. Roca, 2013: An algorithm for the detection and tracking of tropical mesoscale convective systems using infrared images from geostationary satellite. *IEEE Trans. Geosci. Remote Sens.*, **51**, 4302–4315, doi:10.1109/TGRS.2012.2227762.
- Fontaine, E., A. Schwarzenboeck, J. Delanoë, W. Wobrock, D. Leroy, R. Dupuy, and A. Protat, 2014: Constraining mass-diameter relations from hydrometeor images and cloud radar reflectivities in tropical continental and oceanic convective anvils. *Atmos. Chem. Phys. Discuss.*, **14**, 2983–3041, doi:10.5194/acpd-14-2983-2014.
- Johnson, B. T., G. W. Petty, and G. Skofronick-Jackson, 2012: Microwave properties of ice-phase hydrometeors for radar and radiometers: Sensitivity to model assumptions. *J. Appl. Meteor. Climatol.*, **51**, 2152–2171, doi:10.1175/JAMC-D-11-0138.1.
- Kalogiros, J., M. N. Anagnostou, E. N. Anagnostou, M. Montopoli, E. Picciotti, and F. S. Marzano, 2013: Correction of polarimetric radar reflectivity measurements and rainfall estimates for apparent vertical profile in stratiform rain. *J. Appl. Meteor. Climatol.*, **52**, 1170–1186, doi:10.1175/JAMC-D-12-0140.1.
- Kirstetter, P.-E., H. Andrieu, B. Boudevillain, and G. Delrieu, 2013: A physically based identification of vertical profiles of reflectivity from volume scan radar data. *J. Appl. Meteor. Climatol.*, **52**, 1645–1663, doi:10.1175/JAMC-D-12-0228.1.
- Klaassen, W., 1988: Radar observations and simulation of the melting layer of precipitation. *J. Atmos. Sci.*, **45**, 3741–3753, doi:10.1175/1520-0469(1988)045<3741:ROASOT>2.0.CO;2.
- Koffi, A. K., M. Gosset, E. P. Zahiri, A. D. Ochou, M. Kacou, F. Cazenave, and P. Assamoi, 2014: Evaluation of X-band polarimetric radar estimation of rainfall and rain drop size distribution parameters in West Africa. *Atmos. Res.*, **143**, 438–461, doi:10.1016/j.atmosres.2014.03.009.
- Kummerow, C., W. S. Olson, and L. Giglio, 1996: A simplified scheme for obtaining precipitation and vertical hydrometeor profiles from passive microwave sensors. *IEEE Trans. Geosci. Remote Sens.*, **34**, 1213–1232, doi:10.1109/36.536538.
- Leary, C. A., and R. A. Houze Jr., 1979: The structure and evolution of convection in a tropical cloud cluster. *J. Atmos. Sci.*, **36**, 437–457, doi:10.1175/1520-0469(1979)036<0437:TSAEOC>2.0.CO;2.
- Martini, M., N. Viltard, S. Ellis, and E. Fontaine, 2015: Ice microphysics retrieval in the convective systems of the Indian Ocean during the CINDY–DYNAMO campaign. *Atmos. Res.*, **163**, 13–23, doi:10.1016/j.atmosres.2014.12.013.
- Moumouni, S., M. Gosset, and E. Houngninou, 2008: Main features of rain drop size distributions observed in Benin, West Africa, with optical disdrometers. *Geophys. Res. Lett.*, **35**, L23807, doi:10.1029/2008GL035755.
- Nelder, J. A., and R. Mead, 1965: A simplex method for function minimization. *Comput. J.*, **7**, 308–313, doi:10.1093/comjnl/7.4.308.
- Protat, A., and Coauthors, 2009: Assessment of *CloudSat* reflectivity measurements and ice cloud properties using ground-based and airborne cloud radar observations. *J. Atmos. Oceanic Technol.*, **26**, 1717–1741, doi:10.1175/2009JTECHA1246.1.
- Sánchez-Diezma, R., I. Zawadzki, and D. Sempere-Torres, 2000: Identification of the bright band through the analysis of volumetric radar data. *J. Geophys. Res.*, **105**, 2225–2236, doi:10.1029/1999JD900310.
- Steiner, M., R. A. Houze Jr., and S. E. Yuter, 1995: Climatological characterization of three-dimensional storm structure from operational radar and rain gauge data. *J. Appl. Meteor.*, **34**, 1978–2007, doi:10.1175/1520-0450(1995)034<1978:CCOTDS>2.0.CO;2.
- Stephens, G. L., and C. D. Kummerow, 2007: The remote sensing of clouds and precipitation from space: A review. *J. Atmos. Sci.*, **64**, 3742–3765, doi:10.1175/2006JAS2375.1.
- Szyrmer, W., and I. Zawadzki, 1999: Modeling of the melting layer. Part I: Dynamics and microphysics. *J. Atmos. Sci.*, **56**, 3573–3592, doi:10.1175/1520-0469(1999)056<3573:MOTMLP>2.0.CO;2.
- Testud, J., S. Oury, R. A. Black, P. Amayenc, and X. Dou, 2001: The concept of “normalized” distribution to describe raindrop spectra: A tool for cloud physics and cloud remote sensing. *J. Appl. Meteor.*, **40**, 1118–1140, doi:10.1175/1520-0450(2001)040<1118:TCOND>2.0.CO;2.
- Uijlenhoet, R., M. Steiner, and J. A. Smith, 2003: Variability of raindrop size distributions in a squall line and implications for radar rainfall estimation. *J. Hydrometeorol.*, **4**, 43–61, doi:10.1175/1525-7541(2003)004<0043:VORSDI>2.0.CO;2.
- Viltard, N., C. Burlaud, and C. D. Kummerow, 2006: Rain retrieval from TMI brightness temperature measurements using a TRMM PR-based database. *J. Appl. Meteor. Climatol.*, **45**, 455–466, doi:10.1175/JAM2346.1.
- Zawadzki, I., W. Szyrmer, C. Bell, and F. Fabry, 2005: Modeling of the melting layer. Part III: The density effect. *J. Atmos. Sci.*, **62**, 3705–3723, doi:10.1175/JAS3563.1.

4 AN INVERSE METHOD FOR DROP SIZE DISTRIBUTION RETRIEVAL

Article submitted to MDPI 'Remote Sensing'

An inverse method for Drop Size Distribution retrieval from polarimetric radar at attenuating frequency

Matias Alcoba¹, Hervé Andrieu² and Marielle Gosset^{1,*}

¹ Géoscience Environnement Toulouse, GET (CNRS-IRD-Université de Toulouse III-CNES)

² Laboratoire Eau et Environnement, IFSTTAR

* Correspondance : Marielle.gosset@ird.fr; Tel: +33(0)637502211

Abstract: A method which formulates the retrieval of Drop Size Distribution (DSD) parameters from polarimetric radar variables at attenuating frequency as the solution of an inverse problem is presented. The proposed method leads to a solution that best reconstitutes the polarimetric radar observables along the bins of radar radials. DSDs are represented by normalized Gamma distributions defined by three parameters (D_m, N_0^*, μ). The direct problem that describes polarimetric radar observables, including attenuation and their dependency on DSD parameters is analyzed based on T-matrix scattering simulations. The principle of the inverse algorithm and the crucial importance of the information a priori are discussed. The inverse algorithm and its application to the DSD retrieval are then presented. The inverse method is applied to an African Monsoon Multidisciplinary Analysis (AMMA) field campaign that deployed an X-band dual-polarization Doppler radar and optical disdrometers in Benin, West Africa in 2006 and 2007. The dataset is composed of X-band polarimetric radar PPIs and disdrometer data of 15 organized convective systems observed in 2006. The *a priori information* on DSD parameters is derived from the polarimetric radar observables, by means of relationships suited to these type of rain events. The proposed retrieval method of DSD parameters

leads to the following results: i) the obtained DSD fields show a better spatial consistency than the a priori DSD fields, ii) the polarimetric radar observables are better reproduced from the obtained DSD parameters than from the a priori ones, iii) the comparison with time series of DSD parameters derived from disdrometer data confirms that the inverse method results in an improved estimation of DSD parameters compared to a priori ones. These promising results indicate that DSD retrieval based on the inverse theory framework and considering the whole radial improves the coherence of DSD estimates at radar image scale, compared to retrieval obtained from polarimetric radar observables processed gate by gate. A more comprehensive evaluation in different climatological contexts would be required to confirm these first results.

Keywords: Radar polarimetry; Drop size distribution retrieval; inverse problem; attenuation correction; X-band radar; tropical rainfall

4.1 Introduction

Rainfall is usually defined as a flux of water, which monitoring is very important at all scales (local to global) in many applications, from climate research to flash flood prediction. Rainfall estimation has greatly benefitted from the progress of weather radar and the development of dual-polarization methods. In addition to quantitative rainfall estimation, radar techniques have provided some insight in the microphysics and the dynamics of storms, enabling a 3D analysis of winds and hydrometeor type and density within clouds and precipitation ((Fabry 2015) for a recent review). A whole branch of weather radar research has been devoted to rain or cloud Drop Size Distributions (DSD), with two purposes: i) characterizing DSD and its variability as a source of uncertainty in radar estimation of rainfall ((Atlas et al. 1999; Lee and Zawadzki 2005; Lee et al. 2004; Steiner, Smith, and Uijlenhoet 2004; Uijlenhoet, Steiner, and Smith 2003; Cao et al. 2008)) and ii) deriving information on the DSD from the radar measurements itself ((Vivekanandan, Zhang, and Brandes 2004; Koffi et al. 2014; Bringi et al. 2002)). The determination of the DSD over various spatial and temporal scales is interesting for a range of scientific applications. With a better knowledge of the DSD, accurate and physically based characterization of rain can be obtained and used for many meteorological and hydrological applications: rain rate estimation, rain erosivity, satellite and radar remote sensing studies, rain microphysics, cloud modeling, among others. Most

of the early work on the DSD was based on disdrometers and mainly focused on investigating if some standard form of DSD could be defined ((Torres, Porrà, and Creutin 1994)). Based on these studies, on observations and on theoretical considerations on cloud/rain microphysics, it is commonly accepted that rainfall DSD can be represented by a Gamma law governed by three parameters characterizing: the number of drops, the characteristic diameter, the shape ((Testud et al. 2001)). The exponential DSD initially proposed by Marshall and Palmer (Marshall and Palmer 1948) is a particular case of gamma DSD; other laws like lognormal or 4 parameters extended gamma have also been proposed, but are less commonly used. Many studies have been devoted to analyzing how the DSD parameters vary with rain bulk variables (rain rate, radar reflectivity factor, liquid water content, median-volume diameter) and to find expressions for the DSD function and parameters, that reduce the variability ((Testud et al. 2001; Lee et al. 2009)). A well adopted solution consists in normalizing the DSD and the drop diameters by one or two integral moments of the DSD ((Torres, Porrà, and Creutin 1994; Testud et al. 2001) among others).

Another topic of research is the time-space variability of the DSD parameters and its relation with the physical processes inside the clouds and precipitation. (Moumouni, Gosset, and Houngninou 2008) highlighted the variability between and within West African squall lines, with a marked partition between convective and stratiform DSDs. This is consistent with several authors (Uijlenhoet, Steiner, and Smith 2003; Testud et al. 2001; Tokay and Short 1996) who also reported a marked jump in the DSD characteristic number (' N_0 jump') between convective cells and the stratiform trail. (Hachani et al. 2017) based on a five-year DSD climatology across the Mediterranean Cevennes–Vivarais region showed the influence on the DSD of the orographic environment, season, weather patterns and rainfall types. (Steiner, Smith, and Uijlenhoet 2004) demonstrated that different rainfall generation processes lead to different types of DSD and different relationships between the characteristic number and diameter.

Disdrometers provide only punctual information on the DSD and no information on its spatial variability unless an extensive (hence expensive) network of disdrometers is used. Polarimetric weather radar, on the other hand, can provide spatially distributed information on rain microphysics. Radar polarimetry has lead to significant progress in rainfall characterization. In addition to the reflectivity factor (Z_H , expressed in dBZ), a polarimetric radar provides the differential reflectivity ($Z_{DR} = Z_H - Z_V$, expressed in dB, with H and V denoting horizontal and vertical components of the polarized wave

respectively), the cross-correlation coefficient (ρ_{HV}) and the differential phase shift (ϕ_{DP} expressed in degrees). The range derivative, called the specific differential phase shift (K_{DP}) can be estimated from ϕ_{DP} . Because of the drop oblateness increases with their diameter ((Bringi and Chandrasekar 2001)), Z_{DR} is well related to the mean drop diameter of the DSD. ϕ_{DP} , is influenced by the amount of water along the path and by the oblateness of the drops – it is closely related to the attenuation along the path and can be used to correct it ((Gourley, Tabary, and Parent du Chatelet 2007; Gosset, Zahiri, and Moumouni 2010a; Carey et al. 2000; Bringi, Keenan, and Chandrasekar 2001; Matrosov et al. 2005)). K_{DP} can be used to estimate the rainfall rate (R in mm/h), ρ_{HV} helps distinguishing melting hydrometeors, and altogether the polarimetric variables can help determining the dominant type of hydrometeors and non-meteorological echoes. First radar polarimetry was investigated for rainfall estimation. Different methods have been proposed and compared ((Tabary et al. 2011), (Chen, Chandrasekar, and Bechini 2017)). The retrieval of DSDs was first proposed as a mean to improve rainfall estimation from polarimetric variables ((Gorgucci et al. 2001a)). (Gorgucci et al. 2001b; Gorgucci et al. 2002) proposed the β -method, improved in (Gorgucci, Chandrasekar, and Baldini 2009), to retrieve the parameters of a DSD gamma distribution. This method introduces the additional parameter β , □slope of the empirical equation expressing the drop ratio axis in function of the drop diameter. The authors first express β from polarimetric variables and derive the DSD parameters from polarimetric variables (Z_H, Z_{DR}, K_{DP}) by means of power laws whose coefficients depend on β . The constrained gamma method ((Zhang, Vivekanandan, and Brandes n.d.; Brandes, Zhang, and Vivekanandan 2004)) is based on an empirical relation between the slope (λ) and the shape (μ) parameters of the DSD, from which are derived the relations expressing the DSD parameters as functions of Z_H and Z_{DR} . According to (Kim, Maki, and Lee 2010; Anagnostou et al. 2008), the constrained gamma method performs better than the β -method. (Raupach and Berne 2017) developed a method applicable to a double-moment normalized DSD, defined by two parameters. (Koffi et al. 2014) tested in Africa DSD retrievals based on empirical relationships. All these studies rely on empirical (mostly power law) relationships between the DSD parameters and the radar variables. Other studies proposed statistical frameworks to account for the stochastic nature of the DSD. (Islam, Rico-Ramirez, and Han 2012) used a tree-based genetic program to retrieve the parameters of a gamma DSD from Z_H and Z_{DR} . (Cao et al. 2010) proposed a Bayesian approach with DSD parameters as state variables to estimate rainfall rate from S-band polarimetric radar. (Wen et al.

2018) formulated the retrieval of DSD parameters from S-band polarimetric radar variables as an inverse problem.

The studies above do not explicitly account for radar attenuation by rain, either because they are based on S-band radar or because the radar reflectivities were corrected for attenuation before DSD retrieval. For X-band radars, the variables (Z_H, Z_{DR}) must be corrected for attenuation to avoid underestimation of the DSD parameters. (Kim, Maki, and Lee 2008; Park et al. 2005; Shi et al. 2017) adapted the self-consistent method proposed by (Bringi, Keenan, and Chandrasekar 2001) for attenuation correction of X-band data. (Gorgucci, Chandrasekar, and Baldini 2009) also used a self-consistency method. (Raupach and Berne 2017) proposed a variation on the ZPHI algorithm ((Testud et al. 2000)). In most studies a relationship between the path integrated attenuation and the differential phase shift is used as in (Matrosov et al. 2002), (Testud et al. 2000) and (Bringi, Keenan, and Chandrasekar 2001). (Kalogiros et al. 2014) presented the self-consistent with optimal parameterization (SCOP) algorithm to correct X-band radar for attenuation. (Gou, Chen, and Zheng 2019) proposed an improved version of the attenuation correction for C-Band. (Koffi et al. 2014; Gosset, Zahiri, and Moumouni 2010a) followed (Matrosov et al. 2005) and found that a simple attenuation correction based on a linear relationship between attenuation and ϕ_{DP} gave robust results; in these papers the linear coefficient is derived on the radar data itself using (Carey et al. 2000). (Chang, Vivekanandan, and Chen Wang 2014) formulated the attenuation estimation of X-band polarimetric radar by means of a variational algorithm. (Yoshikawa, Chandrasekar, and Ushio 2014) noticed that the two-step procedure that applies sequentially attenuation correction and then DSD retrieval may result in errors and inconsistency in the retrieved DSD. They proposed a three step procedure, based on a cost function minimization, to retrieve the DSD along all the gates of a radar radial. In (Yoshikawa, Chandrasekar, and Ushio 2014) the first step is an iterative method based on a simultaneous calculation of the forward and backscattering effects of DSD in order to insure consistency in the assumptions used for all radar variables.

The present study builds upon these papers and formulates the retrieval of a radial profile of DSD parameters from X-band polarimetric radar in the framework of inverse theory ((Tarantola 2005; Menke 2018)). The objective is to retrieve the parameters of DSD distributions (here, gamma) that best reconstitute the measured polarimetric radar observables along a radial. The proposed model expresses the radar observable as a function of DSD parameters along the radial, explicitly accounting for the attenuation.

The retrieval method presented in this study can be viewed as an evolution of the method proposed by (Yoshikawa, Chandrasekar, and Ushio 2014). Its originality lies in the following points: i) an extension to X-band polarimetric data affected by attenuation of the statistical approach proposed by (Cao et al. 2010) and applied to S-band radar data, ii) a solution of the inverse problem by an algorithm different from that used by (Wen et al. 2018) that did not account for attenuation and from (Yoshikawa, Chandrasekar, and Ushio 2014) who do not explicitly account for *a priori* information, iii) a special attention given to the *a priori* information, a key point in inverse methods in presence of non-linear models or for solving underdetermined problems, v) a test of the method with X-band radar data in West Africa, on case studies with intense rainfall and heavy attenuation – challenging conditions for DSD retrieval.

Section 2 introduces the radar and disdrometer dataset gathered in West Africa, and the typology of the studied convective rainfall systems. Section 3 provides a detailed description of the forward problem relating polarimetric radar variables at attenuating frequency and the DSD along the radar beam. Section 4 introduces the inverse model framework and its advantages for DSD retrieval. The practical implementation and sensitivity to model parameters and to the *a priori* information is discussed. Section 5 provides the quantitative results and statistics when the radar retrieved DSD is compared with disdrometer data. The conclusions and perspective of this work are proposed in section 6.

4.2 Study area and dataset

This work was initiated as part of the African Monsoon Multi-disciplinary Analysis (AMMA) program ((Lebel et al. 2010)). One of many AMMA objectives was a better characterization of the meso-scale convective systems (MCS) which bring most of the rainfall during the West African Monsoon ((Depraetere et al. 2009)). For this purpose, several super sites were equipped during AMMA, including one in Northern Benin near the town of Djougou situated in the upper basin of the Oueme river. This area has been equipped as a hydro-meteorological observatory since the late 90s, with a dense network of rain and stream gauges, as part of the AMMA-CATCH observing system ((Galle et al. 2018)). During the AMMA intensive observation period, from 2005 to 2007, a X-band polarimetric radar was installed in Djougou. Several disdrometers ((Moumouni, Gosset, and Hounninou 2008)) complemented the experiment during this period. The dataset and some results that are a starting point for the present study are summarized below.

4.2.1 X-band polarimetric Radar data

The X-port X-band polarimetric radar was developed by the Institut de Recherche pour le Developpement (IRD) as a transportable unit to study rainfall associated with tropical convection ((Cazenave et al. 2016)). The radar operates at 9.4 GHz with simultaneous transmission and reception of horizontal (H) and vertical (V) signals thanks to an orthomode feed. The peak transmitted power in each polarization is 50 kW, and the 1.4 m antenna provides a 1.4° radar beam. For the present dataset, the radar pulse length is set to $1\mu s$ and the radar pulse repetition frequency is 1 kHz. The raw data from 128 instant pulses are processed in order to provide the radar variables every range gate (150 m length) along a given azimuth. The stored radar variables are: radar reflectivity in horizontal and vertical polarization (z_H and z_V), differential phase shift (ϕ_{DP}), cross polarization correlation coefficient (ρ_{HV}), and Doppler radial velocity calculated for each polarization (V_H and V_V). In this work, the radial velocity is used only to detect and remove ground clutters. During AMMA the radar was located in Djougou ($9.66^\circ N$, $1.69^\circ E$) and operated with a ‘volumetric’ protocol composed of 12 successive Plan Position Indicator scans (PPI) in a sequence of 5 or 10 min. In the present work only the PPI with elevation 2.8° is used; it is low enough to avoid the melting layer (which is quite high and stable at 3.5 to 4 km height in this region) and better than the lowest elevation angles (0.9° - 1.8°) in terms of ground clutter contamination.

To derive K_{DP} from the measured Φ_{DP} , two sliding window filters are applied, first a median filter length of 25 gates and then a convolution with a Gaussian filter of length 10 gates and standard deviation of 5 gates length. The median filter first eliminates the main noise variability of about 5 - 10° . Then the Gaussian convolution smoothes the gate to gate gaps generated by the local median filter. The filtering reduces the noise in the derived K_{DP} and limits the effect of the differential scattering phase shift. We find that this simple filtering compares well with the filtering technique proposed by (Hubbert and Bringi 1995) that was implemented on the same dataset in (Koffi et al. 2014).

In the results presented in section 4, the other observed variables have also been smoothed in order to minimize the influence of the noise in the DSD retrieval.

4.2.2 Optical disdrometer data

Optical disdrometers were installed in three locations in the AMMA Benin super-site: Copargo ($1.53^\circ E$; $9.83^\circ N$) situated 18 km from the radar, Nangatchiori (about 10 km from the radar) and Djougou at the radar site. As described in (Moumouni, Gosset, and

Houngninou 2008), the instruments are based on an optical principle. A near-IR rectangular single or double-beam of light is attenuated by the falling rain drops. A dedicated processing transforms this raw information into the diameter and fall velocity of the drops. For the present dataset the rain drop spectra are acquired every minute with 22 diameter classes from 0.06 mm to 6.5 mm. The whole data base (described in (Moumouni, Gosset, and Houngninou 2008)) is composed of 11.640 spectra, belonging to 93 different storms and a total of 1220 mm rainfall acquired in 2005 (Nangatchori, Djougou), 2006 (Copargo, Djougou) and 2007 (Djougou) by one (or two) of the disdrometers. The quality of the dataset was verified by comparing the rain rates distributions and daily total collected by each disdrometer with the closest rain gauge ((Moumouni, Gosset, and Houngninou 2008)).

In the present work, radar retrieval of the DSD is compared solely with the dual beam disdrometer (Delahaye et al. 2006) that operated in Copargo during the peak of rainy season (June-September) 2006, for two reasons: i) this disdrometer is the most distant from the radar and best suited to analyze the effect of attenuation on the radar signal, and ii) dual beam disdrometers provide a more precise estimation of the DSD because the drops fall through two successive beams, which reduces the uncertainty on drop velocity estimation and detection of multiple drops (Delahaye et al. 2006)

4.2.3 Previous findings from this dataset

(Moumouni, Gosset, and Houngninou 2008) and (Moumouni 2009) provide an extensive analysis of the AMMA DSD dataset. They investigated which form of DSD and normalization best fitted the observed spectra. They also analyzed the variability of the DSD characteristics and its relation to bulk variables like the rain rate or water content, and the type of rainfall (convective or stratiform; organized squall lines versus local convection). Their main conclusion is that the double moment normalization of the DSD introduced by (Testud et al. 2001) provides a good framework to represent the shape, fit the parameters and explain the variability of the observed DSDs. The DSD is therefore expressed:

$$N_G(D_m, N_0^*, \mu; D) = N_0^* F\left(\frac{D}{D_m}, \mu\right) \quad (\text{eq. 4.1})$$

where the three parameters of the normalized DSD distribution are the volume weighted mean diameter D_m , the scaling parameter of concentration N_0^* , and the shape parameter μ . D_m and N_0^* are defined by :

$$D_m = \frac{M_4}{M_3} \text{ with } M_n = \int_0^\infty N(D)D^n dD \quad (\text{eq. 4.2})$$

$$N_0^* = \frac{4^4}{\pi \rho_w} \frac{LWC}{D_m^4} \text{ with } LWC = \frac{\pi \rho_w}{6} M_3 \quad (\text{eq. 4.3})$$

where M_n is the moment of order n of the DSD distribution, ρ_w is the density of water, and LWC is the total liquid water content.

$F(X, \mu)$ represents the shape of the normalized distribution, in our case the gamma function well fitted on the observed DSD. As discussed by (Testud et al. 2001), this choice insures the independence between D_m, N_0^* on one side, and μ , the shape parameter of the gamma law :

$$F(X, \mu) = \frac{\Gamma(4)(\mu+4)^{\mu+4}}{4^4 \Gamma(\mu+4)} X^\mu \exp[-(\mu+4)X] \quad (\text{eq. 4.4})$$

(Moumouni, Gosset, and Houngninou 2008) confirmed on the African DSD the findings of (Testud et al. 2001): the normalized DSD function F is remarkably stable and independent of the rain type. The variability of the DSD within and between systems is well explained by the variability of the parameters N_0^* and D_m . Another finding from (Moumouni, Gosset, and Houngninou 2008) consistent with (Testud et al. 2001) and (Tokay and Short 1996) is the existence of a ‘ N_0 jump’ or clear distinction in the DSD characteristics between the convective and stratiform rain. For a given rain rate, N_0^* tends to be higher, and corollary D_m smaller in convective rain; this existence of relative large drops for low or moderate rain rates in the stratiform part can be explained by the melting of large aggregates in this part of the squall lines ((Alcoba et al. 2016)(Cazenave et al. 2016)). The characterization of the shape parameter μ from disdrometer spectra is more delicate. (Moumouni, Gosset, and Houngninou 2008) showed that very different values of μ are obtained if the moment method is used or if μ is fitted directly on the shape of the DSD. No clear variability of μ as a function of the other DSD parameters or bulk variables was found.

The combined radar/disdrometer dataset, together with the AMMA-CATCH rain gauges has been used in (Gosset, Zahiri, and Moumouni 2010b) and (Koffi et al. 2014) to study the influence of DSD variability on the polarimetric variables and to test various attenuation correction, rain rate and DSD estimation algorithms.

(Koffi et al. 2014) used reflectivity (Z_H^{corr}), differential reflectivity (Z_{DR}^{corr}), both corrected for attenuation and (K_{DP}) to test various expressions of DSD parameters N_0^* and D_m . The best estimation of these two parameters was evaluated on four rain events by

comparison with the Copargo disdrometer. The comparison between radar and disdrometer derived DSDs proved satisfactory, with a correlation coefficient above 0.6 for N_0^* and 0.5 for D_m and low relative biases in both cases (less than 3 % for N_0^* and 1% for D_m respectively). The proposed power-law expressions are:

$$\log_{10}(N_0^*) = a + b Z_H^{corr} + c \log_{10}(K_{DP}) + d \log_{10}(Z_{DR}^{corr}) \quad (eq. 4.5)$$

$$D_m = e Z_{DR}^{corr f} \quad (eq. 4.6)$$

with $a = 2.16$, $b = 0.039$, $c = 0.41$, $d = -2.04$, $e = 1.699$, $f = 0.353$. K_{DP} in $[^\circ km^{-1}]$, Z_H^{corr} and Z_{DR}^{corr} (in dB), D_m in $[mm]$ and N_0^* in $[m^{-3}mm^{-1}]$.

As detailed in section 4, the fields of N_0^* and D_m derived from above will be used as *a priori* solution for the new DSD retrieval scheme presented in the next sections.

4.3 Forward modelling of polarimetric radar observables

4.3.1 Measured radar variables at X-band

At attenuated frequencies like X-band (and to a lesser extend C-band), radar measurement is strongly influenced by the effect of the atmosphere and especially the precipitation, encountered along the path. This is reminded in the equations below for the three variables of interest which are actually measured by the radar, the reflectivities and the differential phase shift:

$$Z_{H,V}^{att}(r) = Z_{H,V}(r) + 10 \int_0^r -0.1 * K_{H,V}(s) ds \quad (eq. 4.7)$$

where H and V denote polarization, $Z_{H,V}^{att}$ is the attenuated reflectivity measured at range r , $Z_{H,V}$ is the intrinsic reflectivity of the volume of precipitation at range r , and $K_{H,V}$ is the specific attenuation (in dB/km) along the radial.

The differential reflectivity is derived as the ratio (or difference when the reflectivities are in dBZ) between Z_H and Z_V . Its measured value Z_{DR}^{att} at range r is expressed:

$$Z_{DR}^{att}(r) = Z_{DR}(r) + 10 \int_0^r -0.1 * (K_H(s) - K_V(s)) ds \quad (eq. 4.8)$$

where the differential attenuation $A_{DP} = K_H - K_V$ is introduced. Similarly the differential phase shift measured at range r , is the sum of the cumulative effect of the specific differential phase shift K_{DP} and the backscattering phase shift δ_{DP} at range r .

$$\Phi_{DP}(r) = \delta_{DP}(r) + \int_0^r K_{DP}(s) ds \quad (\text{eq. 4.9})$$

4.3.2 Polarimetric radar observables/variables

All polarimetric radar variables introduced in the right hand side of Eq (4.7 to 4.9) : $Z_{H,V}, Z_{DR}, K_{DP}, K_{H,V}, A_{DP}$ characterize the interactions between radar waves and precipitation ((Bringi and Chandrasekar 2001)). They depend on the number, size and shape of the raindrops inside the radar beam and also on their phase if other types of hydrometeors than raindrop were considered. A commonly adopted assumption is to consider drops as ellipsoids with a revolution symmetry along their vertical axis (b), and an oblate shape, the horizontal axis (a) being the largest. The shape and deformation of drops as they grow and fall, and the expression of the aspect ratio ($r_a = a/b$) has been the subject of many studies, based on direct or indirect observations. Three recent reviews summarize the literature on rain drop shapes ((Beard, Bringi, and Thurai 2010; Szakáll et al. 2010; Gorgucci, Baldini, and Chandrasekar 2006)). Figure 4-1 illustrates the sensitivity of polarimetric radar variables to the aspect ratio law. In this work, the law proposed by (Andsager, Beard, and Laird 1999):

$$r_a = \begin{cases} 1.012 - 0.1445D_e - 1.028D_e^2 & \text{for } 1.1 \leq D_e \leq 4.4\text{mm} \\ 1.0048 - 0.0057D_e - 2.628D_e^2 + 3.682D_e^3 - 1.677D_e^4 & \text{for } D_e < 1.1 \cup D_e > 4.4\text{mm}, \end{cases} \quad (\text{eq. 4.10})$$

with D_e the equivalent spherical diameter of the drop in mm, is adopted - unless otherwise stated.

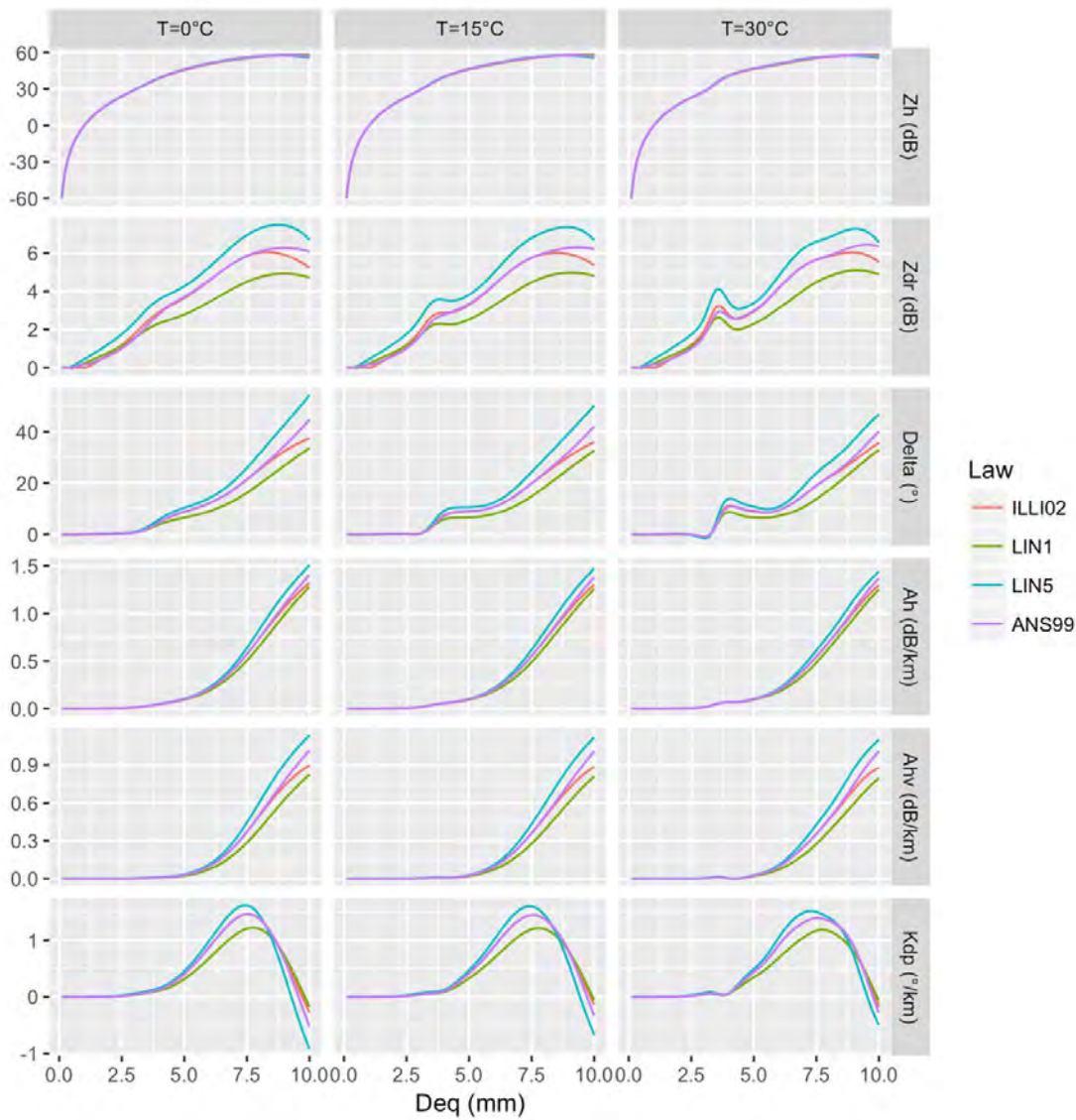


Figure 4-1: One drop T-matrix output from (Mishchenko, Travis and Mackowski 1996) code for three different temperatures and four aspect ratio laws for a 2° incidence angle (elevation). The results are split into a matrix of graphics, the rows are for the different polarimetric variables as indicated on the right vertical axis label and the columns are for the three indicated temperatures. On each plot the indicated radar variable is displayed as a function of the equivalent Diameter D_{eq} . The line colors are for the different aspect ratio laws: ILLI02 is the law described in (Illingworth and Blackman 2002), LIN1 and LIN5 are for the linear law proposed in (Pruppacher and Beard 1970) with oblateness parameter $\beta = [0.052, 0.072]$. The ANS99 law is described in (Andsager, Beard and Laird 1999). Note the low variability due to temperature and the high variability with respect to the aspect ratio laws.

Unlike for small and/spherical drops where simplifying expressions were established for the radar variables (Rayleigh; Rayleigh–Ganz; Mie) as function of the drop dimensions, there is no simple analytical formula to express $Z_{H,V}, Z_{DR}, K_{DP}, K_{H,V}, A_{DP}$ for distribution of drops considered as oblate spheroids. To model explicitly the electromagnetic properties of drops, the T-matrix method for microwave scattering by non-spherical particles ((Mishchenko, Travis, and Mackowski 1996; Waterman 1965; Waterman 1971)) is a reference in weather radar polarimetry and an open source code has generalized its use. The method calculates the propagative and scattering properties of populations of spheroid drops defined by their aspect ratio, their orientation compared to the incident electromagnetic field, their size relative to the wavelength, and their refractive index. In order to account for drop oscillation, a distribution of canting angles can be provided.

The polarimetric radar variables for a given DSD can be estimated by convoluting the T-matrix simulations for a single drop size by the DSD:

$$F_{POL}(N_G, p) = \int_{D_{min}}^{D_{max}} F_{POL}(D, p) N_G(D) dD \quad (eq. 4.11)$$

where F_{POL} denotes the radar polarimetric variable ($Z_{H,V}, K_{DP}, K_{H,V}$ etc.), N_G is the DSD (as in Eq 4.1) with its triplet of parameters (N_0^*, D_m, μ); the vector p contains all the other parameters of the T-matrix model (oblateness law; temperature etc.). By replacing the DSD by its expression (1), Eq (4.11) is rewritten:

$$F_{POL}(N_G, p) = N_0^* \int_{D_{min}}^{D_{max}} F_{POL}(D, p) F\left(\frac{D}{D_m}, \mu\right) dD \quad (eq. 4.12)$$

Eq (4.12) shows the linear dependence of the radar variables ($K_{DP}; Z_{H,V}; K_{H,V}, A_{DP}$) on N_0^* . Z_{DR} which is the ratio of Z_H over Z_V , is totally independent from N_0^* . The dependence on μ and D_m is more complex. Figure 4-2 shows the bulk polarimetric variables calculated with the forward model for a constant $N_0^* = 3000 m^{-3} mm^{-1}$ and for the indicated range of μ and D_m . The polarimetric variables appear very sensitive to D_m and less to μ , except for Z_{DR} . Z_{DR} dependence on D_m is close to linear (as shown in many previous work); K_{DP} and K_H have a dependency close to the 5th power of D_m and Z_H to the 6th power.

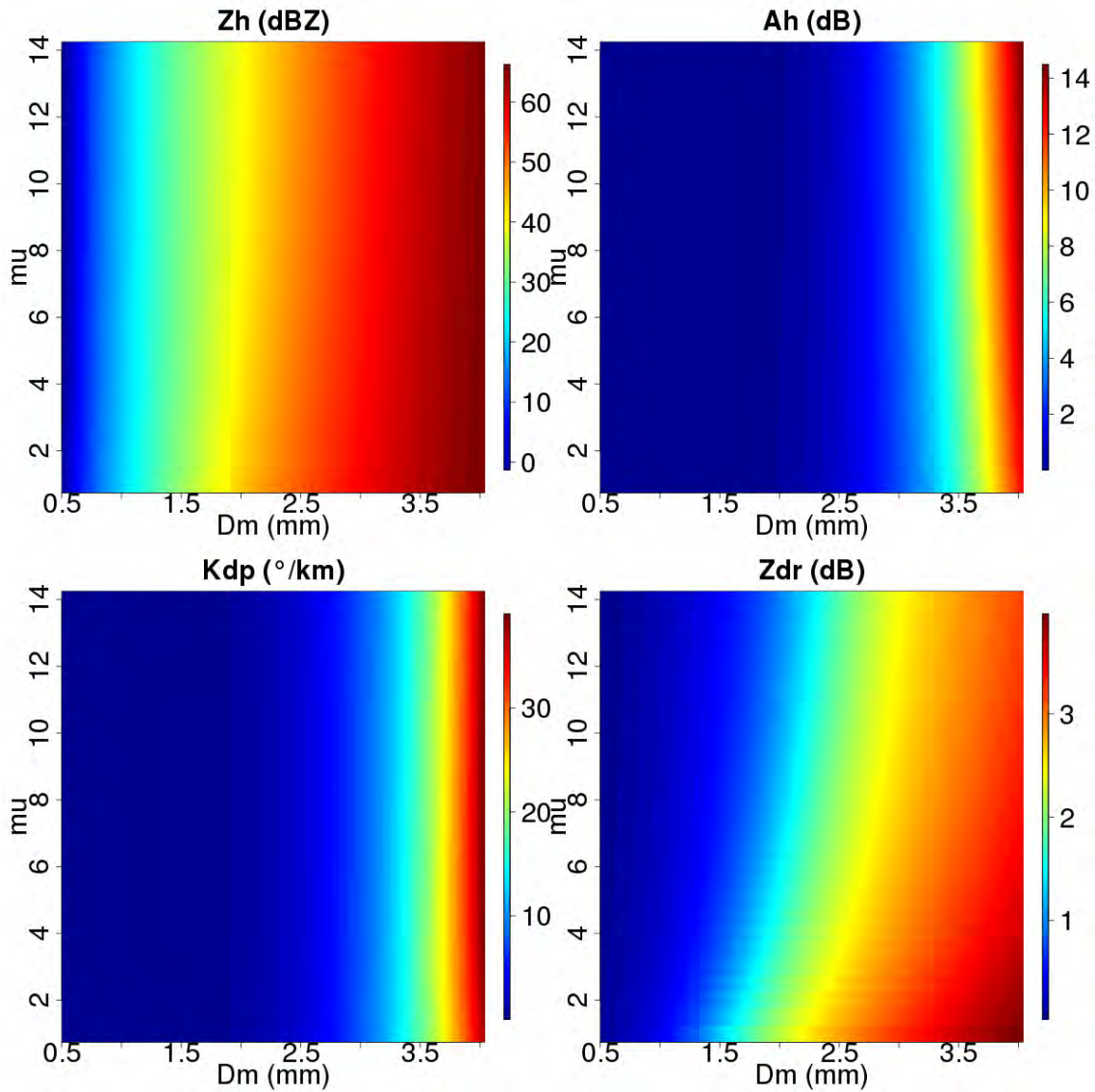


Figure 4-2: T-matrix simulated radar variables Z_H, K_H, K_{DP} and Z_{DR} , for a constant $N_0^* = 3000 \text{ m}^{-3} \text{ mm}^{-1}$ as function of $\mu \in [1, 14]$ and $D_m \in [0.5, 4 \text{ mm}]$, for Temperature 20°C and the ANDS99 (see text) shape law. (The units of the color bar for each variable are indicated in bracket in the plot title).

4.3.3 The forward discretized model between polarimetric radar observables and DSD parameters

The forward model needs to be discretized in view of the inversion. For each radial, the radar data is discretized along n range gates with a spatial resolution Δr . In each radar gate of index i , (located at range $i\Delta r$) the useful radar observables are the triplet of variables $(Z_{Hi}^{att}, Z_{DRi}^{att}, K_{DPi})$, namely attenuated reflectivity in horizontal polarization,

attenuated differential reflectivity, and specific differential phase. In addition, the phase shift Φ_{DPn} at the last gate of the radar radial is also taken as an additional constraint to identify the DSD parameters along the radial. The rain DSD in each radar gate is defined by a triplet of parameters $X_{Gi} = (N_{0i}^*, D_{mi}, \mu_i)$. The objective of the inversion in section 4 is to retrieve these X_{Gi} .

Following Eq (4.11), the system of equations at each gate can be written:

$$Z_{Hi}^{att} = Z(N_{Gi}) - 2 \Delta r \sum_{k=1}^{k=i} K_H(N_{Gk}) \quad (eq. 4.13)$$

$$Z_{DRi}^{att} = Z_{DR}(N_{Gi}) - 2 \Delta r \sum_{k=1}^{k=i} A_{DP}(N_{Gk}) \quad (eq. 4.14)$$

$$K_{DPi} = K_{DP}(N_{Gi}) \quad (eq. 4.15)$$

And in addition for $i = n$

$$\Phi_{DPn} = 2 \Delta r \left[\sum_{k=1}^{k=n} K_{DPk} - \Phi_{DP1} \right] \quad (eq. 4.16)$$

Equations (4.13) and (4.14) are expressed in dBZ. Note that Eq (4.16) is an approximation and does not account for the backscattering phase δ_{DP} at gate 1 and n; however the Φ_{DP} filtering (see section 2) reduces the impact of δ_{DP} and our previous work ((Koffi et al. 2014; Gosset, Zahiri, and Moumouni 2010b)) showed that the actual effect of δ_{DP} is low.

The vector regrouping the attenuated reflectivity, attenuated differential reflectivity, specific differential phase in the n successive gates and the total differential phase shift at gate n , for a radar radial is denoted $\mathbf{Y} = [Z_h^{att}, Z_{dr}^{att}, K_{dp}, \Phi_{DPn}]$. The vector regrouping the parameters of the gamma DSD in the n successive gates of the same radar radial is denoted $\mathbf{X} = [N_0^*, D_m, \mu]$, N_0^*, D_m, μ being the vectors regrouping each parameter in the n successive gates of this radial. The vector \mathbf{Y} has a length of $[3n + 1]$ and the vector \mathbf{X} has a length of $[3n]$.

The relationships between polarimetric radar observables and DSD parameters along a radar radial are regrouped in the non-linear model m based on Equations 4.11 to 4.16:

$$\mathbf{Y} = \mathbf{m}(\mathbf{X}) \quad (eq. 4.17)$$

The objective of the inversion is to retrieve the vector \mathbf{X} that best explains the radar observables \mathbf{Y} measured along each radar radial. The next section explains the method used to reach this objective.

4.4 The inverse problem to retrieve DSD from observations

4.4.1 Inverse modeling framework

The retrieval of the DSD triplets all along the radial based on the system of equations (4.17) is a typical inverse problem. The proposed approach is to solve this problem within the framework of inverse theory, as detailed in (Menke 2018) and (Tarantola 2005), with the algorithm proposed by (Tarantola and Valette 1982). Let us notice that inverse and variational approaches are close and use similar algorithms. The difference between the two approaches might be found in the initialization of the parameters to retrieve, called “*a priori* information” in the inverse theory.

In the problem to solve (Eq 4.17), the input data are the variables measured by a polarimetric weather radar regrouped in a vector denoted \mathbf{Y}^0 . The parameters to retrieve are the three parameters of the Gamma DSD distributions along a radar radial, components of the vector \mathbf{X}_G . The solution minimizes the following expression:

$$\begin{aligned} \Phi(\mathbf{Y}, \mathbf{X}) = & [\mathbf{m}(\mathbf{X}) - \mathbf{Y}^0]^t \mathbf{C}_Y^{-1} [\mathbf{m}(\mathbf{X}) - \mathbf{Y}^0] \\ & + [\mathbf{X} - \mathbf{X}^{prior}]^t \mathbf{C}_X^{-1} [\mathbf{X} - \mathbf{X}^{prior}] \end{aligned} \quad (eq. 4.18)$$

Where Φ is the likelihood function, t signifies transpose, \mathbf{Y}^0 is the vector of observed (attenuated) radar data, \mathbf{X}^{prior} is the vector of *a priori* DSD parameters, \mathbf{C}_X is the covariance matrices of residuals between true and *a priori* values of \mathbf{X} and \mathbf{C}_Y the covariance matrix of measurement errors.

The statistical distributions of both $[\mathbf{Y} - \mathbf{Y}^0]$ and $[\mathbf{X} - \mathbf{X}^{prior}]$ are assumed to be unbiased and Gaussian. (Menke 2018) showed that the solution vector \mathbf{X}' satisfies:

$$\mathbf{X}' = \mathbf{X}^{prior} + \mathbf{C}_X \mathbf{J}^t [\mathbf{J}^t \mathbf{C}_X \mathbf{J} + \mathbf{C}_Y]^{-1} [\mathbf{Y}^0 - \mathbf{m}(\mathbf{X}') + \mathbf{J}(\mathbf{X}' - \mathbf{X}^{prior})] \quad (eq. 4.19)$$

Where \mathbf{J} is the matrix of (first-order) partial derivatives of the model m . If the model m is nonlinear, (Tarantola 2005) demonstrates that the solution can be obtained by an algorithm which can be written:

$$\begin{aligned} \mathbf{X}_{k+1} \approx & \mathbf{X}_k + \alpha [\mathbf{J}_k^t \mathbf{C}_Y^{-1} \mathbf{J}_k + \mathbf{C}_X^{-1}]^{-1} [\mathbf{J}_k^t \mathbf{C}_Y^{-1} \langle \mathbf{Y}^0 - \mathbf{m}(\mathbf{X}_k) \rangle \\ & + \mathbf{C}_X^{-1} \langle \mathbf{X}_k - \mathbf{X}^{prior} \rangle] \end{aligned} \quad (eq. 4.20)$$

In which \mathbf{X}_k constitutes the result of the k^{th} iteration, $\mathbf{J}_k = \frac{\partial \mathbf{m}(\mathbf{X}_k)}{\partial (\mathbf{X}_k)}$ is the Jacobian matrix of (first order) partial derivatives of the model at point \mathbf{X}_k . Further information about the stability, convergence and uniqueness of the solution of such nonlinear problems can be found in Chapter 9 of (Menke 2018) and in (Tarantola and Valette 1982).

The general case of inverse problems involving non-Gaussian statistics has been addressed by (Tarantola 2005). Additional terms could be added to $\Phi(\mathbf{Y}, \mathbf{X})$ in order to take into account some additional constraints on the parameters. The α parameter in Eq (4.20) is used to control the convergence of the gradient descend algorithm: for highly nonlinear problems a low value for α helps avoiding brutal jumps on the descent and divergence.

According to Eq (4.18), the solution provided by the inverse algorithm results from a compromise between two extreme states: i) a solution that perfectly fits the observed data through the theoretical model and ii) a solution remaining very close to the *a priori* information on the parameters. This compromise solution depends on the *a priori* confidence put on the various terms of the system. If the confidence in the observed data (as defined by the covariance matrix \mathbf{C}_Y) is weak, the problem is underdetermined and the *a priori* information takes a dominant role. If the problem is overdetermined (very good quality data in sufficient number, or weakly informative *a priori* values of the parameters as defined by the covariance matrix \mathbf{C}_X) then the *a priori* information plays a minor role.

The next sections present and discuss the implementation of this inverse algorithm to retrieve DSD parameters from polarimetric weather radar observables on radar radials. The principle of the proposed method is: i) start with an *a priori* DSD based on the empirical power laws suited to the local climatology (equations 4.5 and 4.6); the DSDs are retrieved gate by gate, based on attenuation corrected data, and ii) rely on the inverse method to improve this initial solution and provide a distribution of DSDs along the entire range which is consistent with the observed radar variables.

The implementation of the inverse algorithm requires the definition of : i) the vector \mathbf{Y}^0 of radar data and its covariance matrix \mathbf{C}_Y which characterizes the level of confidence in the data, ii) the vector $\mathbf{X}^{\text{prior}}$ of *a priori* values of DSD parameters and its covariance matrix \mathbf{C}_X which contain the initial guess of the parameters and the error covariance assumption, iii) the applications conditions of the algorithm.

4.4.2 The vector \mathbf{Y}^0 of radar data and its covariance matrix \mathbf{C}_Y

The covariance matrix of measurement errors \mathbf{C}_Y is assumed fully diagonal, which means that the measurement error of each radar observable is independent from the measurement error of the same variable measured at a different radar bin, and independent from the other radar observables, including at the same location. The diagonal of the

matrix C_Y can be written $diag C_Y = [\sigma_{Z_H}^2, \sigma_{Z_{DR}}^2, \sigma_{K_{DP}}^2, \sigma_{\Phi_{dpn}}^2]$. Where $\sigma_{Z_H}^2, \sigma_{Z_{DR}}^2, \sigma_{K_{DP}}^2$ are vectors, and their components are the variances of measurement error of the (attenuated) reflectivity Z_H^{att} , the (attenuated) differential reflectivity Z_{DR}^{att} and the differential phase shift K_{DP} . $\sigma_{\Phi_{dpn}}^2$ is the variance of measurement error of the phase shift at gate n .

The variance of measurement errors associated with Z_H^{att} and Z_{DR}^{att} can be estimated on the base of the fluctuations of the measured reflectivities. The error on K_{DP} is quite high due to the noisy nature of Φ_{DP} and its derivative. After some sensitivity analysis we have adopted the following constant values (for all radar gates) : $\sigma_{Z_H} = 3 \text{ dBZ}$, $\sigma_{Z_{DR}} = 0.5 \text{ dB}$, $\sigma_{K_{DP}} = 1 \text{ deg/km}$ and $\sigma_{\Phi_{DP} n} = 2 \text{ deg}$.

4.4.3 A priori information: DSD parameters and associated covariance matrix

The *a priori* value of the parameters X^{prior} is derived from the polarimetric radar observables, thanks to the relationships proposed by (Koffi et al. 2014) and detailed in Section 2.3 (Eq. 4.5 and 4.6). The radar measurement of reflectivity and differential reflectivity which are used for that purpose must first be corrected from attenuation. The self-consistency correction method proposed by (Bringi, Keenan, and Chandrasekar 2001) is used to estimate the attenuation at any gate of the radar radial and to correct observed values of Z_H and Z_{DR} for attenuation. Then the *a priori* values of N_0^* and D_m are provided by the Eq (4.5) and (4.6). The attenuation correction is only used to derive the *a priori* vector. Then the inversion is applied on Z_H^{att} and Z_{DR}^{att} , and accounts for the attenuation explicitly (see the Jacobian calculation in Appendix A).

The *a priori* value of μ is more difficult to set as the bulk radar variables do not carry any information about the shape of the DSD. The choice of the *a priori* value of μ is based on (Moumouni, Gosset, and Houngninou 2008) who showed by fitting gamma laws on observed DSD of the same dataset, that convective precipitation tends to have higher values of μ than stratiform precipitation. They showed that the values of μ fall in the interval $\mu \in [0.5, 12]$. We choose to set a constant *a priori* value of $\mu = 2$ for all the radar gates as the stratiform rainfall is more frequent in the radar PPIs.

$$\mu_i^{prior} = 2.0 \quad (eq. 4.21)$$

The covariance matrix of parameters stands for the errors between the *a priori* values of parameters and the true values. We assume that the covariance between the variables

N_0^*, D_m, μ is equal to 0.0, which is consistent with previous findings on the property of normalized DSD. We also decided not to impose any covariance between these variables to avoid over-constraining the algorithm.

For each radial the matrix \mathbf{C}_X is then a “block-diagonal” matrix of size $[3n \times 3n]$ composed by three sub-matrixes:

$$\mathbf{C}_X = \begin{pmatrix} \beta_{N_0^*} & & \\ & \beta_{D_m} & \\ & & \beta_{\mu} \end{pmatrix} \text{ with } \beta_{par}^{ij} = \sigma_{par}^2 \exp\left(\frac{-d_{ij}}{d_{corr}}\right) \quad (\text{eq. 4.22})$$

Where σ_{par}^2 is the estimated *a priori* variance of the parameter *par*, that is N_0^*, D_m, μ and d_{ij} the distance between the gates *i* and *j* of a radial. For this work, $d_{corr} = 3 \text{ km}$ has been adopted which is consistent with the spatial correlation of the DSD parameters in the study region.

The standard-deviation on parameters is defined as a fraction of its *a priori* value and expressed:

$$\sigma_{D_m} = \varepsilon D_m^{prior}, \sigma_{N_0^*} = \varepsilon N_0^{*prior} \text{ and } \sigma_{\mu} = \varepsilon \mu^{prior} \quad (\text{eq. 4.23})$$

We set the value of the coefficient $\varepsilon = 0.5$ - or in other words, a relative uncertainty of 50% for all three parameters- by testing the convergence speed of the algorithm.

4.4.4 Application conditions

The calculation of the Jacobian matrix of the partial derivatives of the radar observables Y with respect to the parameters on vector X is detailed in the Appendix A. As in Figure 1 and 2, the calculation of the radar variables as a function of raindrop size and shapes is based on T-matrix modeling with the (Andsager, Beard, and Laird 1999) ratio law (Eq 4.10), and a temperature equal to 20°C (compatible with observations in Africa). The convergence parameter α in the algorithm (Eq (4.20)) is set to $\alpha = 0.1$, in order to insure a careful convergence of the algorithm. At each iteration of the algorithm described in Equation (4.23), the convergence is evaluated through the normalized root mean square error (*NRMSE*) between the retrieved (Y_n) and observed (Y^0) attenuated polarimetric variables $[Z_{DR}; Z_H; K_{DP}]$. This variable is written: $NRMSE = NRMSE_{ZDR} + NRMSE_{ZH} + NRMSE_{KDP}$. The condition fixed to stop the algorithm is $NRMSE < 0.25$. A value of *NRMSE* of 0.25 is equivalent to a mean residual variance of 8% between each retrieved and observed polar variables. Typically, a stable solution is reached after 4-5 iterations, the maximum number of iterations we experienced being 20.

4.5 Results

4.5.1 Retrieved DSD, sensitivity to model parameters and gain from the *a priori* solution

Figure 4-3 illustrates the retrieval along a given radial, extracted from the 2006 July 28th case study (Azimuth 251°; 7h58 UTC; 2.8° elevation PPI). The observed system is typical of African squall lines and K_{DP} shows two peaks of convective rainfall at 42km and 53km range, and stratiform rainfall at 30-40 km, while the system is moving away from the radar (Westwards). The left column shows 4 radar variables along the radial: the attenuated Z_H , the attenuated Z_{DR} , the differential phase shift Φ_{DP} and the specific differential phase shift K_{DP} . On each plot the observed variables (in black) are displayed together with the radar variables simulated (attenuation included) from the *a priori* DSD (blue) and from the inverse model framework (red). On the right column the 3 retrieved DSD parameters N_0^* , D_m , μ (red) are compared with the *a priori* solution (blue).

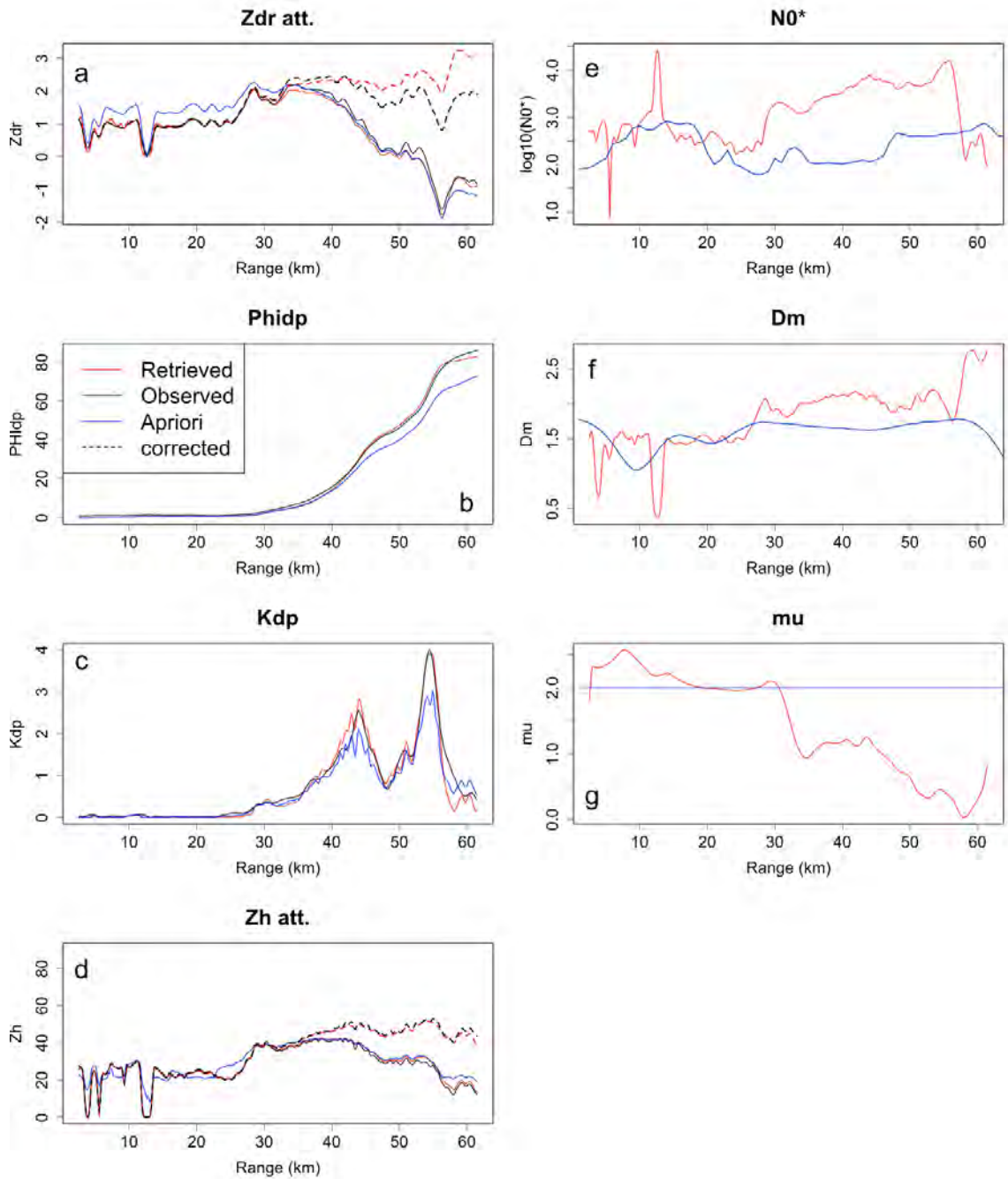


Figure 4-3: Example of the observed, a priori and retrieved attenuated polar variables and DSD parameters for a given radial (251° azimuth of 28/07/2006 07h58 2.8° elevation PPI). a) to d): Values of the indicated 4 radar variables as a function of range: the attenuated Z_{DR} , the differential phase shift Φ_{DP} , the specific differential phase shift K_{DP} and the attenuated Z_H . On each plot the observed variables (in black) are displayed together with the radar variables simulated (attenuation included) from the a priori DSD (blue) and from the inverse model framework (red). On a) and d) the dotted lines are the attenuation

corrected reflectivities Z_{DR} , Z_H , in red, based on the inverse method and in black, based on the (Bringi et al. 2001) method (see text), f) to h) the 3 retrieved DSD parameters N_0^* , D_m , μ (red) are compared with the a priori solution (blue).

The simulated radar variables associated with the inverse method are globally much closer to the observations than the radar variables simulated with the *a priori* DSD parameters, thus illustrating the principle of the inverse model: starting from an *a priori* information and finding a solution more consistent with the observations. The difference between the retrieved solution and the observation is higher for K_{DP} which may be due to the high relative uncertainty prescribed on this observation (section 4.3). In this example the attenuation is high, due to the intense rainfall seen by the X-band radar. It can be noticed that the constraint imposed on Φ_{DP} by Eq (4.16) is efficient, and ensures a low bias in the integrated K_{DP} allowing a good estimation of the attenuation. Concerning Z_{DR} and Z_H , the observed and retrieved values are very close all along the radial.

On the right column in Figure 4-3 the retrieved parameters [N_0^* , D_m] show peaks at the convective rainfall range (~54km). The peak of D_m at the end of the radial may be an artifact related to high peak of Z_{DR} : at the end of the radial the radar signal get closer to the noise level and the variables are less reliable (also confirmed by low values of the cross correlation coefficient ρ_{HV} – not shown).

Figures 4-4 and 4-5 illustrate the retrieval of DSD parameter maps. The presented PPI is at 2.8° elevation for the 12/09/2006 event at 19h08 UTC. As for Figure 4-3 the case is typical of an African squall line, with a marked line of convective cells on the West front followed by stratiform rain. The fields of N_0^* , D_m , μ retrieved by the inversion (Figure 4-4 top) and from the *a priori* solution based on (Koffi et al. 2014) (Figure 4-4 bottom) exhibit some differences. The inverse method leads to better spatial consistency in the DSD field. The radial stripes that appear on the field N_0^* for the *a priori* (bottom left in Figure 4-4) have disappeared though the inverse method (top left in Figure 4-4). The stripes in the *a priori* solution are quite typical of radial to radial inconsistency in ϕ_{DP} which have a strong effect on the DSD retrieval when the attenuation correction based on this variable is applied prior to -and independently of- the retrieval (the 2 step problem already noticed by (Yoshikawa, Chandrasekar, and Ushio 2014)). The improved radial to radial consistency obtained with the inverse method is noteworthy as this is not imposed by the algorithm (only a spatial correlation of 3km inside the radial is imposed by the

covariance matrix) – it is an indirect benefit of the inverse method which absorbs better the observation uncertainty. The previously observed jump ((Moumouni, Gosset, and Houngninou 2008)) between relatively high value of N_0^* in the convective cells and lower values in the stratiform parts is well reproduced in the field. The stratiform and convective regions are clearly differentiable. Comparing the *a priori* field of N_0^* and the retrieved, we observe clusters of high N_0^* values in the convective region of the retrieved field (yellow dots) associated with convective cells which are less highlighted in the *a priori* field. A global overestimation of D_m in the *a priori* is corrected by the algorithm - this will be further confirmed by the results in Figure 4-6.

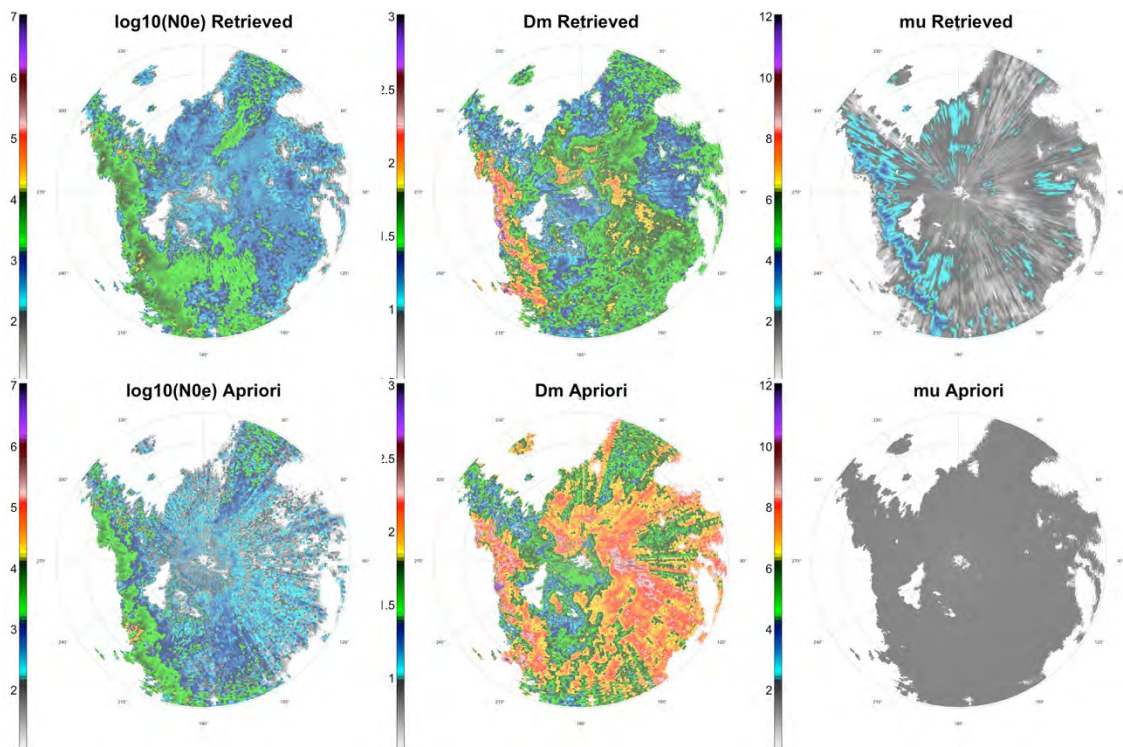


Figure 4-4: : Retrieved (top) and a priori (bottom) maps of DSD parameters for the 2.8° PPI for the 12/09/2006 event at 19h08 UTC. As indicated the columns, from left to right are for: : $\log_{10}(N_0^*)$, D_m (mm) and μ .

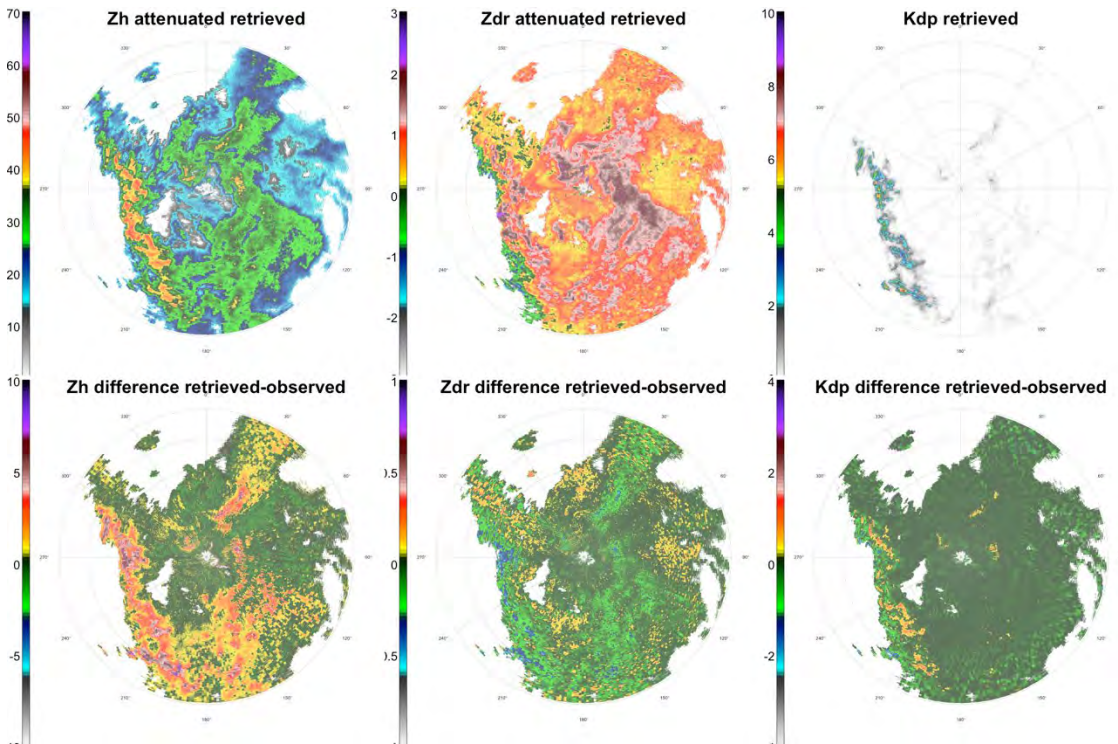


Figure 4-5: : Retrieved fields of attenuated radar observables and respective residuals relative to the observations. Same PPI than Figure 4-4. From left to right attenuated Z_H [dB], attenuated Z_{DR} [dB] and K_{DP} [deg/km]. Nota: the color bar range is different for the variables (top) and errors (bottom).

The retrieved values for μ are globally higher than the *a priori* value (constant $\mu = 2$) and especially in the convective part. This is consistent with what was observed statistically with the disdrometer by (Moumouni, Gosset, and Houngninou 2008). As illustrated in Figure 4-2, the radar variables have a relatively low sensitivity to μ (except for Z_{DR}) and μ is therefore less constrained by the observations than the two other DSD parameters. Nevertheless, it is interesting to see that the retrieved values of μ increase in the convective part of the rainfall field, which is consistent with our knowledge.

Figure 4-5 shows the retrieved radar variables fields and the absolute errors with respect to the observed fields (residuals). For K_{DP} the residuals are non-biased (thanks to the strong constraint on ϕ_{DP} at the end of each radial). Z_{DR} shows little or no bias in the fields indistinctly of the type of rainfall. All the errors in the model are absorbed by Z_H in the convective part, where the attenuation is high. As seen in the residual map of Z_H (Figure 4-5 bottom left), there is a positive bias in the retrieved Z_H in the convective region. The same bias can be observed in the Figure 4-3d in the retrieved Z_H at 54km.

4.5.2 Comparison of Disdrometer and radar derived time series

In this section we compare the collocated radar retrieve and disdrometer DSDs. The comparisons are performed for all the organized convective systems observed on site in 2006, as summarized in Table 4-1. The disdrometer was located at 20km north-west of the radar (section 2). At this range the volume scan of the radar is between 0.7 and 1.2 km height considering a $\pm 0.7^\circ$ radar beam width. Considering typical fall speed for drops we could expect a few minutes shift between the radar aloft and disdrometer observation at ground.

Event beginning date and time	Number of PPIs
23/06/2006 4h51	24
25/07/2006 13h22	30
28/07/2006 05h21	27
02/08/2006 01h22	32
05/08/2006 14h57	6
07/08/2006 14h39	7
10/08/2006 16h49	12
14/08/2006 16h44	3
17/08/2006 16h43	28
30/08/2006 15h18	3
31/08/2006 13h09	12
03/09/2006 10h30	16
08/09/2006 16h22	10
09/09/2006 12h33	16
12/09/2006 17h59	18

Table 4-1: List of events recorded by the disdrometer and the radar, and number of PPIs where the inversion was applied.

Figure 4-6 shows time series of DSD parameters retrieved by the radar (*a priori* and inversion) and observed by the disdrometer for three cases that illustrate the variety of obtained results. The DSD retrieved with the inverse model (red) exhibits a good dynamic through the three events when compared with the disdrometer (black circles) and the consistency is better than for the *a priori* solution (green). The improvement between the *a priori* solution and the inverse method is more marked for N_0^* ; the retrieved is much smoother than the *a priori* value and closer to the ground reference. Nevertheless, a bias on N_0^* appears for some events (the highest on 17/08/2006) and is only partially corrected by the inversion. A calibration problem on the reflectivities could be the cause of this

retrieved bias on N_0^* - at the moment the calibration constant is not parameterized in the inverse model but could be included in future extension of the model.

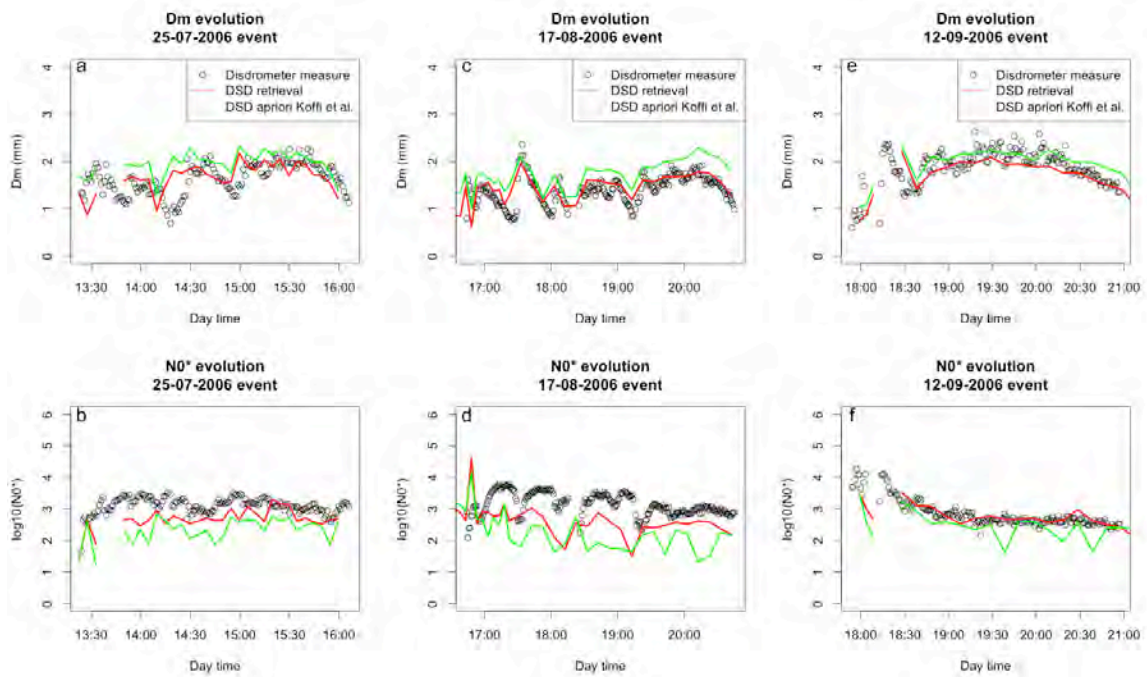


Figure 4-6: Time evolution of D_m (top) and $\log_{10}[N_0^*]$ (bottom) retrieved through the inverse method (red), a priori (green) and observed (black) by the disdrometer for three events. The parameters from the inversion are collocated at the radar gate where the disdrometer is located (see text).

The plot in Figure 4-6e is for the same event (12/09/2006) as the DSD fields showed in Figures 4-4 and 4-5. At 19h08 the DSD retrieved shows a better agreement with the ground reference than the *a priori* which seems to overestimate (as seen also in the DSD maps).

As discussed in section 4.4, some choices need to be made in the inverse model application based on prior knowledge on the DSD parameters and on the observation uncertainty. Figure 4-7 illustrates the sensitivity of the retrieval to some of these parameters like: the observation uncertainty attributed to each observed variables (Equation (4.23)); the drop shape law used in the T-matrix calculations and the initialization of μ . We have also tested different temperatures in the T-matrix calculations (0°C-15°C-30°C), and found that impact negligible (not shown).

Chapter 4: An inverse method for drop size distribution retrieval

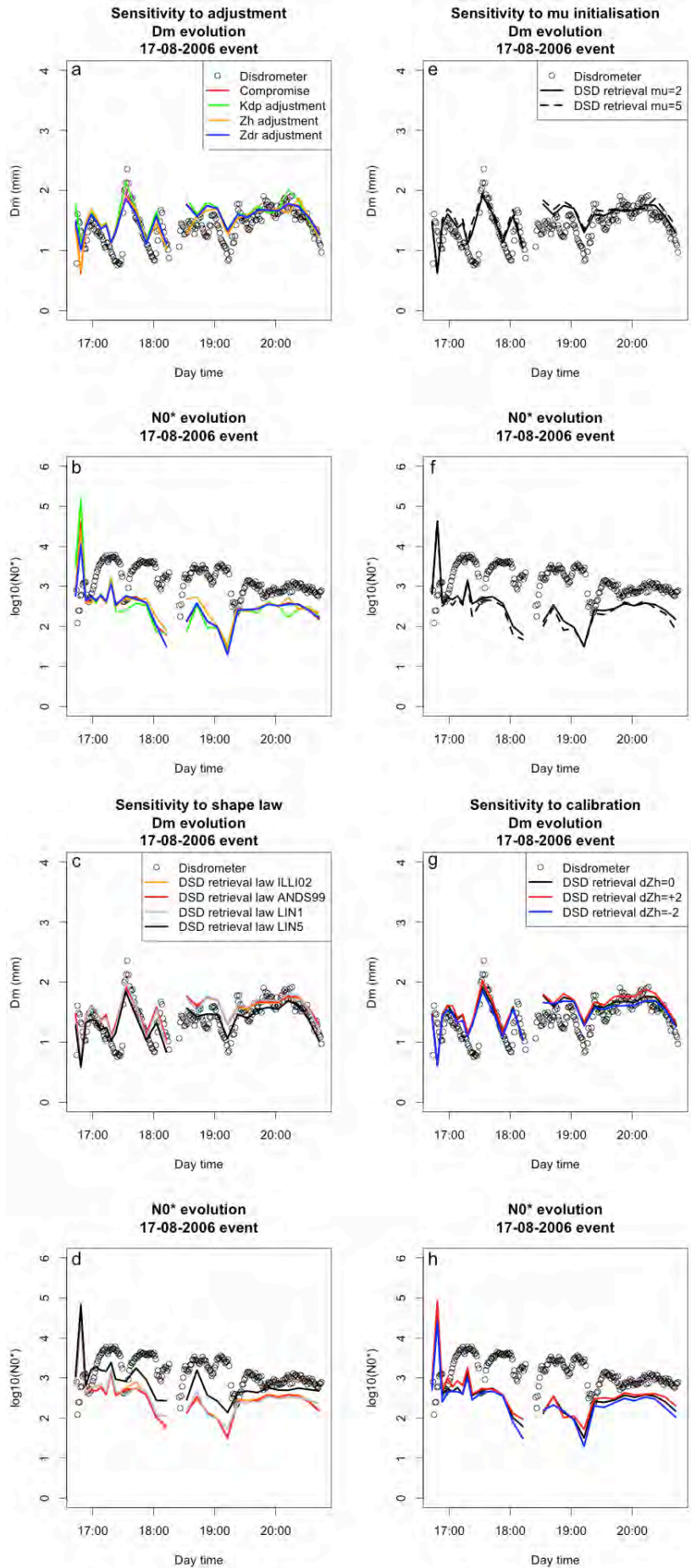


Figure 4-7: Sensitivity of the retrieved D_m (top) and $\log_{10}[N_0^*]$ (bottom) on the 17-08-2006 event to several parameters of the inverse model :a-b) sensitivity to the relative observation errors : red, the default parameters as in section 4.2; green, reduced error and therefore more weight on KDP; orange, more weight on ZH; blue, more weight on ZDR. c-d) sensitivity to the aspect ratio law (as indicated on color legend). e-f) sensitivity to μ initial value. g-h) sensitivity to a calibration of error of +/- 2dBZ on ZH. As in Figure 6 the retrieval is compared with the disdrometer data (black circles).

Modifying the uncertainty associated with an observed variable (Eq (4.23)), thus increasing or decreasing the relative confidence in this variable, is equivalent to changing its weight in the retrieval. The Figure 4-7a-b show the results on the time series retrieval of the 17/08/2006 event. The red curve shows the default compromise solution (as in Figure 4-6b and e) $\sigma_{ZDR} = 0.5 \text{ dB}$ $\sigma_{KDP} = 1^\circ/\text{km}$ $\sigma_{Zh} = 3 \text{ dBZ}$, the green curve is for an increased confidence in K_{DP} with $\sigma_{KDP} = 0.1^\circ/\text{km}$, the orange curve for an increased confidence in Z_H , with a value $\sigma_{ZH} = 0.1 \text{ dBZ}$ and the blue curve for an increased confidence in Z_{DR} , with $\sigma_{ZDR} = 0.01 \text{ dB}$. The ‘orange’ solution which relies more on Z_H leads to some outliers, but also some points show a better comparison to the ground reference, for example the D_m drop at 19h10 UTC. The adjustment with more weight for K_{DP} and Z_{DR} are very close to the compromise solution.

The sensitivity to the drop shape law is larger, as the T-matrix coefficients are impacted (Figure 4-1). In Figures 4-7c and 4-7d we show the retrievals for four drop shape law (ILLI02, ANDS99, LIN1 and LIN5 see Figure 4-1). For the law with the highest aspect ratio (LIN5) the retrieved D_m decreases as only relatively small diameters are needed to fit the observed Z_{DR} . Conversely N_0^* increases to compensate D_m decrease while keeping the same constraint on Z_H and K_{DP} . For this drop shape assumption (LIN5) the bias observed on N_0^* in Figure 4-7 decreases; this could mean that the drops are indeed more oblate for this event or that more extreme drops are present, or that a given parameter (here the oblateness) may compensate some other source of uncertainty (as an unaccounted miss-calibration). Various model parameters can compensate each other as the problem is globally under –constrained. The sensitivity to the initialization of μ is illustrated Figure 4-7e,f: for a higher initial μ (thus a narrower DSD) the retrieval leads to a higher D_m (thus lower N_0^*). In the natural range of variation of μ [2-5] the sensitivity

is less than for the drop shape law. The effect on the DSD retrieval of a calibration bias on Z_H (+ or $- 2$ dBZ) is illustrated in Figure 7g,h. It leads to a slight over (under) estimation of the DSD parameters (the effect is stronger for the *a priori* solution; not shown). In future versions of the algorithm, a calibration constant could be included as an additional parameter in the retrieval.

Figures 4-8 and 4-9 illustrate the improvement in DSD retrieval compared to the *a priori* solution in terms of global statistics over the entire disdrometer record (in 2006). Figure 4-8 shows the contour plot of observed $[N_0^*, D_m]$ pairs, superimposing the disdrometer (orange) and radar (blue) derived datasets. The overall agreement is stronger for the inverse method (left plot) than for the *a priori* solution based on (Koffi et al. 2014). In particular, the range of retrieved N_0^* is in better match with the disdrometer for the inverse method, while the *a priori* solution generates more extreme values.

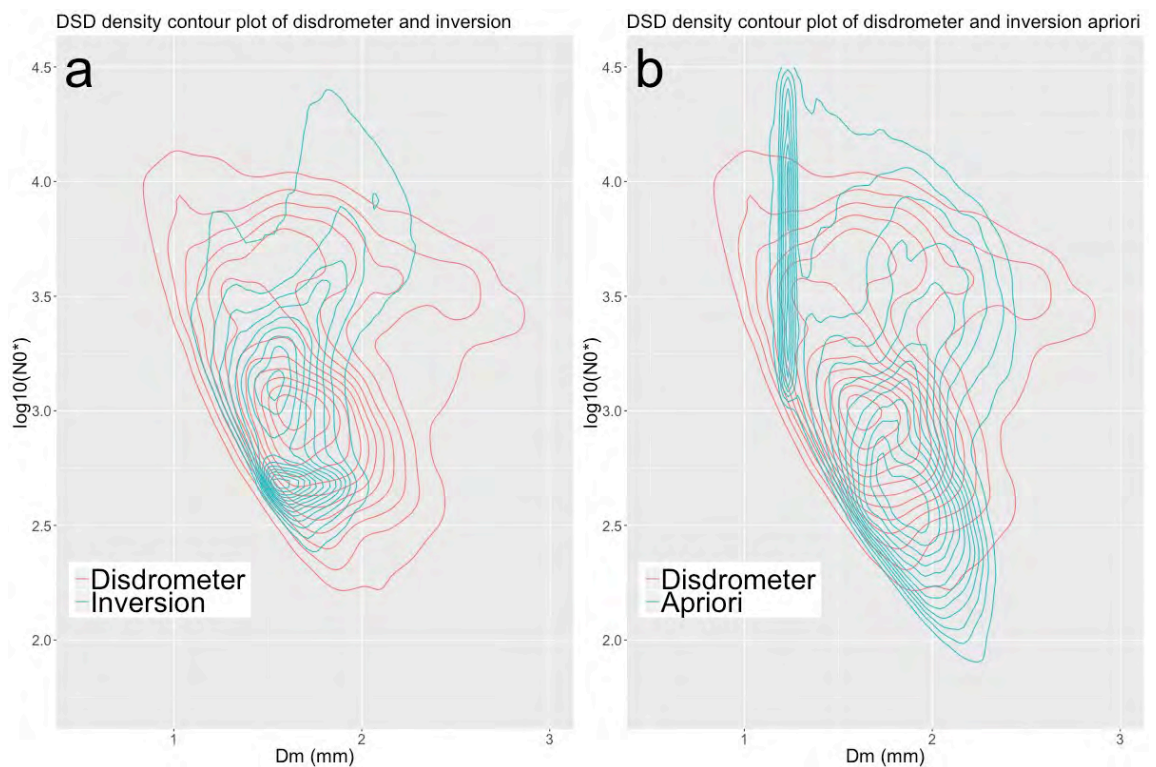


Figure 4-8: : Contour plot on N_0^* - D_m space of distributions of disdrometer DSD and radar retrieved DSD. Left plot: inverse method; Right plot: a priori DSD. The retrieval is for 12/09/2006 event, 7 PPI from 17h59 UTC to 18h48. The disdrometer data is over 2006 and 2007 seasons. The number of N_0^* - D_m pairs in each set are: $N_{inv} = 4 * 10^5$ points for the retrieval and $N_{disdro} = 7 * 10^3$ for the disdrometer.

Figure 4-9 displays the scatter plot of radar retrieved versus collocated disdrometer measurement for all events reported in Table 4-1. Again the improvement when the inverse method rather than the *a priori* two-step method is used is highlighted. The global statistics are improved in terms of correlation and bias, and the reduction in the spread is noticeable. Note that the retrieval skill, as displayed in Figure 9 is almost unchanged when a calibration error of + or - 2dBZ is applied to the reflectivities (not shown).

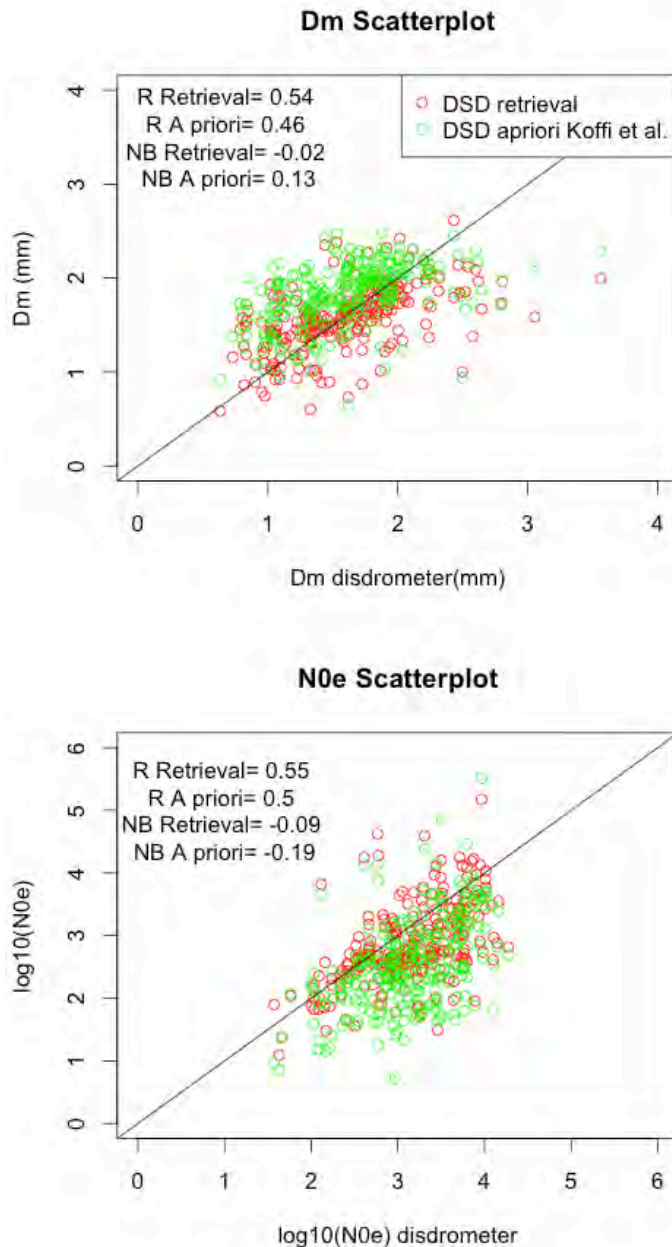


Figure 4-9: Scatterplot of the radar retrieved (Y axis) DSD parameters against the disdrometer (X axis) for collocated radar gate and time step. Top plot, D_m ; bottom, N_0^* . Both the a priori (green) and the inverse method (red) retrieval are

shown. The correlation (R) and normalized bias (NB) compared to the disdrometer for both retrieval are indicated on the plots. 18 rainy systems for a total of $N = 244$ collocated points are displayed.

Figures 4-8 and 4-9 indicate an improvement in DSD retrieval from the a priori to the final solution. However some differences remain between the disdrometer and radar retrieved DSDs. The distribution of median diameter D_m is narrower on radar than on the disdrometer dataset (Figure 8). Some of these differences are unavoidable given the different nature of the two datasets. The radar samples a larger volume of atmosphere and higher above ground than the disdrometer.

4.6 Conclusion

A method based on an inverse model to retrieve DSD parameters from radar polarimetric observations at attenuated frequency is presented and tested on X-band data in Africa. Three parameters of a gamma DSD (the volume weighted mean diameter D_m , the scaling parameter of concentration N_0^* and a shape parameter, μ) are retrieved at each range gate along a radial. The DSD range profile for the entire radial is found at once, as the solution which best matches the radar observations. The procedure does not need a previous attenuation correction because the forward and inverse model account explicitly for the path integrated attenuation in the measured reflectivities. In line with the approach developed by (Yoshikawa, Chandrasekar, and Ushio 2014), this framework ensures a global consistency between the retrieved DSD and all radar variables. It reduces the errors brought by the uncertainty in the attenuation correction procedure. The inversion procedure is an iterative algorithm which finds the solution for the entire radar radial; it can make use of a strong constraint –like the differential phase shift at the last gate – to insure robustness.

The forward model needed for the inversion relates the observed radar variables to the DSD along the radial. This model is based on explicit calculations of radar variables (reflectivities in horizontal and vertical polarization; specific differential phase shift; specific attenuation coefficient for each polarization) as a function of drop sizes and shapes. T-matrix calculations for drops considered as oblate spheroids were used for this purpose. By convoluting the T-matrix output and the DSD, the radar variables were pre-calculated for gamma DSD over a range of values of the 3 parameters of interest D_m, N_0^*

and μ . Based on these calculations the partial derivative of the radar variables (the Jacobian), needed in the inversion procedure, are computed. These calculations were made for several assumptions concerning the aspect ratio of drops and the sensitivity to the prescribed temperature also analyzed (and found to be small). In addition to i) the observed radar variables, and ii) the radial profile of the 3 DSD parameters to be retrieved, many other parameters and *a priori* information need to be prescribed to the inverse model

The results of the inversion were evaluated through direct comparisons with disdrometer data and also by analyzing the global consistency of the solution compared to the '2 step' empirical method from (Koffi et al. 2014). 15 rainfall events, for a total of 244 PPI were used for direct comparison between the disdrometer and the radar DSD retrieved at the closest pixel. The correlations between the time series, for D_m and for N_0^* are about 0.55, and improved compared to the *a priori* solution. These numbers are similar to the scores obtained when radar retrieved DSD is compared with disdrometer data in other studies (Raupach and Berne 2017) at non attenuating frequencies. This is quite remarkable given the intense attenuation encountered in the study region in West Africa.

Compared to empirical methods, the proposed inverse model, by providing an overall retrieval of the range profile of DSD, leads to a solution which is more consistent with all observed radar variables, and shows a better spatial consistency. This is apparent on the retrieved DSD maps based on any given PPI; the spurious radials that tend to appear with the 2 steps method because of errors brought by the attenuation correction are more consistent with the inverse method. This improved consistency in the retrieval is also shown when the frequency distribution and co-distributions of N_0^* and D_m are analyzed. The distributions retrieved with the inverse model are closer to the disdrometer derived ones, and show less spread than those from the empirical method.

These results appear promising, but a more comprehensive assessment of the proposed method is required. For that purpose, various datasets representative of different climatological contexts are needed. In addition, it would be interesting to compare it with the method proposed by [47], in order to assess their respective advantages and drawbacks. If these methods were to be used with operational radars and in real time, the optimization of the processing time compared to retrieval accuracy should be analyzed. Some improvement and new implementations could be added to the inverse model. In the current version the calibration of reflectivities is assumed to be correct, but a calibration

Chapter 4: An inverse method for drop size distribution retrieval

(slowly varying) constant could be added in the model and retrieved as a parameter. We showed for one case study (Figure 4-5) that one extreme shape law best fits the observations, and discussed that this could be a compensation for a calibration error rather than a real rainfall microphysics feature. If we consider a linear axis ratio law with a parameter β (Eq 4.10) we can consider a new inversion with the parameter β as a variable in the parameters space as we can calculate the partial derivatives of $[Z_{DR}, Z_H, K_{DP}]$ with respect to β (Jacobian). Also the calibration coefficients, ΔZ_H and ΔZ_V could be added to the parameters space as its Jacobian can be computed.

The retrieval a posteriori error covariance is a by-product of the inverse model which is currently not used; in the future it could be used to generate ensembles instead of using a single retrieved DSD field for each PPI.

Author Contributions: The work presented was carried out in collaboration with all authors. All authors contributed to the writing of the manuscript, and conceived and designed the content of this paper, M.G. coordinated the deployment of the disdrometer and weather radar in Africa, H.A contributed to the formalization of the inverse problem and M.A performed the calculations and figures.

Funding: This research was partially funded by the French Centre National d'Etudes Spatiales (CNES) under the TOSCA program in link with the Megha-Tropiques satellite mission. The deployment of the radar and disdrometer in Africa was funded by Institut de Recherche pour le Développement (IRD) as part of the Anayse Multi-disciplinaire de la Mousson Africaine (AMMA) program.

Conflicts of Interest: The authors declare no conflict of interest.

Appendix: Jacobian matrix of partial derivatives

The Jacobian matrix is the derivative of the polarimetric radar observables with respect to the DSD parameters.

The radar observables are regrouped in the vector $[Z_H^{att}, Z_{DR}^{att}, K_{DP}, \Phi_{DPn}]$ which has $(3n + 1)$ components, n being the number of gates of a radar radial. The number of parameters is $3n$, (N_0^*, D_m, μ) at each of the n radar gates. The Jacobian J is composed of 12 sub-matrices

Chapter 4: An inverse method for drop size distribution retrieval

The matrix $\frac{\partial \Phi_{DP\ tot}}{\partial D_m}$ involves only the value of Φ_{DP} at the end of the radial, thus the matrix is dimension $[1 \times n]$. As Φ_{DP} is a cumulative variable, then, matrix is:

$$\frac{\partial \Phi_{DP\ tot}}{\partial D_m} = \left(\frac{\partial \Phi_{DP\ tot}}{\partial D_m^1} \quad \dots \quad \frac{\partial \Phi_{DP\ tot}}{\partial D_m^{n-1}} \quad \frac{\partial \Phi_{DP\ tot}}{\partial D_m^n} \right) \quad (eq. 4. A4)$$

A variation of dD_m at the first gate will add $\frac{\partial \Phi_{DP}^1}{\partial D_m^1}$ to all the following radar gates.

The sub matrixes are estimated using finite difference method with pre-calculated tables of variation of the polarimetric variables for a range of DSD parameters. We have pre calculated tables for the different radar observables for a range of $N_0^* \in [500; 10^5]$ by steps of $500\ m^{-3}mm^{-1}$ for $D_m \in [0.05, 7]$ by $0.02\ mm$ and for $\mu \in [1, 14]$ by steps of 0.5 . The matrix \mathbf{J} is calculated at the initial iteration (*a priori* vector \mathbf{X}^{prior}) and then update at each iteration \mathbf{X}^k .



© 2019 by the authors. Submitted for possible open access publication under the terms and conditions of the Creative Commons Attribution (CC BY) license (<http://creativecommons.org/licenses/by/4.0/>).

PART 1 CONCLUSIONS

In the first part of the thesis we have presented two applications of inverse methods to retrieve information on the characteristics of precipitation. In both applications, the method is based on a forward model that links radar observables to a simplified model of rainfall microphysics.

The first application, a simplified Bright Band model is inverted to retrieve the parameters of the PSD: N_0^* , D_m and the pre-factor of the density law α_d of frozen particles. The solution is the PSD that best fits to the observed shape of the bright band. As only three parameters are retrieved per VPR, the inversion technique used is the ‘simplex’ algorithm. The retrieved values of the pre-factor of the density law are compatible with the in situ density law observed by the airborne probe. A simple model of melting snow is enough to retrieve realistic values of the density above the isotherm 0°C.

The model has however three simplifying assumptions: 1/ No aggregation or break-up was considered during the melting. 2/ We considered the observed VPR as the real VPR, neglecting the beam broadening effect, and 3/ The degree of melting inside the BB was parameterized as a simplified function of height. We also considered a fixed exponent β_d in the density law.

The second assumption has a low impact as the profile was constructed with radar observations within 25 km range. The broadening of the radar beam at this distance has little effect (no smoothing of the BB peak). The third assumption concerning the degree of melting of the hydrometeors can impact the shape of the simulated BB. The used model of melted fraction of a particle depends only on the height of 0°C isotherms and the bright band bottom. We can imagine that the melted fraction of a particle with height depends on the particle diameter: big particles could melt slower than little particles. Also the differential falling velocities of particles were not considered. This can change BB shapes and thus the retrieved parameters. Another limitation of the study is the constant exponent β_d , which was set through the airborne observations. Though, the inversion of both parameters $[\beta_d, \alpha_d]$ is difficult because their effects on Z_H compensate.

The first assumption, concerning the break-up and aggregation could be studied by combining the two methods presented in this part. For future work we can compare the airborne observed PSD with the below retrieved DSD of chapter 4 method, under the trace of the airplane. The DSD retrieval could also be done at different heights using

different PPI to evaluate the evolution of the DSD due to break-up, coalescence and evaporation.

For the bright band inversion only the reflectivity profile was used. For future work the polarimetric information could also be modelled and used to increase the information allowing a more complex model of the melting layer.

The second inversion technique presented is a DSD parameters retrieval in all bins of a radial. The inversion is performed on the attenuated measured variables. With the T-matrix model of scattering by oblate drops, we found the parameters of the DSD best describing the polarimetric attenuated variables. The solution is a compromise between the different observed variables, bringing global coherence to the radial. Due to the high dimension of the problem and the high nonlinearities, the inversion is sensitive to the a priori value. The main assumption of the inversion is the ratio shape law of the drops. In a future version of the inversion algorithm we can try to find an optimal parameter linked to the ratio shape law, in a similar way than the β -method by [Gorgucci et al 2002]. Also the calibration of the reflectivity could be added into the inversion procedure. A main objective for this method for future developments is to retrieve ensembles of DSD fields instead of a single field. In the framework of the inversion theory we can compute the solution uncertainty with the error covariance matrix, permitting the production of ensembles. The method is slow compared to power law relations, making it difficult to apply in a real time framework.

The technique was validated with one rainy season in West Africa. Validation in other climatic regions could be interesting to test the performance of the algorithm. The validation disdrometer in the study was at 20km from the radar. A farthest disdrometer or the comparison with rain gages could show an eventual benefit of the method in terms of attenuation, compared to a two-steps procedure.

PART 2

COMMERCIAL MICROWAVE LINKS FOR RAINFALL MONITORING

This part the manuscript is dedicated to rainfall retrieval using commercial microwave links (CML) from telecommunication companies. In the first part we showed the value of radars observation to retrieve precipitation characteristics, but radars are expensive and have a poor implantation in tropical countries.

The attenuating effect of rainfall on CML has been known for several decades. The first work quantifying the attenuation induced from rainfall are from the late 60' and 70' (Atlas and Ulbrich 1977; Semplak 1970; Olsen, Rogers, and Hodge 1978). In the last decade, researchers proposed using the measured attenuation levels in CML to derive precipitation measurements as a new opportunistic technique, especially useful where no other source of data is available (Messer 2006; Overeem, Leijnse, and Uijlenhoet 2011; Doumounia et al. 2014). The CML networks are maintained by the telecom operators and their density covers large parts of the globe, especially densely populated regions.

To monitor rainfall through CML we first must separate the rainfall induced attenuation from the other sources of attenuation. As we have seen in chapter 2 and chapter 4, the attenuation by rain drops depends on the drop size distribution over the path of the EM wave. The specific attenuation can be linked to the rainfall by a power law relation which depends on the assumptions made on the DSD. The algorithms used to classify rainy periods from raw attenuation time series can lead to false alarms and non-detection. The

Chapter 4: An inverse method for drop size distribution retrieval

following chapter is focused on the quantitative estimation of precipitation using CMLs and the different sources of the uncertainty and bias.

Chapter 6 addresses the evaluation and algorithm calibration of a CML dataset from Niamey, Niger, using 3 rain gauges. We also analyze the sampling differences between a link and a rain gauge and the possible impact on the link-gauge rainfall time series comparison. This analysis is based on simulation using the DSD maps derived from polarimetric radar in Chapter 4.

CML networks are not optimized for rainfall measurement but for telecommunication purposes. The CML in the network operate at various frequencies, with a distribution of length, position and orientation, designed by the telecommunication operator. This leads to heterogeneous measurements in terms of spatial sampling and rainfall measurement accuracy. The problem of combining CML observations to produce regularly gridded rain maps is addressed in chapter 7. A prospective method based on neural network is tested.

5 RAINFALL MEASUREMENT FROM MICROWAVE LINKS: PRINCIPLE AND SOURCES OF UNCERTAINTY

Mobile telecommunication companies use radio-frequencies to transmit some of their signal through the network. The commercial micro-wave links (CML) are composed of a transmitter and a receiver, communicating thanks to antennas located on towers, one at each end of the link. The microwave signal at the receiver fluctuates because of attenuation by rainfall along the path; this is the basis for CML based rainfall estimation, as illustrated in Figure 5-1.

This chapter describes the principle rainfall measurement from CMLs. First the various terms of a CML attenuation budget are presented and the methods used to isolate rain-induced attenuation. Then the relationship between specific attenuation (K) and rainfall rate (R) is discussed.

In the second part of this chapter we detail the various sources of uncertainty in rainfall measurement from microwave links. We discuss their dependencies on the microwave link characteristics and their relative strength.

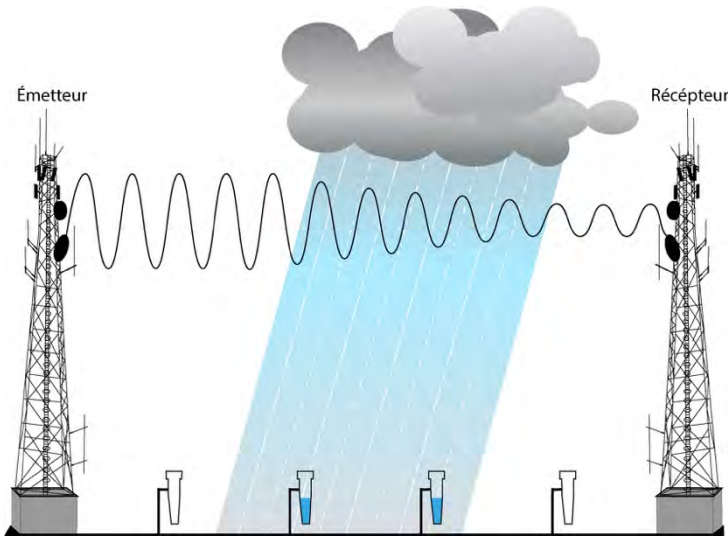


Figure 5-1: Schematic representation of a line-of-sight microwave link

5.1 Measurement principle

5.1.1 Microwave link attenuation budget

The CML transmitted and received power levels can be extracted from the the telecom companies' network monitoring system (NMS). The equipment may change from one company to another allowing different time resolution of the data and access to different information. Assuming that the company provides the average received (RSL) and transmitted power (TSL) for a given time step (typically 15 minutes) in logarithmic unit (dBm in general) the raw average attenuation is given by:

$$A_{raw} = TSL_{avg} - RSL_{avg} \quad (eq. 5.1)$$

The average measured raw attenuation by microwave links A_{raw} [dBm] can be decomposed in different terms when rainfall occurs (Zinevich, Messer, and Alpert 2010; Schleiss and Berne 2010; Goldshtein, Messer, and Zinevich 2009; Leijnse, Uijlenhoet, and Stricker 2007; Chwala et al. 2012):

$$A_{raw} = A_{rain} + B + A_{wa} + A_{other} \quad (eq. 5.2)$$

A_{rain} denotes the integrated path attenuation due to rain in [dB], A_{wa} denotes the attenuation due to wet antenna [dB]. The baseline signal, ie. the attenuation level before rainfall occurs, is noted B . A_{other} includes all other sources of apparent attenuation (for instance misalignment of antennas due to wind burst during the storm etc) not included in the baseline B . The baseline level of attenuation B includes all sources of attenuation during dry periods: the free-space propagative loss, the antennas gain and the electronic losses.

In the following sections we detail the different terms of the above equation.

5.1.2 Attenuation-Rainfall relation

The specific attenuation K_t [dB/km] is defined as the total attenuation A_{rain} [dB] in a path, divided by the CML path length L . K_t , is closely related to the third moment of the DSD, and thus to the rainfall rate. Assuming that the total extinction cross section σ_{ext} can be expressed by a power law of the particle diameter D : $\sigma_{ext} \sim CD^n$ with n and C unknown constant values at a given frequency and temperature (Atlas and Ulbrich 1977), then the specific attenuation become a n-order moment of the DSD. Two different moment of the DSD can be related by a power law (Torres, Porrà, and Creutin 1994; Lee et al. 2004). K_t and R being moments of the DSD we can relate them by a power law:

$$\frac{A_{rain}}{L} = K_t[\text{dB}/\text{km}] = aR^b \quad (\text{eq. 5.3})$$

Many authors considered the attenuation-rainfall power law relation to convert rainfall attenuations to rainfall rate. Two types of approaches exist:

- the first are theoretical calculations of K_t with Mie scattering (or T-matrix for polarimetry) considering either observed or parameterized DSD.
- The second are empirical procedures comparing observed K_t and R and fitting linear relations in the log-log space.

The works from (Semplak and Turrin 1969; Atlas and Ulbrich 1977; Olsen, Rogers, and Hodge 1978) gave the firsts systematic estimation of coefficients $[a, b]$ of the power law relationship depending on the DSD parameterization, temperature and frequency, and showed the strong empirical evidence of the power law relation approximation with little

Chapter 5: Rainfall measurement from microwave links: principle and sources of uncertainty

deviation for strong rain rates. (Atlas and Ulbrich 1977) showed that the above relationship becomes linear ($b = 1$) at $\lambda = 0.9 \text{ cm}$ (ie. $f = 33 \text{ GHz}$).

The b coefficient in eq. 5.3 is close to 1 for many of the frequencies used on CMLs. This is an asset. The quasi-linearity between the path integrated attenuation (PIA) and specific attenuations along the path: $A_{rain} = \int_0^r K_t(r)dr$ means that the PIA is a good estimator of the path average rain rate.

In order to establish attenuation-rainfall relationship (usually called K-R relationship) for West-African convective systems we have used the DSD data from disdrometers observation in Benin presented in Chapter 4. To compute the complex refractive index m of the liquid water at microwave frequencies for a range of temperatures [1-40°] we have used the model from (Ray 1972). Then the attenuation cross section σ_{ext} in Mie regime was calculated with the method of (Bohren and Huffman 2004). The attenuation cross sections σ_{ext} are shown in figures 2-5 and 2-6 depending on temperature and wavelength.

For a given observed DSD $N_{obs}(D)$ we can compute the observed rainfall rate R and the corresponding attenuation considering the extinction cross section σ_{ext} . K-R relationship are established by fitting a linear law of observed R and K in the log-log space. Figure 5-2 shows the K-R relations at 18 and 23 GHz (frequencies of Niamey CML network presented in chapter 5). The black dots show each observed DSD for the year 2006 with the 2D disdrometer (list of MCs systems sampled on table 4-1). The black line is the fitted K-R law from the DSD observations. The results are then compared with one moment (rainfall) DSD parameterization (Moumouni 2009) and the classical Marshall-Palmer parameterization. For Moumouni's parameterization of DSD using one moment (rainfall R in [mm/hr]) we have:

$$N_0^* = 775R^{0.42} \quad [m^{-4}] \quad (eq. 5.4)$$

$$D_m = 1.55R^{0.13} \quad [mm] \quad (eq. 5.5)$$

$$\mu = 5.27 \quad (eq. 5.6)$$

For Marshall-Palmer parameterization with rainfall:

$$N(D) = N_0 e^{-\Lambda D} \quad (eq. 5.7)$$

$$N_0 = 8000 \text{ [m}^{-3}\text{mm}^{-1}\text{]} \quad (\text{eq. 5.8})$$

$$\Lambda = 4.1R^{-0.21} \text{ [mm}^{-1}\text{]} \quad (\text{eq. 5.9})$$

The variables N_0^* and D_m are the DSD parameters of (Testud et al. 2001) parameterization, defined in chapter 1 and used in chapter 3. N_0 and Λ are the parameters of Marshall-Palmer classical exponential DSD parameterization.

The parameterization of Moumouni is inside the 95% confidence interval as expected, as the parameterization was done with the same DSD data. The Marshall-Palmer parameterization is below the 95% confidence interval of the fit leading to an overestimation of rainfall for a measured attenuation.

Figure 5-3 show the coefficients $[a, b]$ of the K-R law fitted for the range [1-60 GHz] for three different temperatures. The K-R relationship is nearly linear in the range 20-30 GHz, best suited for rain monitoring from CML due to the lower impact of rainfall variability on the retrieval. The temperature seems to have a big impact on the coefficients, but the impact in the K-R relation is lower than expected because the variations of coefficients $[a, b]$ regarding the temperature are anti-correlated, compensating the effect. Table 5-1 summarize the retrieved coefficients $[a, b]$ for 23 and 18 GHz (frequencies of Orange Niamey dataset, chapter 6).

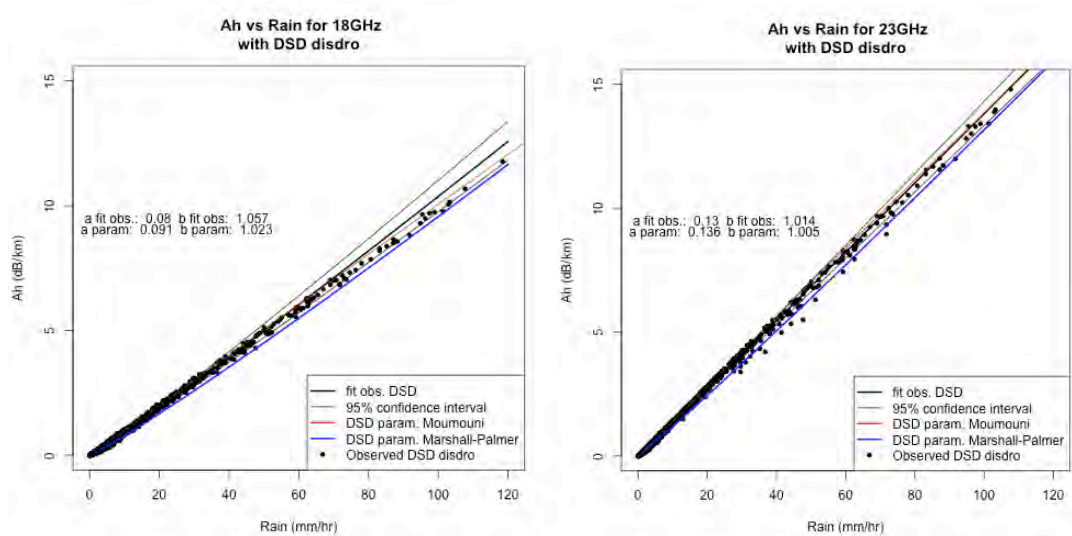


Figure 5-2: K-R laws retrieved from DSD observations. The black dots show each observed DSD. Black line the fitted K-R law. The results are then compared with

(Moumouni et al. 2008) DSD parameterization and the classical Marshall-Palmer parameterization

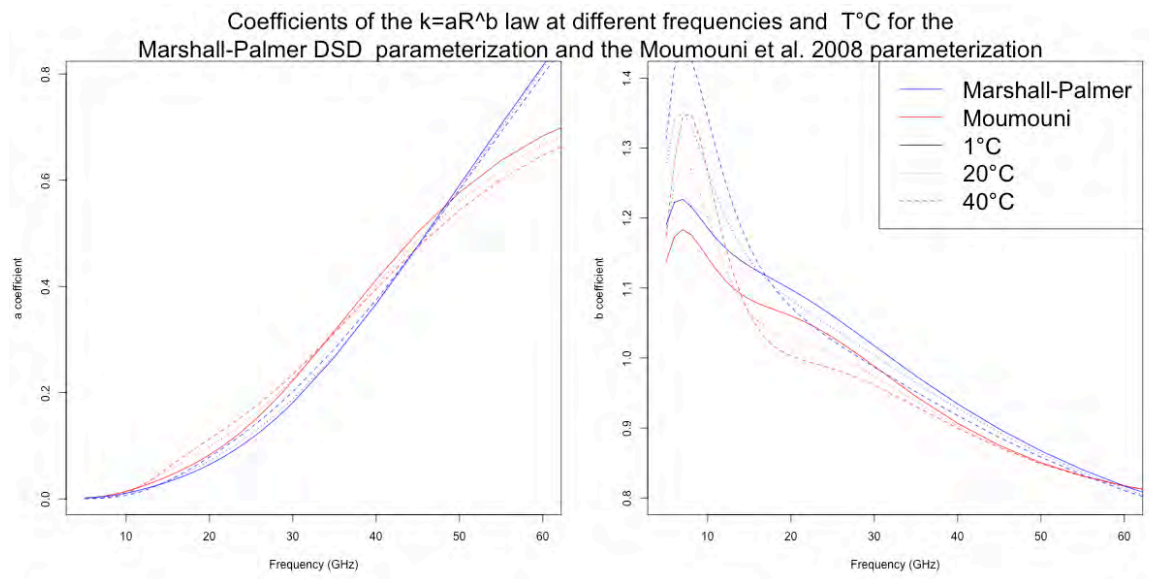


Figure 5-3: Coefficients of the K-R law fitted with the Marshall-Palmer parameterization and the Moumouni & al. 2008 parameterization for measured DSD in Benin

	18 GHZ		23 GHZ	
	a	b	a	b
Moum 10°C	0.0713	1.0535	0.1218	1.0300
Moum 25°C	0.0826	1.0305	0.1334	1.0085
MP param 10°C	0.0522	1.1072	0.0949	1.0688
MP param 25°C	0.0568	1.1000	0.1031	1.0534

Table 5-1: K-R law coefficients for 18 and 23 GHz for Moumouni et al. 2008 parameterization and Marshall-Palmer parameterization for two temperatures.

5.1.3 Baseline and wet-dry period detection

The baseline level of attenuation is defined as the attenuation level in a CML without rainfall. The wet-dry classification is based on the measured attenuation. The baseline level can be subjected to significant variations over time. Many factors can impact the level of the baseline:

- Atmospheric conditions (humidity, temperature)
- Variation on the electronic response of the equipment
- Changes in wave propagation conditions (misalignment of the antenna)
- Type of signal provided by operator and the sampling

Several algorithms have been proposed to establish decision rules to determine wet/dry periods (Leijnse, Uijlenhoet, and Stricker 2007; Schleiss and Berne 2010; Wang et al. 2012). The stationarity or not of the baseline signal is an important feature as the baseline detection algorithms for non-stationary signals need to account for the temporal variation.

In stationary baseline signals two main decision rule algorithms are usually applied. The first is the simple threshold method where the decision rule is based on a fixed attenuation threshold (Leijnse, Uijlenhoet, and Stricker 2007):

$$\begin{cases} \text{rain if } A_{raw} > a_0 \\ \text{dry if } A_{raw} \leq a_0 \end{cases} \quad (\text{eq. 5.10})$$

Where A_{raw} is the raw attenuation and a_0 is the chosen threshold, which may vary depending on the noise levels of the raw attenuation, the equipment, the link length, and the weather conditions. The optimal choice of a_0 is made by minimizing the non-detections (too restrictive) and rain false alarms (too permissive).

The second algorithm used in stationary signals is based on the temporal variability of the attenuation (Schleiss and Berne 2010). Choosing a sliding window on length n representing a duration t_n , the decision rule is based on a threshold on the local variability σ_{t_n} of the measured attenuation, as attenuation during rainfall events exhibits a higher variability than during dry periods:

$$\begin{cases} \text{rain if } \sigma_{t_n} > \sigma_0 \\ \text{dry if } \sigma_{t_n} \leq \sigma_0 \end{cases} \quad (\text{eq. 5.11})$$

Chapter 5: Rainfall measurement from microwave links: principle and sources of uncertainty

The choice of the number of time steps n , to calculate local attenuation variabilities is delicate. It depends on the climatic rainfall variability and also on the time step resolution and type of data provided by the operator (nature and precision of the signal). (Schleiss and Berne 2010) choose $t_n = 25 \text{ min}$ sliding window for 30s resolution data.

More complex situations can be found if we observe strong temporal drifts in the attenuation for dry periods. The drifts may occur due to variations in the atmosphere due to temperature, pressure and humidity (changing the refraction index and thus the propagation of the MW signals). Also the atmospheric effects result in hardware instabilities leading to temporal drifts. To take into account the temporal variation of the baseline, more complex methods have been proposed: the factor graph which assumes the baseline to vary linearly over time with parameters who can vary (slowly) over time (Reller, Loeliger, and Diaz 2011). Another method is based on a Markov switching algorithm which is not based on an empirically estimated threshold parameter and shows better results than threshold-type classifications (Wang et al. 2012). Finally, (Chwala et al. 2012) developed a spectral method adapted to their large set of data: the classification is made by comparing the local normalized Fourier Transforms (FT) of the attenuation signals to a set of reference dry/wet FT signals (valuable for signals with a good temporal resolution). The work of (Cherkassky, Ostrometzky, and Messer 2014) uses the min/max raw attenuations to classify the periods into three types of precipitation: snow, sleet, rainfall, based on the kernel Fisher discriminant analysis. Other methods can use external information to classify wet/dry periods, for example IR information from geostationary satellites in (van het Schip et al. 2017).

5.1.4 Wet antenna

The wetting of the antenna during rainfall events creates a layer of water on the shield of the antenna. That water layer is an extra attenuation source to the total measured attenuation which should be removed to avoid biases on the rainfall rate estimation.

There is not a clear consensus in the CML rainfall estimation community on the method to adopt for quantifying the wet antenna attenuation. In a first approach, the attenuation

Chapter 5: Rainfall measurement from microwave links: principle and sources of uncertainty

caused by wet antennas expressed by (Kharadly and Ross 2001) and extended by (Minda and Nakamura 2005) states that the wet antenna attenuation depends on the rainfall rates and thus on the rainfall attenuation A_{rain} with the following characteristics:

- An exponential increase of A_{wa} for increasing values of $K_t [dB/km]$, bounded with a maximum value.
- An exponential decrease with time after the rainfall event (due to antenna progressive drying)

The exponential laws can be fitted with simultaneous data of rain gages (or disdrometers) and CML. The various coefficients of the exponential laws retrieved can vary depending on the CML frequency, antenna type, antenna shield or even temperature or wind direction. The exposition to wind or heat of the antenna can lead to a faster drying or to a thinner water layer in the shield.

(Leijnse, Uijlenhoet, and Stricker 2008) adopted a more physical approach by expressing the thickness of the water layer in the antenna l by a power law of the rainfall rate R . The principal features of Leijnse approach are:

- $l = \gamma R^\delta$ law
- Increasing A_{wa} for increasing R without a bounded A_{wa} .
- $A_{wa}(R)$ frequency dependency.

The coefficients γ, δ were fitted to observed data by converting the estimated empirical antenna attenuation to a water layer thickness l by calculating the theoretical attenuation caused by a flat layer of water in an antenna at a certain frequency. Then a set of $A_{wa}(R)$ laws for different frequencies were derived. The exponent coefficient found $\delta = 0.24$ leads to an increasing value of a A_{wa} with the rainfall rate R . However, the $l(R)$ law can be dependent on the antenna type and shield as well as the weather conditions: wind, antenna location, temperature.

The quality of the fitting was poor due to few gauges present on the link path and distant from several hundred meters from as well as using a long CML (4.89km) which can lead to errors due to the spatial variability, even for a close to linear $K - R$ relation at 27 GHz.

A dedicated experiment to estimate the wet antenna effect is described in (Schleiss, Rieckermann, and Berne 2013). They used four disdrometers disposed along a CML of 38 GHz and length 1.85 km to estimate the specific attenuation (with T-matrix model).

Then they build a model of the wet antenna dynamics by removing to the CML signal the rainfall component. The main features of its wet antenna model are:

- Wet antenna attenuation bounded at 2.3 GHz maxima
- Exponential increase with time toward 2.3 dB (firsts 5-10 min of rainfall)
- Exponential decrease with time when rain stops (drying time between 2h and 30min)
- Non dependent on rainfall rate attenuation (rainfall rate)

The study (Schleiss, Rieckermann, and Berne 2013) shows evidence that the wet antenna attenuation does not depend on the rainfall rate for rainfall rates below 8 mm/hr. He describes the wetting of the antenna as a collection of droplets stuck in the antenna rather than a thin layer of water as modeled by (Leijnse, Uijlenhoet, and Stricker 2008). But this study (and others from (Chwala et al. 2012) or (Rayitsfeld et al. 2012)) were made in mid latitudes regions (Switzerland, Nederland, Germany and Israel) where the rainfall rates involved are low compared to tropical MCS. The wet antenna attenuation should be quantified and studied in more detail in tropical regions for strong rainfall rates related to convective precipitation which can be greater than 100 mm/hr.

5.1.5 Other sources of atmospheric attenuation

This section describes other atmospheric sources of attenuation of MW. The main absorbers in atmosphere in MW frequencies are oxygen and water vapor. Non-precipitating suspended droplets (clouds, haze) and suspended dust particles can also cause attenuation. This section only provides an overview of these sources of attenuation and does not get into the detailed models. Table 5-1 summarizes the magnitude of specific attenuation by different atmospheric phenomena.

If we consider no variation of these elements during rainfall events, their contribution to the total path integrated attenuation between a pair of antennas is included in the baseline and thus removed. However, at high frequency and in tropical region, these factors may vary during the storm itself. Further analysis would be needed to asses this problem.

Oxygen

Oxygen is the main absorber of MW frequencies in a dry atmosphere. The amount of energy absorbed by oxygen depend on the frequency of the MW signal and on the quantity of oxygen (depending mainly on the atmospheric pressure and temperature).

The absorption spectra of MW by oxygen is composed 44 absorption lines in the [1-1000GHz] range of frequencies. The absorption spectrum between the lines (peaks) is composed by a continuum which increase with frequency. For frequencies below 100GHz, the continuum contribution is low (attenuation $< 0.01 \text{ dB/km}$).

There is, however an absorption peak centered at 60 GHz. The work (Liebe, Hufford, and Cotton 1993) show laboratory measurements of the absorption peak around the 60 GHz for different pressures. At 6°C and 1013 mbar, in the peak center (60 GHz) the attenuation due to oxygen absorption is up to 15 dB/km . It exists other absorption lines of the oxygen above 350 GHz, which is beyond the frequencies used commonly by telecommunication operators.

Humidity

In a wet atmosphere, water vapor is an important absorber of MW radiation. As for oxygen, the amount of absorbed energy depend on the density of H_2O molecules in the atmosphere.

The absorption spectrum of water vapor is composed by a continuum increasing with frequency and a series of absorption peaks. The main absorption peaks below 100 GHz are at 22.2 GHz and 67.8 GHz frequencies.

(Liebe, Hufford, and Cotton 1993) modeled the absorption by H_2O . Below 100 GHz, at sea level normal conditions, 1013 mbar, 20°C and 40% of relative humidity (RH) the continuum contribution to water vapor absorption is below 0.2 dB/km .

However, the contribution of the 22.2 GHz peak is high. At 0°C , RH=100%, P=1013 mbar, the attenuation is 0.1 dB/km . For 20°C is 0.5 dB/km and for 30°C 0.9 dB/km .

West African mesoscale convective systems are huge perturbation of the atmosphere. As we described briefly in chapter 1, the convective front updraft of moist air is followed by a downdraft of cold dry air from upper layers of the atmosphere leading to a drop of the

Chapter 5: Rainfall measurement from microwave links: principle and sources of uncertainty

absolute humidity in the atmosphere during rainfall. Figure 5-4 shows the records of a meteorological station from AMMA-CATCH observatory, located 50km east from Niamey (13.5311°N ; 2.6613°E) during the 4th August 2007 MCS event. The top plot shows the strong rainfall rates associated to the convective front passage over the station at 17h00 UTC. At the same moment the stations records a drop of the absolute humidity from 21 to 17 g/m^3 . The drop of absolute humidity is accompanied by a drop of temperature from 32°C to 20°C. This drop of temperature leads to an increase of relative humidity, but the total amount of water vapor in the atmosphere decreases during the strong rainfall.

Considering the peak of water absorption at 23 GHz, we have computed the water vapor attenuation at the peak center (23 GHz) following the model of (Liebe, Hufford, and Cotton 1993). The second plot in figure 5-4 shows the specific attenuation due to water vapor during the event. We observe a decrease in the attenuation from 0.5 to 0.4 dB/km during the rainfall event due to the decrease of absolute humidity. Considering a hypothetical measurement of a CML during this event, as the drop of the attenuation is synchronized with the start of the rainfall, the baseline will not account for the water vapor attenuation variation producing a bias in the measurement. However, the variation of 0.1 dB/km is very low compared to other sources of uncertainties as we show later.

Suspended Droplets

Clouds and fog attenuates MW by the same mechanism than rainfall does. (Liebe, Hufford, and Cotton 1993) modeled the effect of a dense fog in the MW path with Rayleigh approximation for a large range of MW frequencies. For an extremely dense fog with a water content of $W = 1 g/m^3$, equivalent to a 50m visibility, at sea level conditions, for 100% RH, for 0°C they state specific attenuation of 0.9 dB/km and for 30°C specific attenuation of 1 dB/km . This correspond to extreme fog conditions. The fog should be considered as a source of rainfall false alarms in regions where it appears recurrently.

Dust

As suspended droplets and rainfall does, the presence of dust particles in the atmosphere can cause scattering and absorption of the MW signal. During a sandstorm in Khartoum-Sudan, (Elshaikh et al. 2009) measured specific attenuations of 0.67 dB/km on a 15 km CML at 13 GHz. In their study they modeled the dust attenuation depending on the visibility (in km). The model predicts specific attenuations of 1 dB/km at K-band (18-26 GHz) for a 50m visibility dust storm, which is a rare event.

(Xiao-Ying Dong, Hsing-Yi Chen, and Dong-Hui Guo 2011) stated that attenuation decreases sharply as the visibility increases from 1m to 1 km. Thus the attenuation due to sand and dust storms is not serious except for storms with visibilities less than a few meters and frequencies higher than 30 GHz.

Insects and other animals

Flying animals can be a potential source of attenuation: birds, bats and insects can cause attenuations on commercial CML. Telecommunication companies informed us about the occasional presence of wasp nests in the antennas.

Chapter 5: Rainfall measurement from microwave links: principle and sources of uncertainty

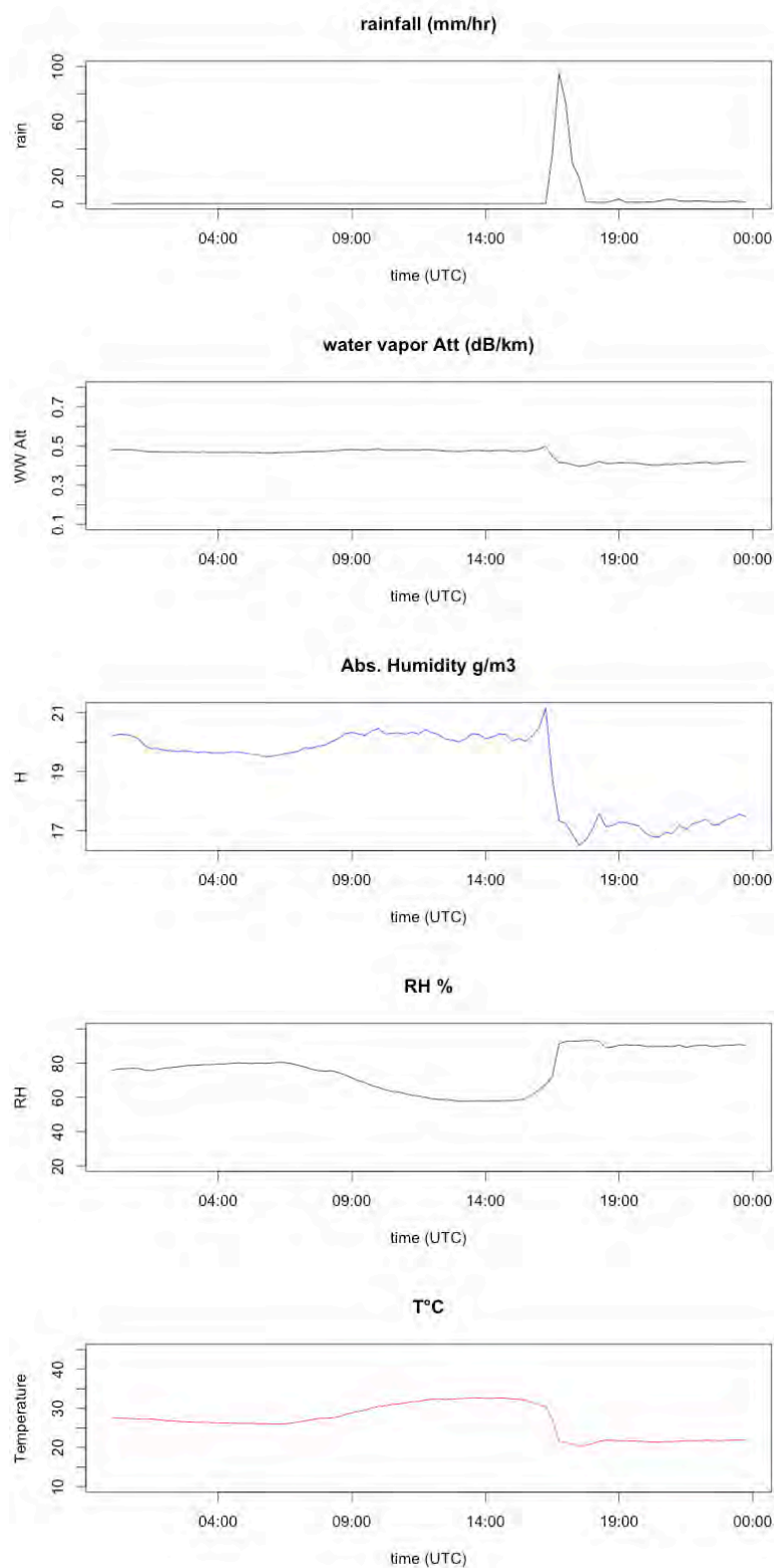


Figure 5-4: Records of the Banizoumbou station, 50km East of Niamey during the 4th August 2007 MCS event. From top to bottom, rainfall rate in [mm/hr], water wapor induced attenuation in [dB/km] absolute humidity in [g/m3], relative humidity in (%) and temperature in °C

	Specific attenuation	Reference
Oxygen	Peak at 60GHz, 6°C, 1013 mbar ~15 dB/km For $f < 50\text{GHz}$ $a < 0.05\text{ dB/km}$	[Liebe et al. 1993]
Water Vapor	Main absorption lines below 100GHz : 22.23 GHz and 67.80 GHz Temperature dependance : 0°C, RH=100%,P=1013mbar,f=23GHZ -> 0.1 dB/km 20°C, RH=100%,P=1013mbar,f=23GHZ-> 0.45 dB/km 30°C, RH=100%,P=1013mbar,f=23GHZ-> 0.9 dB/km	[Liebe et al. 1993]
Fog & clouds	$W=1\text{g/m}^3$ -> heavy fog with 50m visibility: 0°C, RH=100%, p=1013mbar,f=23GHz -> $a=1\text{ dB/km}$ 30°C,RH=100%,p=1013mbar,f=23GHz-> $a=0.9\text{ dB/km}$	[Liebe et al. 1993]
Dust	50m visibility, heavy dust storm : 1 dB/km at K-band (18-26GHz)	[Dong et al 2011] [Elshaikh et al. 2009]
Rainfall	50 mm/hr rainfall at 20°C $a = 6.9\text{ dB/km}$ at 23 GHz $a = 5.0\text{ dB/km}$ at 18 GHz	

Table 5-2: Summary of the different sources of atmospheric attenuation

5.2 Sources of uncertainties in CML based rainfall estimation

Section 5.1 presented the principle of rainfall estimation from CML and listed the various sources of signal fluctuation that need to be removed to quantify attenuation due to rain.

The sources of uncertainty in the different steps of this process are detailed below and some quantitative values provided.

5.2.1 Variability of the K-R relationship

DSD parameterization

Many authors have investigated the impact of the DSD in the attenuation levels of a CML (Leijnse, Uijlenhoet, and Berne 2010; Tat-Soon Yee et al. 2001; Kumar, Yee Hui Lee, and Jin Teong Ong 2010; Das, Maitra, and Shukla 2010).

The K-R laws retrieved at 23 GHz and 18 GHz are shown in figure 5-2. They show different values if we consider the Moumouni parameterization, well suited for West Africa MCS, compared to the Marshall-Palmer parameterization.

Figure 5-5 shows the relative difference (%) in rainfall retrieval with K-R relationship between MP parameterization and Moumouni parameterization (considering Moumouni as the reference). The relative difference is shown by rainfall rate for different frequencies and temperatures. The relative difference increase for low rainfall rates and for lower frequencies. The difference also depends on temperature. For rainfall rate above 20 mm/hr the error is in the range 5-15%. Thus, considering the MP parameterization instead of Moumouni can lead to an overestimation 5-15% of the rainfall rates depending on the frequency and temperature involved.

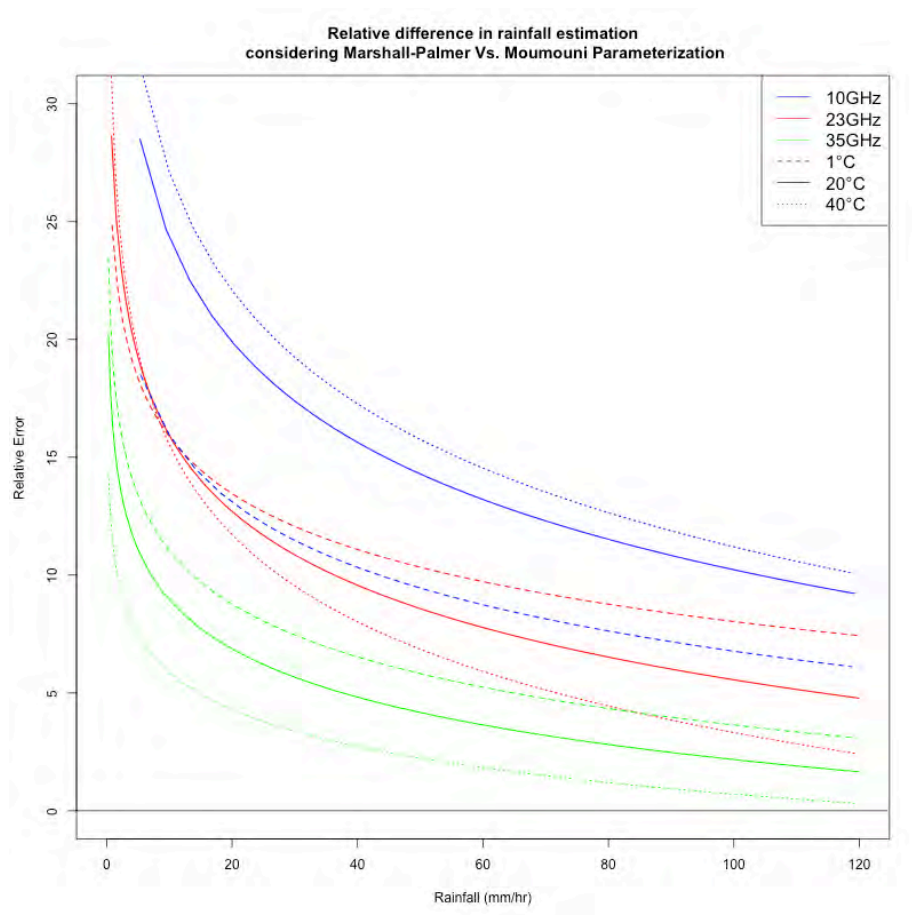


Figure 5-5: : Relative differences in rainfall estimation with K-R law using Marshall-Palmer parameterization compared to the reference Mougouni parameterization for different temperatures and frequencies.

Polarization of the MW signal

The polarization of the MW signal impacts the level of attenuation due to rainfall as the rain drops are flattened in the horizontal direction. Thus, a horizontal polarized signal is more attenuated than a vertical signal for the same rain rate (Bernard Fong, Fong, and Hong 2005; Rincon et al. 1996). In chapter 3 we have considered the Andsanger aspect ratio law of rain drop as well suited to describe radar observations in west Africa MCS. In this section we quantify the relative error due to a lack of information about the polarization of the MW signal.

The K-R law presented in figure 5-2 was calculated considering no polarization of the signal, or spherical equivalent droplets. Figure 5-6 presents the K-R laws calculated for different polarizations with the T-matrix model for a 23GHz signal and the (Andsanger,

Chapter 5: Rainfall measurement from microwave links: principle and sources of uncertainty

Beard, and Laird 1999) aspect ratio law. We observe that the relative differences are greater than those from the different DSD parameterizations. Figure 5-7 and 5-8 show the relative differences considering the round drop as the reference for 10GHz and 23 GHz. At 10GHz the effect of the polarization is lower than for 23 GHz. At 23 GHz a misinterpretation of the attenuation data in terms of polarization can lead to overestimations of 15% and underestimations of 8%. Table 5-3 shows the retrieved K-R law for different frequencies and polarizations.

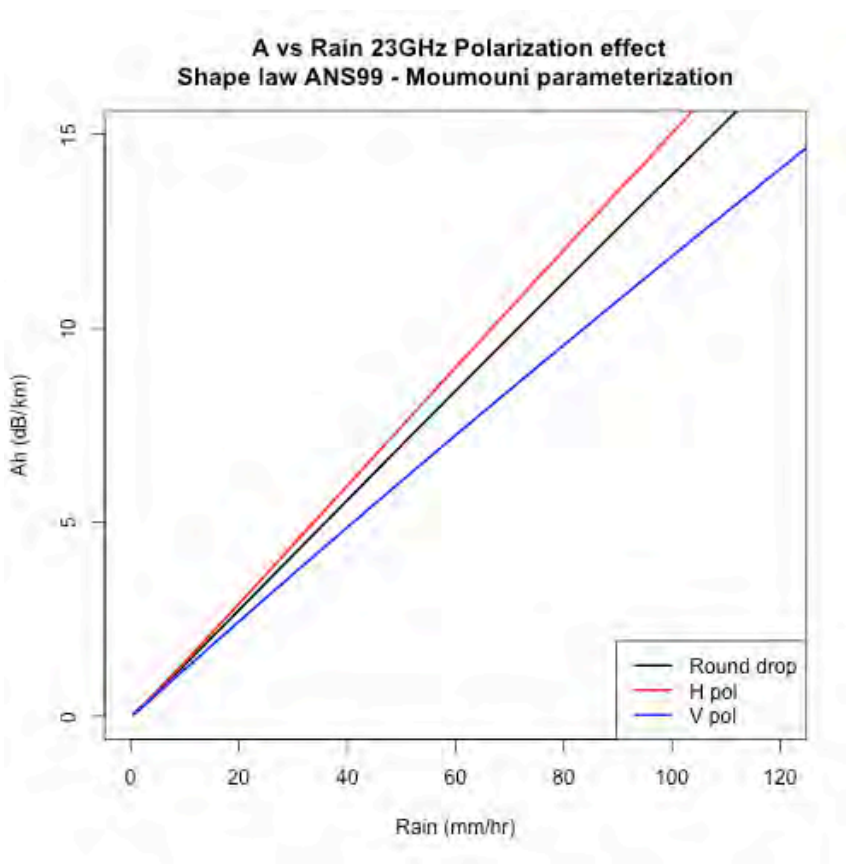


Figure 5-6: K-R laws considering different polarizations at 23 GHz for the [Andsanger et al. 1999] aspect ratio law and Moumouni parameterization.

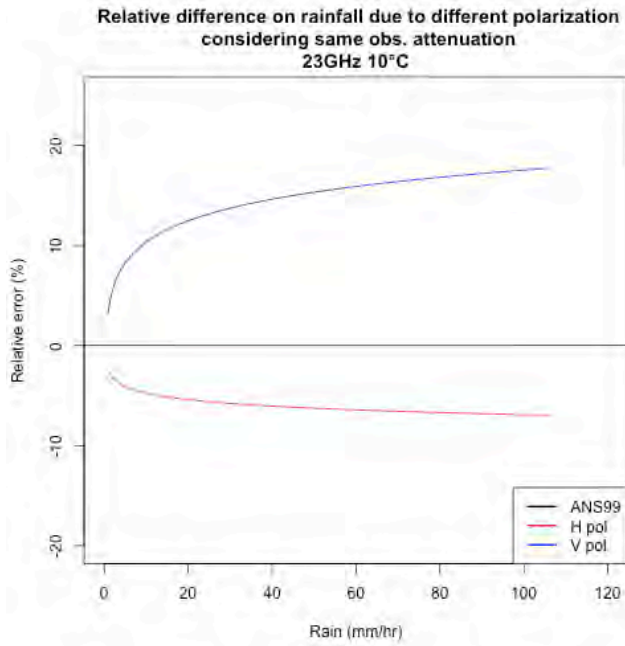


Figure 5-7: Relative difference on rainfall due to different polarization for same observed attenuation level at 23GHz and 10°C. The reference level at 0 error is the round drop (no polarization).

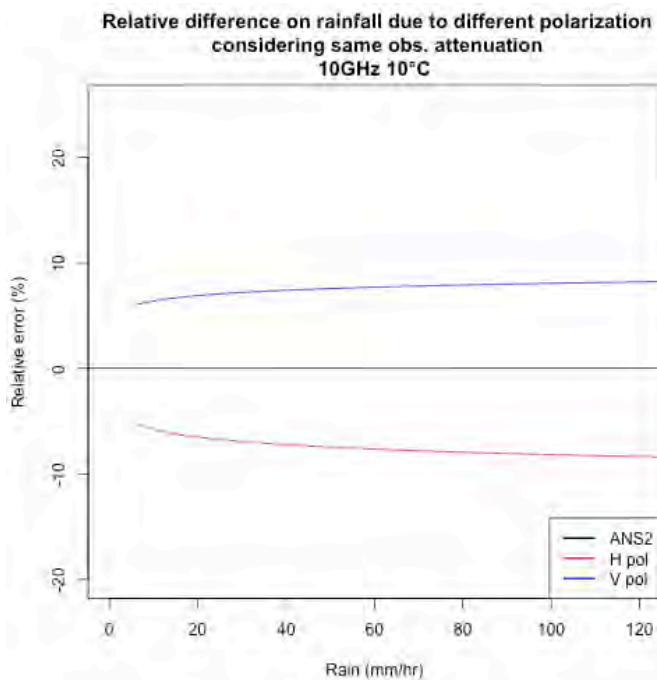


Figure 5-8: Relative difference on rainfall due to different polarization for same observed attenuation level at 10GHz and 10°C. The reference level at 0 error is the round drop (no polarization).

		a	b
9.8 GHz	H	0.0120	1.193
	V	0.0109	1.171
	NoPol	0.0115	1.180
11 GHz	H	0.0208	1.148
	V	0.0193	1.080
	NoPol	0.0201	1.095
13 GHz	H	0.0339	1.110
	V	0.0322	1.080
	NoPol	0.0331	1.095
18 GHz	H	0.0733	1.067
	V	0.0708	1.024
	NoPol	0.0719	1.052
23 GHz	H	0.127	1.038
	V	0.119	1.000
	NoPol	0.123	1.028

Table 5-3: K-R law coefficients for different frequencies and polarizations for the Andsanger et al. 1999 aspect ratio law and Moumouni parameterization at 10°C. Calculations of extinction cross-sections with T-matrix model.

K-R law approximation

The K-R relation is an approximation of the link between the true attenuation and the rainfall rate. As showed in figure 5-2 the black dots representing observed DSD are scattered around the fitted A-R law which leads into an uncertainty caused by the approximation. The uncertainty depends on frequency. Also a bias can arise due to the log-log fitting procedure of the K-R law.

Chapter 5: Rainfall measurement from microwave links: principle and sources of uncertainty

Figure 5-9 show the relative error on rainfall between each 1-min observed DSD in Benin and the retrieved K-R law. The uncertainty grows as the frequency lowers. Also, the residual bias lower with higher frequency. The remaining average bias for rain rates $> 50 \text{ mm/hr}$ are -9.5% for 9 GHz , -8% for 13 GHz , -2.4% for 18 GHz and -2.8% for 23 GHz .

The relative errors here were calculated for point scale measured DSD. As the CML measures path integrated attenuations, the uncertainty decrease with longer links and for longer integration sampling time.

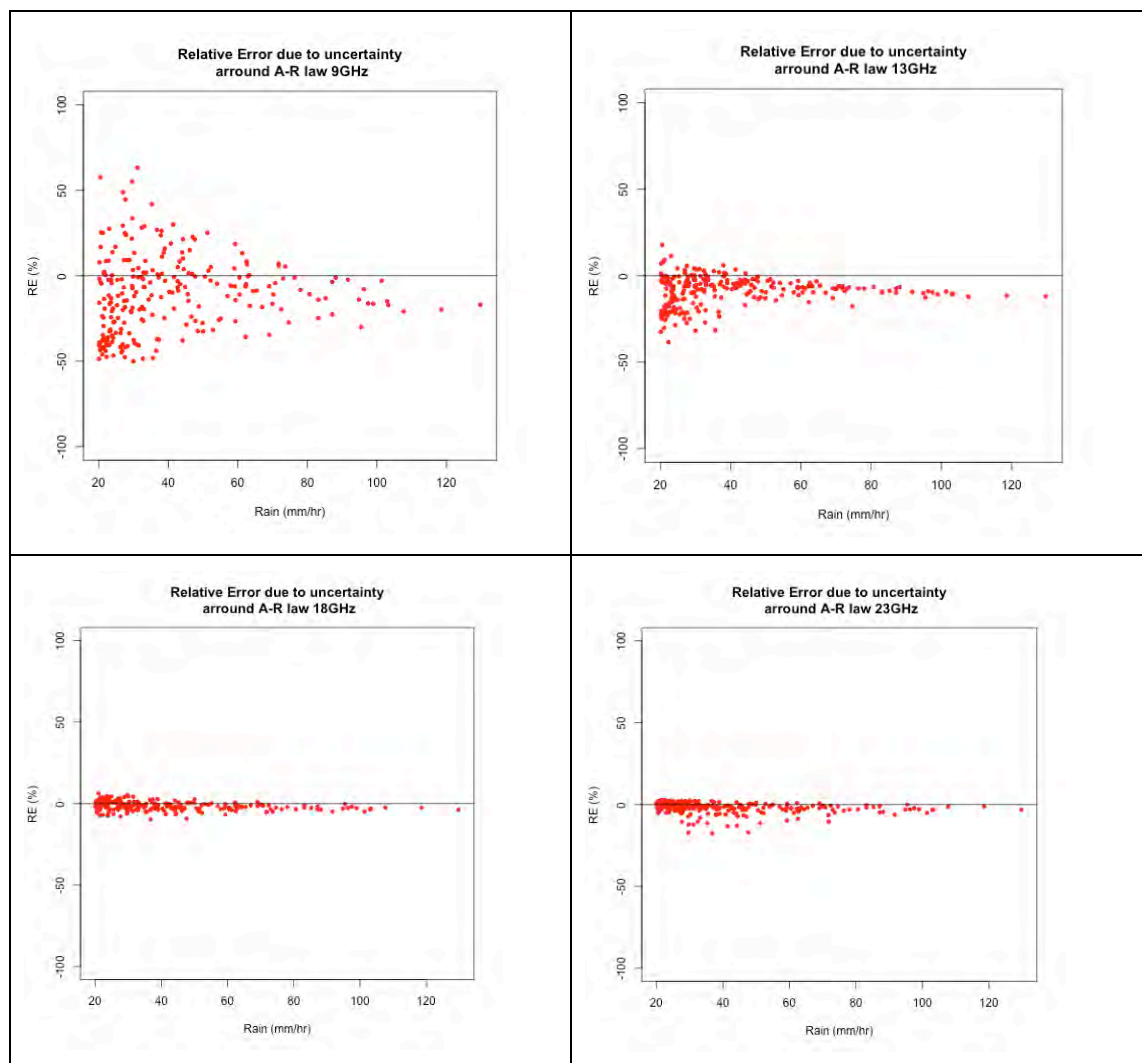


Figure 5-9: Residuals between observed DSD rainfall and fitted A-R law. The uncertainty lower as the frequency increase. The remaining average bias for rain rates $>50 \text{ mm/hr}$ are -9.5% for 9 GHz , -8% for 13 GHz , -2.4% for 18 GHz and -2.8% for 23 GHz

Spatial variability of rainfall

The K-R relation is quasi linear as the b coefficient in equation 5.3 is near 1. In Figure 5-3 presenting the retrieved b coefficient against frequency, we can see that the relation becomes linear for the Moumouni parameterization of DSD around 28 GHz at 20°C. For frequencies below 10 GHz the relation moves away from linearity as $b > 1.2$, specially for higher temperatures, and also, for frequencies above 40 GHz, as $b < 0.9$.

In that situations the spatial variability of DSD can lead into errors as the path average rainfall is not equal to the retrieved rainfall, and the rainfall $R(s)$ is highly variable along the path s :

$$\int_0^L aR(s)^b ds \neq a \left[\int_0^L R(s) ds \right]^b = \frac{A_{rain}}{L} \quad \text{if } b \neq 1 \quad (\text{eq. 5.12})$$

In they work (Berne and Uijlenhoet 2007) the authors have estimated the impact of the DSD variability along CML of different lengths and frequencies with a stochastic generator of DSD profiles of different lengths. They computed the expected attenuation K , the real rainfall, the relative error and the uncertainty due to the path averaged rainfall using fitted K-R laws. They found the following characteristics:

- A mean relative bias of -2% for a 4 km link due to the K-R fitting
- An uncertainty range due to DSD variability between 15-10% for 23GHz [0-5km] CML.
- A bias due to a wrong DSD parameterization between [0; -20%] (using climatological DSD parameterization)

Our results are in agreement with their findings. They have retrieved a mean relative bias of -2% for short links due to the K-R fitting. We found in the last section -3%. Considering that we have calculated at the point scale and they have considered spatial variability of DSD.

We also have a similar magnitude in the error due to a wrong DSD parameterization. By considering Marshal-Palmer parameterization, we found biases at the point scale around [5; 20%].

5.2.2 Quantization step

In the work (Zinevich, Messer, and Alpert 2010) the authors build a complete error model of the CML rainfall measurement including the quantization step.

The systems monitoring the CML in Telecom companies usually stores the Tx and Rx data signals for a quantized level of attenuation. Our datasets are quantized at 0.1 dB or 1 dB (depending on the zone). As mentioned above, a rough quantization step can absorb the baseline variations due to noise.

A rough quantization step leads to a minimal detectable rainfall R_{min} which depends on the frequency f , the link length L and the quantization step Δ_a of the attenuation provided by the telecom company. The $K - R$ relation being a power law (eq 5.3), it follows that the minimal detectable rain is:

$$R_{min} = \left(\frac{\Delta_a}{2aL} \right)^{1/b} \quad (eq. 5.13)$$

Where L is the link length and $[a, b]$ are the $K - R$ law parameters at a certain frequency.

Figure 5-10 and figure 5-11 shows the minimal detectable as a function of the link length for different frequencies at $\Delta_a = 1$ dB and $\Delta_a = 0.1$ dB quantization steps. As we can see the lower the frequency and the shorter the link length the minimal detectable rain get high values corresponding to convective rainfall. Follows that short links and rough quantization step can lead to systematic non-detections of rainfall.

Considering the maximum span of attenuation $\pm \Delta_a/2$. Figure 5-12 represent the maximum relative uncertainty due to 1 dB quantization step for different rainfall rates and link lengths a 23 GHz link.

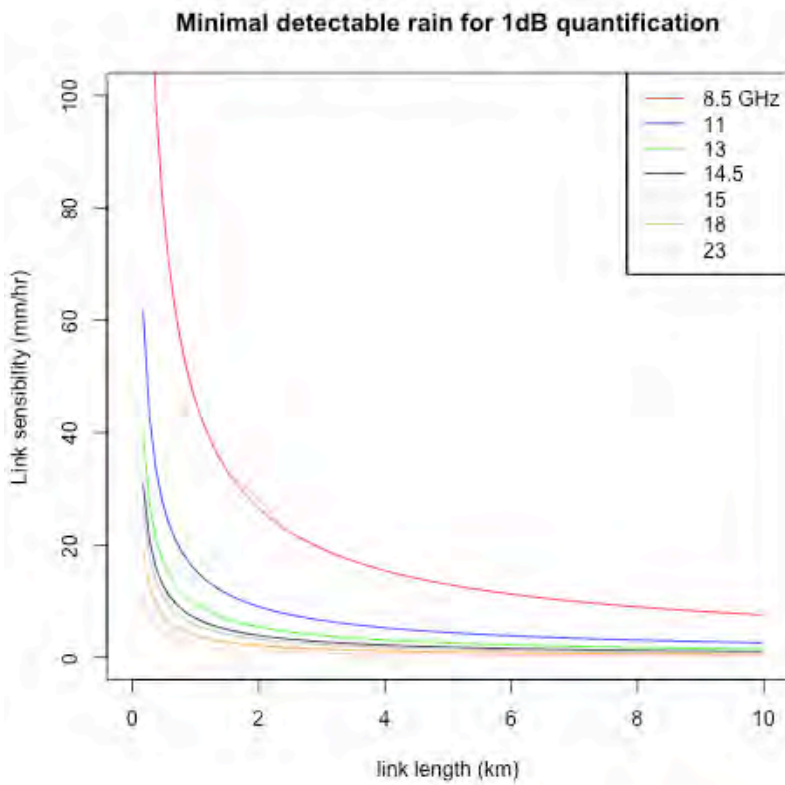


Figure 5-10: Minimal detectable rain in function of link length and frequency at a 1 dB quantification step of the attenuation. For low frequency and short links the link sensitivity is very high.

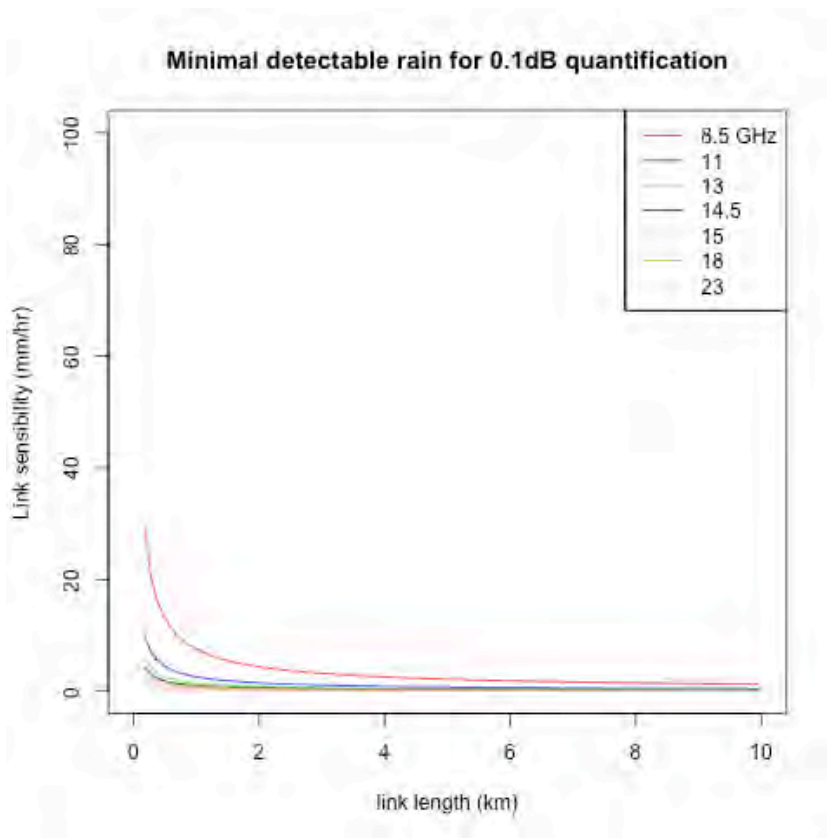


Figure 5-11: Minimal detectable rain in function of link length and frequency at a 0.1 dB quantification step of the attenuation.

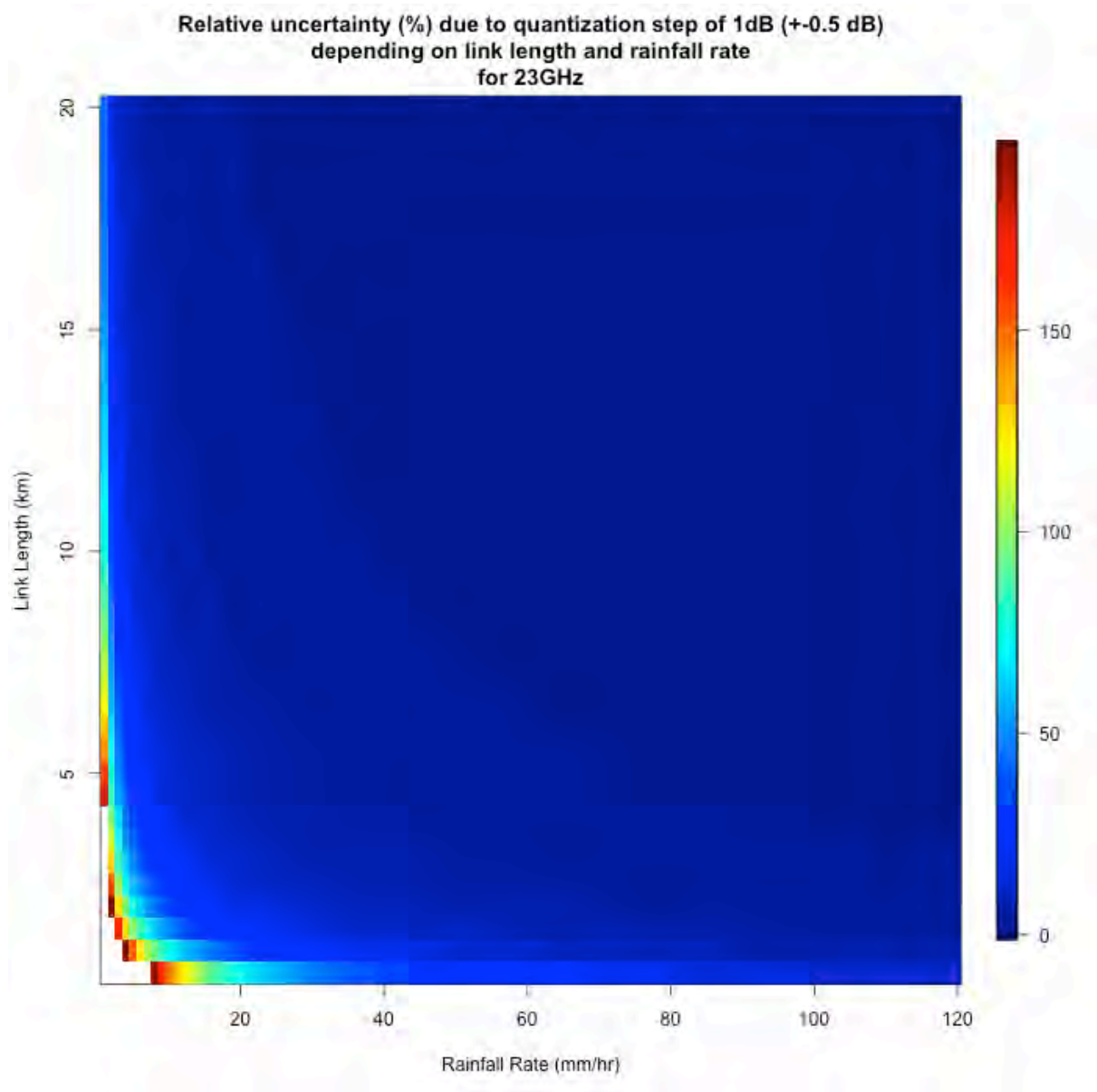


Figure 5-12: Relative uncertainty due to quantization step depending on link length and rainfall rate for 23 GHz CML and 1 dB quantization step. The white zone correspond to values of path integrated attenuation below 0.5 dB and thus non detectable rainfall.

5.2.3 Wet antenna attenuation

Different studies (Leijnse, Uijlenhoet, and Stricker 2008; Schleiss, Rieckermann, and Berne 2013; Rahim et al. 2012) agree on the range of the wet antenna effect: for rainfall rates higher than 20 mm/hr and frequencies in [10 – 30 GHz] range, the wet antenna attenuation (for both antennas) is in the range [2 – 4 dB]

The relative effect of wet antenna attenuation in rainfall estimation varies with the link length and rainfall rate. Considering a fixed value of antenna attenuation of 3dB, for both antennas, short link and low rainfall rates are more impacted. Figure 5-13 presents the relative bias induced by a fixed 3dB wet antenna attenuation not considered, for a 23 GHz link at different frequencies and lengths. The bias induced can be extremely high for short links and low rainfall rates. Even for high rainfall rates and short links the effect is important.

If not considered, the wet antenna can multiply by a factor 2 or 3 the rainfall amounts in a season.

The wet antenna attenuation is highly variable as discussed. The estimation of the effect can remove the bias but add an uncertainty due the modeling and fitting parameters procedure which is usually very noisy as showed by (Leijnse et al. 2008) and (Schleiss et al. 2013).

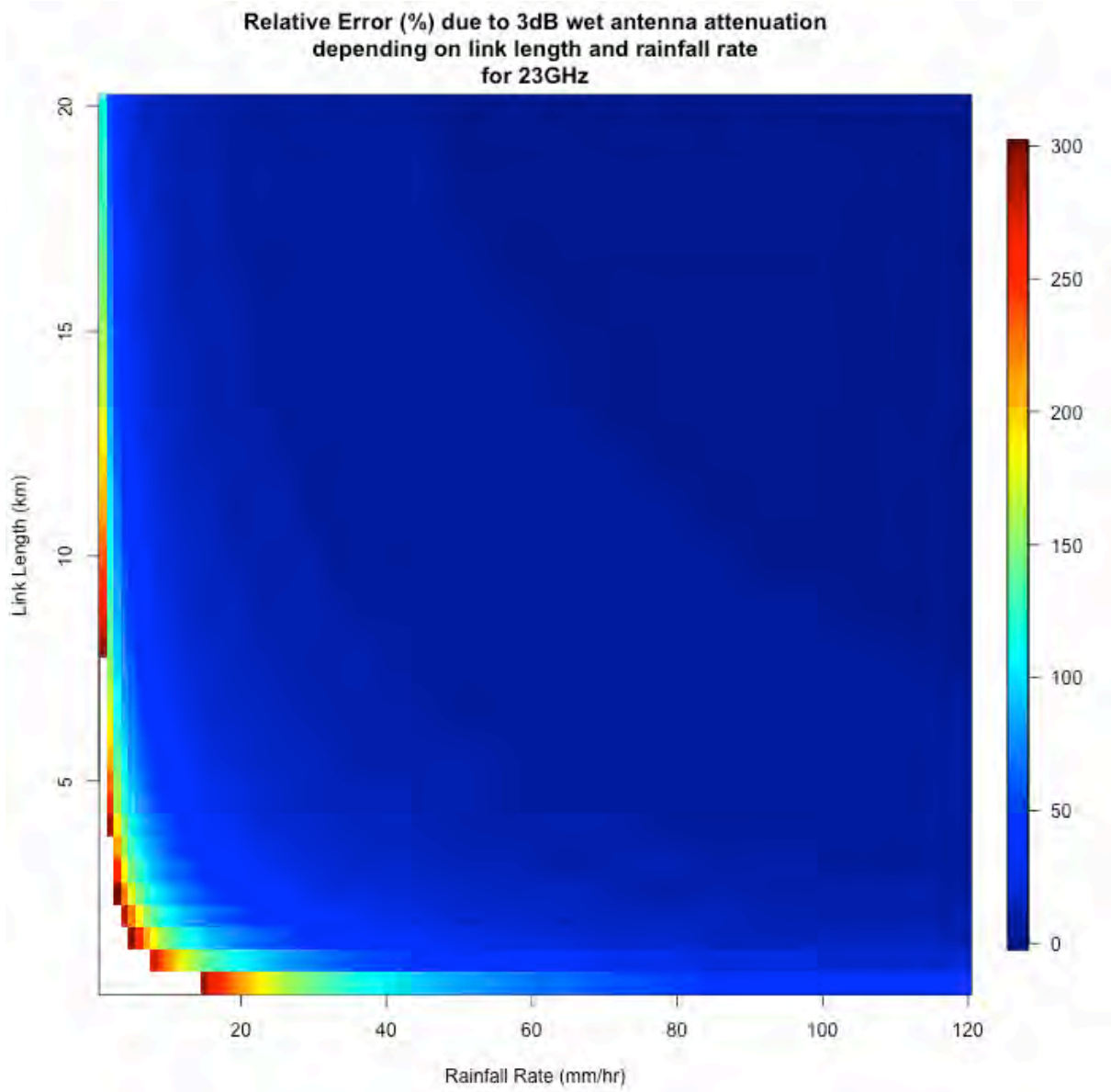


Figure 5-13: Relative Error due to a 3dB wet antenna attenuation not considered.

5.2.4 Quality of raw information

Temporal Sampling

Telephone companies provide data with different temporal resolutions depending on the storage constraints of their servers. We can find in the literature datasets at high temporal resolution (some seconds) usually for one-off studies for a short time period and a limited number of microwave links. In operational frameworks, high temporal resolution data is not stored due to the high volumes of the data. Usually the provided data stored by the monitoring systems of the companies are in a coarser temporal resolution (several minutes).

With high temporal resolution data we can quantify the short time variations of the baseline and the rainfall short time scale variability. Also, the assessment of the wet antenna attenuation with high temporal resolution data allow to monitor the dynamical evolution of the antenna wetting (if a validation dataset is available). Another asset of high temporal resolution data is to quantify the losses due to a coarser temporal resolution in data or a particular sampling strategy (discussed in the section below).

Equation 5.12 presented in section 5.2.2 showing the impact of the non-linear K-R relation on the spatial variability of rainfall has a similar effect on the temporal evolution of rainfall rates (by changing the integral over time). As rainfall is highly variable in space and time, the temporal averaging of attenuations in time deviate from the temporal averaging of rainfall over time when applying the K-R law if $b \neq 1$. The effect of the non-linear time averaging is less dramatic if the time resolution is below the time decorrelation scale, which depends on the climatic regimes.

Sampling Strategy

For coarse time resolution scales (~15 minutes is often found in the literature) different sampling strategies can be found constrained by the software of the telecom companies' servers. The data can be averaged over the 15 minutes or sampled every 15

Chapter 5: Rainfall measurement from microwave links: principle and sources of uncertainty

minutes. The resulting uncertainty in the rainfall retrievals are different: the averaged attenuation over 15 minutes compensates the noise of the baseline at short time scales due to atmospheric scintillation of the atmosphere. For an intermittent sampling every 15 minutes the noise of the high resolution scale is not compensated leading to an uncertainty on the baseline detection equivalent to the value of the noise at short scales. Of course an averaged attenuation value is preferred to smooth the noise of the baseline and to account for the actual average rainfall over the 15 minutes instead of the point measurement rainfall, which may be far from the average due to high temporal variability.

Unfortunately, is hard to access the information in the codes sampling the attenuation in the antennas to know the number of samples of attenuation used during the 15 minutes interval to calculate the averaged attenuation values. The expected variance on the measured average compared to the true average is greater if the number of samples during the 15 minutes is $N = 15$ (1 per minute) or $N = 900$ (1 per second). The resulting uncertainty depends on the number of samples N used to average the attenuation and also on the short scale variability.

In the study (Leijnse et al. 2008) the authors estimates the effect of the sampling strategy errors and uncertainties depending on the link frequency and link length, and compared it to the effect of a rough quantization step. Concerning the errors (bias) due to the sampling strategy they found:

- A growing relative error due to sampling when K-R relation deviates from linearity due to increasing non lineal effects. The relative error due to sampling increase for longer links as the variability of rainfall increases. For high resolution sampling the relative error bias are in $[-8;8\%]$ interval for $[5-50\text{GHz}]$ and length $[1-10 \text{ km}]$. For averaged attenuation over 15 minutes $[10 ; -10\%]$ bias, and for intermittent 15 minutes sampling the bias is $[8;-8\%]$.
- When introducing a rough quantization step (1dB) the resulting biases are absorbed by the rounding effect and the differences of the biases for the different sampling strategies vanishes. The resulting biases are in $[-5; -5\%]$ interval.

Concerning the relative uncertainty due to the sampling strategy they highlight that:

- A higher RMSE (uncertainty) in the intermittent sampling strategy in the interval $[60-100\%]$ compared to the averaged and continuous strategy in the interval $[0-100\%]$
- The effect of the sampling in the intermittent strategy in the uncertainty remains for a rough quantization step.

In conclusion, the intermittent sampling strategy adds an important uncertainty in the data. The bias induced by the different strategies due to nonlinear effect on K-R relation are similar. That bias is masked by the bias induced by the quantization effect.

Attenuation value sampled

The min/max values of the attenuation give a proxy of the variability of the baseline and the rainfall over time which can be used as a proxy of the uncertainty due to temporal rainfall variability.

When the average rainfall over time is no available and only min/max values are, the estimation of average rainfall rates can be estimated with the extreme values using extreme value theory as showed in (Ostrometzky and Messer 2014; Ostrometzky and Messer 2018).

5.2.5 Other sources of errors

Temperature effect on electronics

The temperature variation can affect the electronics systems on the antennas recording the transmitted and received powers. The temperature effect on electronics is not well known and poorly described in the literature.

Considering mesoscale convective systems in West-Africa, the temperature drop when rainfall starts can be very fast and intense. The typical drop of temperature during a MCs can be [-10 ; -15 °C] in less than 15 minutes as shown in the example of figure 5-4. Such fast and extreme temperature drops can affect the signal in an unknown manner.

Antenna misalignment (wind)

The strong winds during intense rainfall events can impact the alignment of the radio link by moving the cellphone towers or the antennas. The expected effect of the wind in the attenuation is an increase of the noise in the baseline or a bias in the baseline if the misalignment of the antennas remains.

Multiple path

Another source of bias is the multiple path propagation of the MW signal. Multipath propagation can occur for different reasons.

For long CML anisotropic propagation of MW in the atmosphere due for example to a change in the gradient of the refraction index of the atmosphere with the altitude can cause a misalignment of the peak of the radiated power and thus a produce loss in the receiver.

The EM power is radiated from the antenna in many directions. The amount of power by direction is determined by the radiation pattern depending on the antenna type. The EM power radiated upper the CML can be redirected to the receiver antenna due to anisotropic propagation from higher layers of the atmosphere. In that case the received power increase reducing the attenuation. The power radiated below the CML line of sight can be reflected by the ground, especially in water or wet surfaces (for MW). In that case the reflected power can reach the receiver antenna increasing the received power and lowering the attenuation.

5.2.6 Conclusions

In this section we have reviewed the different sources of errors and uncertainties in the CML rainfall estimation. Table 5-3 summarizes the main characteristics and magnitudes of the different causes. The DSD parameterization chosen for the K-R law calculation can impact the rainfall retrieval by a 5-15% positive bias if we choose a climatological

Chapter 5: Rainfall measurement from microwave links: principle and sources of uncertainty

parameterization instead of the local fitted (Moumouni). The miss knowing of a possible polarization of the CML signal can also add positive or negative bias depending on the polarization. The effect increase with frequency. The DSD variability affect the estimation in two manners: the point scale variability, reflected by the K-R approximation can add a little bias and a great uncertainty for lower frequencies. The spatial (and temporal) DSD variability add uncertainty for links where K-R relation is non-linear. The effect is increased for longer links (and longer temporal sampling times).

The baseline detection algorithm can add bias (positive or negative) in the retrieved rainfall by creating false alarms or non-detections due to the noise in the signal, and by under or overestimating the rainfall induced attenuation.

When the sampling is intermittent, meaning no average during the sampling time, but instantaneous attenuation measurement, the uncertainty is high due to the noise at fine time scales.

Finally, other sources can affect the measurement, the wind can add noise for high temporal resolution measurements and multiple path propagation of the MW signals can add positive of negative biases.

Cause	Bias	Uncertainty
DSD parameterization	[5-15%] for R>20 mm/hr and [10-40GHz] MP compared to Moumouni with observed DSD in Benin	
Polarization	H Vs No Polar: -8% and -5% V Vs No Polar: +15% and +5% For 23GHz and 10 GHz resp. For ANDS99 ratio law and DSD in Benin	
DSD variability (K-R law approximation)	Residual bias due to log-log fit -3% for 23 GHz -8 for 13GHz	Greater for lower frequencies (decrease with path integration)

Chapter 5: Rainfall measurement from microwave links: principle and sources of uncertainty

DSD spatial variability	Larger for non-linear K-R rel.	Larger for longer links
Baseline	Can create False Alarms or Non detections due to noise signal ratio	
Quantization Step		High uncertainty for short and low frequency CML (100%)
Wet antenna	Huge positive bias (200%) for short links at low frequencies if not corrected	Uncertainty due to rainfall variability on the antennas
Temporal Sampling	Bigger for non-linear K-R rel. and rough temporal averages	
Sampling strategy		High uncertainty due to noise if intermittent sampling
Temperature on electronics	??	??
Wind		Can add noise for high temporal resolution measurements
Multiple path	Positive or negative due to anisotropic propagation and reflections	

Table 5-4: Summary of the different bias and uncertainties of the different causes

6 EVALUATION OF CML RAINFALL MEASUREMENTS IN NIAMEY

In the last chapter we have introduced the principle of rainfall measurement with CML and we have listed and quantified the possible sources of errors and uncertainties associated. In this chapter we address the evaluation of a CML dataset in Niamey for the 2016-2017 rainy seasons, to retrieve rainfall from attenuation measurements and quantify the remaining biases depending on the links characteristics. We evaluate three calibrations with a validation dataset composed by three rain gages.

6.1 Data

Orange has provided two complete rainy seasons (MJJASO) of CML data in Niger for the years 2016 and 2017. Figure 6-1 show the location of the 92 CML of the city of Niamey used in the study and the location of three rain gages. Figures 6-2 shows the availability of CML data per day in Niamey. Some days are missing in the dataset. For 2016, in a two-month period (July-August) only 10-20% of the CML were available.

The frequency of the CML in Niamey are 23 GHz and 18GHz (respectively 85 and 7 links). The distribution of the link lengths in the network is represented in Figure 6-2. The shortest link measuring 245m and the largest 5.44 km.

The data provided was the average, minimal and maximal transmitted power (Tx) and received power (Rx) at the time step of 15 minutes. The quantization step is 1dB.

We made a first data quality control based on the correlation of the time series of each CML with their neighbors (developed in the appendix 3).

Chapter 6: Evaluation of CML rainfall measurements in Niamey

The validation dataset is composed by 3 tipping bucket rain gages at 5 minutes' resolution resampled at 15 minutes, represented by blue dots in figure 6-1.

Figure 6-3 show the number of collocated samples (rain gage – CML) at 15 minutes' resolution by class of CML length.

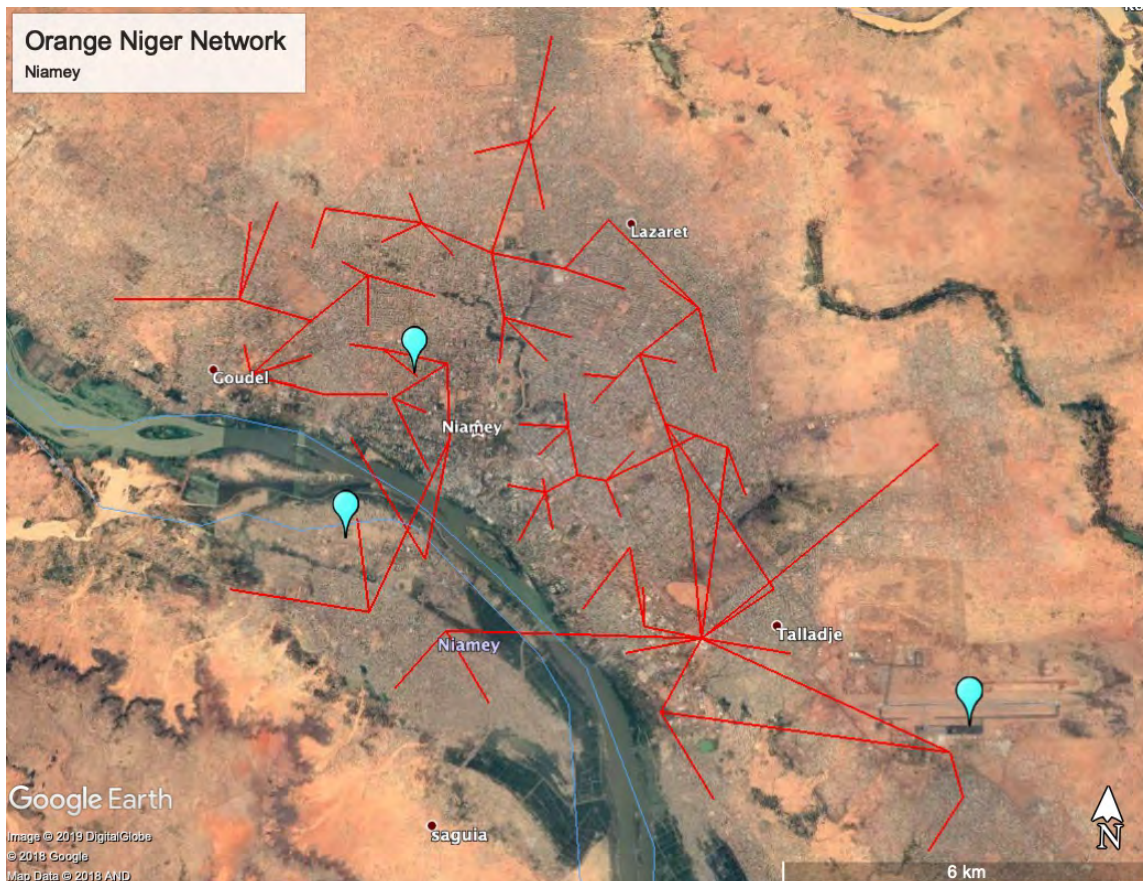


Figure 6-1: CML Orange network in Niamey. Blue dots represent the location of the AMMA-CATCH rain gages

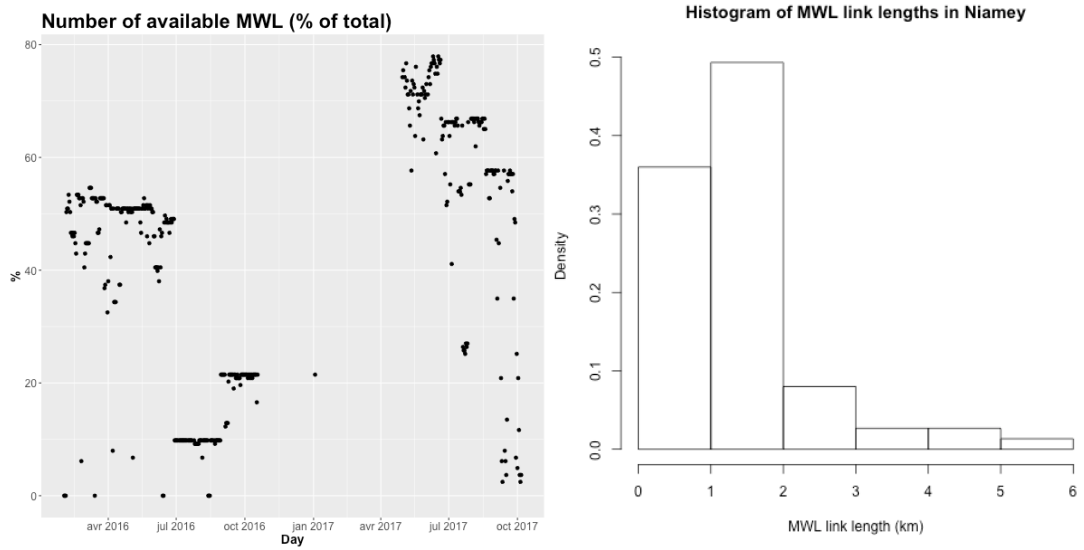


Figure 6-2: Available CML data per day for 2016-2017 seasons in Niamey and histogram of CML lengths in the Niamey Orange Network.

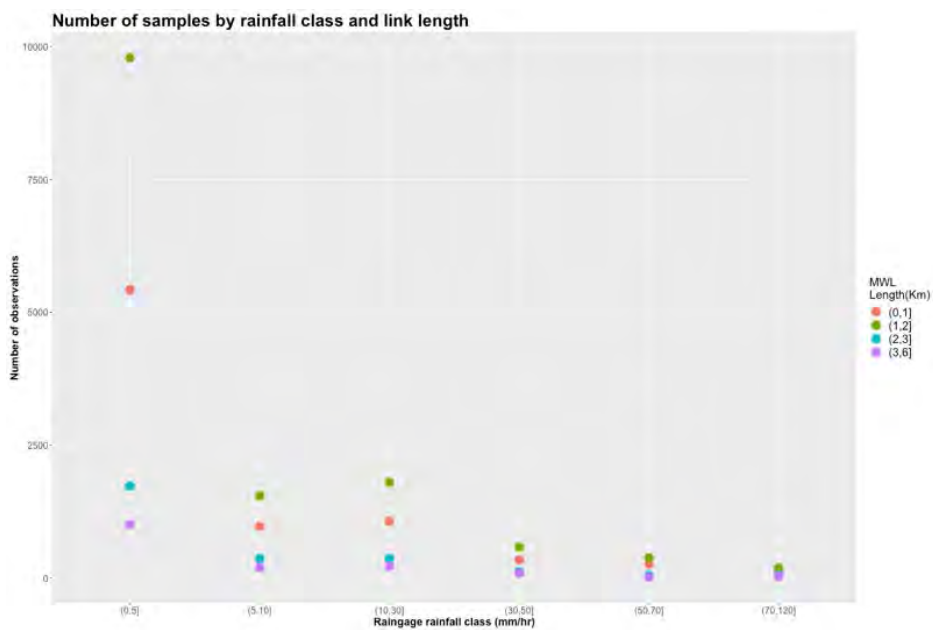


Figure 6-3: Number of collocated samples in the data set by link length and rainfall class.

6.2 Baseline detection

The raw attenuation levels of Orange CML in Niger do not show noise in the dry periods (due to the rough quantization step). The noise levels of the mean attenuation (and min/max) are lower than 1dB (quantization step). Figure 6-4 shows the observed raw attenuation (black line) for a CML of 23 GHz and 1.43 km length in Niamey for the event of 11/05/2017. We see a stable baseline attenuation in dry periods with some isolated jumps of 1dB (jump of -1dB before 2AM). The baseline attenuation is also stationary during the season. In that context of very stable and stationary baseline we decided to apply the simple threshold method presented in equation 5.10 in Chapter 5. The threshold a_0 is determined in a daily basis and calculated as the mode of the attenuation probability density function $p(A_{raw})$:

$$B = a_0 = mode(A_{raw}) \quad (eq. 6.1)$$

Where $mode(.)$ is the mode of the distribution of A_{raw} values.

We thus consider that the baseline is the more probable attenuation value for a day, as the attenuation is rounded to 1dB and the value is repeated. This value is calculated daily to prevent possible changes in the attenuation in dry periods during the rainy season due for example to a wrong alignment of the receiver and transmitter antennas caused by wind. The daily basis calculation can lead to erroneous estimation of the baseline for events lasting one day or more. But the rainy season in West Africa is dominated by MCS which locally last from 1 to 6 hours.

We add a minimal time span condition to prevent single jumps of 1dB. We considered only rainfall events lasting at minimum 30 min to prevent 1dB jumps due to noise.

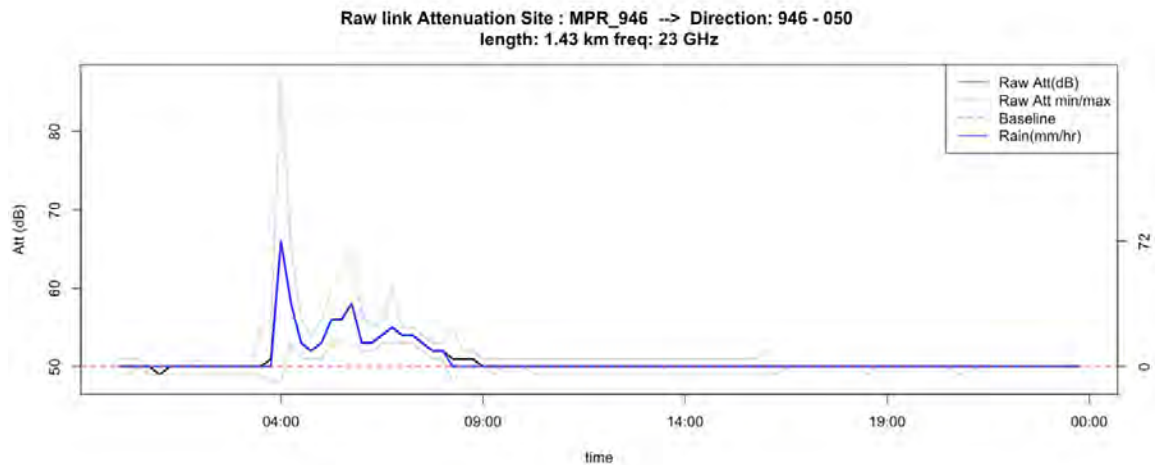


Figure 6-4: : Example of raw attenuation and baseline detection for 11/05/2017 event in Niamey for one CML. The link length is 1.43 km and frequency 23 GHz. The dotted red line shows the baseline detection for the day. The right Y axis represent the rainfall rate in [mm/hr]. The max and min attenuation are also show in light grey. The hyetogram of rainfall at 15 min in the CML has the classical signature of a convective front (peak at 70 mm/hr) followed by a stratiform trail.

6.3 Rainfall retrieval algorithm, calibration with evaluation against gauges

The objective of this section is to describe the calibration procedure of the CML to retrieve reliable rainfall accumulations and to quantify the remaining residual biases depending on the links characteristics. The calibration was done with the comparison of collocated CML and rain gages data at 15 minutes' time steps. Three different calibration where considered, described in the first section. The minimization procedure to retrieve the model parameters is described in section 6.3.1. Then are showed the residual biases depending on the links characteristics, followed by the robustness tests of the different calibrations.

Finally, we show the resulting scatterplots of the retrieved rainfall and the resulting daily accumulation biases for the 2016 and 2017 seasons in Niamey.

Following equation 5.2 of the last chapter we have:

$$A_{raw} = A_{rain} + B + A_{wa} + A_{other} \quad (eq. 5.2)$$

We have estimated the baseline B in the last section. If we consider $A_0 = A_{raw} - B$, and neglecting the other sources of attenuation ($A_{other}=0$) then we have:

$$A_0 = A_{rain} + A_{wa} \quad (eq. 6.2)$$

In order to estimate A_{rain} we should also estimate the wet antenna effect.

6.3.1 Minimizations

The measured attenuation corrected from baseline A_0 (eq. 6.2), can be expressed with the raingage measured rainfall R_g , the K-R law coefficients a, b (eq. 5.3), the link length L , and the wet antenna effect A_{wa} :

$$A_0 = A_{wa} + LaR_g^b \quad (eq. 6.3)$$

In the above equation we do not consider the rainfall spatial variability and consider R_g as a representative value of the average rainfall in the CML path. This statement is close from reality for short links and low CML-gage distances.

To calibrate the relation in eq 6.3 we consider three different minimizations with different choices for the parameters of the function f linking the observed attenuation and the rainfall rate:

$$f(R_g; a, b, A_{wa}) = A_{wa} + LaR_g^b \quad (eq. 6.4)$$

The minimizations are based on a non-linear least squares regression, equivalent to minimizing the sum of the squares differences between observations A_0^i and model $f(R_g)$

$$S(a, b, A_{wa}) = \sum_{i=1}^N [A_0^i - f(R_g^i; a, b, A_{wa})]^2 \quad (eq. 6.5)$$

The index i correspond to the each raingage/CML observation. The different calibrations are defined depending on the different choices for the parameters a, b, A_{wa} .

The minimization in eq 6.5 concerns the variable A_0 instead of the rainfall rate R : minimizing R can lead to negative values powered by $1/b$ leading to errors. To avoid the

errors we can filter the dataset for each value of explored A_{wa} resulting in a different dataset for each calculation of $S(a, b, A_{wa})$. This lead to a non-continuous resulting function $S(a, b, A_{wa})$. To avoid the issue we decided to minimize the attenuation as $R_g > 0$, the quantity R_g^b can be always calculated.

Calibration 1

In the first calibration we seek the optimal a, b coefficients of the K-R law and a constant value of wet antenna attenuation $A_{wa} = Cte$ which best explain the observed data. We aim to find the minima RMSE in a three parameters space $[a, b, A_{wa}]$. The solution $[a^{fit}, b^{fit}, A_{wa}^{fit}]$ verify:

$$S(a^{fit}, b^{fit}, A_{wa}^{fit}) = \min[S(a, b, A_{wa})] \quad (eq. 6.6)$$

Calibration 2:

In the second calibration we consider only a two parameter regression, the constant wet antenna attenuation: $A_{wa} = Cte$ and the a parameter of the K-R law. We consider a fixed b^{th} coefficients of the K-R law corresponding to the obtained from the T-matrix calculation with the observed DSD in Benin presented in chapter 5.

$$S(a^{fit2}, A_{wa}^{fit2}) = \sum_{i=1}^N [A_0^i - f(R_g^i; a^{fit2}, b^{th}, A_{wa}^{fit2})]^2 \quad (eq. 6.7)$$

Calibration 3:

In the third calibration we consider a wet antenna attenuation depending on the rainfall rate (Chap 5, section 4.1.5). We used the parameterization of the water layer covering the antenna developed by (Leijnse, Uijlenhoet, and Stricker 2008) considering the proposed parameters and a temperature of 20°C for the calculation of the refractive index of water.

By addition we consider a possible proportional variation of this parameterization due to the possible different characteristic on the antenna. We considered:

$$A_{wa}(R_g) = g * A_{wa}^L(R_g) \quad (eq. 6.8)$$

Where A_{wa}^L is the wet antenna model developed in (Leijnse, Uijlenhoet, and Stricker 2008) and a parameter g to fit to the data. We consider the theoretical $[a^{th}, b^{th}]$ found with the observed DSD in Benin and T-matrix calculation. Calibration 3 is a one parameter minimization (parameter g in eq. 6.9) :

$$S(g) = \sum_{i=1}^N [A_0^i - f(R_g; a^{th}, b^{th}, g * A_{wa}^L)]^2 \quad (eq. 6.9)$$

Calib 3bis:

The calibration 3 is a one parameter minimization. The parameter g to fit to the data, is a multiplicative parameter of the wet antenna model A_{wa}^L , of [Leijnse et al. 2008]. As the wet antenna attenuation $A_{wa}^L(R)$ depends on the rainfall rate, we need R to calculate it.

In calib. 3 we use the raingage rainfall to estimate $A_{wa}^L(R_g)$. In calibration 3bis we do not use the raingage rainfall. For each time step we solve the equation presented in (eq. 6.10).

6.3.2 Minimization procedure

The non-linear least squares minimization was done with a build-in function in R using the Gauss-Newton algorithm. The different parameters were estimated for both 18GHz and 23GHz datasets. Figure 6-5 shows the optimum parameters (green dot) found in the parameters space for the calibration 1 at 23 GHz. The RMSE (minimization criteria) and the global bias are shown. The black crosses in the figure show the location in the parameters space where no bias is found (bias<0.1 mm/hr). The retrieved values are

$a^{fit} = 0.256$; $b^{fit} = 0.862$; $A_{wa}^{fit} = 1.73 \text{ dB}$. The bias is calculated over the attenuations A_0 (eq. 6.3). A negative attenuation corrected from wet antenna lead to a 0 mm/hr rainfall. Thus a 0 bias in the attenuation lead to a positive bias in the rainfall retrieval (as no negative rainfall can be retrieved).

We did a first minimization with the whole dataset and a second minimization with a filtered dataset above 10 mm/h (raingage R_g) to better fit the high rainfall rates. Low rainfall rates are noisier due to the wet antenna effect and the rough quantization step of 1 dB specially for short CML.

Appendix 4 show the RMSE maps for calibration 1 and 2, frequencies 18GH and 23 GHz and the filtered at 10mm/h and non-filtered dataset.

Table 6-1 report the retrieved values for each calibration, frequency and filtering. Green values in the table report theoretical values (not fitted).

The fitted values correspond to the optimal values for the global dataset. However, biases can arise depending on the different characteristics of the links, length, the rainfall class, or the distance to the compared rain gage. In the next section we analyze the resulting biases of each calibration.

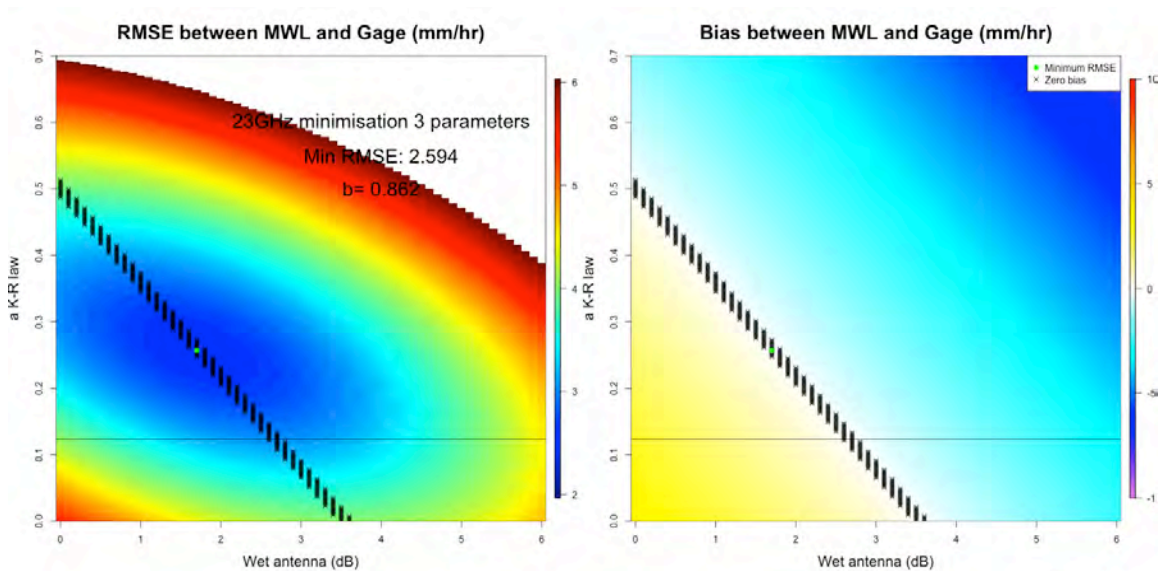


Figure 6-5: Example attenuation minimization for calibration 1 (not filtered) 23GHz in the a-WA space for b=0.862 (minima). Left figure show the attenuation RMSE and right figure the bias.

	Cal 1	Cal 2	Cal 3	Cal. 1 >10mm/h	Cal. 2 >10mm/h	Cal. 3 >10mm/h
a- 23GHz	0.256	0.128	0.123	0.056	0.109	0.123
b- 23GHz	0.862	1.028	1.028	1.178	1.028	1.028
Wet Ant. 23 GHz (dB)	1.73	2.05	$0.36 * A_{wa}^L$	3.92	3.40	$0.32 * A_{wa}^L$
RMSE (dB) 23GHz	2.594	2.613	2.577	4.273	4.283	4.331
Nobs 23GHz	23318	23318	23318	4962	4962	4962
a- 18GHz	0.052	0.064	0.072	0.005	0.056	0.072
b- 18GHz	1.103	1.052	1.052	1.581	1.052	1.052
Wet Ant. 18 GHz (dB)	2.03	1.94	$0.31 * A_{wa}^L$	5.17	3.39	$0.21 * A_{wa}^L$
RMSE (dB) 18GHz	3.059	3.061	3.129	5.401	5.580	5.786
Nobs 18GHz	3372	3372	3372	721	721	721

Table 6-1: Parameters fitted to the observed attenuation for the three calibrations, filtered above 10mm/hr and not filtered. The minimal RMSE on attenuation and the

number of observations are reported. The green values correspond to theoretical a prior values (not fitted).

6.3.3 Residual bias of the calibrations

A global minimum RMSE and zero bias in the fitted optimal attenuations of the three calibrations leads to non-zero bias in the retrieved rainfall due to the positive condition of the retrieved rainfall. Also compensations can occur between the different CML lengths and rainfall rates. Figures 6-6 show the average bias by calibration depicted by the raingage rainfall class and CML length. The three bottom figures correspond to the three calibrations with a fitting dataset filtered above 10 mm/h (to best fit high rain rates). The biases are calculated for the entire dataset including $R < 10$ mm/h. The horizontal black line represents the global bias.

We observe that the average biases are high for short links and increase with rainfall rate class. The calibration 3 (considering a wet antenna depending on the rainfall rate) correct some of the bias of short links compromising long links (underestimation). The fitted calibrations filtering the small rainfalls decrease the biases in high rainfall but also globally in small rainfall rates. That is due to higher values of retrieved wet antenna attenuation for filtered datasets: the higher values of retrieved wet antenna attenuation (table 6-1) lead to lower bias on small rainfall due to the increasing cases where the corrected attenuation become negative and thus a zero rainfall is retrieved. The squeeze of the small rainfall lead to a global bias closer to zero, as the relative weight in the dataset of small rainfalls is higher.

Figure 6-7 present the relative biases in % of the raingage rainfall rate average (per rainfall class). The horizontal black lines show the remaining relative global bias. For calibration 3 the relative bias of small rainfall is high compared to the other calibrations.

Figure 6-8 present the bias decomposition in non-detection bias and hit bias per rainfall class. In the original dataset only hits are used. Due to the wet antenna correction some attenuations become negative leading to zero rainfall introducing non-detection biases. As said before, the retrieved wet antenna attenuation for filtered dataset are greater, increasing the non-detection bias for calibrations 1 and 2. The calibration 3 considering a

rainfall dependent wet antenna attenuation show a lower non detection bias and a lower hit bias.

Calibration 1 is a three parameters fit and calibration 2 a two parameters fit. The overall RMSE on attenuation is lower for calibration 1 as expected, as it includes one more parameter. However the difference in the minimal RMSE for calibration 1 and 2 is very low (table 6-1: 2.59 dB for calibration 1 and 2.61dB for calibration 2). The coefficients $[a, b]$ of the K-R law can compensate each other resulting in similar results in term of global RMSE. But the resulting biases for the calibration 2 in rainfall depicted by rain rate and CML length show a better agreement to the raingage observations.

The results show the effect of fitting the parameters for high rainfall rates ($>10\text{mm/h}$) due to the noise in small rainfall: the overall bias decrease, high rainfall rates show lower bias for all CML length, but the small rainfalls are squeezed by introducing a higher wet antenna attenuation. Calibration 3 is less impacted by the filtering of the data set, the retrieved g parameters are relatively close for filtered and non filtered, and the biases are similarly distributed.

In the next section we test the robustness of the different fitting calibrations showing a strong dependence on the dataset for calibration 1.

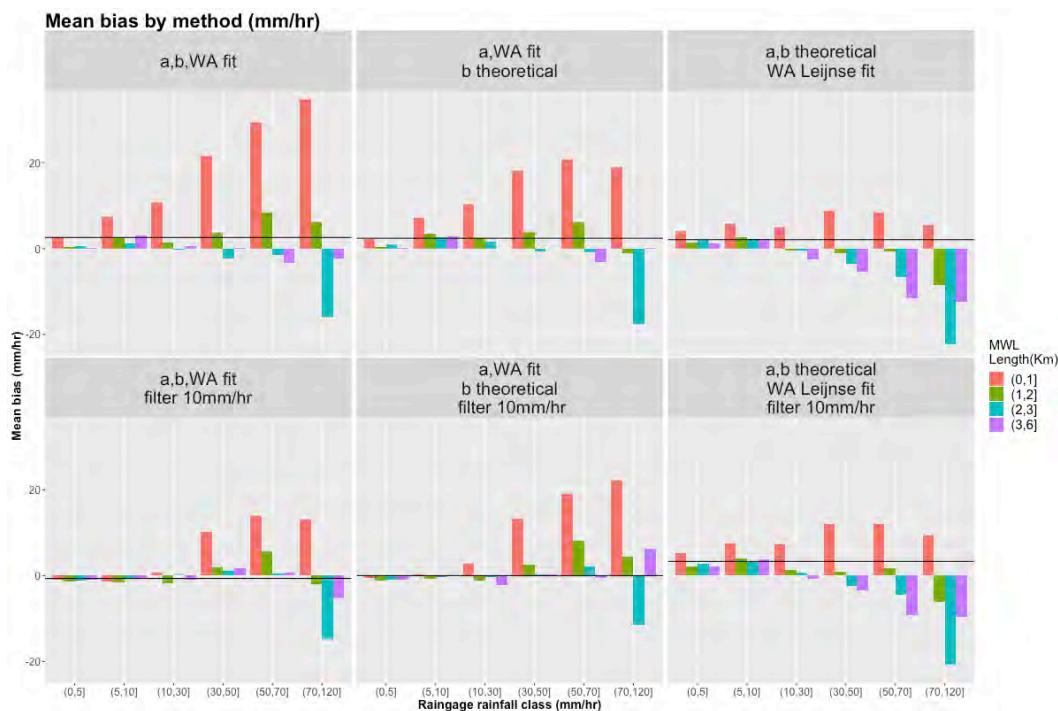


Figure 6-6: Average bias by calibration depicted by rainfall rate and CML length class.

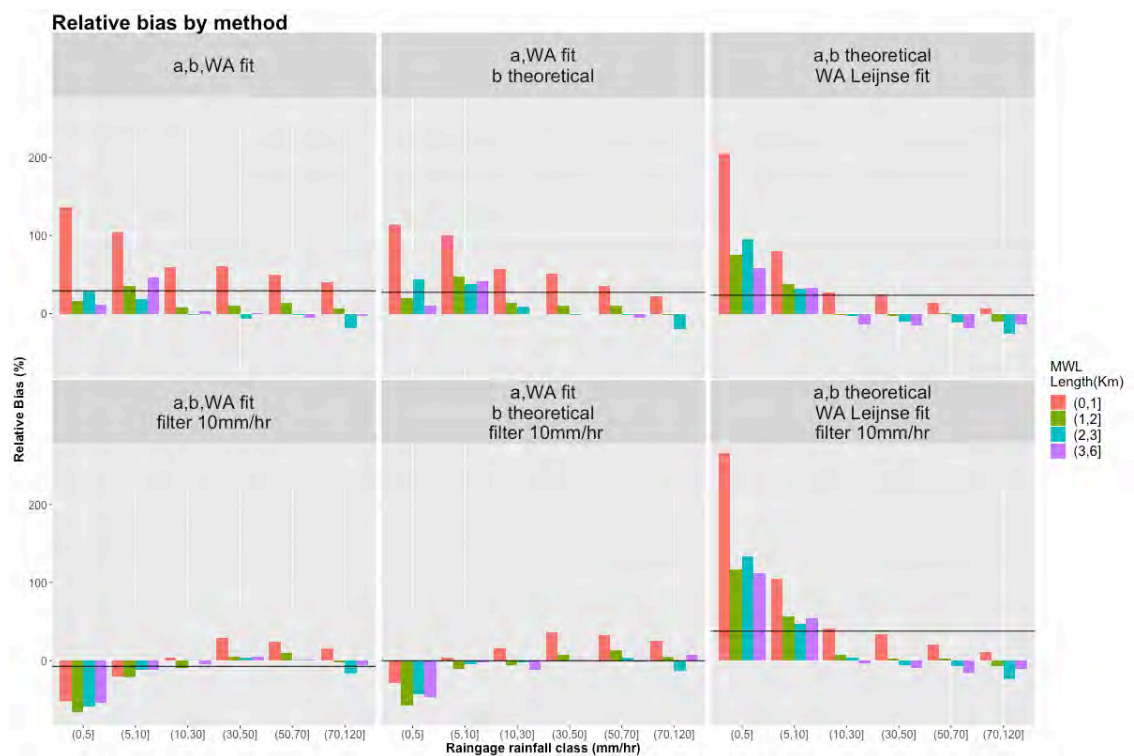


Figure 6-7: Relaitve bias by calibration depicted by rainfall rate and CML length class.



Figure 6-8: Bias decomposition by calibration depicted by rainfall rate.

6.3.4 Calibrations evaluation

Robustness of minimizations

To test the robustness of the parameters fit of the three calibrations we sampled randomly half of the dataset for $N=1000$ iterations and retrieve the parameters (bootstrapping) to test their dependence to the dataset. Figure 6.9 and 6-10 show the scatterplots of retrieved a^L, b^L (for calibration 1) parameters for 18GHz and 23 GHz, filtered above 10mm/hr and not filtered. We show also the histogram of the retrieved wet antenna parameter. We see that the 18 GHz a^L, b^L values have a wider range of variation than the 23 GHz due to the smaller volume of the 18 GHz dataset, which is more evident in the histograms of retrieved wet antenna attenuation. The red dots show the location of the 100% dataset retrieval and the green dot the location of the theoretical a, b . The fits of calibration 1 are very sensitive to the dataset showing low robustness.

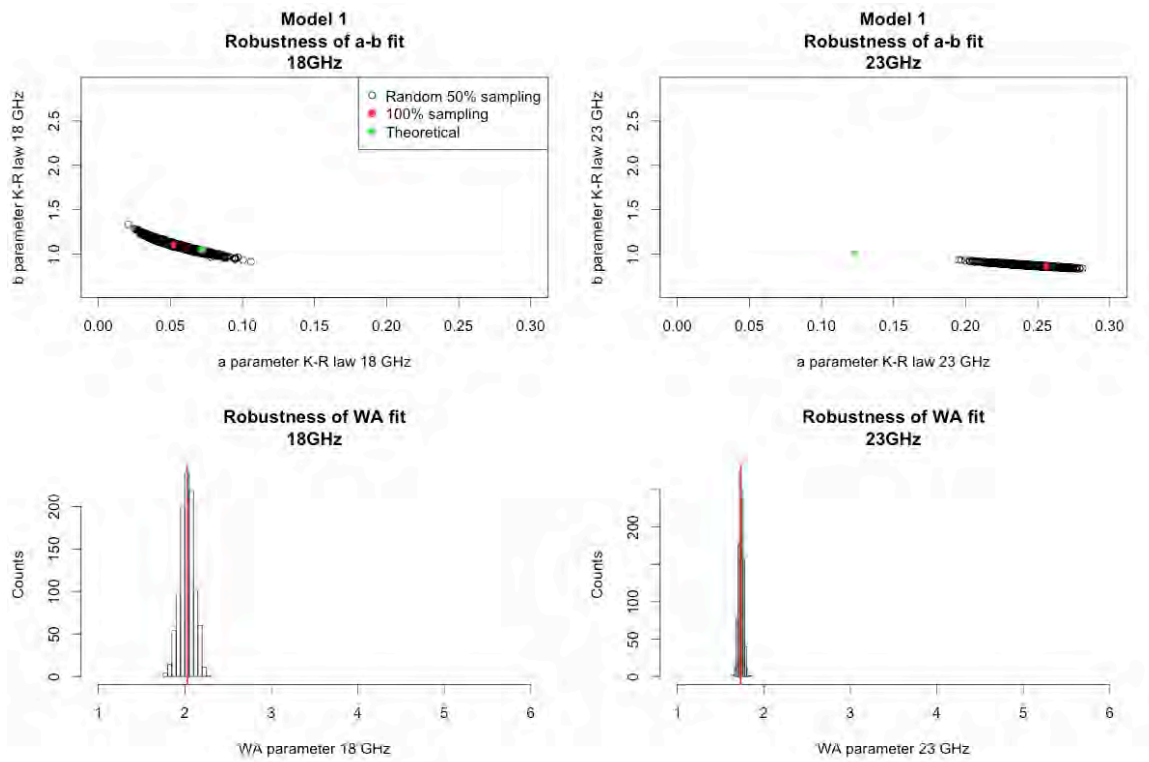


Figure 6-9: Bootstrapping of calibration 1 (not filtered). Left column correspond to 18 GHz dataset. Right column to 23GHz. The top scatterplots are the realizations in the [a-b] space. Bottom histograms are the realizations of WA fit.

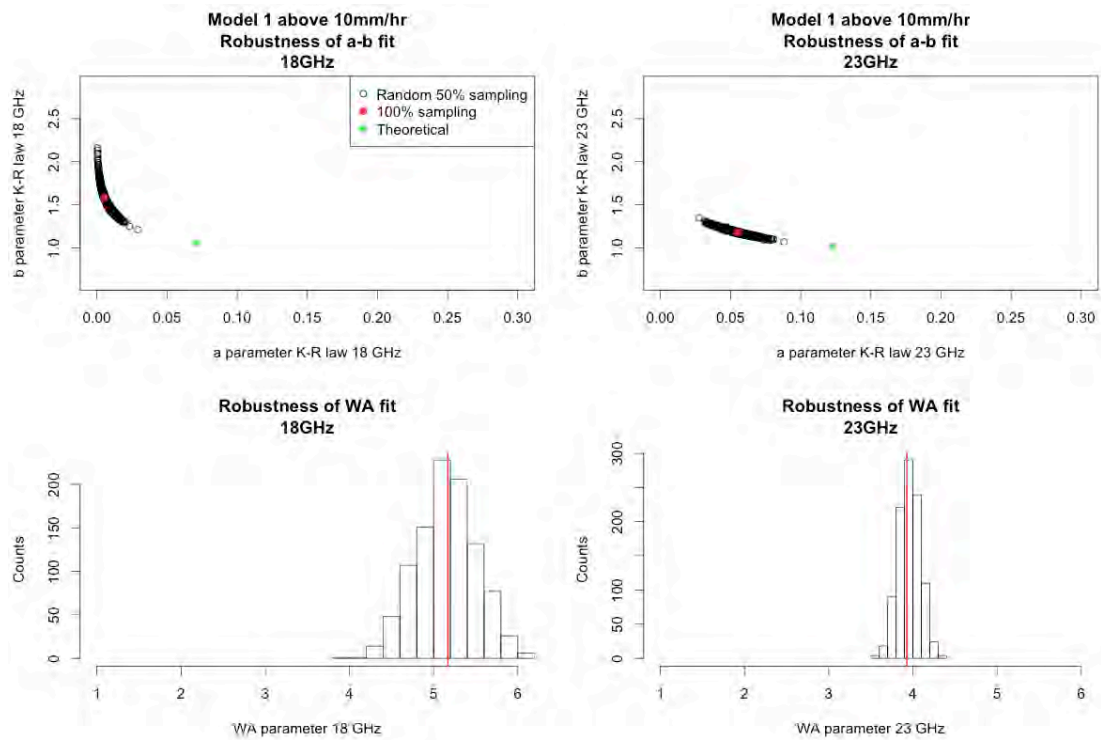


Figure 6-10: Bootstrapping of calibration 1 ($R>10\text{mm/h}$). Left column correspond to 18 GHz dataset. Right column to 23GHz. The top scatterplots are the realizations in the [a-b] space. Bottom histograms are the realizations of WA fit.

Figure 6-11 and 6-12 show the same fitting procedure for 1000 resampling of the dataset for the calibration 2. Black dots on the scatterplot represent each iteration of the minimization in the wet antenna and a coefficient parameter space. We observe a lesser spread of a parameter in calibration 2 compared to calibration 1 due to the fixed value of b : in calibration 1 the compensation of a and b made the fit more sensitive to the dataset, as a range of values become equivalent in terms of minimal RMSE. Also the wet antenna attenuation has a narrower spread. The difference in spread between 18 GHz and 23GHz are due to the lesser number of observations for 18GHz (as seen for calibration 1). The vertical green line shows the theoretical a^{th} which falls into the dots cloud.

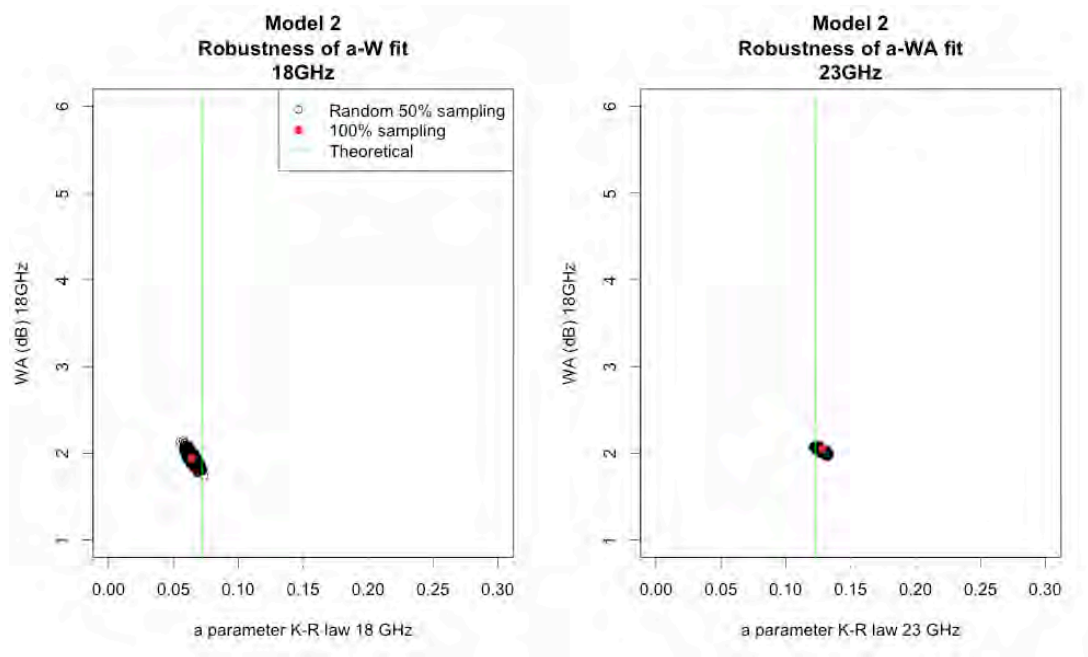


Figure 6-11: Bootstrapping of calibration 2 (not filtered). Left column correspond to 18 GHz dataset. Right column to 23GHz. The scatterplots are the realizations in the [a-WA] space.

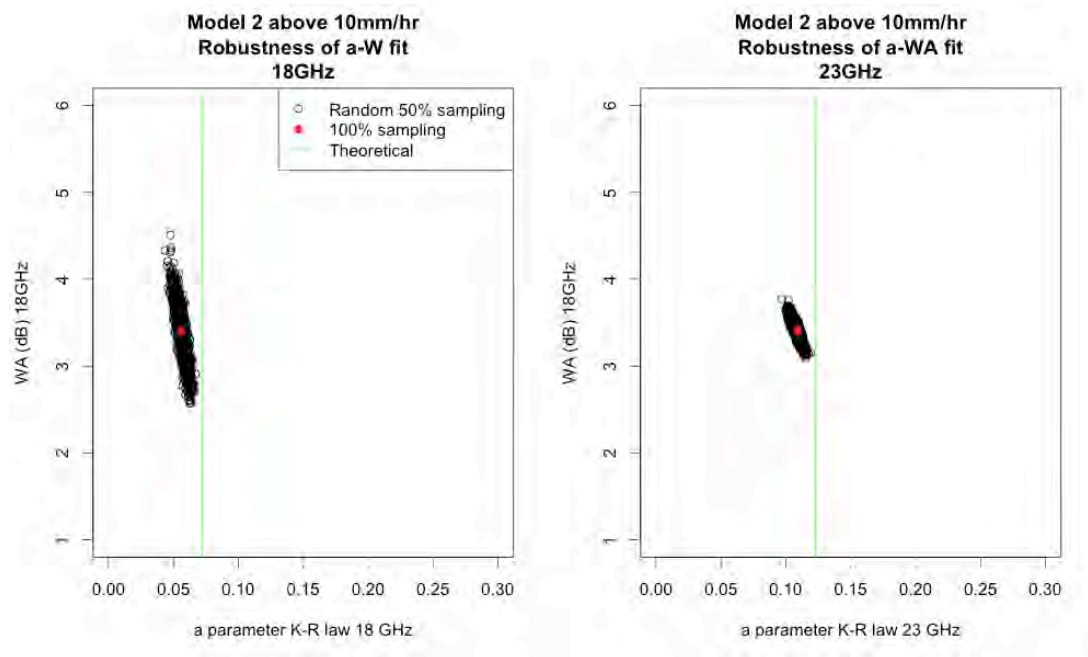


Figure 6-12: Bootstrapping of calibration 2 (filtered). Left column correspond to 18 GHz dataset. Right column to 23GHz. The scatterplots are the realizations in the [a-WA] space.

Figures 6-13 and 6-14 show the histogram of retrieved g parameter for the bootstrapping of calibration 3. The distribution of g fitted for filtered 18GHz has a wide spread and a lower value of g around 0.2. The other histograms for 23GHz and filter/non-filter data set show similar values of g around 0.3-0.35

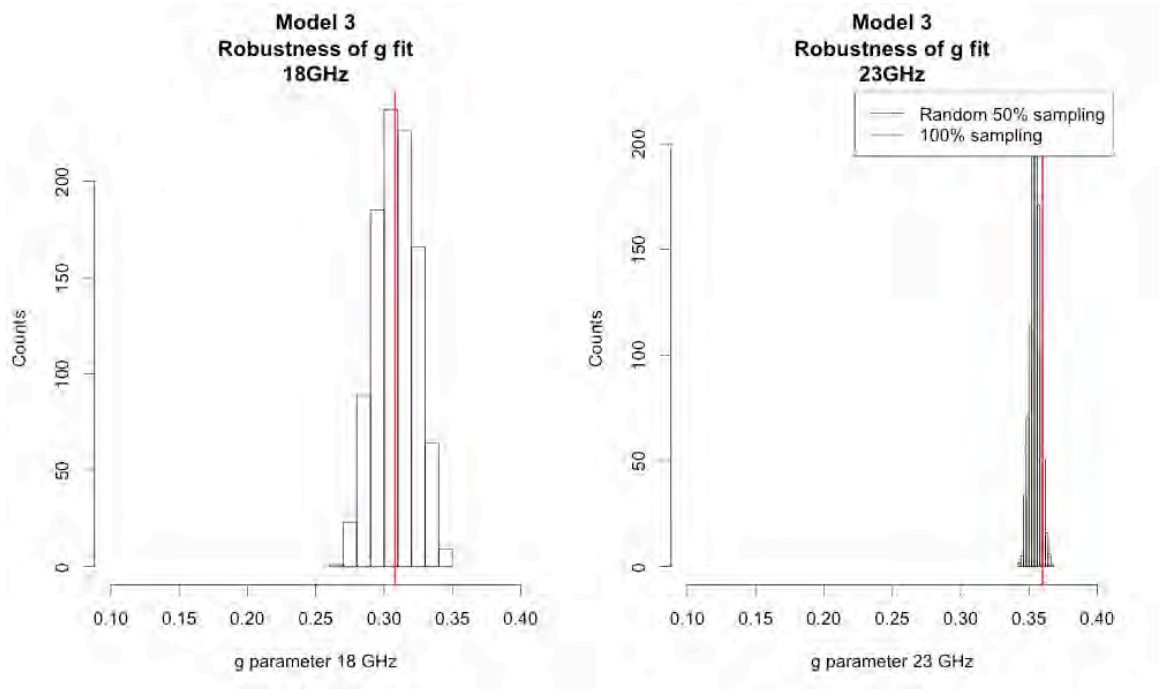


Figure 6-13: Bootstrapping of calibration 3 (not filtered). Left column correspond to 18 GHz dataset. Right column to 23GHz. The histograms are the realizations of the g parameter fitting.

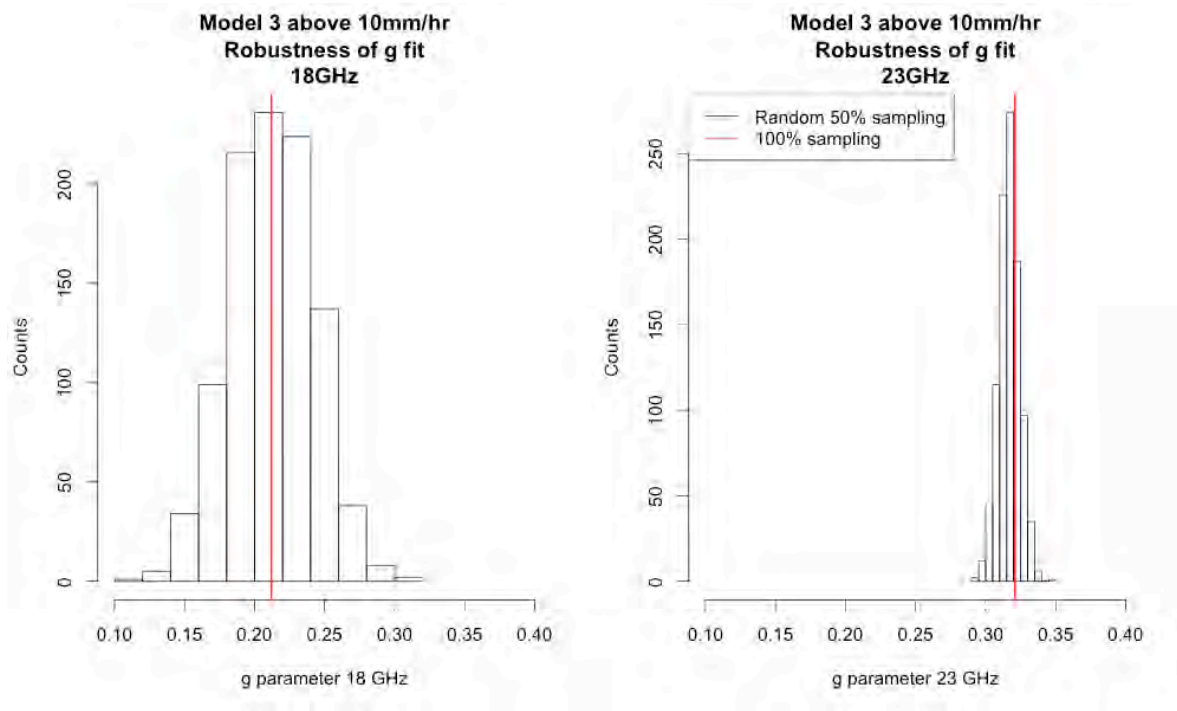


Figure 6-14: Bootstrapping of calibration 3 (filtered). Left column correspond to 18 GHz dataset. Right column to 23GHz. The histograms are the realizations of the g parameter fitting.

We can conclude from the robustness tests that the calibration 2 and calibration 3 fitting procedure are more robust than the calibration 1 due to the compensation of the effect of the parameter a and b in the K-R law. The effect of filtering has an impact on the estimation of the wet antenna attenuation increasing it. When considering a wet antenna attenuation depending on the rainfall rate, the filtering has a lesser impact indicating that the calibration 3 is best suited to correct the attenuation observed by microwave links. Also the residual biases of calibration 3 showed in figure 6-6 to 6-8 shows its ability to correct the overestimation of high rainfall rates for small links, which are relatively more impacted by wet antenna attenuation.

The high values of wet antenna attenuation when filtering the datasets at 10mm/h (for calibration 1 and calibration 2 suggest a rainfall dependency of the wet antenna effect).

The calculation of the wet antenna effect (eq 6.8) for calibration 3 was done using raingage rainfall observations. In an operational situation where only CML observations are available we should estimate the wet antenna attenuation with the observed attenuation.

In the next section we address the impact of using calibration 3 with only the available attenuation (not the observed rainfall by the raingage).

Calibration 3bis calculation of wet antenna with observed attenuation

Considering no rain gage observation of rainfall, the rainfall retrieval from observed CML attenuation needs to solve in R the following equation for each observation:

$$A_0 - 2gA_{wa}^L(R) - La^{th}R^{b^{th}} = 0 \quad (eq. 6.10)$$

Where A_0 is the observed attenuation, A_{wa}^L is the wet antenna effect depending on rainfall as described in (Leijnse et al 2008), L the link length, g the retrieved parameter and $[a^{th}, b^{th}]$ the theoretical parameters of K-R law. The equation 6.10 does not have an analytical solution. The solution is found by finding the zero of the left hand side of the 6.10 equation in a given interval (the numerical solution is found using a common R function at a precision of 10^{-4}).

Figure 6-15 show the relative biases of calibration 3 rainfall retrieval solving equation 6.10 (fitted with filtered rainfall) for each couple observation. The retrieved rainfall without using the raingage rainfall show higher biases than those retrieved using raingage observations. Using only the observed attenuation add a bias on the results compared to the wet antenna attenuation estimated with the ground rainfall. The black line in figure 6-15 showing the global bias is higher than 50%. That indicates an underestimation of the g parameter.

To better estimate a correct value of g we calculated the global bias of the resulting rainfall solving equation 6.10 for each observation for different g in the range $[0.3,1]$ by steps of 0.05.

We found the optimal $g = 0.65$ reducing the global bias close to zero. Figure 6-16 show the relative bias by rainfall class and by CML link length in the same scale than figure 6-15. We still observe a dependence on the CML link length for the high rainrates but the bias is much lower compared to the figure 6-15.

The solution $g = 1$ correspond to the [Leijnse et al 2008] work, which lead to a global bias of -35% for our data. A possible solution for future work is to find the parameters in the calibration of [Leijnse et al 2008] which best describe the observed dataset. The parameters are the refractive index of the antenna cover material, its thickness, and the temperature for the calculation of the refractive index of water.

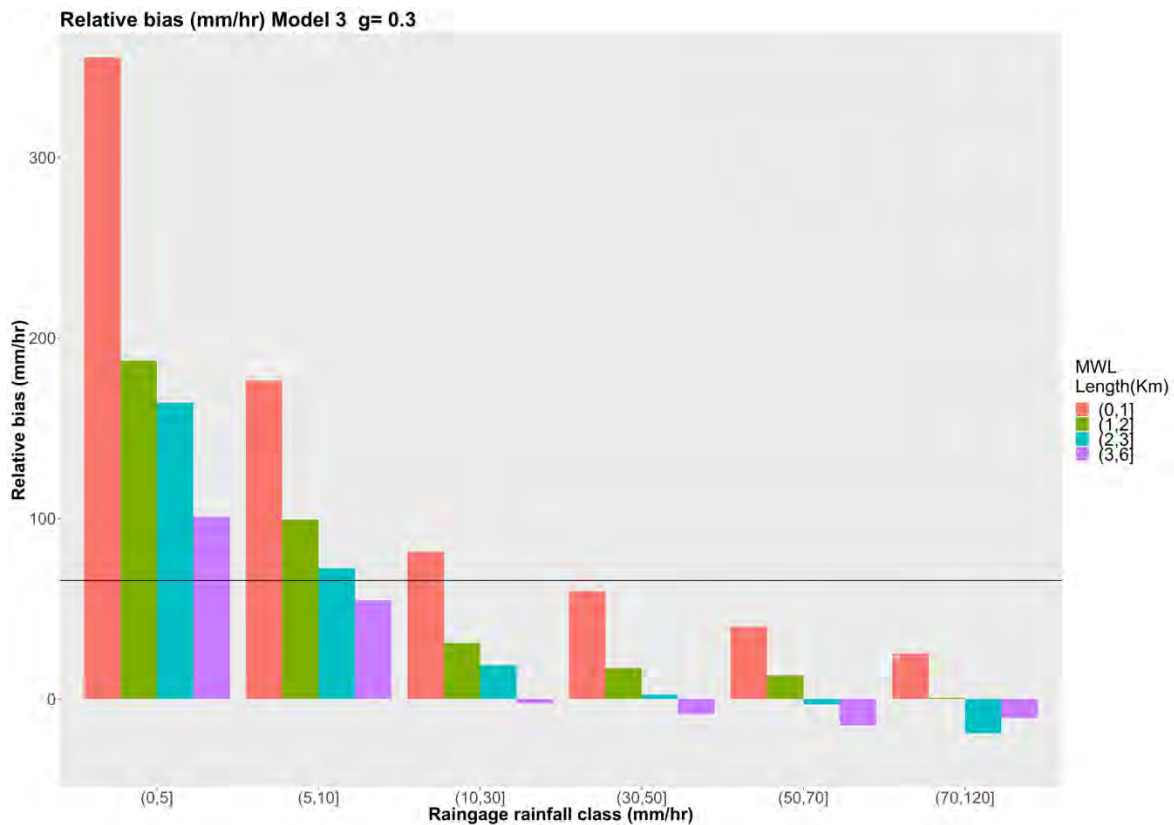


Figure 6-15: Relative bias of rainfall for calibration 3 depicted by rainfall class and CML length with wet antenna attenuation calculated with the attenuation only (eq. 6.10) for the $g=0.3$ parameter found in the minimization in section 6.3.2.

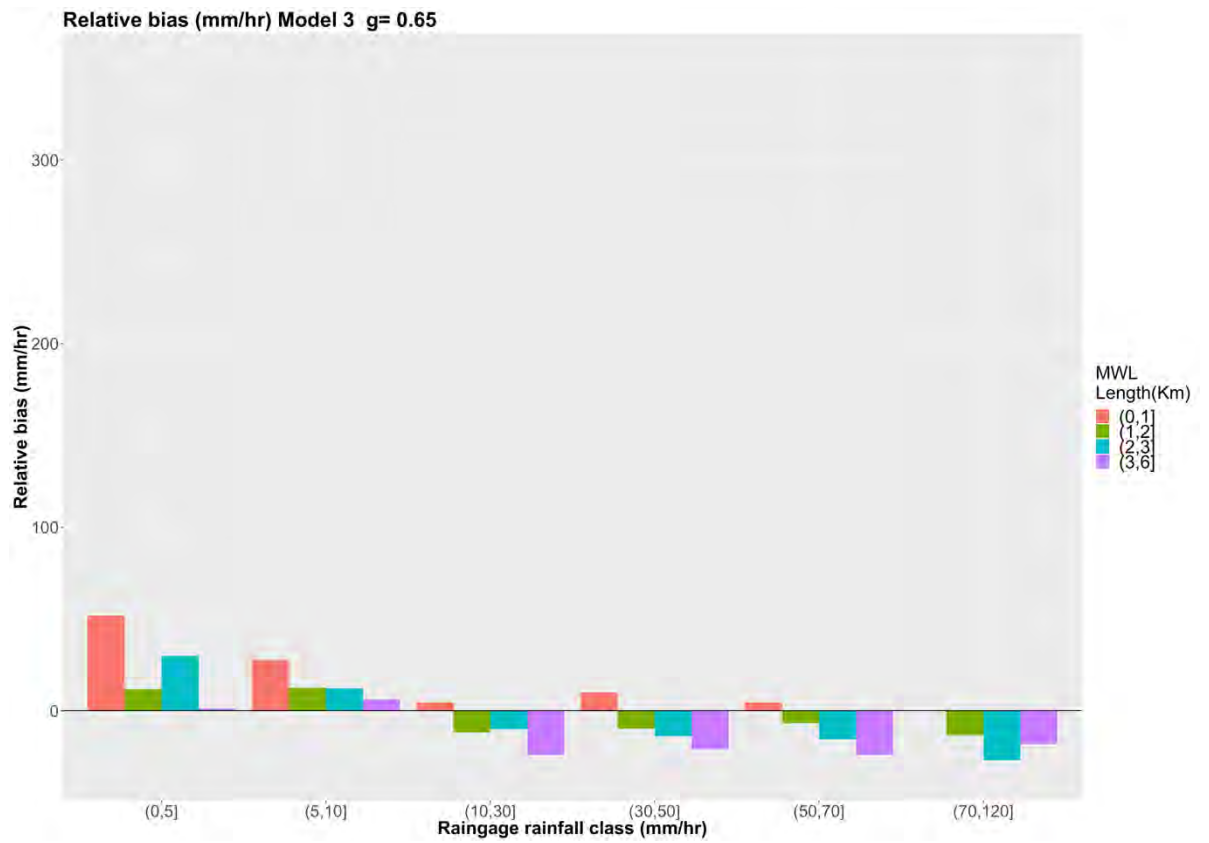


Figure 6-16: Relative bias of rainfall for calibration 3 depicted by rainfall class and CML length with wet antenna attenuation calculated with the attenuation only (eq. 6.10) for the $g=0.65$ parameter found in the new minimization of rainfall (section 6.3.2).

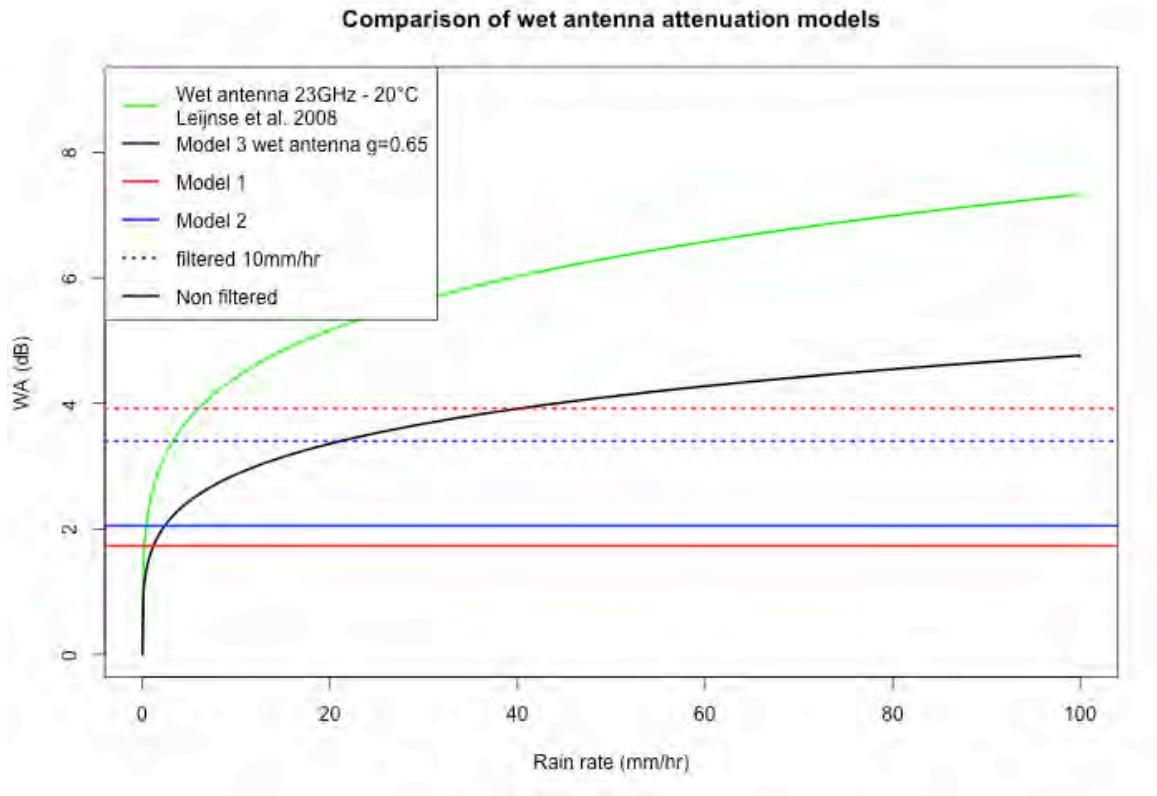


Figure 6-17: : Comparison of the different calibrations of wet antenna attenuation (for both antennas)

Figure 6-17 show the resulting wet antenna attenuation calibrations fitted to the data in the calibration. The red lines shows the constant value for calibration 1, the blue line the constant value for calibration 2. Dashed lines show the fitted values for the filtered datasets. Green line is the wet antenna calculated using the calibration in [Leijnse et al. 2008] and the black line the retrieved calibration ($g = 0.65$). The filtered dataset shows higher values of the wet antenna suggesting the dependency to rainfall of the wet antenna attenuation. We observe also that the original wet antenna calibration of [Leijnse et al. 2008] does not falls into the optimal parameters found.

In the next section we show the resulting scatterplot at 15 minutes colocalisations.

6.3.5 Resulting 15 minutes' gauge-links scatterplots

Figure 6-18 show the resulting scatterplot of the observed attenuations corrected from the wet antenna effect using the fitted parameters of calibration 2 (filtered) versus the observed raingage rainfall. Each plot corresponds to a single CML (only 16 are showed), the frequency, link length and distance to gage are reported in each figure. The red line show the theoretical K-R law derived from disdrometer data. We can notice the high spread for low rainfall rates and short CML (for example for link 8-7). The spread is also more important for links far from the raingage due to the spatial variability of rainfall (link 7-galerie wazir). The theoretical K-R law is adapted to the observed data. Long links close to rain gages show good agreement (link 33-21 or 33-22).

Figures 6-19 to 6-21 show the global scatterplots of retrieved CML rainfall versus raingage rainfall for different CML length classes for the 3 calibrations (filtered at 10mm/hr). The 18 GHz and 23 GHz are mixed. We notice a higher spread for short links due to the relatively higher uncertainty caused by the wet antenna correction and the rough quantization step (Chapter 5). The uncertainty become lower for longer links. Also we notice a residual bias effect on the link length: short links overestimates compared to long links.

An investigation of the CML-gage comparison depending on the CML length with simulations over radar fields is presented in appendix 5. The different sampling of CML and gages may explain some of the observed differences.

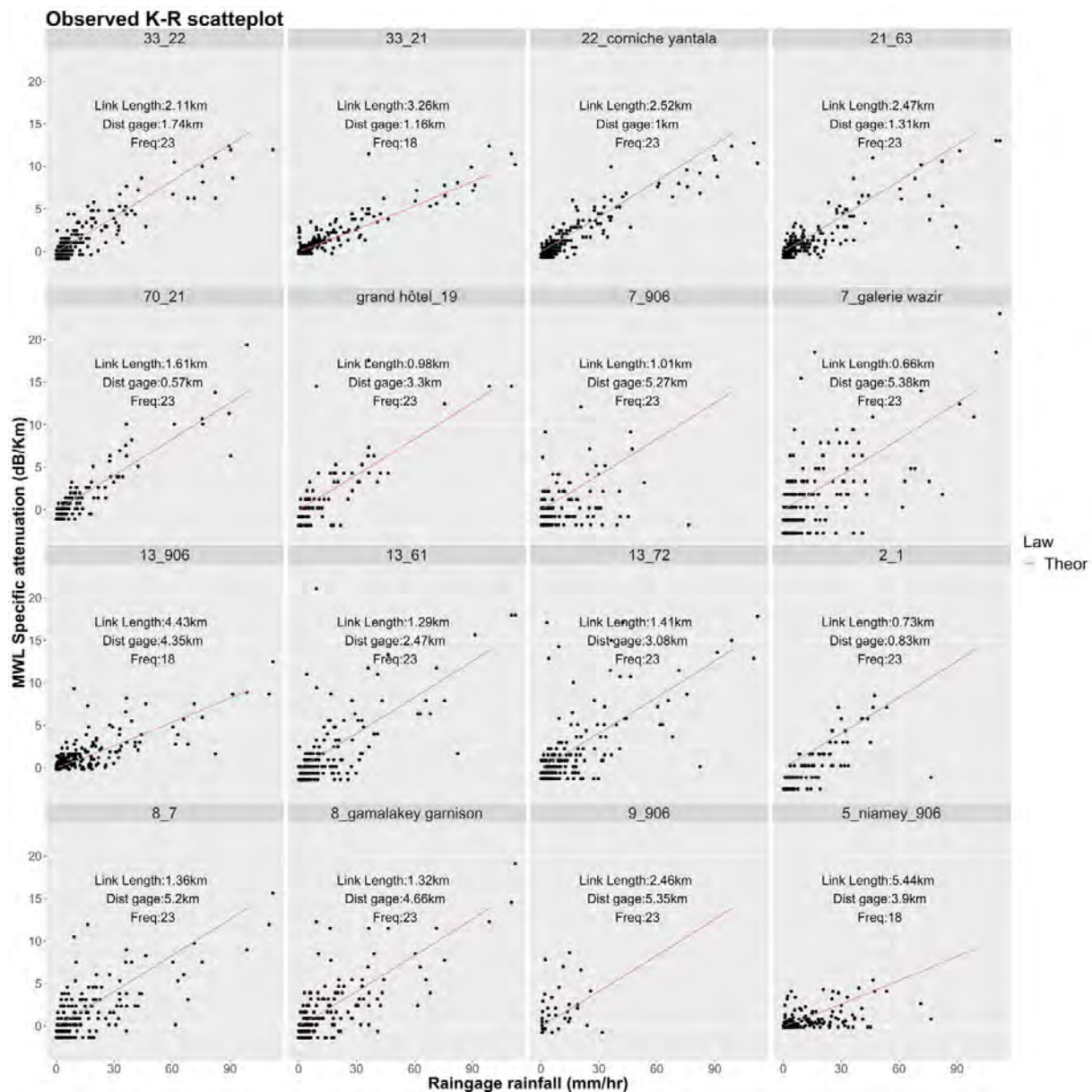


Figure 6-18: Scatterplots of specific attenuation K of CML after wet antenna correction versus rain gage rainfall for calibration 2 (filtered). The red line shows the K-R theoretical law.

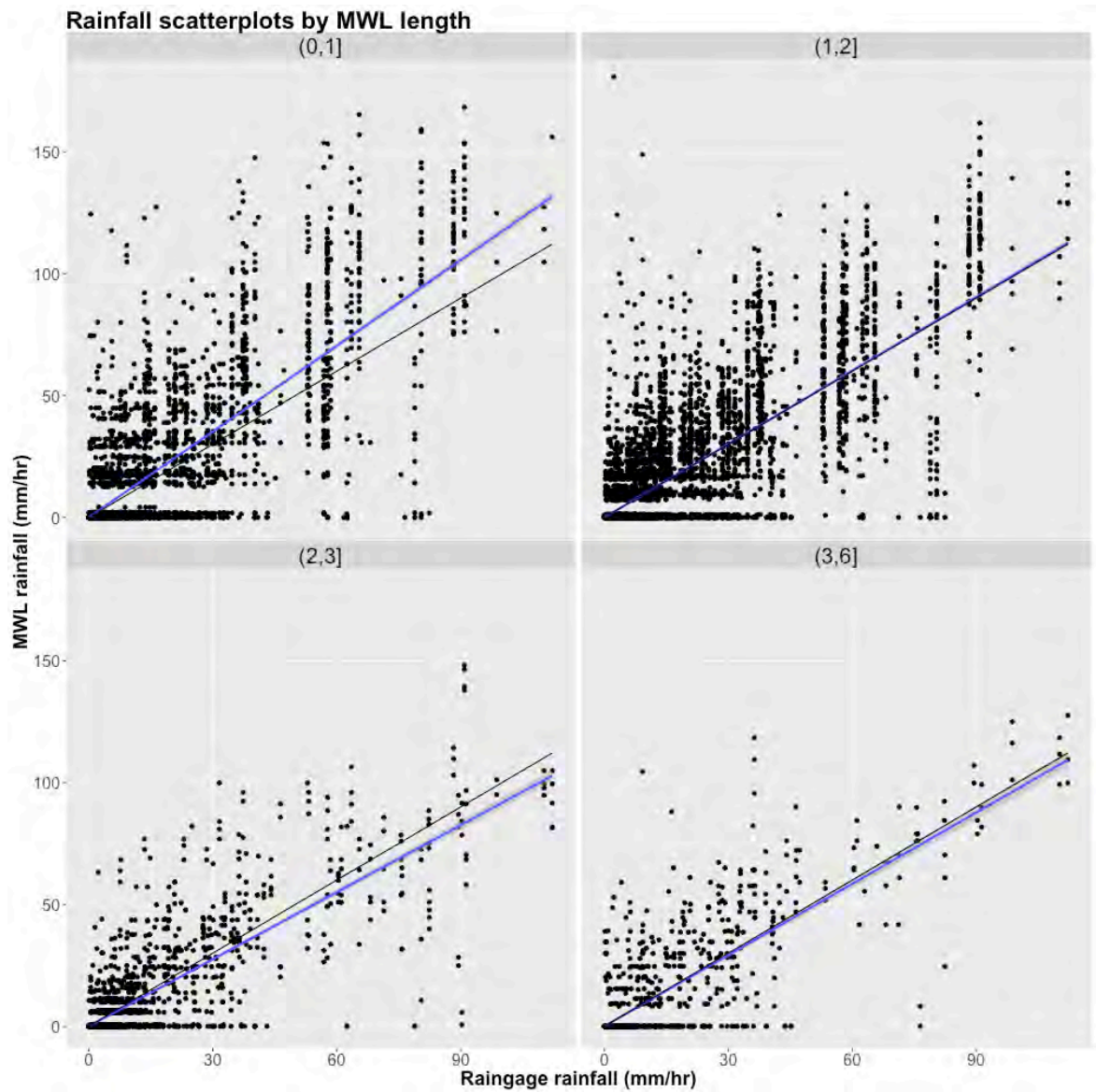


Figure 6-19: Scatterplots of retrieved CML rainfall versus rain gage rainfall for calibration 1 (filtered). The black line shows the identity. The blue line shows the $y=ax$ fit.

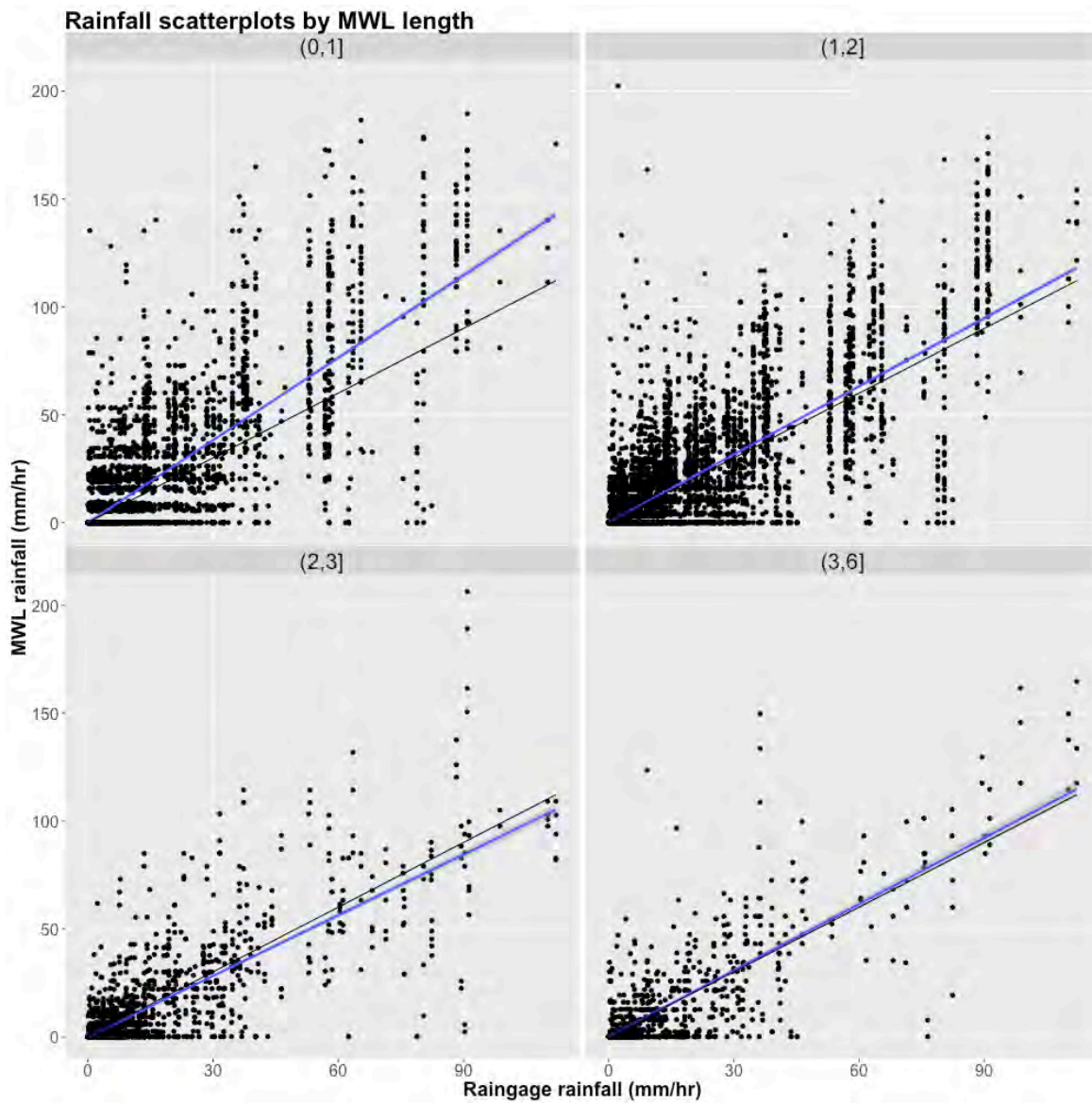


Figure 6-20: : Scatterplots of retrieved CML rainfall versus rain gage rainfall for calibration 2 (filtered). The black line shows the identity. The blue line shows the $y=ax$ fit.

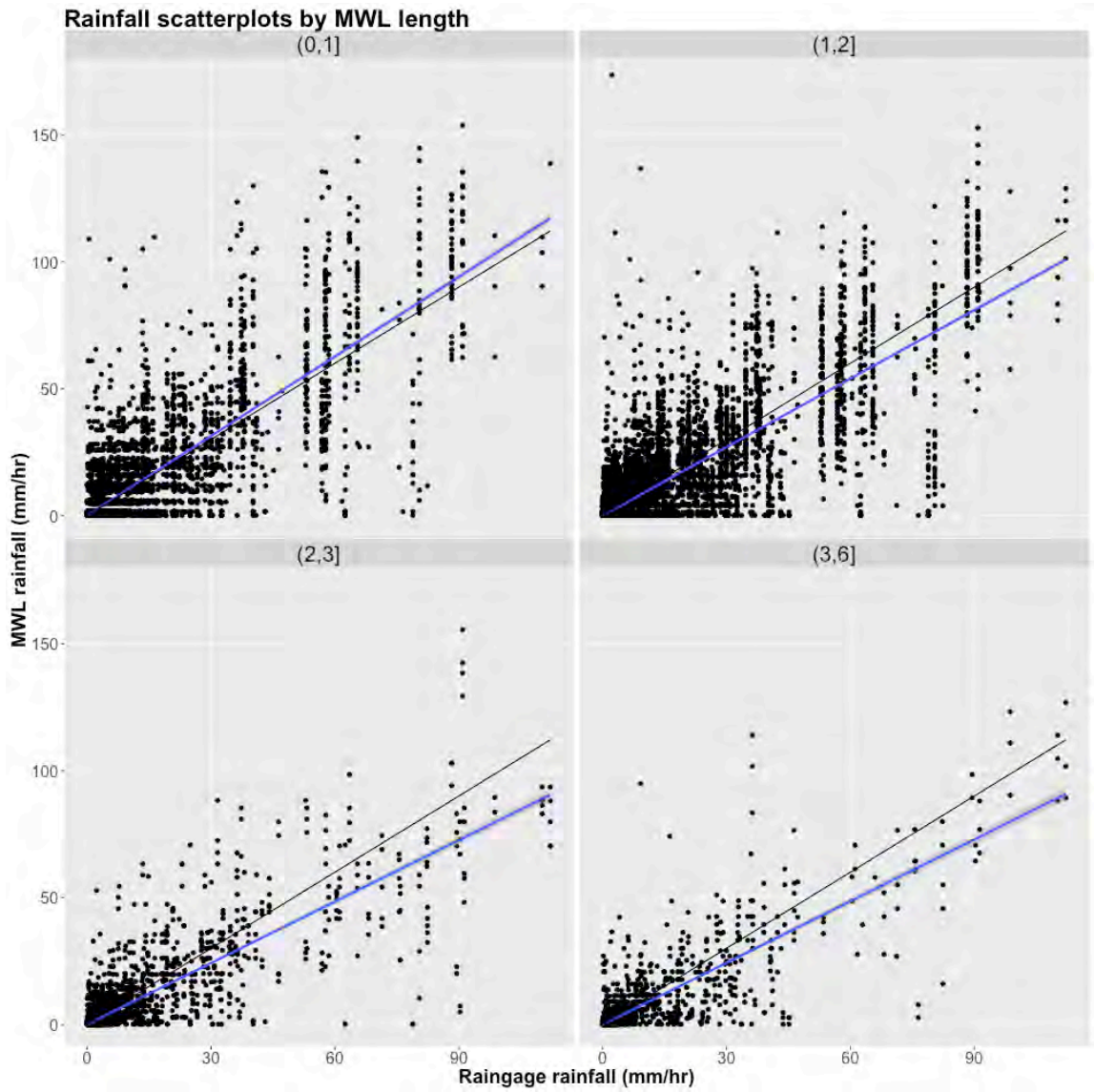


Figure 6-21: Scatterplots of retrieved CML rainfall versus rain gage rainfall for calibration 3 (filtered) with $g=0.65$. The black line shows the identity. The blue line shows the $y=ax$ fit.

6.3.6 Daily rainfall time series

In the above sections we focused on the calibration of the WA effect and the K-R relationship for rainfall retrieval from CML at the 15 minutes' time step. However, the wet/dry classification and the baseline estimation algorithms can lead to false alarms and non-detections impacting the daily amounts of rainfall accumulations. In this section we show the resulting daily global biases for the 2016-2017 seasons in Niamey by CML length class for the fitted calibrations and the presented baseline detection algorithm.

The calibration presented were fitted using the CML-Rain gages hits. The non-detections and false alarms were removed from the analysis. In order to remove CML outliers in daily accumulations we filtered the 15 minutes' time steps following three criteria:

- The rain rates above 200 mm/hr were considered as missing value (NAN). Some peaks of attenuation in non-precipitating days lead to rainfall rates beyond 500mm/hr, which are non-physical. The origin of such strong attenuation are unknown.
- The CML presenting a daily accumulation over 200 mm is considered as NAN for the whole day. Some CML present attenuation patterns non due to rainfall leading to non-realistic daily accumulations.
- In order to have reliable daily accumulations a CML with more than 10% of missing values (NAN) is removed of the daily accumulation.

This criteria could be replaced in the future with more robust filtering based on the self-consistency inside the network using the information from the other CML.

Figures 6-22 to 6-25 presents the daily rainfall accumulations observed by the three raingages average and the daily accumulation for all the CML averaged by class of link length. Each different figure shows the results for a different calibration. The calibration "3bis" correspond to the calibration 3 with a parameter $g = 0.65$. The R2, relative bias, and bias are reported for each link length class in the figures.

Chapter 6: Evaluation of CML rainfall measurements in Niamey

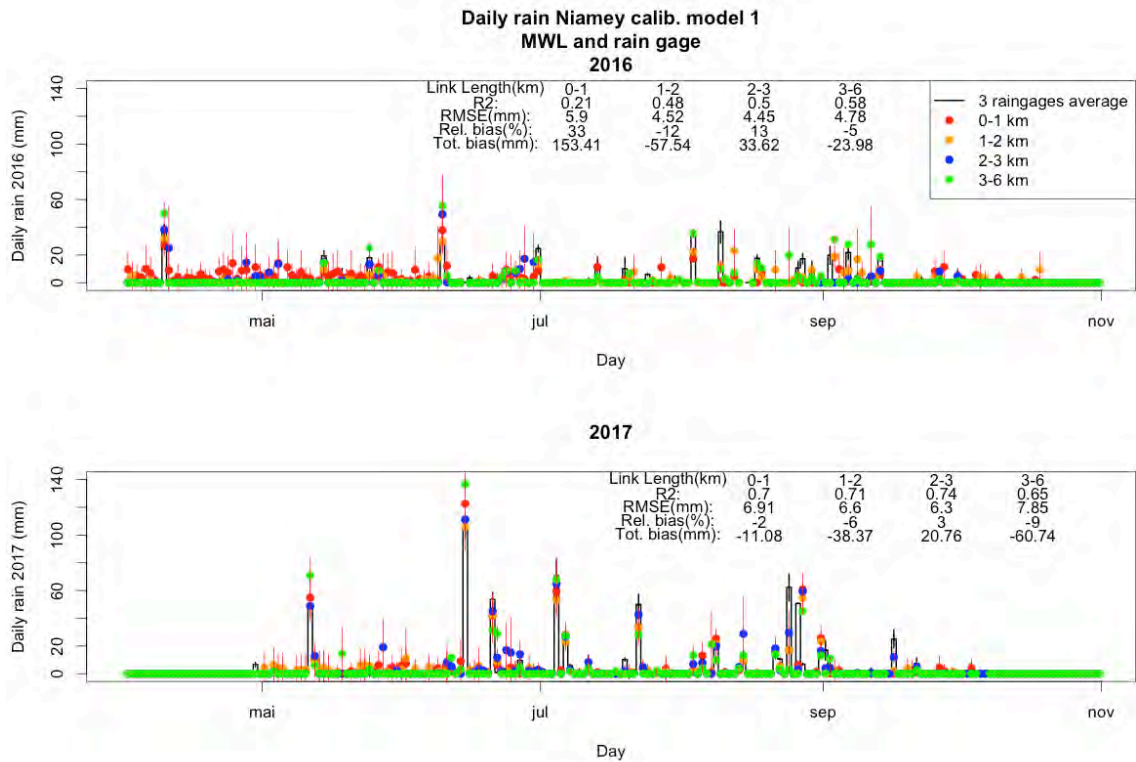


Figure 6-22: Daily rainfall time series for rain gage and CML by length class for calibration calibration 1. The bias is calculated over the season.

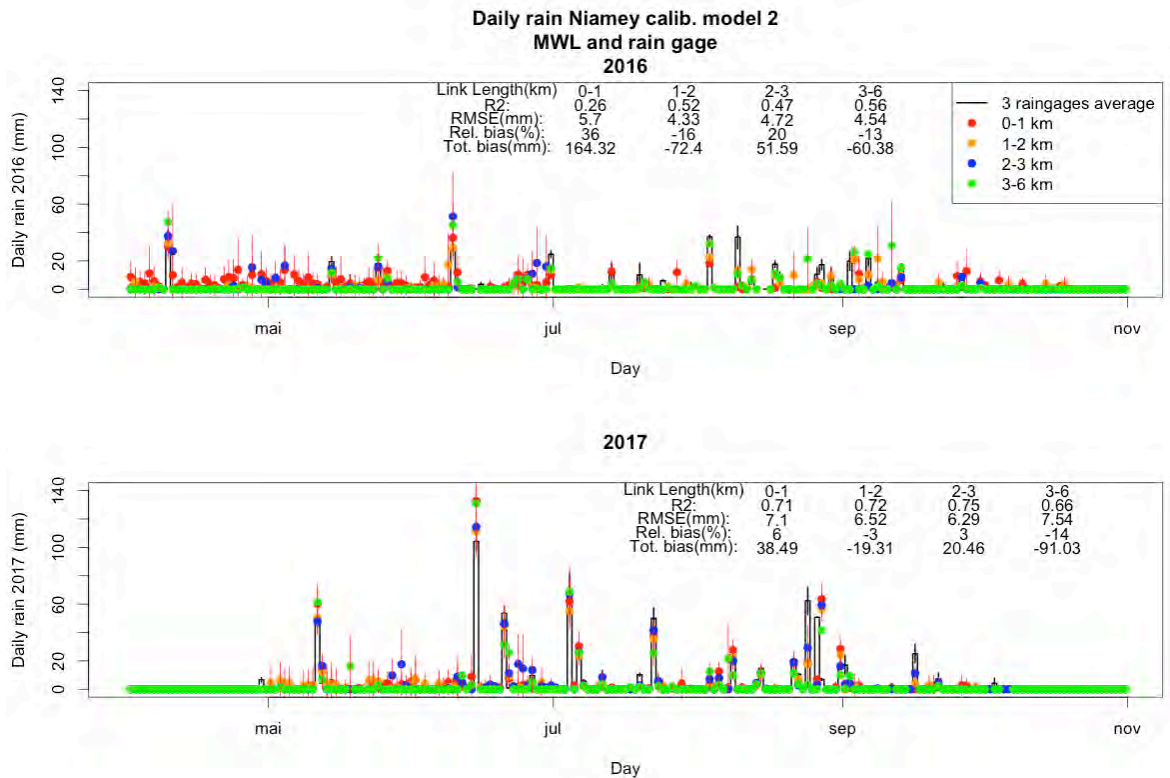


Figure 6-23: Daily rainfall time series for rain gage and CML by length class for calibration calibration 2.

The daily accumulations were calculated by applying the baseline detection described in section 6.2 to the whole CML network and by applying the different calibration calibrations described with the fitted parameter in table 6-1 (for the filtered dataset).

Some links presents anomalous attenuation patterns not explained by rainfall leading to strong values of retrieved rainfall. We remove the values of retrieved rainfall at 15 min higher than 200 mm/hr. No additional criteria were used to improve the retrieved rainfall in Niamey: the internal coherence of the dataset can be used to improve the detection of rainfall events by considering the detection of neighbor CML to remove false alarms.

We can see in figure 6-24 in the begging of season 2016 many false alarms for the [0-1km] CML degrading the scores for short links. Those false alarms are generated by few links detecting huge rainfall rate (higher than 100mm/hr) and can be removed using the information on the other CML of the network. For the three methods the scores are better for the 2017 season as more data were available and the presence well detected strong rainfall events improve the scores.

For calibration calibration 1 and 2 (figure 6-22 and 6-23) the relative biases are low and around zero specially for the year 2017 in which the relative bias is between [-14%,6%] with respect the yearly amount. For the strong events the uncertainty bars linked to the variability of the rainfall in the zone usually overlaps.

Chapter 6: Evaluation of CML rainfall measurements in Niamey

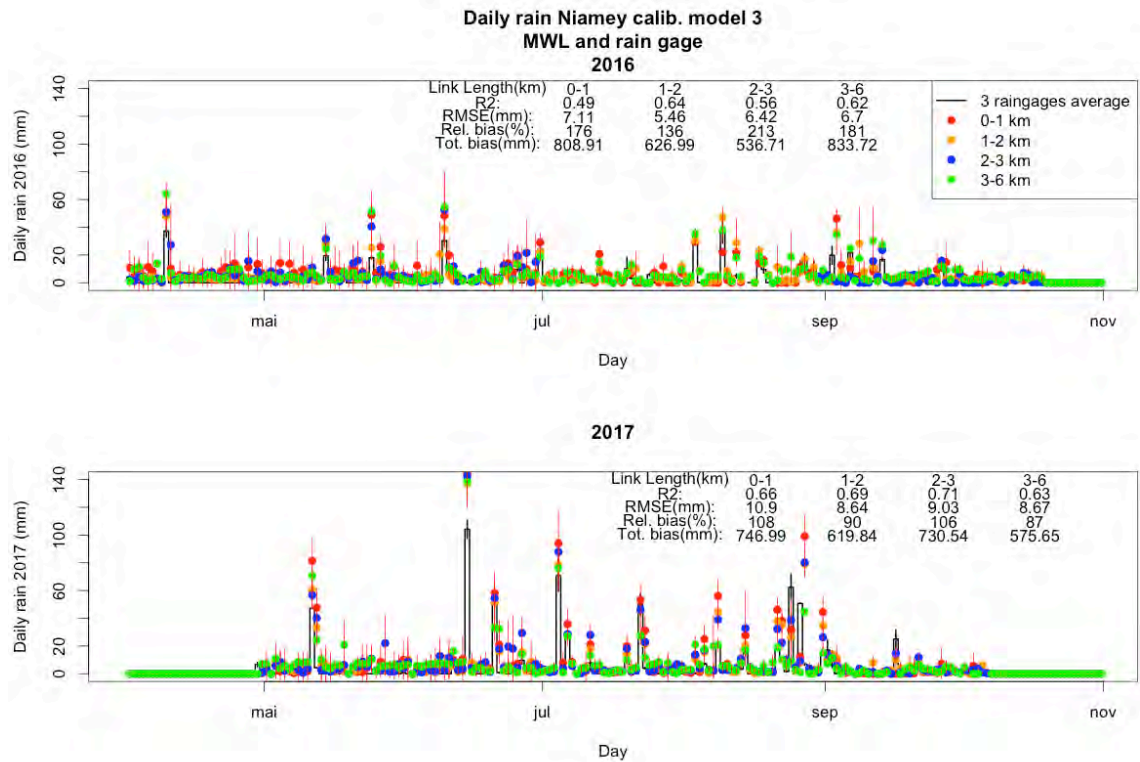


Figure 6-24: Daily rainfall time series for rain gage and CML by length class for calibration calibration 3.

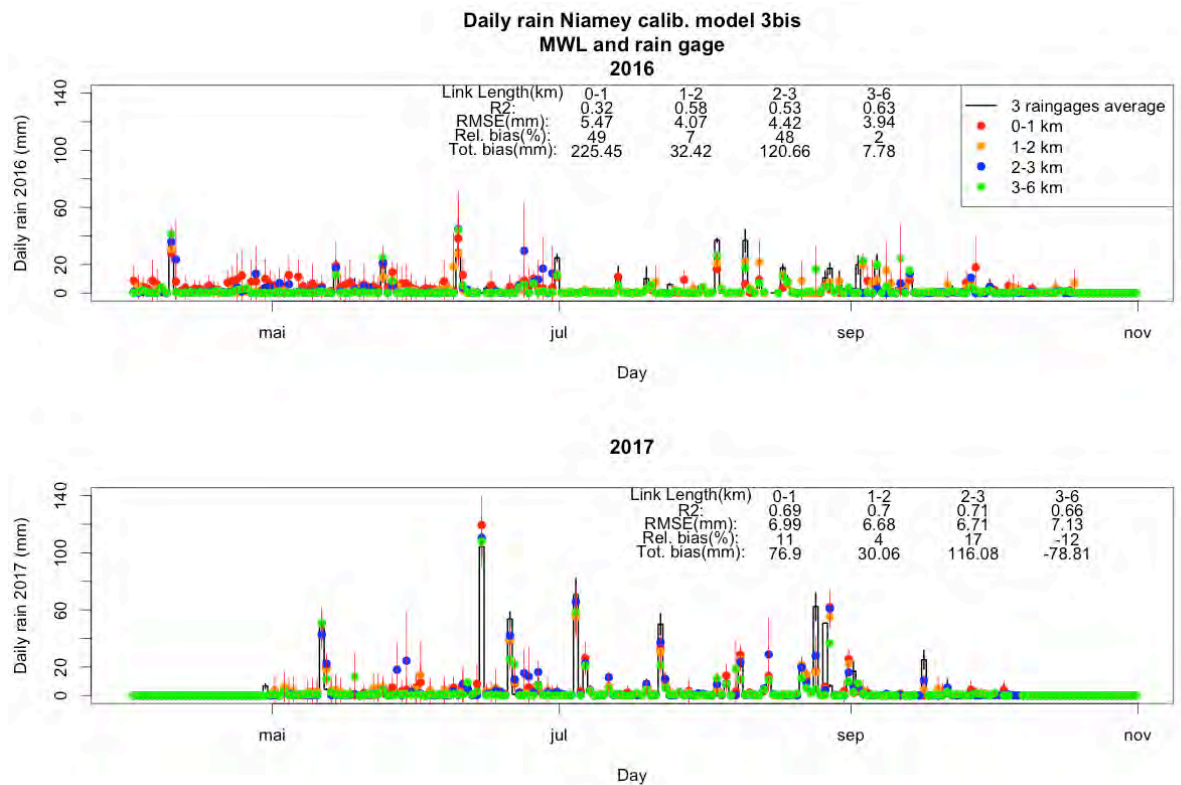


Figure 6-25: Daily rainfall time series for rain gage and CML by length class for calibration calibration 3 bis.

The daily bias can be decomposed into:

- False alarm bias (FA), when CML see rainfall and gages does not
- Non detection bias (ND) when gages see rainfall and CML does not
- Hit bias when both see rainfall
- Total bias, the sum of the three.

The figures 6-26 to 6-29 show the decomposition of the bias by CML link class. As we see, the non-detection bias is very low as only some isolated, low rainfall can be seen by the rain gages and not by the CML network. The false alarm bias has the higher contribution to the global bias, but the false alarms can be substantially removed improving the detection algorithm by using the information of the neighboring CML. The CML more affected are the small links: the false alarm bias decrease for increasing link length. The hit bias also decreases for increasing CML as the uncertainty due to wet antenna and quantization are relatively lower in long links, and the 15 minutes' rainfall retrieval is less biased in long links than short links as seen in section 6.3.3.

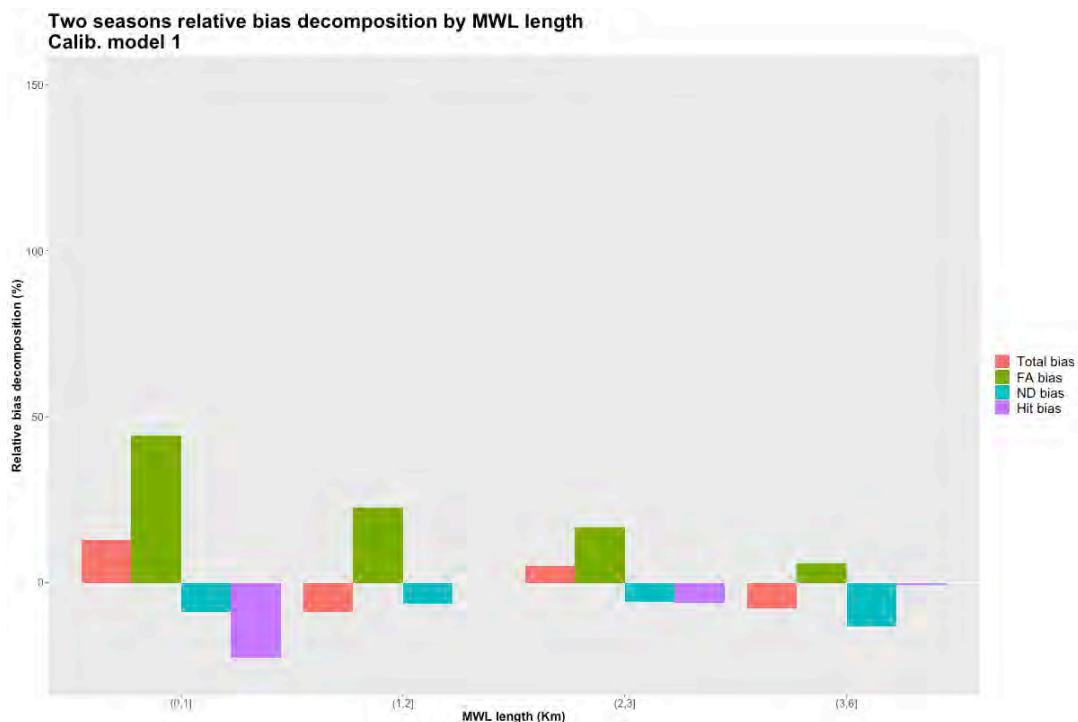


Figure 6-26: : Relative bias decomposition for calibration 1 by CML length class

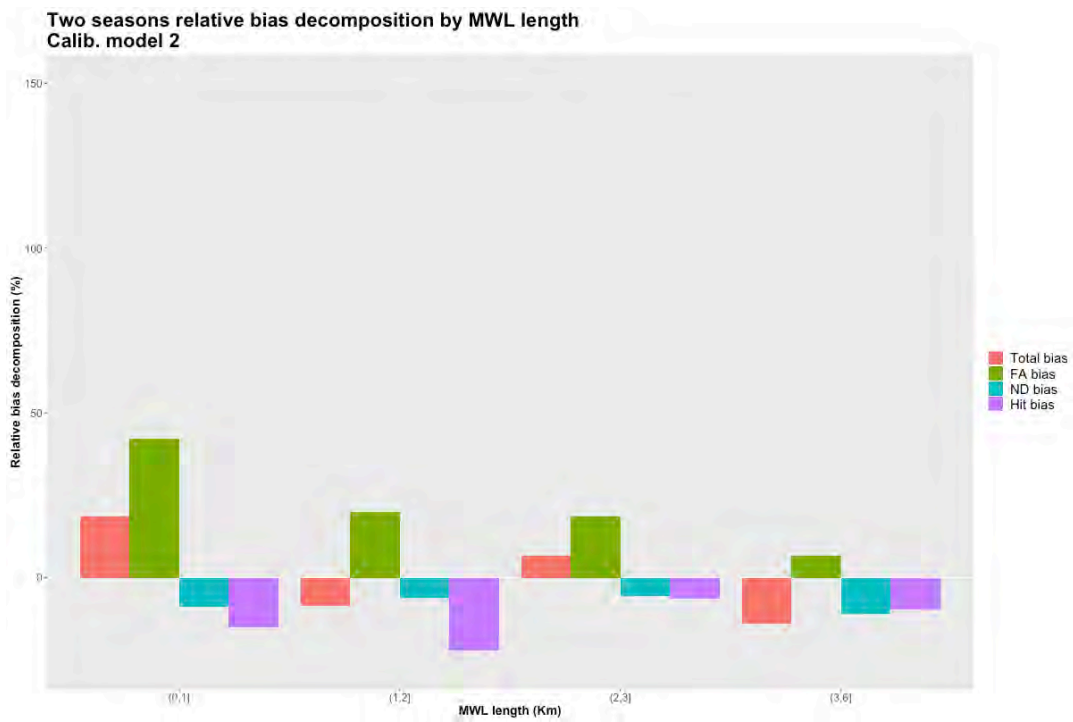


Figure 6-27: Relative bias decomposition for calibration 2 by CML length class

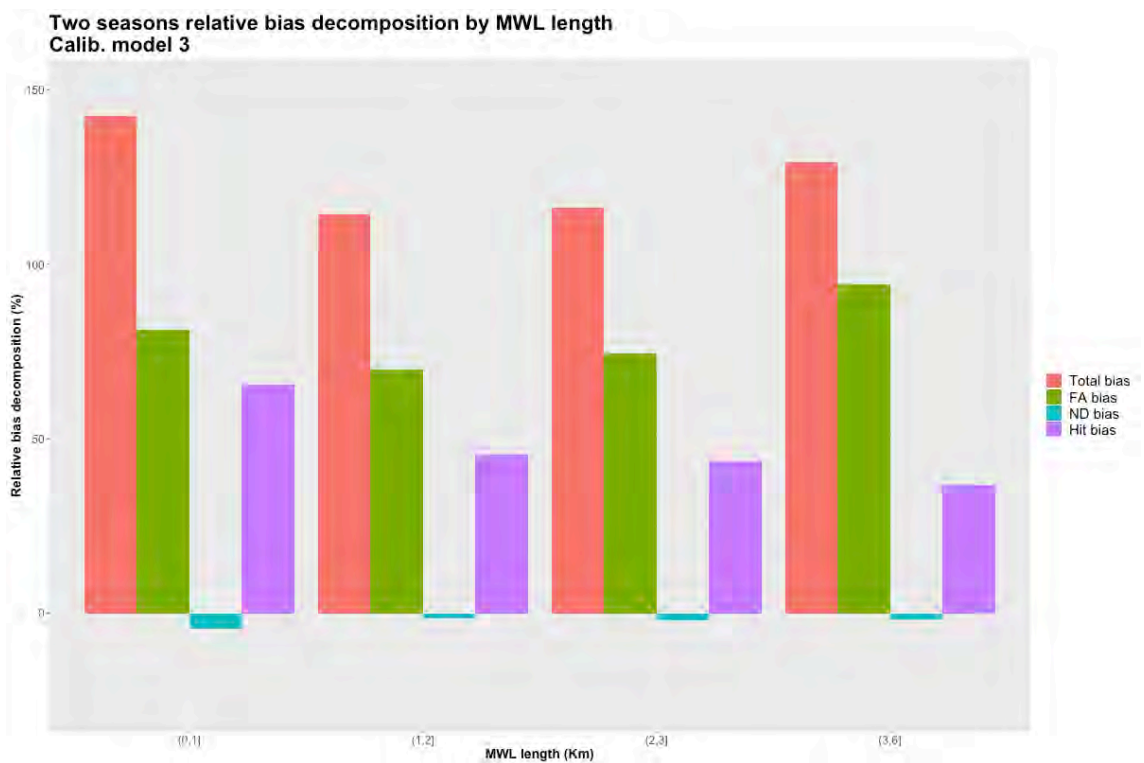


Figure 6-28: Relative bias decomposition for calibration 3 by CML length class

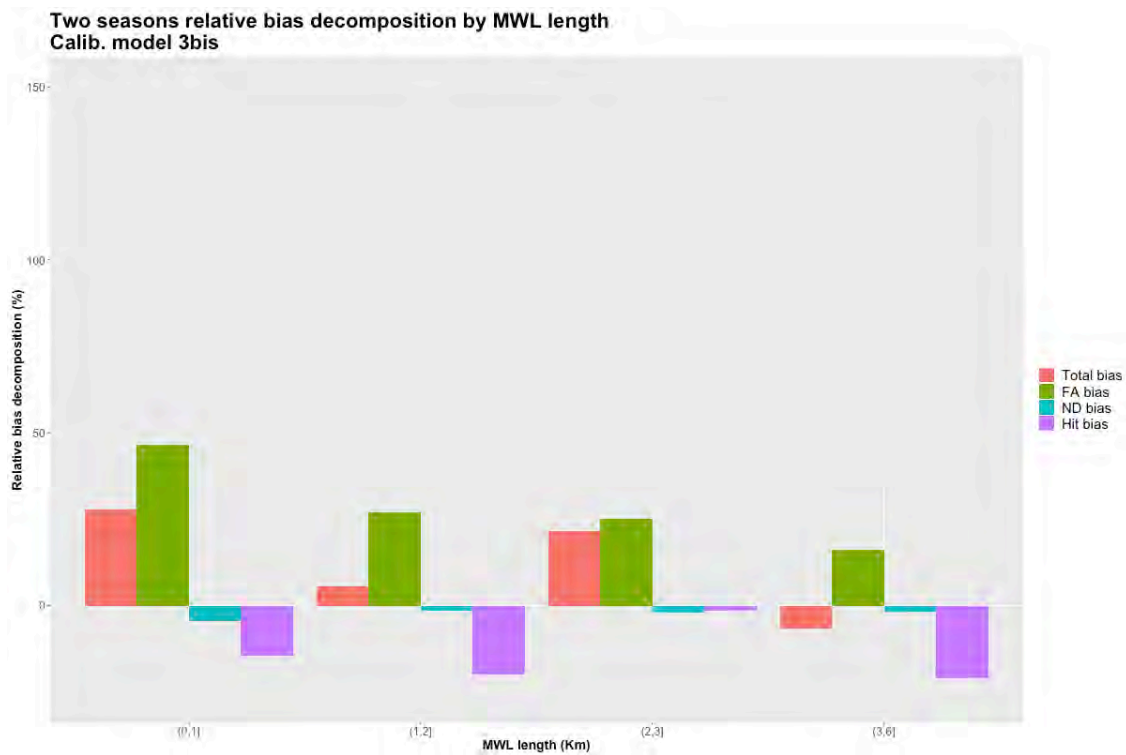


Figure 6-29: Relative bias decomposition for calibration 3 bis by CML length class

6.4 Conclusions

We have evaluated three calibrations of the observed CML attenuations to correct the wet antenna effect and to adapt the K-R law to the dataset. Three raingages in Niamey were used to adjust the parameters. In two calibrations we considered a fixed wet antenna attenuation (not depending on rainfall rate). In the third calibration we considered a varying wet antenna depending on the rainfall rate as stated in the model of [Leijnse et al. 2008]. Concerning the parameters of the K-R law, in the first calibration we fitted both parameters to the dataset. In the second calibration we fitted a considering a fixed b (calculated from observed DSD in Benin chap. 5 theoretical K-R law). In the third calibration we considered a fixed $[a, b]$ from theoretical K-R law (parameters on Table 6-3).

The three calibrations show biases depending on the link length and the rainfall rate. The absolute biases increase with rainfall rates. A behavior appears for different link lengths: short links tend to overestimate and long links to underestimate. This behavior is partially corrected with calibration 3 as the increasing wet antenna with rainfall rate is relatively more important in short links. Robustness tests on the calibrations show a dataset dependency on the fit of calibration 1: the parameters $[a, b]$ of the K-R law compensates and lead to physically inconsistent solutions. When fixing the $b = b^{th}$ (cal. 2) the retrieved a is close from the theoretical value calculated from the Benin DSD $a \approx a^{th}$. The K-R law derived from DSD observations in Benin seems adapted to the CML rainfall observation in Niger either for 18GHz and 23GHz. The filtering of the dataset above 10mm/hr impacts the value of the retrieved wet antenna for cal. 1 and cal. 2: the retrieved values of wet antenna are higher for when fitting to strong rainfall, suggesting a wet antenna attenuation dependency on rainfall rate. The fitted value of the parameter g in calibration 3 is not adapted to calculate the rainfall rate with only the CML attenuation.

Table 6-2 summarize the season relative bias and R2 over the daily time series obtained for the three calibrations depicted by year and link length class. The resulting bias of the three calibrations show encouraging results. For the season 2017, where more data was provided (figure 6-2) the R2 for the season are 0.6-0.7 for all the CML. The bias is mainly drive by false alarm bias (figure 6-26 to 6-29) which can be substantially decreased by improving the conditional detection of daily rainfall using the neighboring CML observations. The hits bias is low [-10 ; 10 %] in the order of magnitude of the differences between rain gages due to the spatial variability of rainfall.

The differential behavior of small CML with respect to long CML can be partially explained by the relative weight of the wet antenna attenuation and the rough quantization step. But also the differences in the sampled rainfall fields can lead to differences when comparing to rain gages. In the appendix 5 we show the differential sampling effect of CML with different lengths when compared to rain gages using simulated observations with radar rainfall fields of DSD parameters. The simulations show an average underestimation of the links increasing with their lengths compared to the rain gages due to the smoothing of the fields. The same trend is observed with simulated data.

In conclusion the evaluation of CML data in Niamey showed the validity of the K-R law derived with the DSD data of similar precipitating systems in Benin. The calibration

suggests a wet antenna attenuation dependency on rainfall rate. The quality of the rainfall retrieval depends on the CML length. Short links are associated with a higher uncertainty (chapter 5) verified with in the Niamey CML evaluation (Table 6-2).

The calibration of the wet antenna correction depending on rainfall was done based on the results of [Leijnse et al. 2008]. Instead of fitting a proportional parameter (g) on the model in [Leijnse et al. 2008] we can foresee for future work a physical model of the wet antenna effect with a dedicated measurement campaign.

CML based products for precipitation monitoring should consider the CML length as a proxy of the uncertainty. For areal rainfall averages (hydrological applications) short CML are less representative as they cover a shorter distance. Also the wet antenna can lead to overestimations and a rough quantization step to a high uncertainty.

		0-1 km		1-2 km		2-3 km		3-6 km	
		2016	2017	2016	2017	2016	2017	2016	2017
Cal 1	R2	0.21	0.70	0.48	0.71	0.50	0.74	0.58	0.65
	Bias	33	-2	-12	-6	13	3	-5	-9
Cal 2	R2	0.26	0.71	0.52	0.72	0.47	0.75	0.56	0.66
	Bias	36	6	-16	-3	20	3	-13	-14
Cal 3bis	R2	0.32	0.69	0.58	0.70	0.53	0.71	0.63	0.66
	Bias	49	11	7	4	48	17	2	-12

Table 6-2: Total season bias (%) and daily R2 against raingage average for the three calibration depicted by year and CML length

		Calib 1 filt 10mm/hr	Calib 2 filt 10mm/hr	Calib 3bis filt 10mm/hr
23GHz	a	0.056	0.109	0.123
	b	1.178	1.028	1.028
	Wet Ant. dB	3.92	3.40	$0.65 * A_{wa}^L$
18GHz	a	0.005	0.056	0.072
	b	1.581	1.052	1.052
	Wet Ant. dB	5.17	3.39	$0.65 * A_{wa}^L$

Table 6-3: Calibration parameters retained to compute daily accumulations. Red values were retrieved by the minimization procedure.

7 RAIN MAPS FROM CML ESTIMATIONS: COMPARISON OF METHODS INCLUDING A NEURAL NETWORK APPROACH

In the last chapter we have adjusted the estimation algorithm and evaluated the rain rate retrieval based on the CMLs from the dense network available in Niamey. For many applications we needed rain maps rather than the retrieval at individual links.

The objective of this prospective chapter is to compare some of the existing mapping techniques commonly used for CML interpolation and a new method based on a neural network (NN). Given the limited CML data set available, the radar rain fields (presented in part 1 of this manuscript) are used as a proxy to simulate synthetic CML data used for training the NN and evaluate the results. This simulation work is complemented with some (limited) evaluation with CML data and rain gauge.

7.1 Introduction

Different techniques have been proposed for mapping (or interpolating) rainfall fields from CML data. A simple solution is to consider the rainfall seen by the CML as a rain gauge in its path center (Overeem, Leijnse, and Uijlenhoet 2011; Overeem, Leijnse, and Uijlenhoet 2016; Rios Gaona et al. 2015) and to interpolate rainfall as is usually done for rain gages (for example kriging or inverse distance interpolation). For sparse networks in

Chapter 7: Rain maps from CML estimations: comparison of methods including a neural network approach

large scales this can be a simple solution if the links information is not redundant (link path lengths lower than distance between links or link lengths small compared to the domain).

In urban contexts the CML density is usually high, offering a rich sampling of rainfall. Microwave links represent a very interesting solution to rainfall monitoring at city scale as pointed out by (Upton et al. 2005). In such scale other techniques are needed to extract the full information from the network. If we consider CML as rain gages in its center, two CML with the same path center and different length can have different values of detected rainfall leading to contradictory information at the same point. More complex algorithms have been applied to extract the spatial information provided by CML networks: the combined localization of the different CML paths gives us information about the spatial distribution of rainfall. In the works (Zohidov et al. 2014; D'Amico, Manzoni, and Solazzi 2016; Roy, Gishkori, and Leus 2014) the authors use the framework of inversion theory to retrieve rain fields. Another technique developed in (Zinevich, Alpert, and Messer 2008) is based on a tomography with a variable grid size. In the cited work the solution is constrained by the CML observed rain and an imposed spatial correlation of the solution. Both techniques show a reliable pattern detection of the rainfall when compared to a reference field. But both techniques have an ill definition of the observation scale as they project the CML network (with variables path lengths) into a grid of variable size. That leads to rainfall fields with a non-realistic distribution of rainfall rates. Another limitation of this techniques is the unrealistic patterns of rain at the boundaries of the mapping zone where less information is provided.

Rainfall has a strong spatial and temporal variability and the probability density function of rainfall rates depends on the observation scale. By construction CML networks have various links lengths and geometries depending on the local constraints and network optimization from the telecom company. Combining observations from links of different length implies combining different observation scales of rainfall, as discussed in chapter 6.

Rainfall from CML has a minimal detectable rainfall R_{\min} which depends on the frequency f , the link length L and the quantization step Δ_a of the attenuation provided by the telecom company, as discussed in chapter 5. The minimal detectable rainfall R_{\min} for a quantization step of attenuation Δ_a was defined in chapter 5 as:

$$R_{\min} = \left(\frac{\Delta_a}{2aL} \right)^{1/b} \quad (\text{eq. 7.1})$$

Figure 5-11 of chapter 5 shows the minimal detectable rain as a function of the link length for different frequencies at $\Delta_a = 1$ dB quantization step. Short links and a rough quantization step lead to non-detections of rainfall.

Figure 7-1 shows an example of the “Gruyere” effect in observation of rainfall from CML in Niamey, Niger: the sinks of rainfall rate come from non-detections of short links due to a rough quantization step (grey lines). The CML network detect rainfall at some links located very close ($\sim 100\text{m}$) to the CML who does not detect rainfall.

A possible solution to this inhomogeneity in the sensitivity of the observations can be filtering links depending on its frequency and length to ensure a threshold of a common R_{\min} . But this solution leads to a loss of valuable local information brought by short links. In addition, short links are more probable to detect high rain rates related to local convective cells.

To retrieve a reasonable value of R_{link} we could use the information of the surrounding links as the rainfall is spatially correlated.

In this chapter we propose an alternative method using a multi-layer neural network (hereafter NN) trained with radar data to retrieve maps from CML information. Multilayer feedforward neural networks are universal approximators and an efficient method to find a function linking a set of input data to an output set of variables (Haykin 1994). They are particularly good estimating non-linear and non-continuous functions.

The idea is to retrieve the spatial properties of rainfall (as seen by a radar) in a context of limited (and uncertain) spatial information. The simulated CML training dataset is constructed with radar rain fields in order to simulate real observations of attenuation with a quantization step. The radar fields are then used as the reference field to feed the backpropagation algorithm for the NN learning.

In section 7.2 we describe the three methods of mapping compared in this work: the NN, the kriging interpolation and the tomography. In section 7.3 we describe the radar dataset and the construction of the virtual CML observations to train the NN. In section 7.4 we show the validation of the three methods compared to the reference simulated data. In

section 7.5 we show a cross-validation study in Niamey with the 2016-2017 Orange data calibrated in chapter 6. Finally, in section 7.6 we discuss the results and conclude.

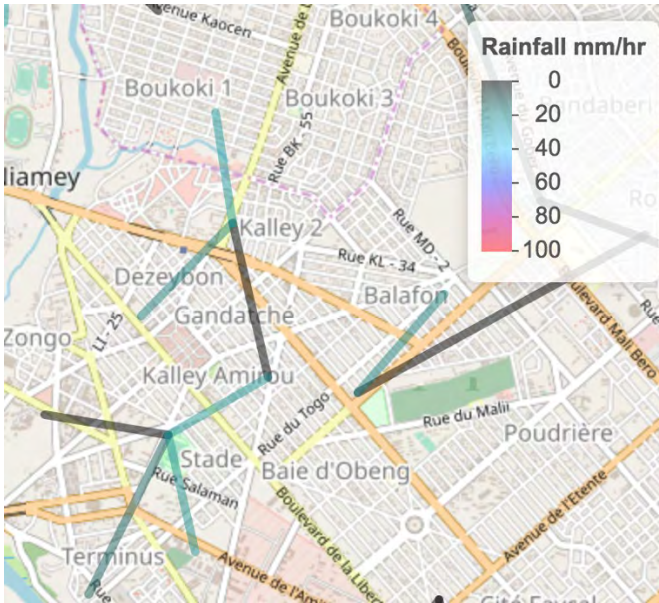


Figure 7-1: Zoom on the Niamey CML network. The bars represent the location of the CML and their color the Rainfall estimation (without wet antenna correction) for the 25/05/2016 event at 11h30 UTM. Some CML are black as they do not detect a jump in attenuation greater than 1dB. The window size is 3x3 Km.

7.2 Rain mapping from links: common methods

7.2.1 Simple kriging interpolation

Simple kriging is a geostatistical interpolation technique to estimate fields of a random function (spatially correlated) from a limited sample of point measurements in space. The difference with other simpler techniques (inverse distance interpolation, or Thiessen polygons) is that the weights ω_i of the lineal combination of the input values V_i are given by an estimated space covariance. The estimated value \hat{V}_j at point u_j is:

$$\hat{V}_j(u_j) = \sum_i \omega_i V_i(u_i) \quad \text{with} \quad \sum_i \omega_i = 1 \quad (\text{eq. 7.3})$$

Where \hat{V}_j is a linear combination of the sample of observations V_i at locations u_i . The weights ω_i depends on a space covariance model which can be estimated with the data. An experimental semivariogram $\hat{\gamma}(d)$ is usually estimated with the sampled data:

$$\hat{\gamma}(d) = \frac{1}{2N(d)} \sum_{i=1}^{N(d)} [V_i(u_i) - V_i(u_i + d)]^2 \quad (eq. 7.4)$$

Where $N(d)$ is the number of pairs of data locations at a distance d . The semivariogram is a function of the distance d . It can also be a function of the direction if we consider anisotropic fields. When considering rainfall accumulations, the variogram varies for different aggregation periods: for longer periods the correlation distance increase. The empirical semivariogram is usually fitted to a model.

Kriging estimation is unbiased, and is the best linear estimator of a field if the assumptions holds: it implies that the variogram (or spatial covariance) is well estimated, and the field has stationary properties.

In our study the stationary assumption is not well satisfied as the squall line rainfall has two distinct zones of convective heavy rainfall with different spatial properties compared to the stratiform tail. Figure 7-2 shows the empirical variogram calculated from 40 PPI (1° elevation) of X-port radar rain fields for the squall line event of 03/07/2012. We see two distinct behaviors corresponding to the convective scale (~10km) and the stratiform scale (~50km). More sophisticated kriging techniques exist to take into account different rainfall regimes. In this prospective study we limit to simple kriging with a unique variogram modeled as a double exponential (red curve in figure 7-2). We fitted the empirical variogram with a double exponential: a first exponential with correlation distance of 4 km and a second exponential with a 42km correlation distance.

To apply the simple kriging to the CML network we consider the average rainfall rate through the link path as a punctual rainfall rate at its path center. This assumption implies that we lose the information of path length and direction. The benefits of the method are a small computing time and straightforward implementation.

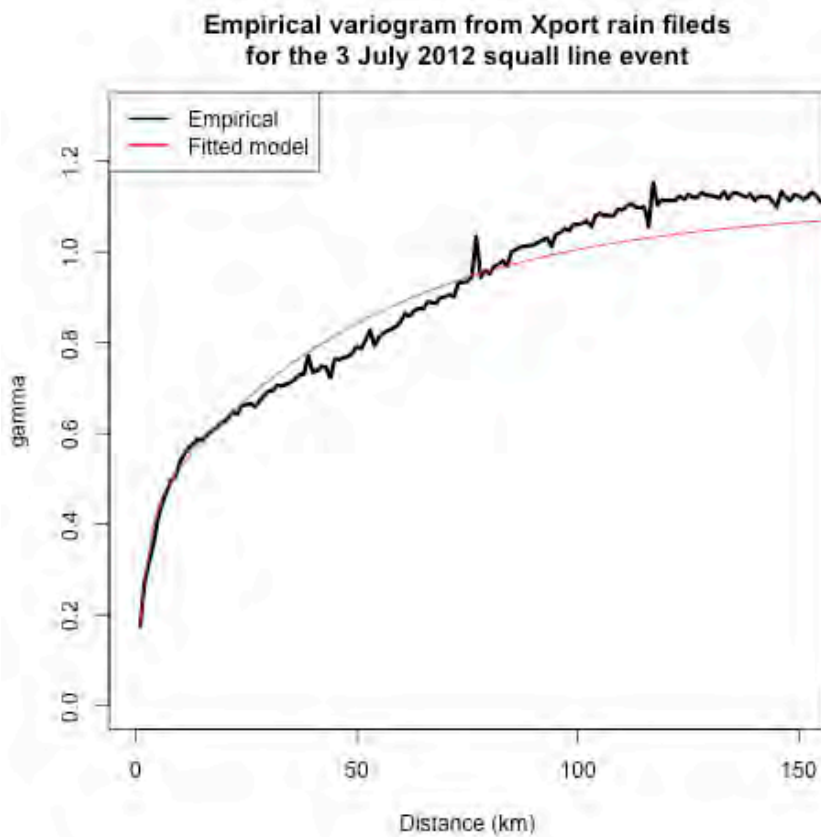


Figure 7-2: Empirical variogram and fitted model from 40 PPI (1° elevation) of X-port radar data of the 03/07/2012 event.

7.2.2 Tomography and kriging

The second mapping technique is a tomography, based on the work of (Zinevich, Alpert, and Messer 2008). The objective of the tomography is to fully describe the geometry of the observations of the CML network in the output target grid, using the location of the CML paths.

If we consider the attenuation measurement A_i of a CML as being the non-linear sum of the rainfall through the pixels r_j of the output target grid we can derive a system of i equations corresponding to each link:

$$A_i = a_i R_i^{b_i} L_i \cong a_i \sum_{j=1}^n l_{ij} r_j^{b_i} \quad (\text{eq. 7.5})$$

Where n is the number of pixels crossed by the link path, l_{ij} the length of the part of the i^{th} link passing through the j^{th} pixel, $[a_i, b_i]$ the coefficients of the K-R relation and R_i the average rainfall rate in the link path (deduced from the measure A_i).

The algorithm consists in finding the values of the rain rate r_j in the pixels, that minimize the functions f_i :

$$f_i(r) = \sum_{j=1}^n l_{ij} r_j^{b_i} - R_i^{b_i} = 0, \quad i = 1, \dots, m \quad (\text{eq. 7.6})$$

Figure 7-3 from (Zinevich, Alpert, and Messer 2008) shows the geometry of a CML over the spatial grid on which we aim to retrieve the values of rainfall r_j .

Usually the number of pixels n is greater than the number of links m and thus the inverse problem is underdetermined and need regularization to find a possible solution among the infinite possible combinations. The choice of (Zinevich, Alpert, and Messer 2008) was to set a spatial correlation among pixels in function of their distance to constrain the solution. That is equivalent to introduce $\sum_{j=1}^n j$ equations per link and thus the problem become overdetermined. The introduction of a spatial correlation constraint the solution with a priori information extracted from previous observation of radar rain fields (variogram).

The tomography can only estimate rain rates in pixels with information, ie. pixels crossed by a CML. The pixels without information are filled with another interpolation technique (kriging in our study).

If the network is dense the tomography bring coherence in the retrieved field by finding a solution which is spatially correlated and which verify the observations of the CML.

But remains the problem of the ill definition of the resolution of the retrieved field (as well for the kriging). As the rainfall distribution in the output target grid is not realistic when compared to real rainfall fields (radar). The spatial correlation imposed in the solution tend to smooth rainfall fields and this can have consequences in hydrology modeling.

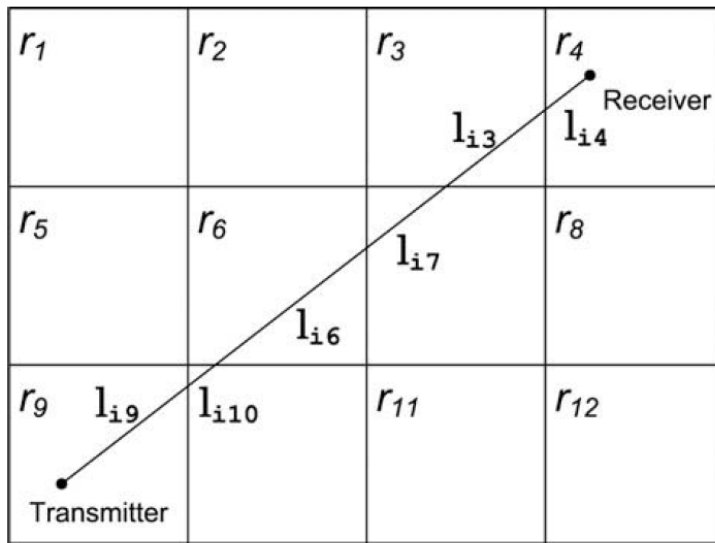


Figure 7-3: : Example of a CML over a regular grid. The total attenuation measured by the CML is considered to be a nonlinear sum of the values of the rainfall r_j at pixel j weighted by the section l_{ij} of the link i over the pixel j . (from Zinevich et al. 2008)

7.2.3 Hierarchical Neural Network

To overcome the limitations of mapping CML data described in the introduction a multilayer feedforward hierarchical neural network (NN) is used. The idea is to train the NN with radar data rain fields and the correspondent artificial CML observations extracted from those fields. We aim to train the NN to learn the situations where a 0 mm/h observation is probably a non-detection due to the high value of the minimal detectable rainfall. The hyper-parameters of a NN are the number of layers and the number of neurons per layer. The hyper-parameters of the NN should reflect the complexity of the function linking the inputs and the outputs. The parameters of a NN are the weights of the different connections between the neurons. NN needs training datasets in order to estimate the parameters (weights) linking the outputs to the inputs. The choice of the training dataset is important. A small training dataset would not correctly represent the different possible situations. Also small training dataset could lead into overfitting of the

training data by the NN. Overfitting avoid the generalization of the function linking the input to the outputs.

The NN architecture developed for this application is showed in figure 7-4. The input layer is a vector composed of 7 characteristics of the 5 closest links relative to the pixel on which we estimate the rainfall (35 inputs), the rainfall at the target pixel is the single output of the NN. To map the rainfall with a trained NN, we execute the trained NN for each pixel in the zone.

The input parameters for each of the CML are the relative distance (in km) from the two antennas to the target pixel $[dX_1, dY_1, dX_2, dY_2]$, the rainfall rate measured by the CML at the current time step P_t , the rainfall rate measured at the previous time step P_{t-1} and the threshold of minimal detectable rain P_{min} which depends on the path length and the frequency of the CML (see figure 5-11). The input vector I is:

$$I = [I_{L1}, I_{L2}, I_{L3}, I_{L4}, I_{L5}] \quad (eq. 7.7)$$

A combination of the information from the 5 closest links I_{Lx} :

$$I_{Lx} = [dX_1, dY_1, dX_2, dY_2, P_t, P_{t-1}, P_{min}]_{Lx} \quad (eq. 7.8)$$

A benefit of the NN is the possibility to add ancillary variables to improve the regression.

The NN has two hidden layers, the first layer is partially connected: there is no causal relation between the coordinates of different links, or the minimal detectable rainfall. The second layer is a fully connected (dense) layer which derive into a single output, the rainfall estimation.

The tests concerning the hyper-parameters of the NN were made with a one-day subset of the data. The metrics used to validate the output was the root mean square (RMS). The objective is to find a compromise between a large number of parameters which can lead to overfitting and a small number which cannot reproduce the complexity of the function linking the input and output. We found that a third hidden layer did not improve the results increasing the computing time. The optimal choice for the first layer is two neurons per input link, one neuron leading to worse results and more neurons not contributing to better results. A similar approach for the second layer derived into $N_2=15$ neurons as the optimal choice.

Chapter 7: Rain maps from CML estimations: comparison of methods including a neural network approach

In section 7.2.3 we describe the training dataset of the NN and in section 7.3 we show the results compared to the other mapping techniques.

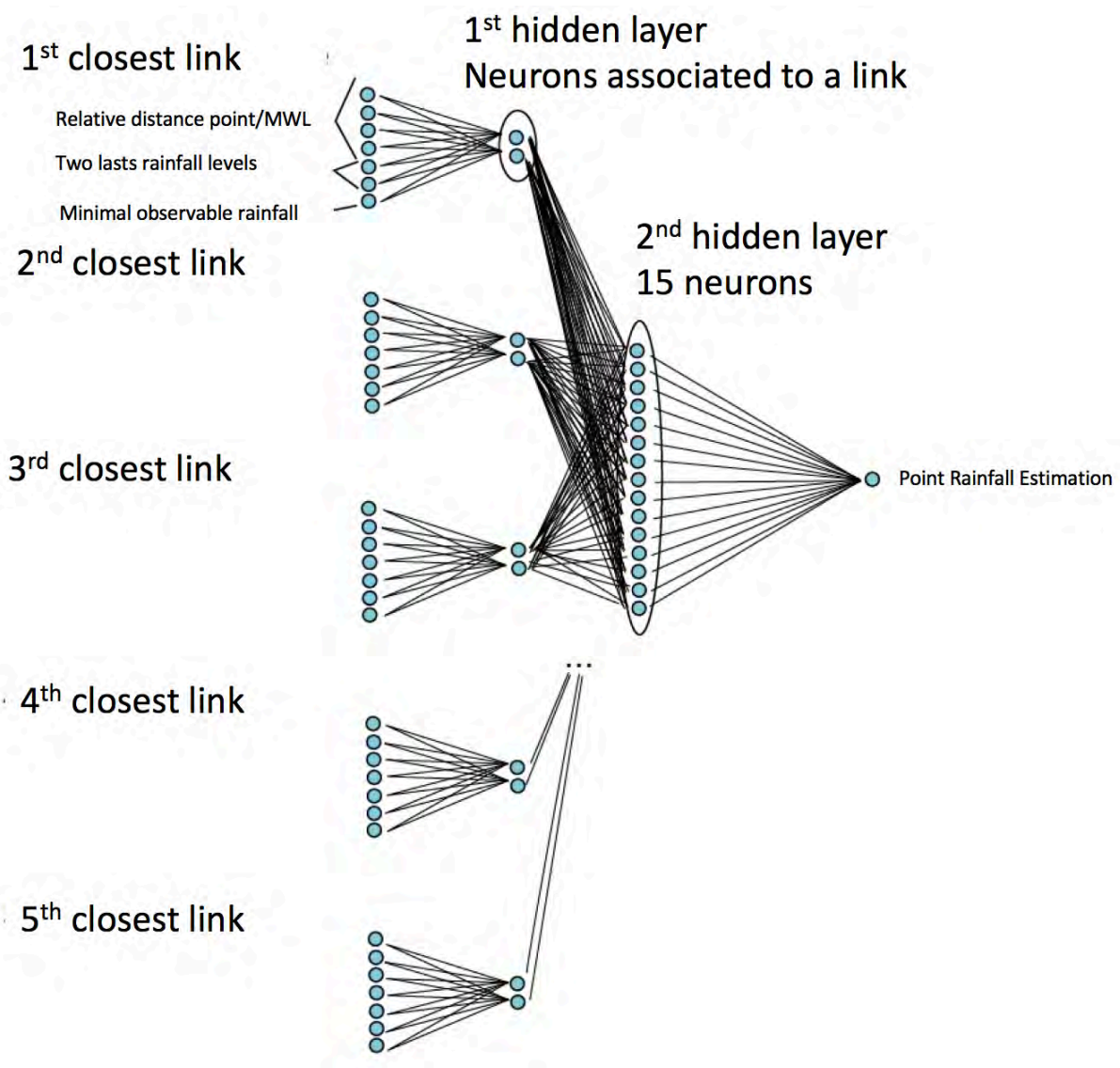


Figure 7-4: Architecture of the NN used in this study

7.3 Synthetic data

In the following section we describe the radar data set used as a reference rainfall field to test the performance of the mapping algorithms. Then we describe the generation of artificial CML and the training dataset.

7.3.1 Radar data and African context

For this study we projected the X-port radar data into a 1 km regular grid by simply averaging the rain rates falling into the regular grid pixels. The CML data provided by telecom companies is at a 15 minutes' time resolution (see Chapter 6). To be consistent with the real CML data we average the instant 1-minute radar rain fields into 15-minutes fields to have proxy fields of a real 15 minutes' spatial variability of rainfall in the West-African monsoon context.

In this study we focus on the retrieval of rainfall from CML networks on a city-scale. We extract three zones of 40km x 40km in the radar maps showed in figure 7-5. The zones were chosen in the western and upper part of the radar fields to avoid extinction cases. The three zones were located far enough from the radar to avoid the central parts affected by ground cluttering.

We used the whole 2013 monsoon season from May to October. We used only 15-min averaged PPI covered at least by 75% of data (less than 25% of missing values) to filter rain fields with poor spatial coverage.

7.3.2 Generation of artificial links from radar data

We have used three different real CML networks of African cities to avoid a network topology dependence in the NN training. The CML configurations are from the cities of Niamey (Niger), Yaoundé and Douala (Cameroun) provided by the telecom operator Orange. The CML networks are shown in black lines (at different scales) on figure 7-6. We can see that the coverage surface of the network varies from each city depending on

its size. Also the number of CML and the frequencies are different for each network. Table A-1 in appendix 6 summarize the characteristics of the three CML networks.

We have considered the real signal frequency of the CML networks which varies from 8.5 GHZ to 23GHZ. The synthetic CML observation were calculated considering both quantization step of the attenuation, 0.1 dB and 1 dB.

The simulated CML observations \widetilde{R}_{link} are computed with the radar pixels R_{rad}^i :

$$\widetilde{R}_{link} = (1/a) * \left[\frac{\text{round} \left(\sum_i L_i a R_{rad}^i, \Delta_{dB} \right) - 0.5}{L} \right]^{\frac{1}{b}} \quad (eq. 7.9)$$

To simulate the CML observations \widetilde{R}_{link} we extract the observed rainfall in the link's path from the radar field. We convert each pixel value of rain R_{rad}^i into attenuation following the K – R relationship weighted by the path length in each pixel L_i . We round the value considering the quantization step Δ_{dB} . The term -0.5 dB in equation 7.9 correspond to an artificial addition of an observation bias to evaluate the capability of the NN to correct possible biases in the observed data (due to a wet antenna for example).

In this study we focus on the uncertainty in the mapped rain field induced by the quantization step and the minimal detectable rain of the links. We also consider a possible bias in the CML observation dataset. We test the ability of the NN to correct the bias introduced artificially in eq. 7.9.

We centered the CML networks in the three zones (figure 7-6). For each zone and for each CML network \widetilde{R}_{link} was calculated using the two considered quantization steps $\Delta_{dB} = [0.1; 1 \text{ dB}]$.

7.3.3 Training data set

To train the NN we used as input the computed values of artificial CML observation \widetilde{R}_{link} and the values of the radar pixels as output. As mentioned above the radar field was divided in three zones of 40km x 40km (see figure 7-5): two zones were used for training keeping the third zone for validation. The different combination of two zones for training and one for validation leads to three different trained NN.

Chapter 7: Rain maps from CML estimations: comparison of methods including a neural network approach

To have a balanced training set representing the different situation in terms of rainfall rates in an equitable manner we filtered the input data set following quotas of average rainfall rates. To equilibrate the convective and stratiform rainfall situations we establish the quotas presented in table 7-3. The whole dataset has an over representation of stratiform rainfall as the convective front usually lasts for 30 min in a 40 km zone. The stratiform rainfall lasts for several hours after the front passage in usual MCS. As the convective rainfall is important regarding accumulations, we decided to have a training set with a representative number convective cases. Thus, we set a maximum number of 15 minutes' rainfall fields in the training set depending on the areal average of rain over the 40x40km domain. Table 7-3 show the number of rainfall field in the training dataset by areal average rainfall. An average rainfall field above 20 mm/hr was only encountered for two PPI in zones 1 and 2, and for three PPI in zone 3 over the 2013 season.

Average Rainfall (mm/hr)	0]0;1[[1;10[[10;20[≥ 20
Number of rain fields	2	30	30	20	2 (3)

Table 7-1: Number of rainfall fields in the training dataset by average areal rainfall in the zone.

The training dataset is composed by the relative distances of the antennas to the point on which we estimate the rainfall rate (4 values), the minimal observable rain and the two lasts rainfall levels of each considered pixel. The training sets are composed by two zones, letting the third zone to validation. Each training set is composed by $2 * 10^5$ pixels.

The training of the Neural Network was performed within 250 epochs for a batch size of 30000 inputs. The loss function chosen was the RMS. The value of the epochs and the batch size was set heuristically by evaluating the convergence rate through each epoch iteration.

This training methodology leads to three different trained NN, each one trained with data from two different zones. We can then estimate the sensitivity to the training dataset. The inter comparison is done on the data not used for training.

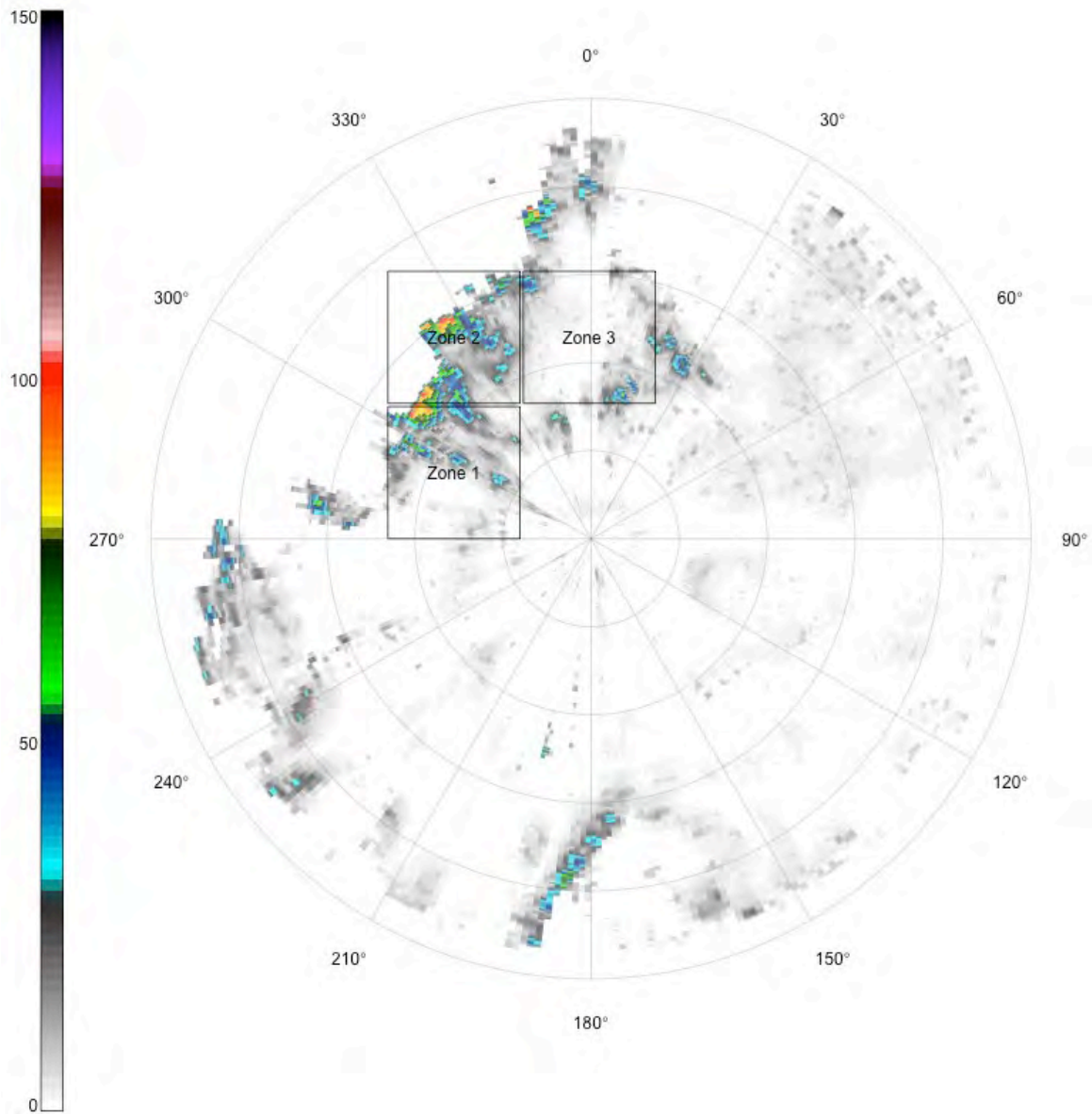


Figure 7-5: Example of a 15min radar field composed by averaging fifteen 1-minute radar fields from X-port radar located in 2013 in Ouagadougou, Burkina-Faso. The three zones used in this study are highlighted.

7.4 Results on synthetic data

This section compares the three mapping methods of artificial CML data to the original radar rainfall fields. In the first section we define the metric for the validation of the maps. Later we assess the efficiency of the different mapping methods and then we inter-compare it globally.

An example of rainfall map for each method is presented in figure 7-6 for a 1dB quantization step. The reference rainfall field is in the left column. The second column shows the maps from the NN method, the third and fourth column the tomography and kriging methods. Each row presents the results for a different real CML network (Niamey, Douala and Yaounde). The reference rainfall field is the same but the size of the mapping zone is different due to the different size of the cities. An interesting asset of the NN technique is the retrieval of rainfall at the limits of the zone where no information is available. In figure 7-6 for the Yaounde mapping we can see a blue zone (~10mm/hr) in the north west of the city. The other techniques tend to the average the observed rainfall at the edges (where there is no spatial correlation with the observed data). The neural network is able to learn from previous rainfall events patterns of spatial distribution from limited information. More examples of fields are included in Appendix 6. Figure A12 of the appendix 6 show a case where the comparison of the NN output to the reference rain field is not as good as in figure 7-6.

Chapter 7: Rain maps from CML estimations: comparison of methods including a neural network approach

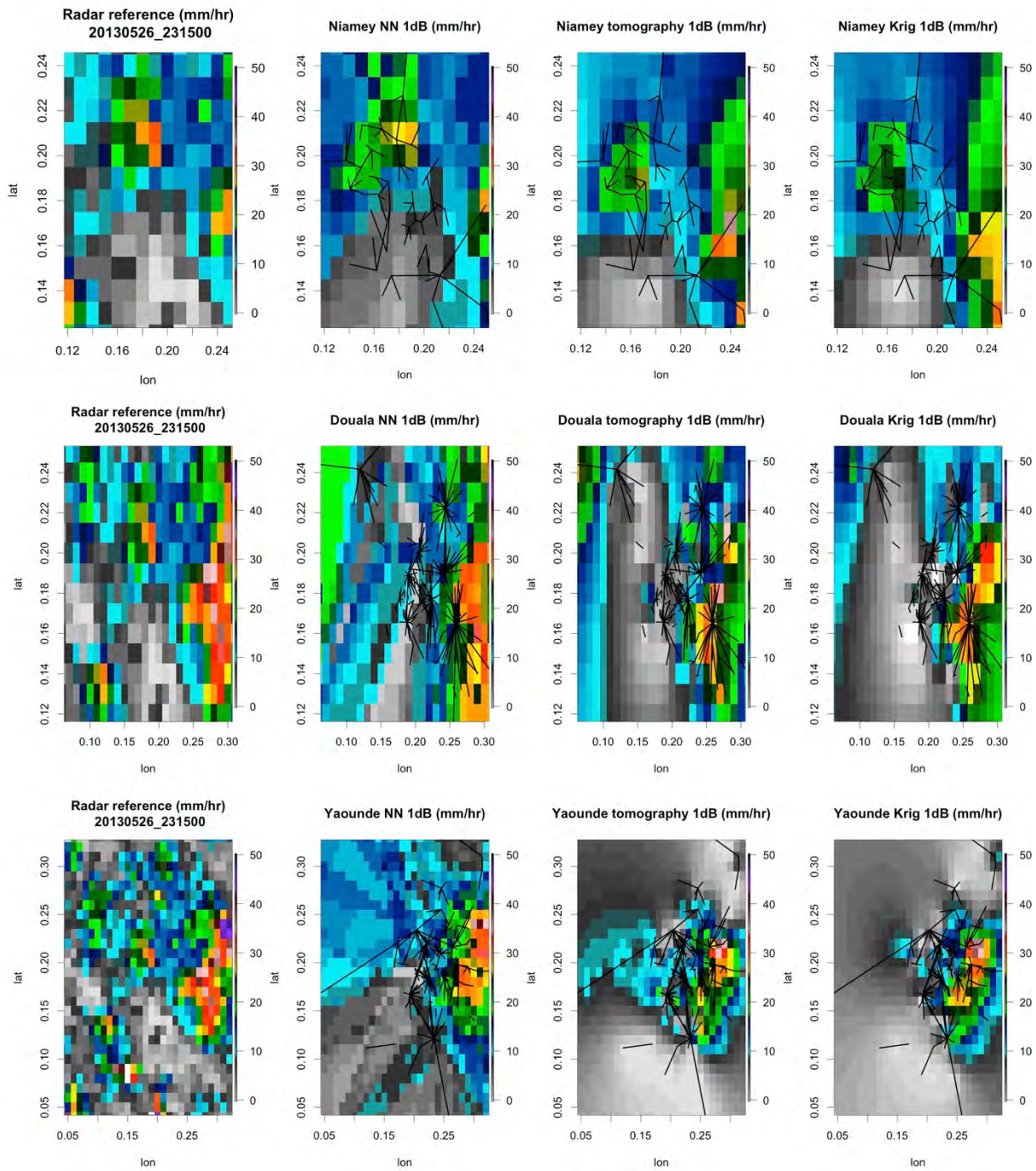


Figure 7-6: Example of mappings for the three methods (columns) and the three different CML networks (lines). Left column is the radar reference field from which are extracted the artificial CML measurements.

7.4.1 Metrics for maps validation

The mapping methods are evaluated by creating scores maps. Each score is calculated for each pixel in the series of the 722 rainfall fields from the season 2013 (figures 7-7 and 7-8). The zone 1 provides 276 rainfall fields, the zone 2, 213 and the zone 3, 232. The Neural Network applied to the artificial CML data from a zone was trained with data from the other two zones. The three trained NN are used in order to validate the fields in the three zones.

The metrics of the comparison is based on two scores. The relative bias defined as:

$$RB = \frac{\overline{R_{CML}}}{\overline{R_{radar}}} \quad (eq. 7.10)$$

Where the bar denotes the mean of the series. R_{CML} the rainfall estimated with a mapping method of the CML and R_{radar} the reference radar rainfield.

And the Pearson's correlation coefficient:

$$R^2 = \frac{(\sum(R_{CML} - \overline{R_{CML}})(R_{radar} - \overline{R_{radar}}))^2}{\sum(R_{CML} - \overline{R_{CML}})^2 \sum(R_{radar} - \overline{R_{radar}})^2} \quad (eq. 7.11)$$

7.4.2 Mapping efficiency of the methods

Figures 7-7 and 7-8 show the R^2 and bias maps for the three methods ordered by columns and for the two attenuation resolutions, 0.1 dB and 1 dB. The results shown are for the maps using the network of Yaoundé. All the score maps for the three city networks are in appendix 4.

In figure 7-7, representing the R^2 over the series of maps, some interesting features appear:

- The Neural Net mapping presents more high values of R^2 than the kriging and inversion.
- The high values for the neural net are clustered in the region near the CML: the R^2 is uniform inside the region on which information exists

Chapter 7: Rain maps from CML estimations: comparison of methods including a neural network approach

- The peaks of R^2 appear on the nodes of the CML network for the NN technique, where redundant information exists. Not true for the kriging and inversion, where the nodes can carry controversial information.
- The three techniques exhibit similar performances outside the CML dense zone, where no information exist.
- As expected the R^2 is impacted by the 1 dB sensibility compared to the 0.1 dB. However, the NN still perform better than the kriging and inversion.
- The inversion technique shows better results along the isolated links
- Inversion and kriging are more network-dependent as they do not handle the sampling limitations.

Figure 7-8 presents the absolute bias maps for the series of events. The maps show the following features:

- There is a global bias (yellow field) on the inversion and kriging coming from the artificial bias addition of -0.5dB in equation 7.9. The NN can partially correct it.
- It exists a strong east-west bias gradient caused by the MCS movement which is less exaggerated in the NN.
- The bias addition on the attenuation values in eq. 7.9 was set to test the ability of the NN to correct a global bias. In real cases global biases can occur such as wet antenna attenuation. If collocated CML and radar data is available, the neural network can be trained with biased data to have correct outputs.

Chapter 7: Rain maps from CML estimations: comparison of methods including a neural network approach

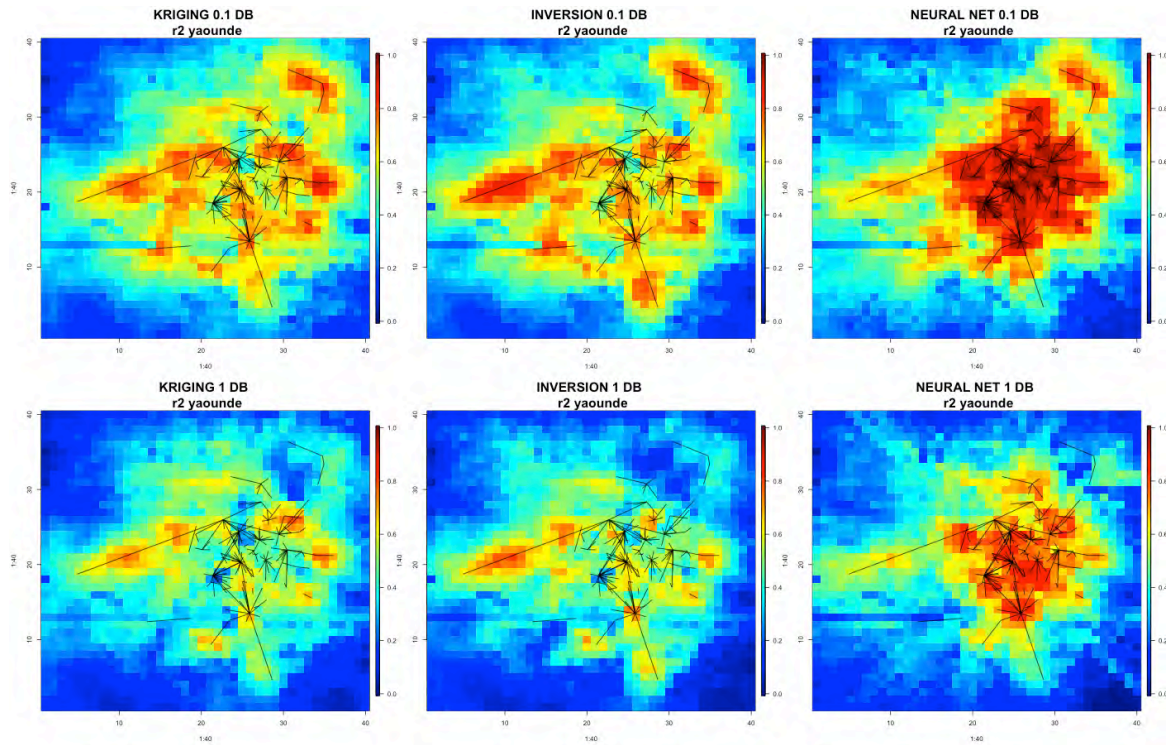


Figure 7-7: R2 maps of the three mapping methods compared to the reference radar rain field for the whole events for 0.1dB and 1dB quantization step (network of Yaoundé). Notice the high values and homogeneity of the R2 for the NN method. Also notice the intermittency of low R2 values in kriging and tomography due to non-detections by short links.

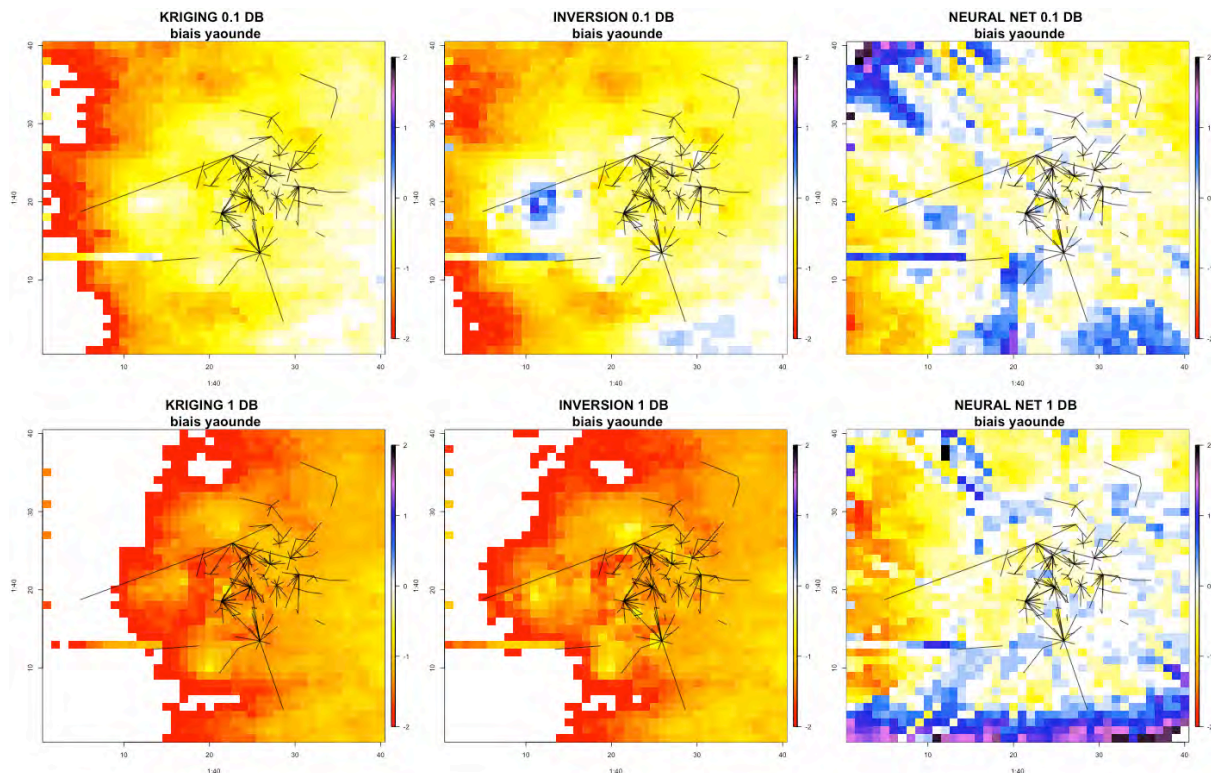


Figure 7-8: Bias maps of the three mapping methods compared to the reference radar rain field for the whole events for 0.1dB and 1dB quantization step (network of Yaoundé). Notice the low bias (white zones) for the NN method compared to the negative bias in the other methods.

7.4.3 Global comparison

This section presents the global comparison of the mapping methods in the form of a Taylor’s diagram. The diagram is based on the relation between centered root means square difference, the standard deviation and the correlation coefficient. The relation lets to have the three scores in the same figure. Figure 7-9 presents the Taylor’s diagram for the three mapping methods represented by different dots. Each different CML network is represented by a different color. The four Taylor’s diagrams present the comparisons to the reference (radar) at 0.1 dB (left columns) and 1 dB (right column), for the pixels with information (crossed by a link) in the first row, and all the pixels in the second row. The

Chapter 7: Rain maps from CML estimations: comparison of methods including a neural network approach

tomography technique is performed on the pixels with information (crossed by a link). The other pixels are filled by kriging.

In the Taylor's diagram the reference (radar) is situated at coordinate [1,0] in green. The closer the point, the better the comparison. We can compare the different points in terms of correlation, represented by the angle from the X -axis. The standard deviation compared to the reference is represented by the range distance of the points and the RMS difference represented by the distance to the reference (point [1,0]).

We can see that at 0.1 dB sensibility, for the pixels with information there is a significant contribution of the NN in terms of correlation, RMS and standard deviation. The result holds for a 1 dB sensibility if we compare the methods by CML network (colors).

However, the NN method does not improve the results when comparing all the pixels in terms of R and RMS. While the distributions remain closer (standard deviation).

The NN bring coherence to the pixels with information as shown in the scores maps of figures 7-7 and 7-8. The rainfall is better estimate with the NN in zones with high density of CML.

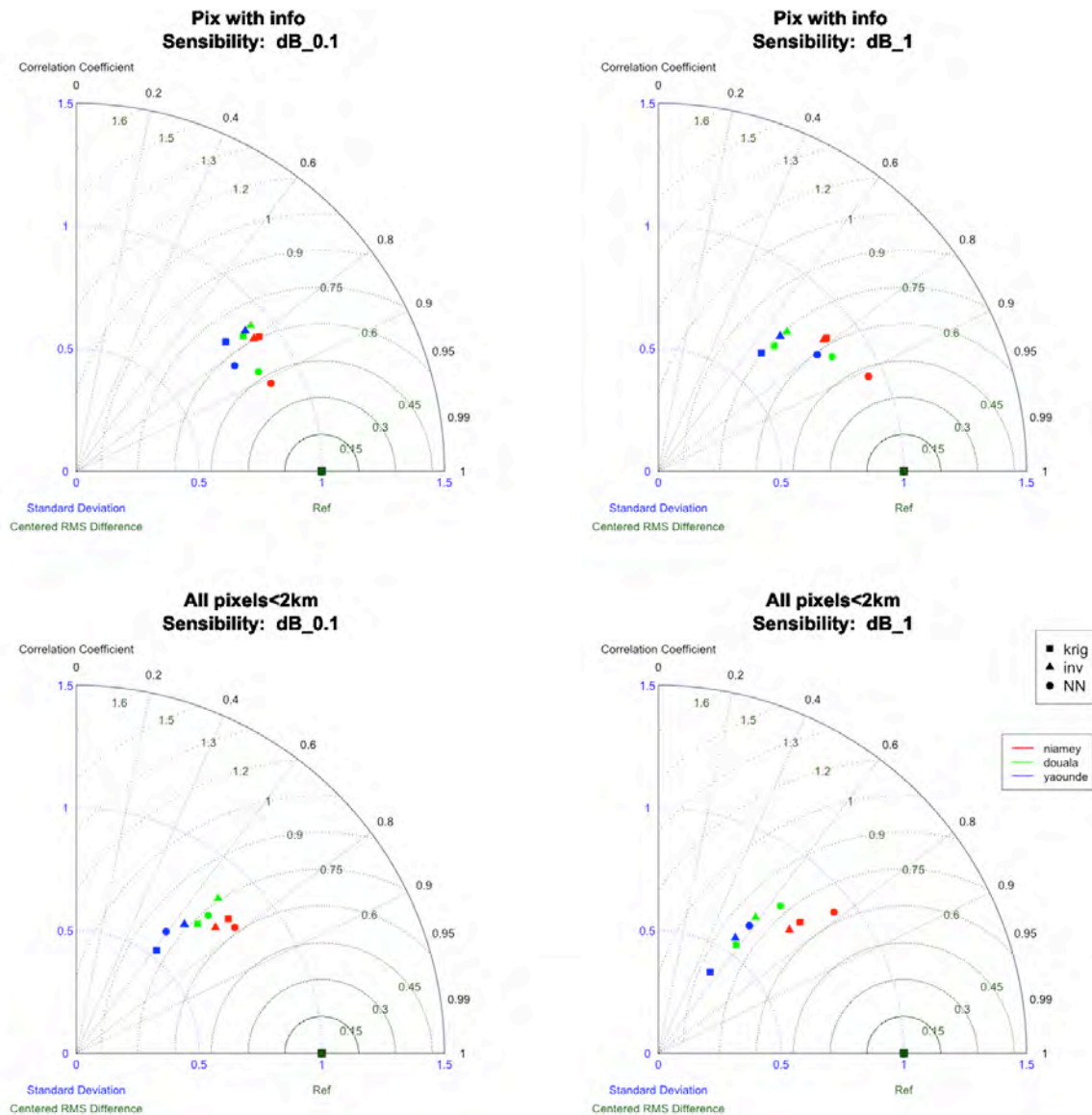


Figure 7-9: Taylor’s diagrams of the three methods for each different network. Left panels are for 0.1 dB quantization step. Right panels for 1dB quantization. The reference (radar fields) is on the [1,0] point. Note the that the circles have a higher correlation, lower RMS and closer standard deviation compared to the other methods for a single network topology.

7.5 Results on real data

In this section we show the application of the mapping methods to real CML data using the three NN trained with the artificial CML data generated with radar fields. To validate the maps, we adopt a cross-validation methodology, which consists in removing a CML, make the mapping without it and comparing the retrieved rainfall to the removed CML observed rainfall.

7.5.1 Data Niamey

We have used the CML data of Orange Niger presented in chapter 6. The attenuation from the wet antenna effect is presented in chapter 6, we used the calibration model 3bis (considering a wet antenna depending on rainfall).

We computed the maps for the 2016 and 2017 rainy seasons using the three NN trained with the artificial CML extracted from radar rain fields presented in section 7.2. The NN used in this section were trained with a dataset of artificial CML where no bias was added: equivalent of removing the factor -0.5 dB of equation 7.9.

We applied the three mapping methods for the events of 2016/2017 season with daily rainfall accumulation greater than 10mm/hr representing a total of 21 events and 253 15-minutes time steps. The average number of 15 minutes steps by event is 12 (3h rainfall duration) with a maxima of 28 time steps for the 14 June 2017 event.

7.5.2 Cross-validation methodology

The cross-validation method consists in mapping the rainfall while removing one CML. Then we compare the retrieved rainfall in the path to the removed CML. Due to the high uncertainty of short CML (Chapter 5 and 6) we used only the CML longer than 2 km for the cross-validation.

The total number of CML with $L > 2\text{km}$ in Niamey is 12. For each 15-minutes time step we apply the algorithms 12 times, each time removing one CML. We obtain a cross-validation dataset of 2300 couples of values (for each trained NN).

7.5.3 Results

Figure 7-10 presents the global results in a Taylor's diagram equivalent to figure 7-9. The reference corresponds to the rainfall seen by the CML removed from the analysis. For the cross-validation with real data the three methods show similar results in terms of correlation coefficient and RMS compared to the results using the artificial dataset in section 7.3.3. The three different NN show a variability in terms of standard deviation from the reference, specially NN2.

Table 7-4 show the false alarm rate (FAR), the non-detection rate (NDR), the hits and the zeros for each method. The FAR, TND, hits and zeros are defined against the total number of couples. The four values are calculated with a threshold of 1mm/hr. The NN show a lower TND and a bigger TFA compared to tomography and kriging.

Table 7-5 show the scores of the different methods for the series of cross-validation couples. The correlation coefficient is slightly higher for the tomography and kriging and the RMSE slightly lower. The bias is lower for two of the three NN.

When using real data from CML the benefits of the NN shown in the simulation in section 7.3 are no longer present. Some elements can explain the different results with real CML observed data:

- The modelization of the CML observations in equation 7.9 used to create artificial dataset is incomplete: the modelization of the uncertainty should be addressed to better characterize the measure of a CML.
- If the uncertainty is addressed, the Neural Network could be trained with the link length as an input as the uncertainty is higher for smaller links (scatterplot of chapter 6 figure 6-19). Training such NN could potentially decrease the relative weight of small CML when mapping rainfall for real data. In the NN presented in this section the small CML were considered as "perfect", only the minimal detectable rainfall was considered.

Chapter 7: Rain maps from CML estimations: comparison of methods including a neural network approach

- The wet antenna effect as showed in chapter 6 is high. To correct the wet antenna attenuation, we considered both antennas wetted. We establish different calibration models: one for a constant wet antenna attenuation, another with a rainfall dependent wet antenna. The CML network carries information about the spatial distribution of the rainfall. Thus we could consider training a NN from artificial measurements of attenuation calculating a wet antenna attenuation for each antenna considering the rainfall rate at the antenna location and the corrected model from (Leijnse et al. 2008).
- In this study we focused on the sampling problem of CML concerning minimal detectable rainfall. In real observations the non-detections due to the correction of the wet antenna are more significant than the non-detections due to the minimal detectable rainfall.
- Finally, the cross-validation is limited by the inherent noise of the validation data. To fully train and validate the NN, collocated observations from radar and CML should be used. Using collocated observations could remove biases on the CML (if we consider no biased radar reference data) and learn the patterns of the rainfall for a location and season.
- The NN showed a significant contribution in pixels with information (figure 7-9) in the simulations. The cross-validation was made mainly on pixels without information as the CML was removed from the analysis.

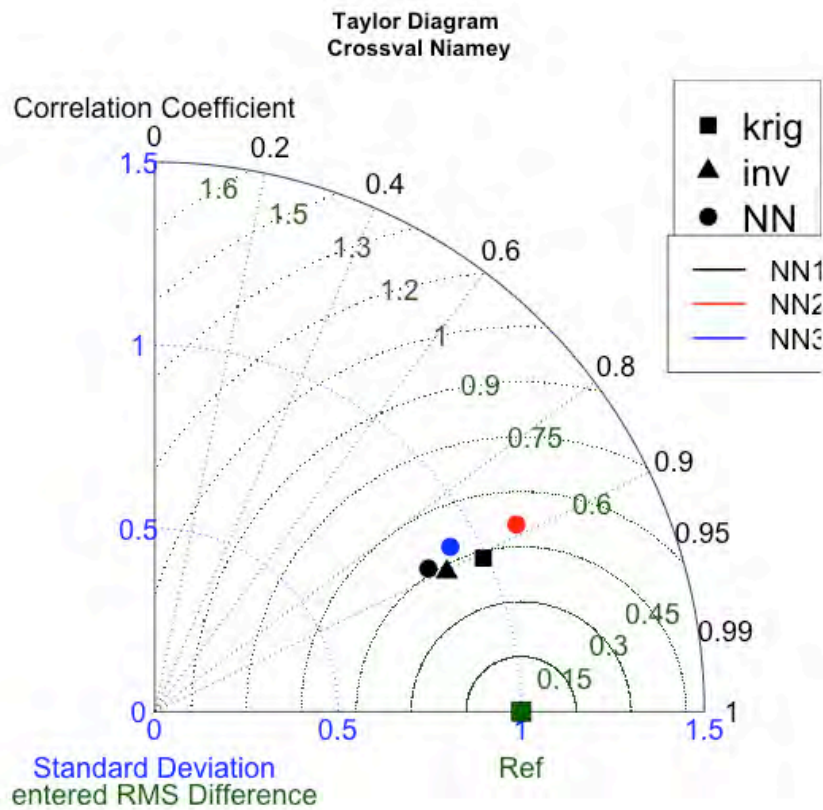


Figure 7-10: Taylor diagram of the three methods of interpolation applied to real data for Niamey 2016/2017 cross-validation with links longer than 2 km. The three NN described were applied to check the variability among them.

Algorithm	FAR (%)	NDR(%)	Hits(%)	Zeros(%)
Krig	13.3	2.0	79.5	5.0
Tomography	12.8	1.8	79.8	5.6
NN1	14.2	1.3	80.3	4.1
NN2	14.5	0.9	80.7	3.9
NN3	14.7	0.7	80.9	3.6

Table 7-2: Detection scores of the different methods in the cross-validation

Algorithm	Bias (mm/hr)	Rel. Bias(%)	RMSE (mm/hr)	R
Krig	-1.3	-10.1	7.8	0.90
Tomography	0.6	4.5	7.6	0.90
NN1	-0.4	-3.0	8.2	0.89
NN2	-2.0	-16.1	9.2	0.89
NN3	-0.2	-1.2	8.6	0.87

Table 7-3: Scores of the different methods in the cross-validation

7.6 Discussion and perspectives

We have shown with simulations that a simple NN architecture with a reliable artificial training data set can be an alternative method to map rainfall from CML information. The technique account for the sampling deficiencies inherent to the measure of rainfall by CML. The minimal detectable rainfall is a limitation when considering a sensitivity at 1 dB for short links. In order to use all the available information our method show better results than others in the pixels with dense information (kriging and inversion) which do not account the sensitivity. The maps are less smoothed than those from kriging (or inversion). It is possible to create ensembles by training different NN from different data which may be a tool to assess the uncertainty on the spatial distribution of rainfall.

When applying to real data the benefits of the proposed method are equivalent (not better) to previous methods. In order to improve the method for real data, we can model the uncertainty and the wet antenna attenuation of the simulated CML measurements. A better solution could be to train NN with real collocated radar and dense CML network.

This preliminary results show the potential of NN to interpolate data from inhomogeneous sources. The training data set can be improved by using real collocated measures from radar and CML. As the real data is affected by errors which may be antenna dependent

Chapter 7: Rain maps from CML estimations: comparison of methods including a neural network approach

(wet antenna depending on the equipment) or by different atmospheric situations (relative humidity increase during rainfall) the training of a NN with real data and a reference rainfall field could improve the results. In this situation, a NN could absorb the bias of the CML measured rainfall.

Another interesting feature of NN is that secondary information such as temperature or humidity can be added to the input data set of the NN to improve the regression of rainfall. In other climatic regimes, where there is seasonal variability in the precipitation systems, the season, or month can be added as an input variable. We can also consider the topography of a region affecting the rainfall rates by adding it to the input, similar to a co-kriging method.

We have seen in the results section that the density of the network is a key factor regarding the comparison with other methods. As the network density decreases, the tomography method shows better results. The tomography shows better results with isolated CML. On bigger scales with lower network density we can investigate the combination of CML with satellite data from either microwave low orbit satellite or IR geostationary data to retrieve combined CML-satellite rainfall products from machine learning algorithms.

The training dataset for this study was limited to one season of radar data in the Sahel. The MCS are organized systems which represent large areas of rainfall. Such technique for different climatic zones, with sparse rainfall could not be an efficient solution.

CONCLUSIONS AND PERSPECTIVES

FIRST PART

In the first part of this manuscript we have introduced the precipitation observation with polarimetric weather radars. We have then presented two original techniques to retrieve information on the hydrometeors characteristics with the modeling of the remote sensing observation.

The first inversion is based on a simple model of the hydrometeors melting layer as seen by radars. The bright band is a peak of reflectivity seen by radars caused by the bigger size of melting hydrometeors compared to raindrops due to the lower density of ice crystal and the presence of water in those melting crystals. The shape of the bright band is driven by different processes: fall speed, temperature gradient, break-up, aggregation of particles and the density of the falling particles. As different studies already shown the properties of the BB depend on the particles density and type. In the showed study we demonstrate that the BB shape could be used to infer the particles' density law above the bright band.

By simplifying the model considering a fixed melted fraction depending on the height, we can derive shapes of bright band depending only on the particle size distribution and the pre-factor of the density law. With a simple three parameters inversion for each vertical profile of reflectivity we found pre-factors of the density law close to that observed in-situ by the on flight probe (Fontaine et al. 2014). We also found denser particles when approaching the convective front, in agreement with the hydrometeor

Conclusions and perspectives

classification retrieved by fuzzy logic with polarimetric radar observation, presented in the companion paper (Cazenave et al. 2014). Three important simplifying assumptions where:

- No aggregation or break-up of particles during the fall
- Observed VPR considered as the real VPR
- Fixed degree of melting during the fall depending only on height

The aggregation and break-up of the particles during the fall lead to changes in the DSD and thus can generate errors in the density estimation as the shape of the BB is sensitive to the DSD. The DSD (or PSD) evolution during the fall could be assessed with the DSD inversion presented in chapter 4, at least on the rainfall layer. By inverting polarimetric radar variables at different radar PPI elevations and studying the vertical evolution of the DSD, we could evaluate break-up and aggregation rates during fall.

The second assumption of the BB inversion rely on considering the observed VPR as the real VPR. As the scanning volume resolution of the radar echoes increase with the range, the apparent VPR is smoothed for high ranges, because of the rougher vertical resolution. This effect is attenuated by selecting the radar pixels within 25 km radius to construct the VPR. If this method should be implied for higher radar ranges a VPR correction need to be addressed as (Kirstetter et al. 2013).

The third assumption follow (Boudevillain and Andrieu 2003) by considering a fixed symmetric vertical profile of melting fraction of the hydrometeors. A more complete description on the real thermodynamics of the melting particle was made by (Klaassen 1988; Zawadzki et al. 2005). Such description could improve the physics description of the BB. But a great number of unknown parameters should be addressed. We could make the BB model more complex by increasing the observations constraining it. The other polarimetric variables could be inserted in the inversion. Then the type of the hydrometeors should be represented in the T-matrix simulations.

The second inversion of polarimetric radar data presented in chapter 4 aims to retrieve the DSD parameters of each pixel of a radar PPI. With radar polarimetry we measure three independent variables linked to the drops characteristics in the sampling volume: $[Z_H, Z_{DR}, \phi_{DR}]$. In the literature we can found different techniques to retrieve DSD parameters (Gorgucci et al. 2001a; Koffi et al. 2014; Raupach and Berne 2017). All these

Conclusions and perspectives

studies rely on empirical relationships between DSD parameters and radar variables. Also the proposed studies did not account explicitly for radar attenuation in the DSD retrieval. In the West-African context of strong convective rainfall rates, and X-band radar observation, the attenuation correction is a crucial step for QPE or DSD retrieval (Kacou 2014). In the proposed inversion method, we account explicitly for attenuation as we use as input variables the non-corrected from attenuation radar variables. Three parameters of a gamma DSD [D_m , N_0^* , μ] are retrieved at each range gate along a radial. The procedure avoids using the common two steps procedure (attenuation correction and DSD parameters retrieval) which can lead into errors. The direct model to calculate polarimetric observables from oblate drops is based on the T-matrix model (Mishchenko, Travis, and Mackowski 1996).

The presented framework ensures a global consistency between the retrieved DSD and all the radar variables. The inversion it is made at once for each radial in an iterative procedure. This radial-based inversion can make use of strong constraints, as the total differential phase shift at the last gate, insuring coherence and robustness. As a priori guess (algorithm initialization) we used the empirical DSD parameter retrieval from polarimetric variables found by (Koffi et al. 2004).

The inversion output was compared to in-situ DSD data recorded by a disdrometer located at 20 Km from the radar showing good consistency between observed and retrieved DSD. Some events present although bias on the retrieved N_0^* .

The major assumption of the inversion is the drop shape law. The sensitivity tests on the drop shape laws showed the high dependency of the results to that assumption. The future version of the algorithm could include an additional parameter linked to the aspect ratio law similar to the β -method by (Gorgucci et al. 2002). The β parameters is the linear coefficient of the oblateness-diameter shape law. Also we can include a Z_H or Z_{DR} calibration to correct from possible wrong calibration of the polarimetric variables.

The presented study was validated with one disdrometer at 20 km from the radar. A future validation with more disdrometers, located farther of the radar, could test the ability of the method to estimate the attenuation.

The high dimension of the problem (650*3 x 650*3 matrices) and the high non-linearity (exponential decrease of Z_H due to attenuation) make the iterative algorithm slow for real time applications. Also, the high non-linearity makes it sensitive to the a priori initial state.

Conclusions and perspectives

However, the method combine all the available polarimetric information using a physical model of the observation to retrieve DSD fields consistent with the observations. With the proposed methodology we can impose global physical constraints either in integrated quantities (imposed total differential phase shift) or on the solution (correlation between radial gates, or correlation between retrieved variables).

SECOND PART

The second part of the thesis address the rainfall observation using microwave links. In the initial chapter we described the principle of rainfall rate estimation from raw attenuation data of a microwave link telecommunication companies. First the raw attenuation can be easily calculated from the raw transmitted and received power of the microwave link. An important step follows to estimate the rainfall induced attenuation. For that purpose, the wet and dry period detection and the baseline level detection (attenuation level without rainfall) algorithms are applied. The wet/dry and baseline detection algorithms depend on the fluctuations and temporal drift of the attenuation signal. In the simple case of low noise signals without temporal drift, the usual algorithms used in the literature are based on thresholds of the attenuation (thresholds on the attenuation variability or on the attenuation values). Then a K-R power law is used to convert the estimated rain induced attenuation into rainfall rate. The K-R law can be estimated using DSD parameterizations or DSD measurements from disdrometers.

Other sources of attenuation can bias the raw attenuation signal. Among them, the more important is the wet antenna attenuation caused by the presence of a water film over the antennas of the link during rainfall. Other sources of attenuation can cause errors in the rainfall estimation: humidity variation, fog or dust are some of them.

The rainfall spatial variability in the CML is a source of uncertainty specially for non-linear K-R laws. The K-R law can also be a source of error if a wrong parameterization of the DSD is used. The baseline detection algorithm can lead to wrong detections and false alarms leading to an error in the rainfall accumulations. The quantization step of attenuation, if it is rough, it adds uncertainty on the rainfall retrievals, specially for small CML. Also the sensitivity of the CML to rainfall is affected by a rough quantization step. The type of variable sampled the telecom companies and the sampling is also a source of

Conclusions and perspectives

uncertainties. Some companies provide only maximum attenuation values. Then a correction must be done.

Chapter 6 of the thesis was focused on a real dataset of attenuation of CML from Orange company in Niamey, Niger. The data from 92 CML during two seasons was provided at 15 minutes' time step. Three tipping bucket raingage at 5 minutes were used to calibrate the rainfall retrievals. First a data quality control is used to filter CML with suspicious data. The quality control is based on the correlation of each CML with the other depending on the distance. As the rainfall fields are spatially correlated, the pattern of the correlograms are a proxy of the quality of the data. Some CML were removed from the analysis with this argument.

Later we used all the gage/CML collocations to test three calibration models. The objective of the calibration is to find the best $[a, b]$ parameters from the K-R law and the best wet antenna attenuation which fits the rain gage data. The different models consider one, two or three varying parameters, as we have a theoretical K-R law calculated from observed DSD in the zone. In the third model we have considered a rainfall dependent wet antenna attenuation.

We evaluate the robustness of the models by a bootstrapping test. The bootstrapping showed that the fitted parameters of model (model 1) are less robust than the other models. Model 1 seems to over fit the data, and the retrieved $[a, b]$ are not physically coherent. The retrieved a of the K-R law from Model 2 has low variability in the bootstrapping, showing robustness. Also the retrieved a^{fit} is close to the theoretical a^{th} from K-R relation calculated with observed DSD. Model 3 has also a low variability of the retrieved parameter, the scaling parameter of the wet antenna model of [Leijnse et al 2008.].

Model 3 needs the solution of an equation for each collocation as the wet antenna attenuation depends on rainfall, which is unknown. When using only the attenuation (not ancillary information from rain gages) and optimizing the scaling parameter, model 3 give the best results in terms of bias. The remaining bias show low dependency on the CML length and rainfall rate compared to model 1 and model 2. Considering a rainfall independent wet antenna attenuation (model 1 and model 2) induce a bias which depend on the rainfall rate and CML length.

The resulting daily time series, when filtering well enough the outliers CML show a very good consistency with rain gages, with R2 in the order of 0.7 and bias around [-10 ; 10%].

Conclusions and perspectives

However, there is a remaining effect on the link length. Long links underestimate compared to short links which seems to overestimate. We show an effect of the different sampling on the CML and the raingage. The different sampling is driven by the link length. Using the retrieved DSD fields of chapter 4, we simulated CML and raingage sampling to show the effect. However, the retrieved number are difficult to compare due to the limited number of CML observations.

Instead of estimating the wet antenna effect by minimizing the observed attenuation with raingage observations we could made a dedicated experiment in the zone to estimate the wet antenna effect. By installing several disdrometer (or rain gages) in a CML path we could deduce the wet antenna effect for different rainfall rates.

The final chapter is about combining the information from a spatial network of CML to create rainfall maps in a regular grid. We presented an original, potential technique, based on machine learning to map rainfall from limited spatial information.

We find in the literature different techniques to interpolate rainfall from linear averages from dense CML networks. Two common techniques are based on simple kriging from Geostatistics theory, and tomography, from inversion theory. For the simple kriging we consider the CML as a punctual rainfall measurement. It is enough for low density CML measurement, but for dense measurement we lose the spatial information provided by the link path location. The tomography uses the location of the link's path to find a possible solution, constrained by a spatial covariance imposed. Both techniques cannot include the sampling uncertainty caused by the attenuation quantization step of the attenuation.

In order to train a neural network we create a synthetic dataset of CML observation from rainfall radar fields. In the synthetic data we have simulated the quantification step of the attenuation. The neural network was trained with the reference radar field as output and the simulated CML observations as input.

The resulting rainfall fields from the NN present variability of rainfall at the edges of the zone. A common issue with interpolation techniques is in the edges, where the interpolated value tends to the average of the observations. The NN can predict values other than the average. When comparing the R2 maps, and bias maps of the three techniques, the NN can bring coherence in the zones where the information is denser (ie. the nodes of the CML). The introduced bias on the artificial data is corrected by the NN.

Conclusions and perspectives

When using real data the benefits of the technique are more difficult to show in that configuration. The noise of real data can hide the benefits. Using a cross-validation approach, the noise of the “validating” link can hide the improvement. Also we showed that the major contribution of the technique, at this stage, is in the pixels with information. In the cross-validation we validate by definition in the pixels without information, as the link is removed from the analysis. An future validation of the technique should be done using either collocated radar maps and MSL data or several rain gages in 1km pixels.

Also the wet antenna attenuation correction could be learned by the NN in future versions, if collocated radar data and CML data is used to train the NN. This prospective chapter showed the potential use of machine learning to map rainfall from heterogeneous sources of information, using a reference rainfall field.

GLOBAL PERSPECTIVES

The CML networks are constantly evolving. In West-Africa the population growth and wide use of mobile telephones is increasing the number of CML in populated areas. In Europe the long CML interconnecting villages, and cities are being replaced by optic fiber, but the future 5G technology will need the installation of CML at higher frequencies. Also the MW bands used for telecommunication are increasing the frequency due to the high demand and overbooking of traditional frequencies.

High frequencies are more sensitive to rainfall. Even frozen particles can attenuate signals at 80GHz or more, being potentially a source for snow rate estimation. In this thesis we showed the CML rainfall estimation without polarization. A double polarization attenuation measurement can improve the rainfall estimation. In part 1 of the thesis we show a DSD retrieval using polarimetric information. Using double polarization CML we can expect retrieving DSD instead of rainfall rates. Also double frequency CML can lead to similar approaches.

In developed countries the precipitation observation is done by networks of radars covering the countries. But still some regions are uncovered, mostly mountainous regions where radar beams are blocked by the orography. CML can be a solution to complete the precipitation observation in mountainous valleys. Then arise the question about the CML-radar merging, which opens a new field.

Conclusions and perspectives

In a large scale, we can track precipitating systems with CML networks potentially in real time. The temporal sampling of microwave precipitation satellites is poor and depend on the orbit and the location. The IR geostationary satellite can track precipitating systems at high resolution, but their quantitative estimate of rainfall has huge errors. Combination of IR geostationary tracking and CML rainfall estimation could improve the characterization and now-casting of precipitating systems.

Opportunity measures are an interesting source of data which can increase the observations in poorly equipped regions. Then come the question about how to combine heterogeneous measurements with traditional measures.

APPENDIX 1: QUASI-NEWTON ALGORITHM DEMONSTRATION

In the theory of inverse problems one often considers a non-linear model $M(X)$

describing the link between physical parameters X and observations Y_{obs} which are vectors in the parameters and observations spaces (respectively \mathfrak{M} and \mathfrak{D} spaces). The minimization techniques (considering observations and their uncertainties, physical parameters with the desired shape and a theoretical model) rely on the minimization of the misfit function S (or cost function) which can be written as:

$$2S = \|M(X) - Y_{obs}\|_{\mathfrak{D}} + \|X - X_{prior}\|_{\mathfrak{M}} \quad (eq. A1.1)$$

The misfit function can be seen as the sum of the distances separating the model with its parameters $M(X)$ to the observation Y_{obs} set plus the distance separating the parameters X to the a priori value of the parameters X_{prior} . The distance is computed in two different spaces \mathfrak{M} and \mathfrak{D} with their own metrics. The metric of the observation space \mathfrak{D} is defined by the uncertainties related to the observations and their correlations. Although the metric of the parameters space \mathfrak{M} is related to the variability of the parameters and their covariances. In the simplified situation of independent covariance in X and Y one can write the relation in A1.1 as:

$$2S = \sum \frac{|M(X) - Y_{obs}|}{\sigma_D} + \sum \frac{|X - X_{prior}|}{\sigma_M} \quad (eq. A1.2)$$

Where σ_D is the uncertainty related to the observation, and σ_M is the variability of the solution. The solution of an inverse problem should be interpreted as a distribution of probabilities as the observation and also the X_{prior} are interpreted as a PDF. The resulting PDF can be seen as a Gaussian for linear problems, and getting away from Gaussian as the problem is getting away from linear. The expression in 1 can be write in matricial notation as:

$$2S = (M(X) - Y_{obs})^t R^{-1} (M(X) - Y_{obs}) + (X - X_{prior})^t B^{-1} (X - X_{prior}) \quad (eq. A1.3)$$

Where R and B are the covariance matrix of observations and a priori respectively. Minimizing A1.3 means to find a compromise between observation, its errors and the a priori knowledge on the solution. Many minimization methods rely on the gradient γ of model S , to find the “descent path” to the solution. That methods are very efficient in

Appendix 1: Quasi-Newton algorithm demonstration

problems which are not too far from linear. For strongly nonlinear problems one can converge to local minima and other techniques are suitable. The gradient of the misfit function at the point X_0 : $\gamma_0 = \frac{\partial S}{\partial X}$ from equation A. 1.3:

$$\gamma_0 = J_0^t R^{-1} (M(X) - Y_{obs}) + B^{-1} (X - X_{prior}) \quad (eq. A1.4)$$

Where $J_0 = \frac{\partial M}{\partial X}$ is the gradient of the model M at point X_0 (the Jacobian matrix). The Jacobian matrix can be sometimes determined explicitly. Many problems use indeed numerical methods such finite differences (as we use in our problem).

The Hessian matrix ε of the misfit function (second derivatives of J) can now be write from A. 1.4:

$$\begin{aligned} \varepsilon_0 &= \frac{\partial \gamma_0}{\partial X} = J_0^t R^{-1} J_0 + B^{-1} + \frac{\partial J_0}{\partial X} R^{-1} (M(X) - Y_{obs}) \\ \varepsilon_0 &\approx J_0^t R^{-1} J_0 + B^{-1} \quad (eq. A1.5) \end{aligned}$$

Considering only the first terms of the derivative.

Now if we consider the series development of gradient of the misfit at first order around X_0 we have:

$$\gamma(X) \approx \gamma_0 + \varepsilon_0 (X - X_0) \quad (eq. A1.6)$$

Make the steepest descent is equivalent to set:

$$\gamma(X) = 0 \quad (eq. A1.7)$$

A. 1.6 and A. 1.7 lead to:

$$\begin{aligned} X &\approx X_0 - \varepsilon_0^{-1} \gamma_0 \\ \Rightarrow X_{n+1} &\approx X_n - \varepsilon_n^{-1} \gamma_n \quad (eq. A1.8) \end{aligned}$$

Equation A1.8 is known as Newton algorithm. Replacing A. 1.4 and the approximation A1.5 in A1.8 is known as the quasi-Newton algorithm (due to the Hessian approximation) which is:

$$\begin{aligned} X_{n+1} &\approx X_n + [J_n^t R^{-1} J_n + B^{-1}]^{-1} [J_n^t R^{-1} (M(X) - Y_{obs}) + B^{-1} (X - X_{prior})] \\ X_{n+1} &\approx X_n + [J_n^t R^{-1} J_n + B^{-1}]^{-1} [J_n^t R^{-1} \delta y + B^{-1} x] \quad (eq. A1.9) \end{aligned}$$

APPENDIX 2: SELF-CONSISTENCY CORRECTION

In chapter 3 we used the self-consistency method developed by (Bringi, Keenan, and Chandrasekar 2001) as a first guess of attenuation along the radial. Then, during the inversion procedure we modify the A_h iteratively retrieved. The method is an estimation of the attenuation A_h and differential attenuation A_{dp} by constraining the cumulative attenuation in the radial by the change on the differential phase $\Delta\phi_{DP} = \phi_{DP}(r_1) - \phi_{DP}(r_0)$ where r_1 and r_0 are the ending and starting range of coherent signal. Under this constraint we have (Bringi et al. 2001 for details):

$$A_h(r) = \frac{Z_h^{obs}(r)^b (10^{0.1b\alpha\Delta\phi_{DP}} - 1)}{I(r_1, r_0) + (10^{0.1b\alpha\Delta\phi_{DP}} - 1)I(r, r_0)} \quad (eq A2.1)$$

Where

$$I(r, r_0) = 0.46b \int_r^{r_0} Z_h^{obs}(r)^b ds \quad (eq A2.2)$$

The coefficients α and b can be found from the following empirical relations:

$$A_h = aZ_h^b \quad (eq A2.3)$$

$$A_h = aK_{dp}^c \quad (eq A2.4)$$

Z_h here represents the corrected reflectivity in $mm^{-6}m^{-3}$, A_h is in dB/km , K_{dp} in $^\circ/km$. The α and b coefficient in the power law relations are sensitive to the temperature and drop shape laws. α is much more sensitive than b as K_{dp} is much more sensitive to drop shape. The coefficient b varies in the range [0.76 ; 0.84] (Delrieu, Caoual, and Creutin 1997) at X band and α varies from 0.05 to 0.11 $dB/^\circ$.

For that reason, the self-consistency correction method does not fix the α coefficient. The optimal α is chosen by comparing the calculated ϕ_{DP}^{cal} (from A_h estimation in eq A. 2.1) and the observed ϕ_{DP} considering eq A. 2.4 as linear:

$$\phi_{DP}^{cal}(r, \alpha) = 2 \int_{r_0}^r \frac{A_h(s, \alpha)}{\alpha} ds \quad (eq. A2.5)$$

The α value is chosen by minimizing the error E_ϕ :

Appendix 2: Self-consistency correction

$$E_{\phi} = \sum_{i=1}^N |\phi_{DP}^{cal}(r_i, \alpha) - \phi_{DP}(r_i)| \quad (eq. A2.6)$$

Similar to the Z_h correction, in the self-consistency method Z_{DR} is corrected by an estimation of A_{DP} :

$$A_{DP}(r) = \gamma A_h^d(r) \quad (eq. A2.7)$$

Where $d \sim 1$ in X-band frequencies. The optimal value γ of is chosen by a similar method constraining the Z_{DR} in the last gate of the radial r_0 with the corrected Z_h (Bringi et al 2001):

$$Z_{DR}(r_0) = p 10 \log_{10}(Z_h(r_0)) - q \quad (eq. A2.8)$$

Where p and q are the coefficients of empiric Z_{DR} - Z_h law which is very noisy.

APPENDIX 3: DATA QUALITY CONTROL

In order to create a reliable calibration dataset, we first made a quality control to filter suspicious CML data. The criteria used to evaluate the quality of each CML is based in the self-consistency with the rest of the network. As the distance between CML is small (few Km) with respect to the temporal sampling time (15 min) the CML should be correlated with neighbor CML and with the rain gages at 15 min.

Figure A-1 shows the correlograms of 16 CML. Each point on the correlograms represent the Pearson's correlation coefficient R between the current link an another link of the network plotted against its distance D (from the CML centers). The red dots in the figure represent the three rain gages. The correlation was calculated between the raw attenuation over both seasons, 2016-2017 and the raingage rainfall rates. The number of available time steps vary for each CML. The correlations showed in Figure A-1 are impacted by the number of samples as the R coefficient of a shorter time series is more impacted by an out layer point than a long time series. Nevertheless, the correlograms show a common structure: the correlation decrease with distance as expected. The red dots representing the rain gages are often situated near the linear fit (black line).

Among the 16 showed links, two of them present a very low correlation for all the CML distances (21-Moov Univ. and 42-Bnifando). The correlograms show no internal coherence with the CML data set and with the rain gages. We establish a decision rule to filter CML with low correlation data based on the intercept parameter of the linear fit:

$$\text{remove if } R_{fit}(0) < 0.3 \quad (\text{eq. A3.1})$$

Where $R_{fit}(D)$ is the fitted linear correlation law against distance. All the CML with a correlation R lower than 0.3 for a distance 0 was filtered from the data. Among the 166 CML (92 unique links, and 166 counting A->B and B->A), 31 where removed using the internal coherence criterion. Many of the lowest correlation points of the correlograms in figure 6-2 disappear when filtering by the above criteria.

In order to create a calibration dataset, we have used all the gage-CML rainfall collocations. For each CML the nearest of the 3 Niamey rain gages was used for comparison. The gage-CML distance was calculated from the center of the CML. For the

Appendix 3: Data quality control

2016-2017 the total number of 15' rainy time steps is 816 for 77 different days, 43 days in 2016 and 34 days in 2017. The non-detections and false alarms from the CML were filtered: only the hits were used in the comparison to avoid the effects of rain/ no-rain detection algorithm and focus on the wet antenna effect and the K-R law. The total number of CML-gage couples of observations is 26690. Figure 6-3 show the number of samples by raingage rainfall class and by CML length. The CML length class (1,2] km is overrepresented and the more intense rainfall the lower number of samples.

Appendix 3: Data quality control

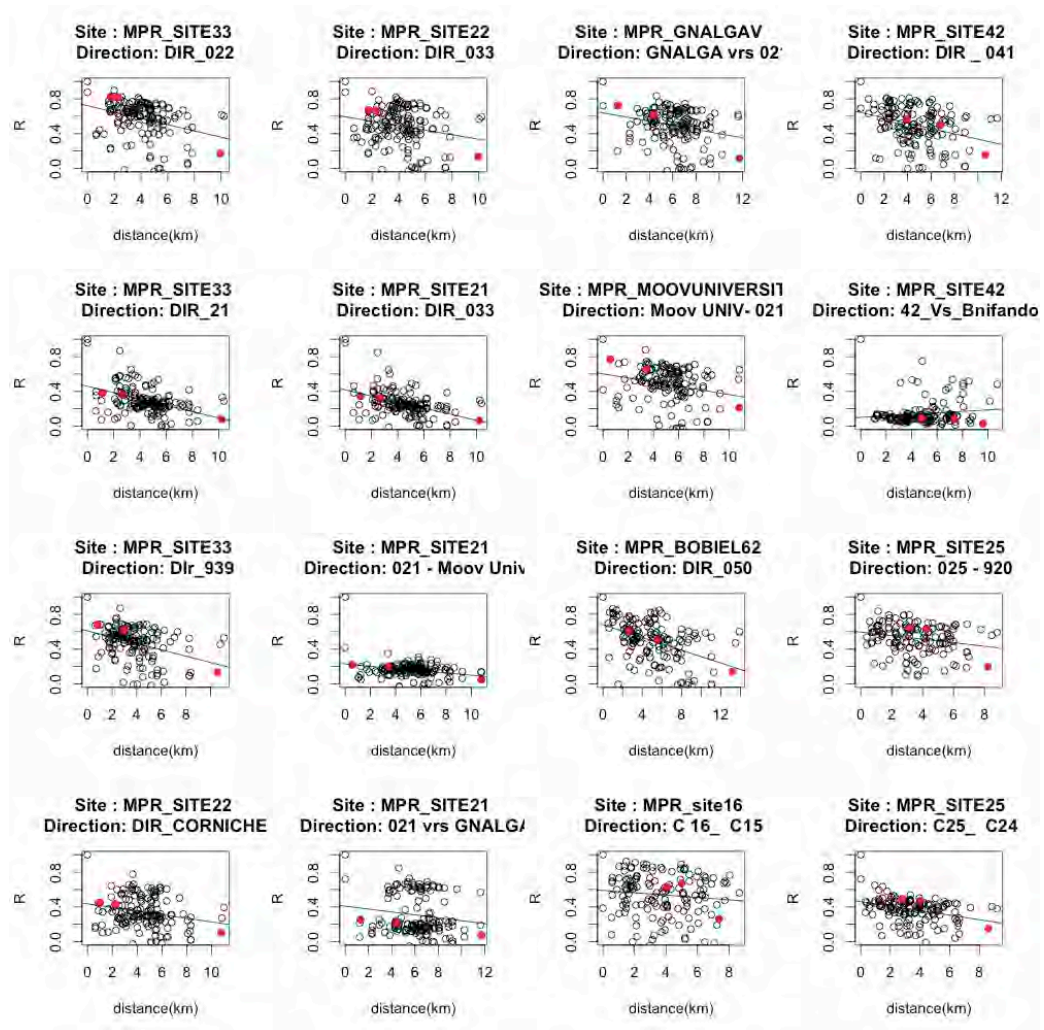


Figure A 1: Correlograms for 16 CML in Niamey. Correlation to the other CML in the network plotted against distance between CML. Red dots indicates the correlation with the three rain gages

APPENDIX 4: MINIMIZATION OF CALIBRATION PARAMETERS OF CML-GAGE DATASET IN NIAMEY

Model 1: 3 parameters minimization

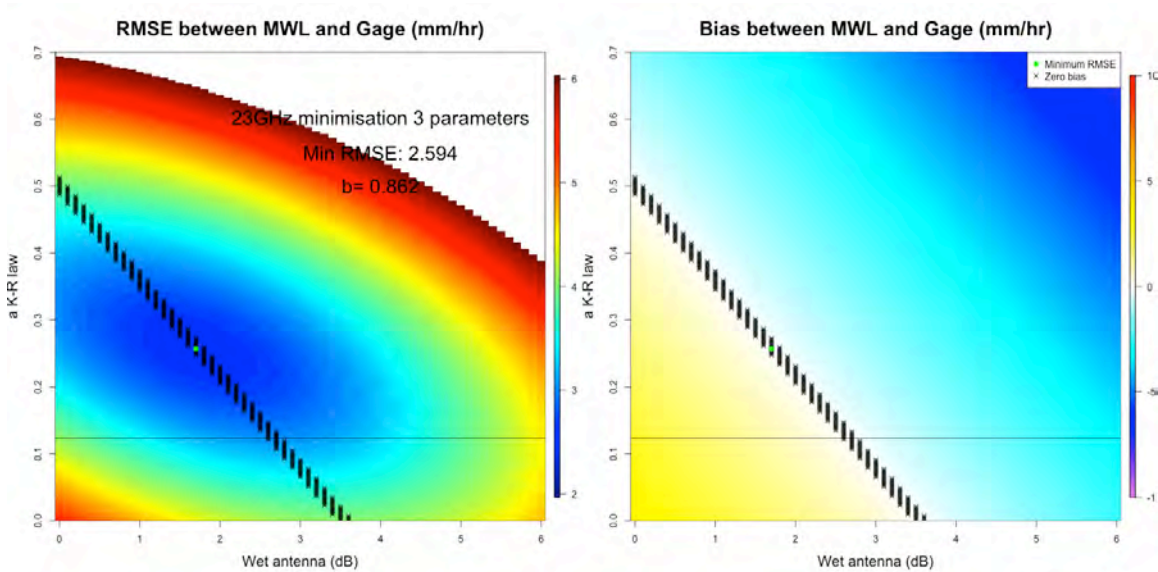


Figure A 2: Example of attenuation minimization for model 1 (not filtered) 23GHz in the a -WA space for $b=0.862$ (minima). Left figure show the attenuation RMSE and right figure the bias.

Appendix 4: Minimization of calibration parameters of CML-gage dataset in Niamey

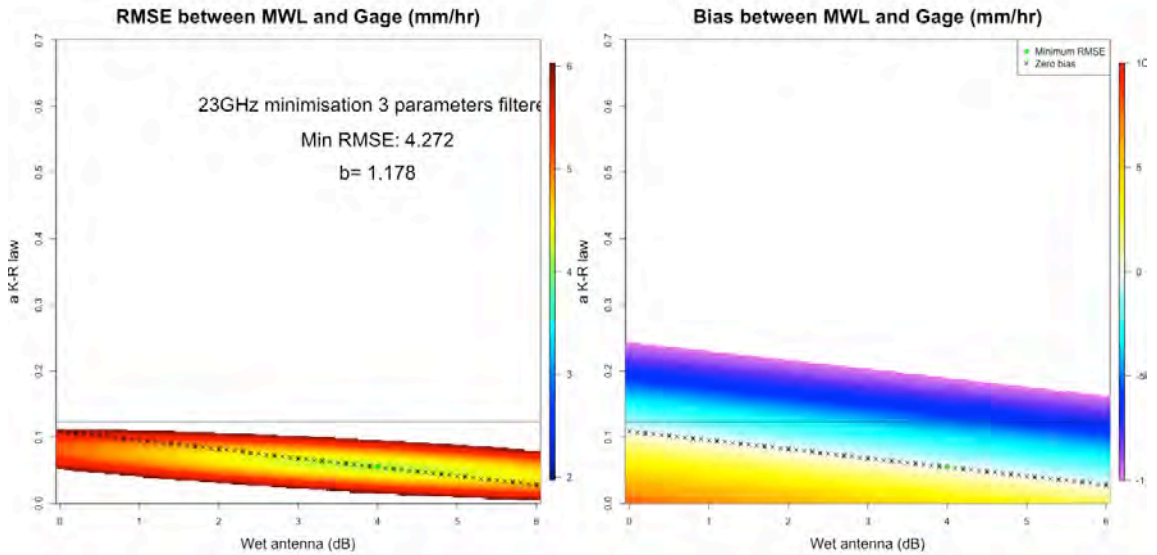


Figure A 3: Example of attenuation minimization for model 1 (filtered) 23GHz in the a-WA space for b=0.862 (minima). Left figure show the attenuation RMSE and right figure the bias.

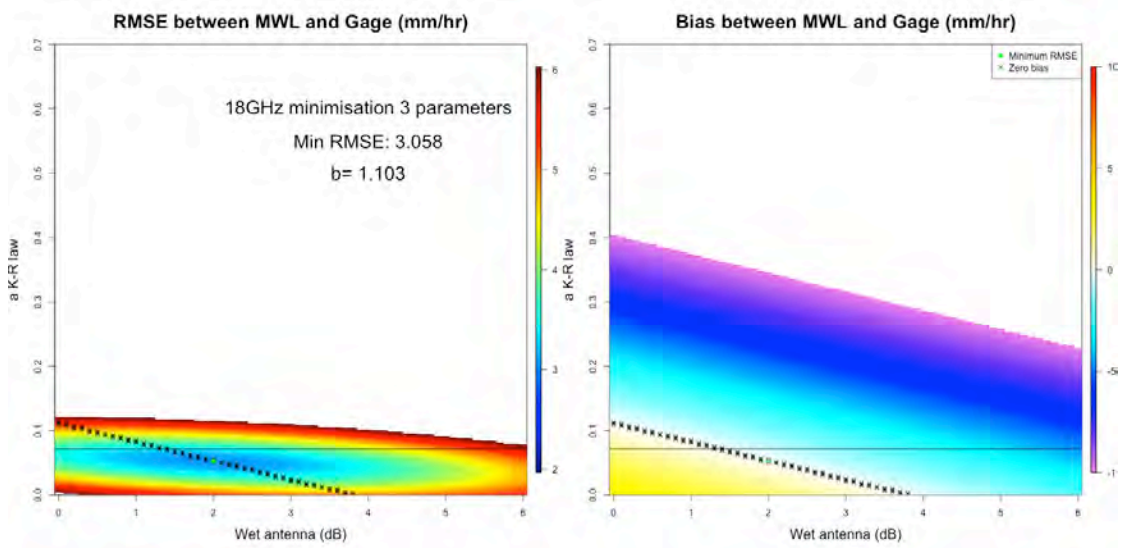


Figure A 4: Example attenuation minimization for model 1 (not filtered) 18GHz in the a-WA space for b=0.862 (minima). Left figure show the attenuation RMSE and right figure the bias.

Appendix 4: Minimization of calibration parameters of CML-gage dataset in Niamey

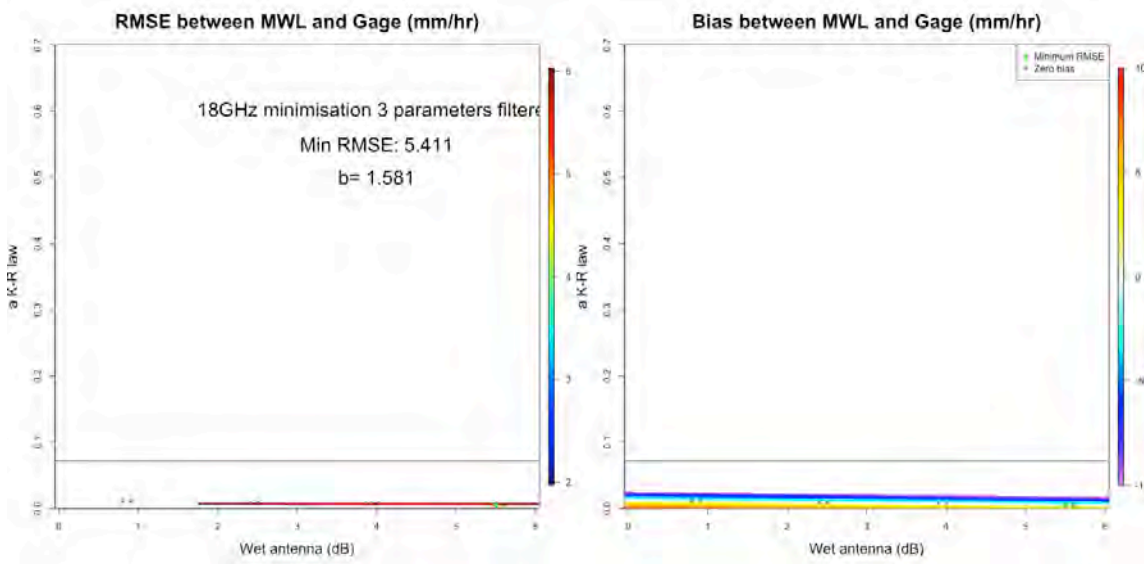


Figure A 5: Example attenuation minimization for model 1 (filtered) 18GHz in the a-WA space for $b=0.862$ (minima). Left figure show the attenuation RMSE and right figure the bias.

Model 2: 2 parameters minimization

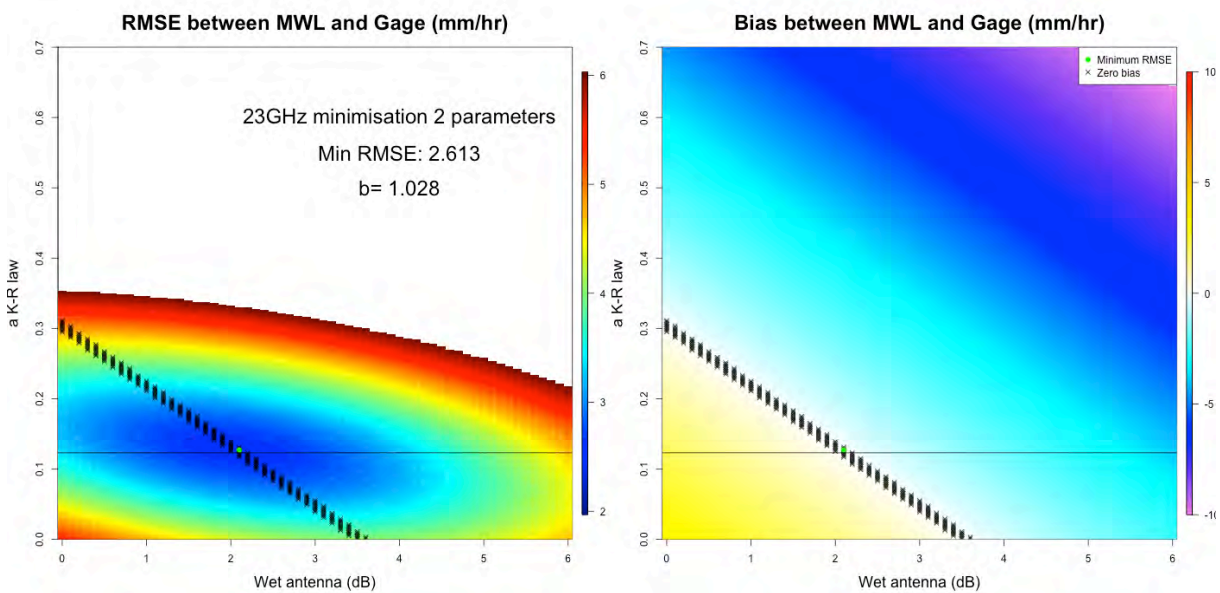


Figure A 6: Example attenuation minimization for model 2 (not filtered) 23GHz in the a-WA space for $b=0.862$ (minima). Left figure show the attenuation RMSE and right figure the bias.

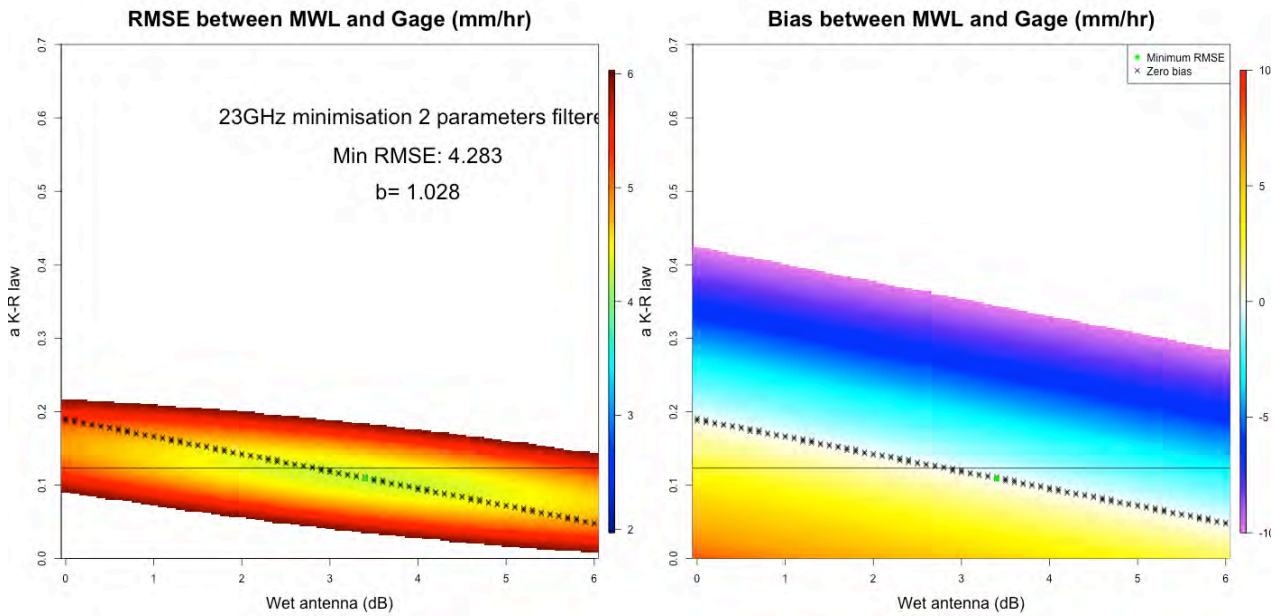


Figure A 7: Example attenuation minimization for model 2 (filtered) 23GHz in the a-WA space for b=0.862 (minima). Left figure show the attenuation RMSE and right figure the bias.

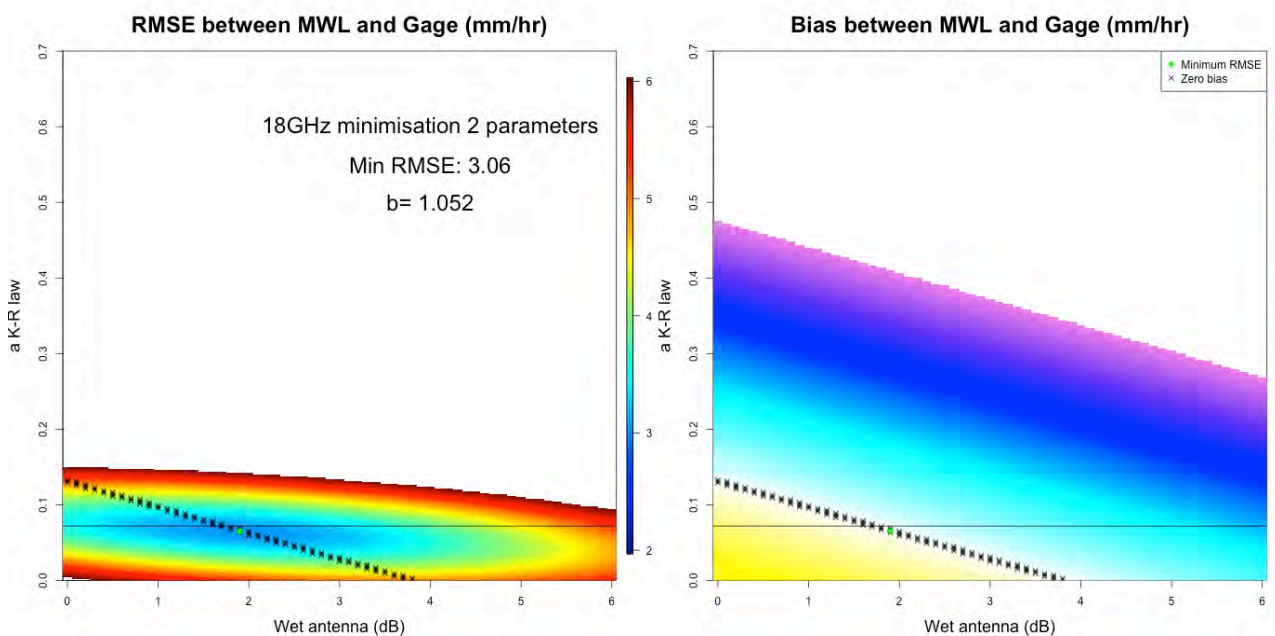


Figure A 8: Example attenuation minimization for model 2 (not filtered) 18GHz in the a-WA space for b=0.862 (minima). Left figure show the attenuation RMSE and right figure the bias.

Appendix 4: Minimization of calibration parameters of CML-gage dataset in Niamey

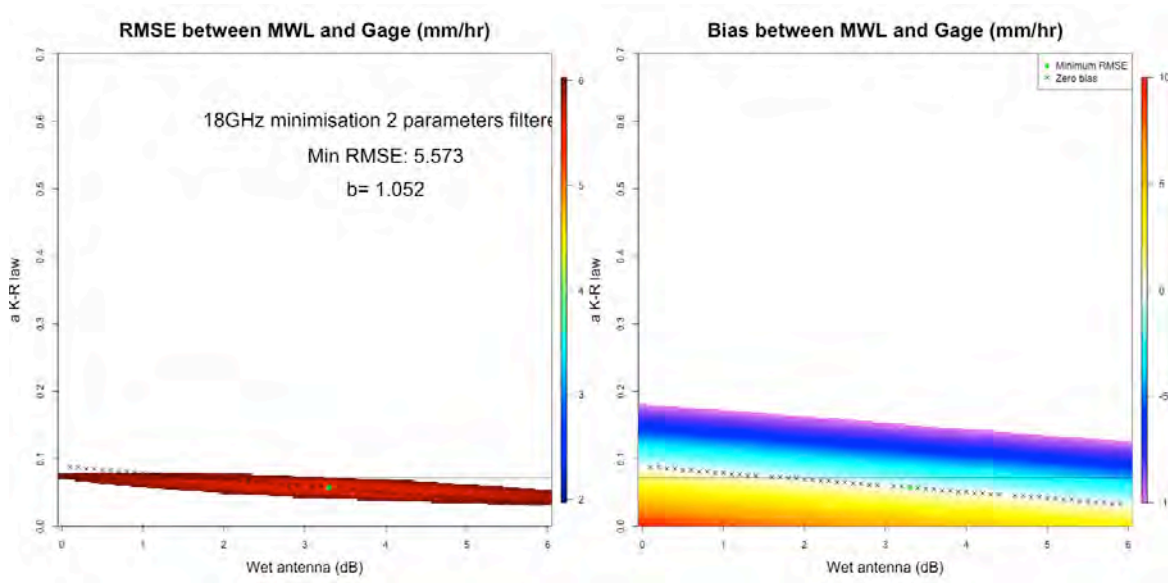


Figure A 9: Example attenuation minimization for model 2 (filtered) 18GHz in the a-WA space for b=0.862 (minima). Left figure show the attenuation RMSE and right figure the bias.

APPENDIX 5: INVESTIGATION OF THE BIAS DEPENDENCY ON LINKS' LENGTH USING SIMULATIONS

The scatterplots in figures 6-19 to 6-21 show a differential behavior of short and long links compared to the rain gage after the wet antenna correction. In this section we assess the differential behavior of path averaged rainfall rates at 15 minutes for different spatial scales when compared to point scale observations with simulations of the spatial sampling of links and rain gages.

The statistical properties of the rainfall fields depend on the scale of observation. (Guillot and Lebel 1999) fit a geostatistical model to their observations to reproduce random fields with similar characteristics than the observed depending on the scale. Another study in the region (Panthou, Vischel, and Lebel 2014) fit the probability density function of rainfall rates (PDF) describing the annual maxima of rainfall depending on time and space scales to evaluate the annual probability of extreme events.

Concerning the gage-CML comparison we compare point scale to lineal averages. It is not the aim of this section to fit a theoretical model to the data, as the cited studies. Though it should be interesting for future work. In this section we try to reproduce the observed CML/gage differences with an empirical method.

We simulate the space-time sampling of rainfall by CML and rain gages with radar DSD fields. The objective is to reproduce the scatter plots showed in figure 6-19 to 6-21 with realistic DSD parameters fields. We use the DSD retrieved with the inversion method showed in the chapter 4 of this PhD. The DSD fields were retrieved from X-port X-band polarimetric radar located in Benin in 2006. The DSD used correspond to squall lines MCS, which are the characteristic rainfall systems of Niger.

In the first section we show the methodology to simulate the CML and gage observation at 15 minutes sampling from DSD fields. In the following section we show the simulated CML at different lengths compared to the simulated raingage to show the effect of different samplings in the comparisons.

A5.1 Time-space effect on the PIA-rainfall relationship: simulation study based on the DSD fields

The sampling of rainfall by a microwave link R_L of length L for a duration Δt , can be defined with the spatio-temporal field of rainfall $r(x, y; t)$:

$$R_L(L, \Delta t) = \int_0^L \int_0^{\Delta t} r(x, y; t) ds dt \quad (eq. A5.1)$$

Where s is the segment of the CML in the XY space. The rain gage sampling $R_{L=0}$ can be defined as an integration of the point (x_0, y_0) over the time scale:

$$R_{L=0}(x_0, y_0, \Delta t) = \int_0^{\Delta t} r(x_0, y_0; t) dt \quad (eq. A5.2)$$

In this section we simulate a realistic set of estimated \tilde{R}_L with radar rainfall fields. The accentuation in \tilde{R}_L denotes an estimation and the L denotes the link length. When $L = 0$ is considered to be the rain gage. The objective is to compare \tilde{R}_L for different lengths L to \tilde{R}_0 .

As a proxy of real rainfall fields $r(x, y; t)$, we used high resolution DSD parameters fields retrieved from Xband radar data. For more details about the DSD fields, the inversion algorithm and the DSD parameters the reader can consult the chapter 3 of this work.

The aim of using radar fields is to access the finest spatial variability of rainfall. However, the temporal variability of rainfall is not well resolved by the radar as two consecutive PPIs (same elevation) have a time lag of 10 minutes.

X-port radar measures instantaneous rainfall in two dimensions (range, azimuth) at a resolution of 150m in range and 1° in azimuth. To overcome the time resolution limitation, we consider one space dimension as the time dimension. In this region the squall lines move usually westwards with a mean speed of 50 km/hr [Vischel et al 2011]. If we consider a theoretical CML situated along south-north direction, we can consider the east-west direction as the time dimension of the rainfall. That is equivalent to consider a translation of the field over the CML (and gage). The sampling of the CML can thus be represented by a rectangle over the PPI and the raingage by a line.

Figure A-10 represents a possible sampling of a CML (black rectangle) and a gage located in its center (white line). In this example the CML is 10 km long and the time distance

Appendix 5: Investigation of the bias dependency on links' length using simulations

considered is $Vdt = 50 \frac{km}{hr} \times 15 \text{ min} = 12.5 \text{ km}$. The black rectangle sampling region (simulated CML) is equivalent to consider a North-South $L = 10 \text{ km}$ CML and an advection of the rainfall field over it at a speed of 50 km/hr.

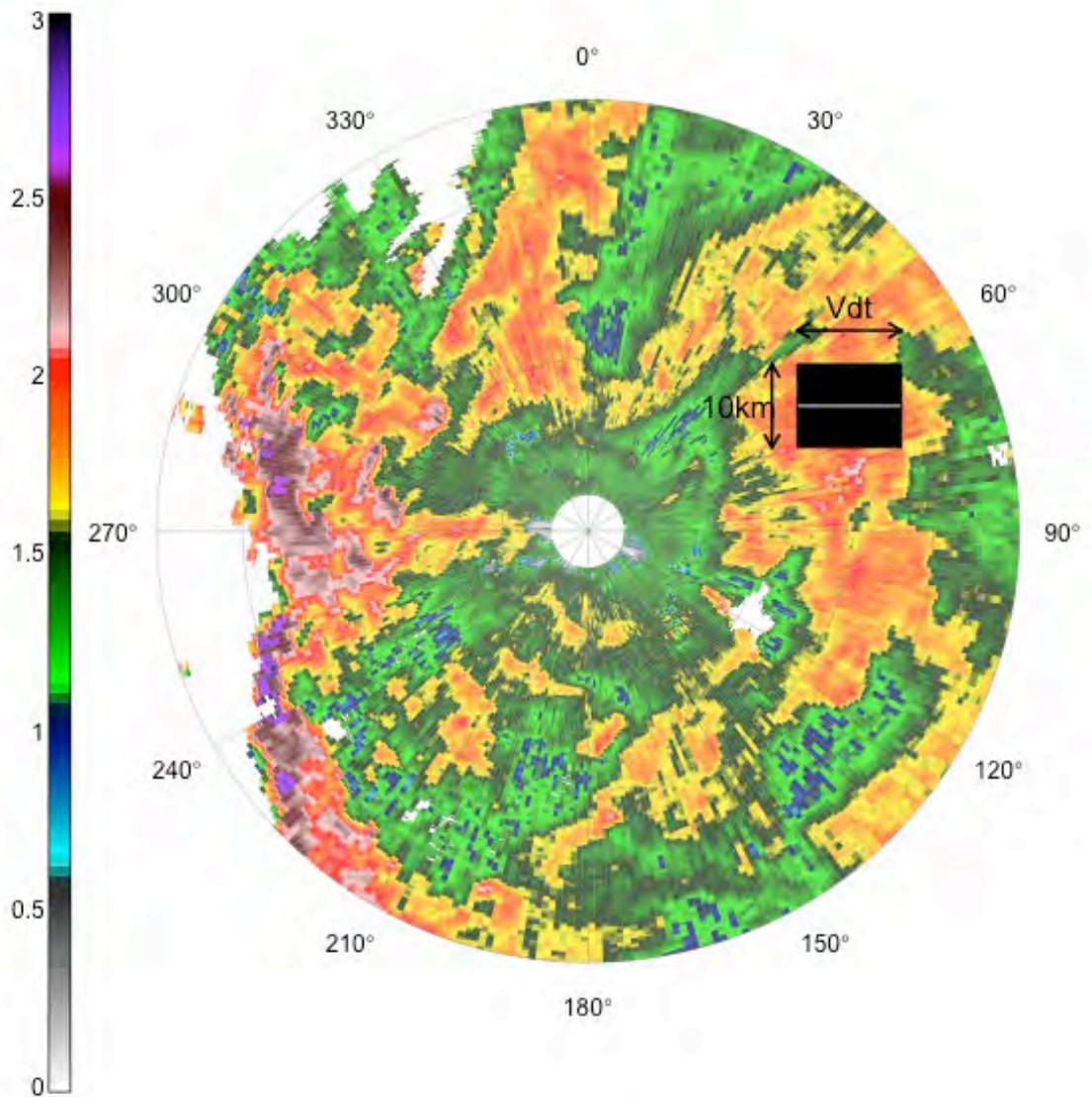


Figure A 10: Radar field of retrieved equivolumetric median diameter D_m (mm) from X-port PPI of the 12th September 2006 event at 18h48. The retrieval technique is presented in chapter 3 of this work. The convective front at the west part of the PPI is characterize

The sampling equation in 6.11 is approximated by its discrete form considering the X axis as time:

Appendix 5: Investigation of the bias dependency on links' length using simulations

$$\widetilde{R}_L = \frac{1}{n_{pix}} \sum_{Y_1}^{Y_2} \sum_{X_1}^{X_2} r_{radar}(x,y) dx dy \quad (eq. A5.3)$$

Where $r_{radar}(x,y)$ is the radar rainfall field (PPI), and n_{pix} the number of pixels falling un the zone . The length $[Y_1, Y_2]$ is the link length L and the length $[X_1, X_2]$ the considered temporal drift $V dt$.

In practice, as the radar geometry is range-azimuth (ρ, φ) instead of X, Y we compute the simulated rainfall as:

$$\widetilde{R}_L = \frac{1}{n_{pix}} \sum_{\rho, \varphi \in \mathcal{D}_L} r_{radar}(\rho, \varphi) \quad (eq. A5.4)$$

Where $r_{radar}(\rho, \varphi)$ is the rainfall rate of a pixel in the domain \mathcal{D}_L defined by a rectangle of sizes $L_{link} \times V dt$ and n_{pix} the total number of pixels in the domain \mathcal{D}_L .

As we have the DSD parameters for each pixel, we can compute also the expected measured specific attenuation \widetilde{K}_L for each sample (equation 2.23):

$$\widetilde{K}_L = \frac{0.4343}{n_{pix}} \sum_{pix \in \mathcal{D}_L} \int_{D_{min}}^{D_{max}} N_{pix}(D) \sigma_{ext}(D) dD \quad (eq. A5.5)$$

With $N_{pix}(D)$ the DSD in the pixel in $[m^{-3}]$ and σ_{ext} the extinction cross section in $[cm^2]$ from Mie scattering. We then can convert the expected measured attenuation \widetilde{K}_L into the expected measured rainfall with the K-R law to evaluate the impact of the non-linear sum:

$$\widetilde{R}_L^{NL} = a \widetilde{K}_L^b \quad (eq. A5.6)$$

Where a, b are the coefficients of the K-R law.

The comparison of \widetilde{R}_L and \widetilde{R}_0 is a proxy of the effect of the different scale sampling between CML and rain gage. . The comparison of \widetilde{R}_L^{NL} and \widetilde{R}_0 adds the effect of the non-linear K-R relation to the spatial sampling effect.

The sampling of the CML is simulated by averaging the rainfall rates of pixels included in the zone. The sampling of raingage is simulated by a 1D line representing the time dimension (white line in figure A-10). More precisely we considered the gage sampling zone as a flat rectangle with a vertical extension of 500m to have enough pixels falling inside. As the minimal size of the radar pixel in the fields are 87m x 120m (range 5km) and a maximal size of 870m x 120m (range 50km), in practice the 500m scale is the so called the ‘‘point scale’’.

Appendix 5: Investigation of the bias dependency on links' length using simulations

We used the output of the inversion of polarimetric radar data corresponding to the 12th September 2006 event, between 18h28 and 20h08 UTC, meaning 11 different PPI. All the PPI of the event were not used to avoid the extinction of the signal when the convective front is located eastwards of the radar. We use only the PPI after the convective front passage over the radar to have a realistic sample of the stratiform part as well as the convective front. Figure A-10 represents the equivolumetric median diameter D_m field, of the gamma DSD: we see the convective front characterized by high D_m in the western part of the PPI.

For each PPI we have simulated the sampling of CML for lengths in the range [1-20km] and a gage situated at its center. In order to have a big number of samples to be statistically robust we moved the sampling zone represented in figure A-10 over the whole PPI area, avoiding the center disk. To decrease the computing time, we only considered 1/2 ranges and 1/2 azimuths. Anyway two consecutive ranges or azimuths are very correlated.

A5.2 Results

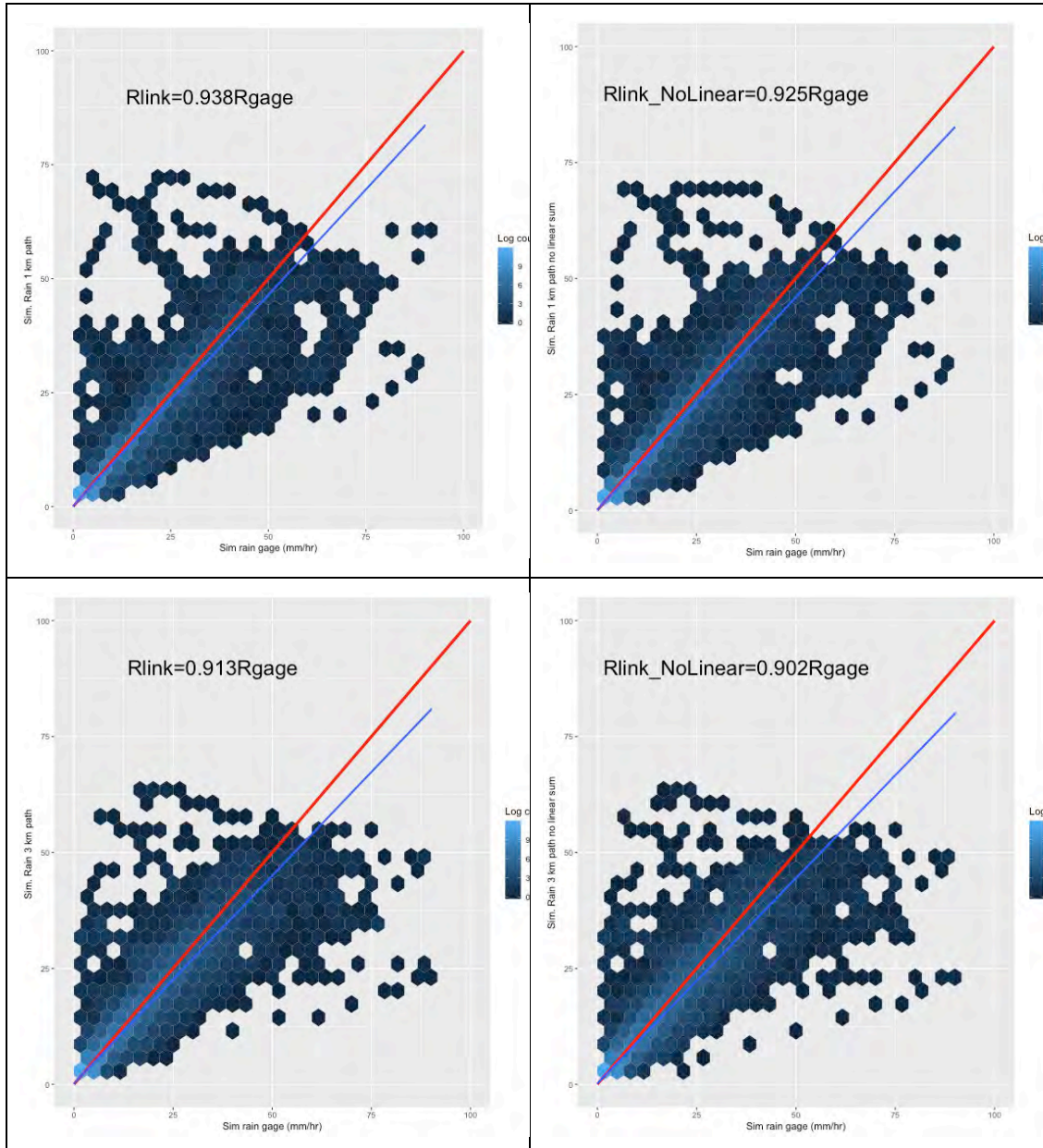
Figure A-11 show the scatterplots of \widetilde{R}_L vs \widetilde{R}_0 and \widetilde{R}_L^{NL} vs \widetilde{R}_0 . The right column shows \widetilde{R}_L^{NL} vs \widetilde{R}_0 and the left column \widetilde{R}_L vs \widetilde{R}_0 . The top line figure are for a 1 km CML, the middle line for 3 km and the bottom line for a 5 km CML. We see the effect of the CML length: for increasing lengths \widetilde{R}_L tend to be lower than \widetilde{R}_0 : for increasing sampling zones the average rainfall tends to be lower. We thus observe the similar trend observed with real data.

At 23 GHz the exponent of the K-R law is close to 1 ($b = 1.028$), thus the impact due to averaging variable rainfall is low. Comparing the values on the right and left columns the coefficients are very close.

Another point worth noting is the threshold effect that appear in long links. In the 5 km scatterplot in figure A-11 there is no observation of rainfall greater than 58 mm/hr while the raingage at the same location (center of the CML) measure rain rates up to 88 mm/hr. Equivalent to figure 4.19, the figure 4.24 shows the value of the scale coefficient depending on the link length for the different simulations. We see a clear scaling law with distance.

Appendix 5: Investigation of the bias dependency on links' length using simulations

The simulation of CML sampling and rain gage sampling over a radar field of DSD parameters can partially explain the differential behavior of short and long links when compared to rain gages.



Appendix 5: Investigation of the bias dependency on links' length using simulations

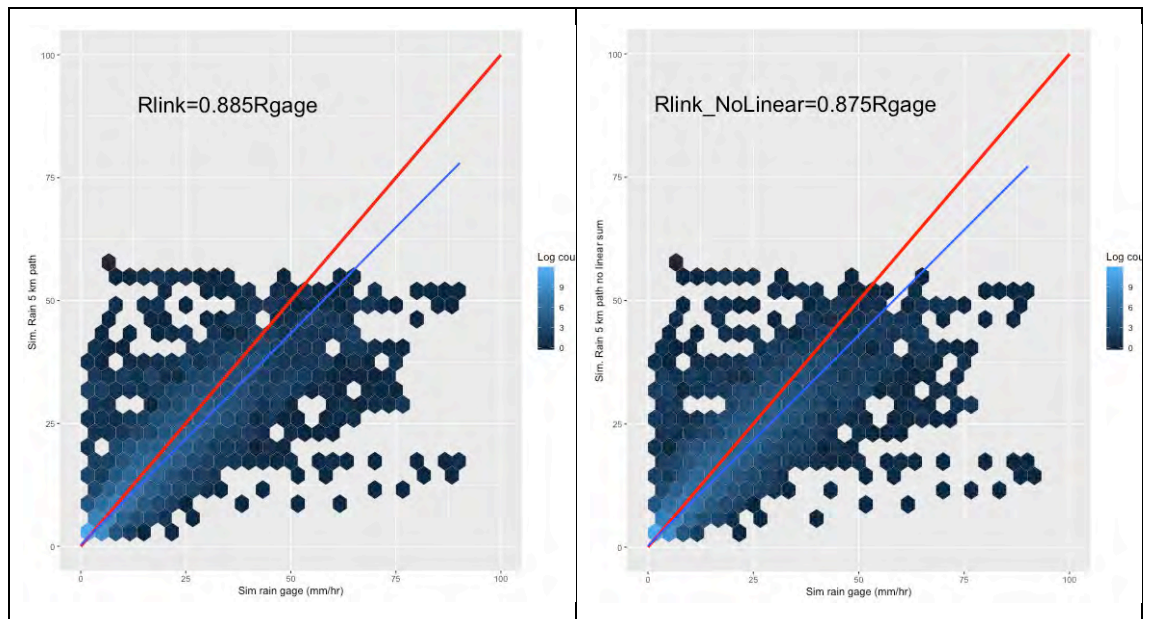


Figure A 11: Scatterplots of simulated CML sampling versus raingage sampling with radar DSD fields. Left column considering a linear sampling of the rainfall by the CML, left column considering nonlinear sampling with the K-R law. From top to bottom the rows are for CML lengths of 1km, 3km and 5km. Blue lines are the fitted linear law. Red lines are $y=x$. For longer links the CML tends to underestimate (smooth) the rainfall rates.

APPENDIX 6 : ADDITIONAL FIGURES OF CHAPTER 7

	Nlinks	Frequencies (GHz)					Mean Length (Km)	Min Length (Km)	Max Length (Km)	Density (Km/Km2)
Niamey	85	freq		18	23	1.37	0.51	5.44	0.49	
		Nlinks		7	78					
Douala	209	8.5	11.5	14.5	15	1.62	0.12	6.59	0.82	
		20	1	137	51					
Yaounde	168	8.5	11	13	14.5	2.11	0.17	19.16	0.36	
		24	1	1	89					53

Table A 1: Characteristics of the CML networks used for the rainfall mapping

Appendix 6 : Additional figures of chapter 7

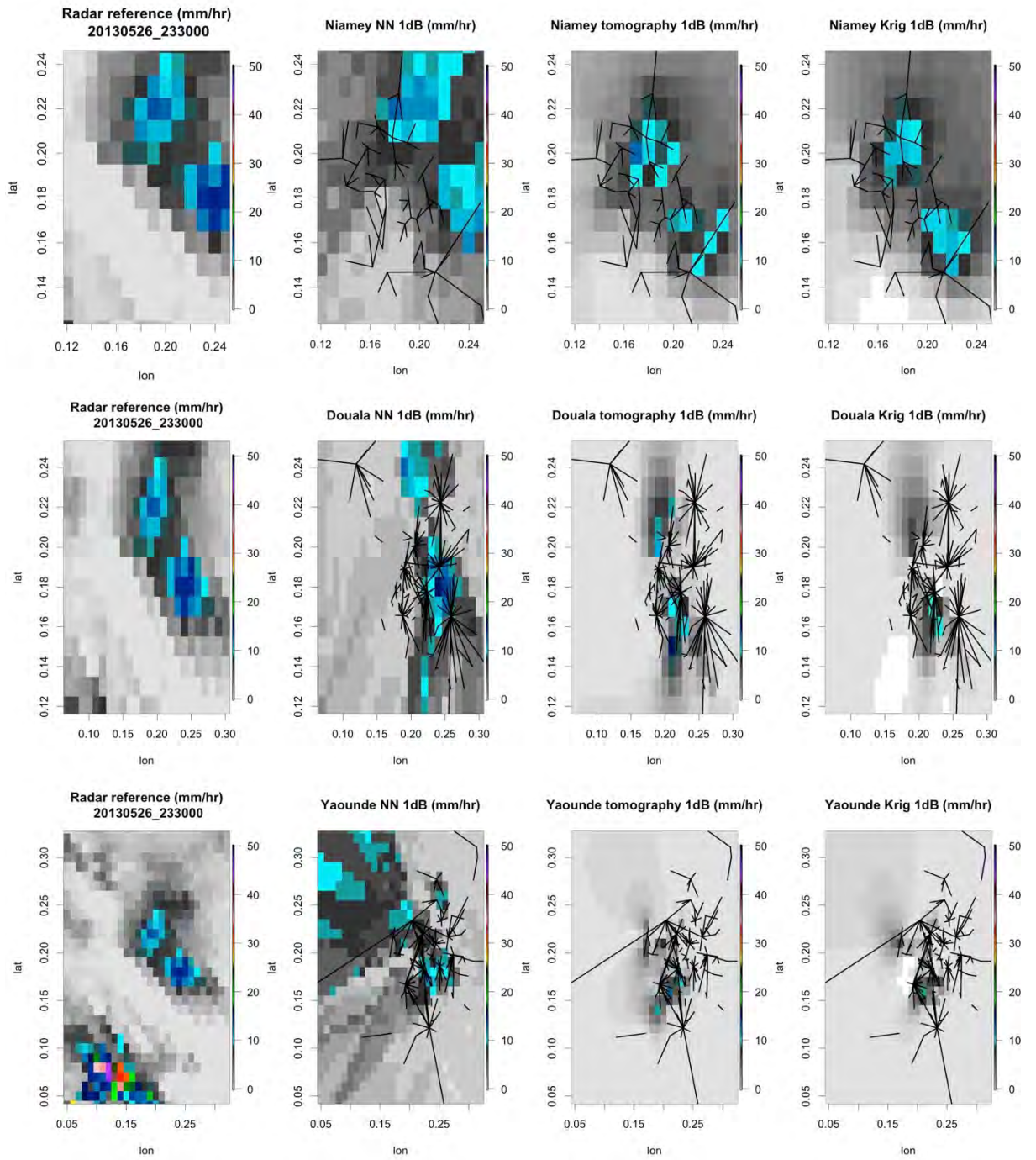


Figure A 12: Additional examples of mapping techniques.

Appendix 6 : Additional figures of chapter 7

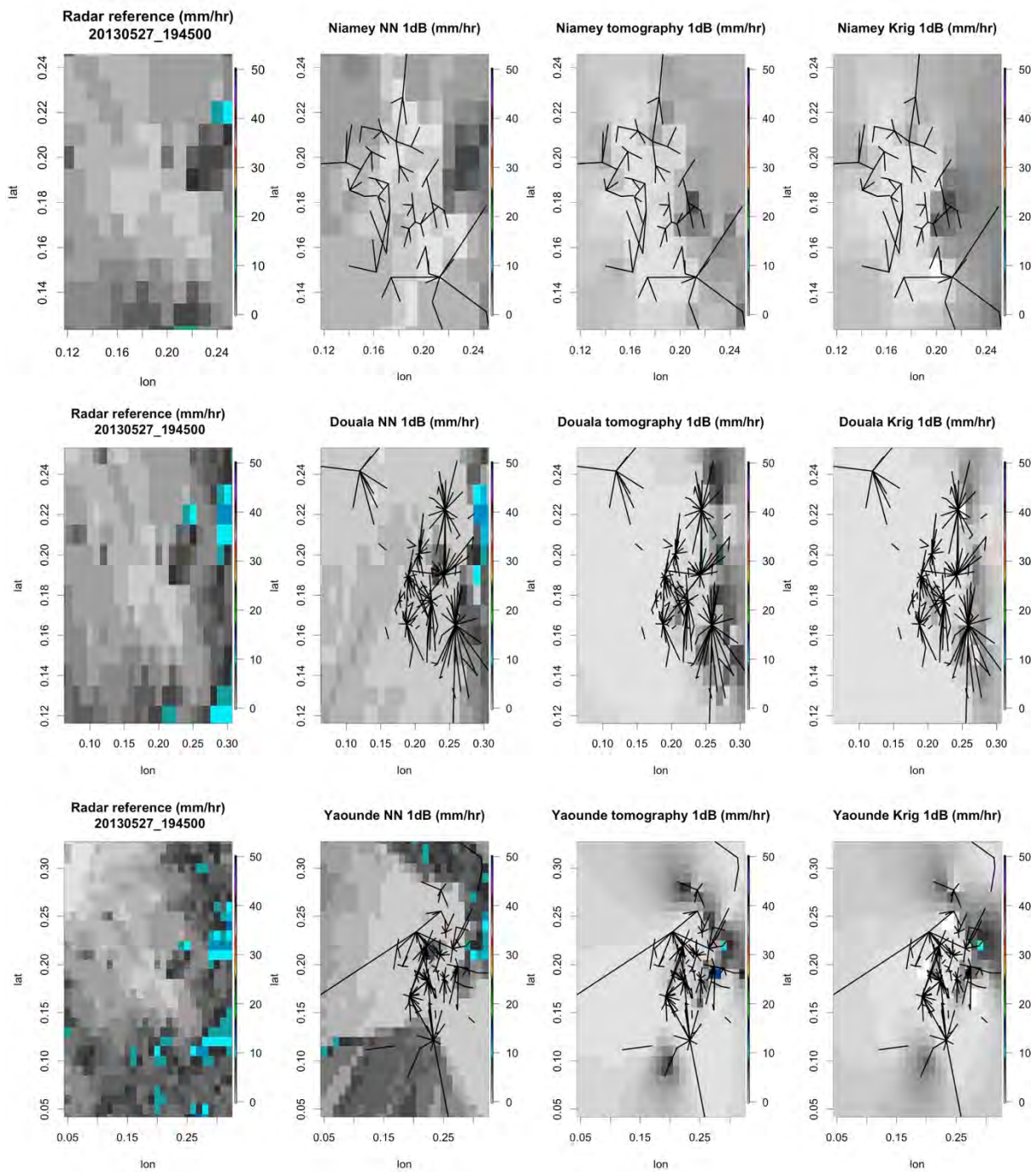


Figure A 13:Additional examples of mapping techniques

Appendix 6 : Additional figures of chapter 7

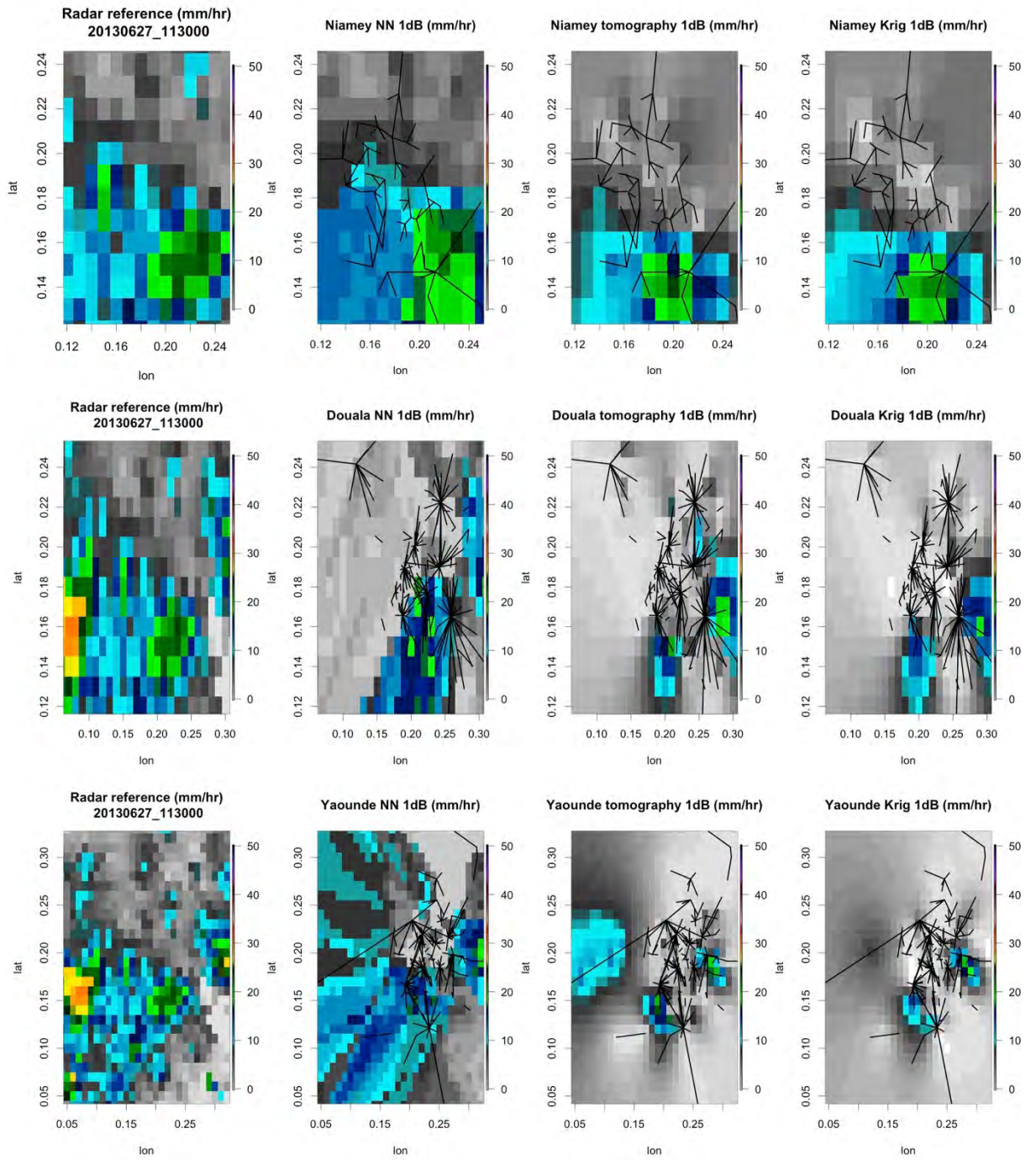


Figure A 14: Additional examples of mapping techniques.

Appendix 6 : Additional figures of chapter 7

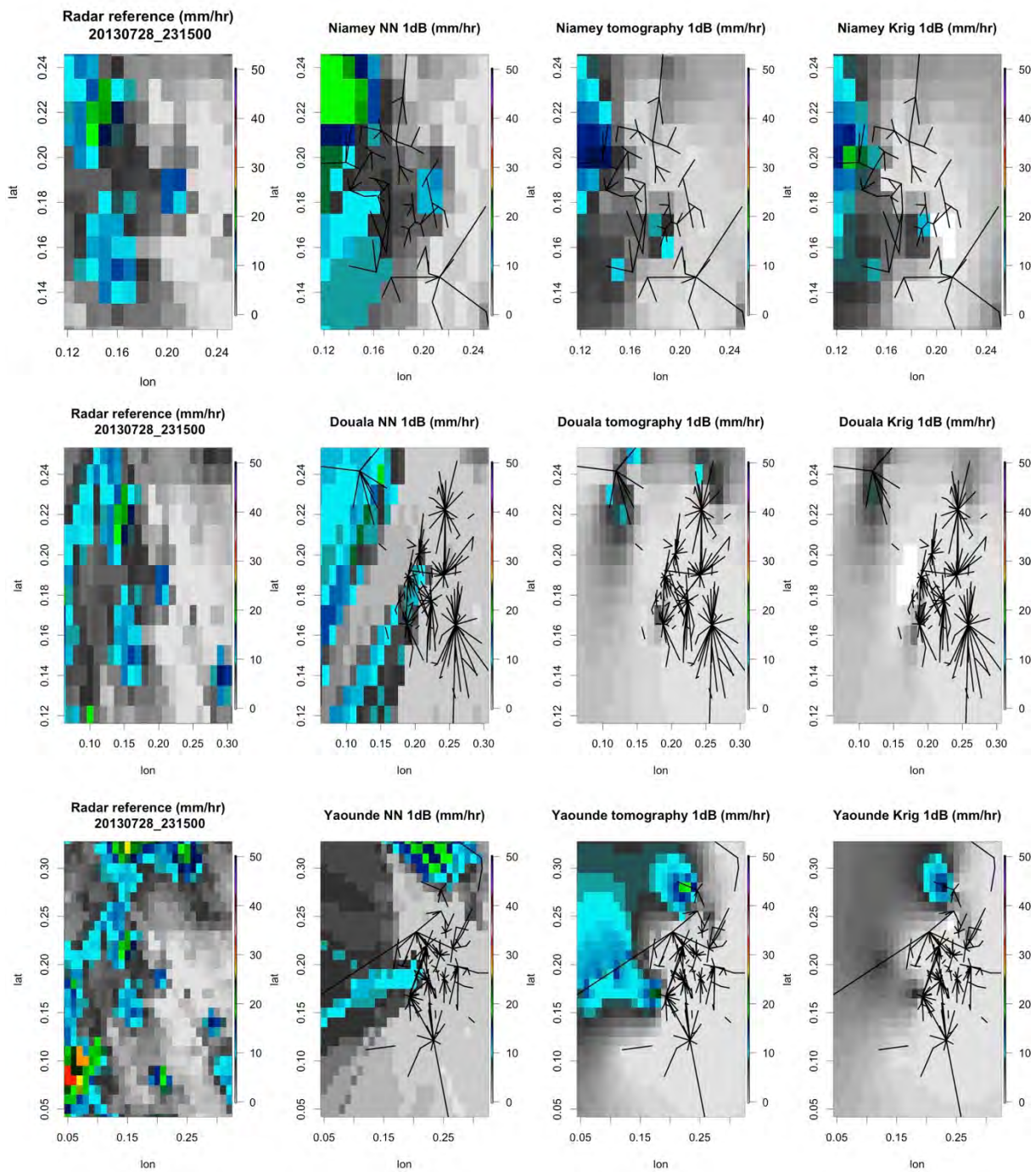


Figure A 15: Additional examples of mapping techniques.

Appendix 6 : Additional figures of chapter 7

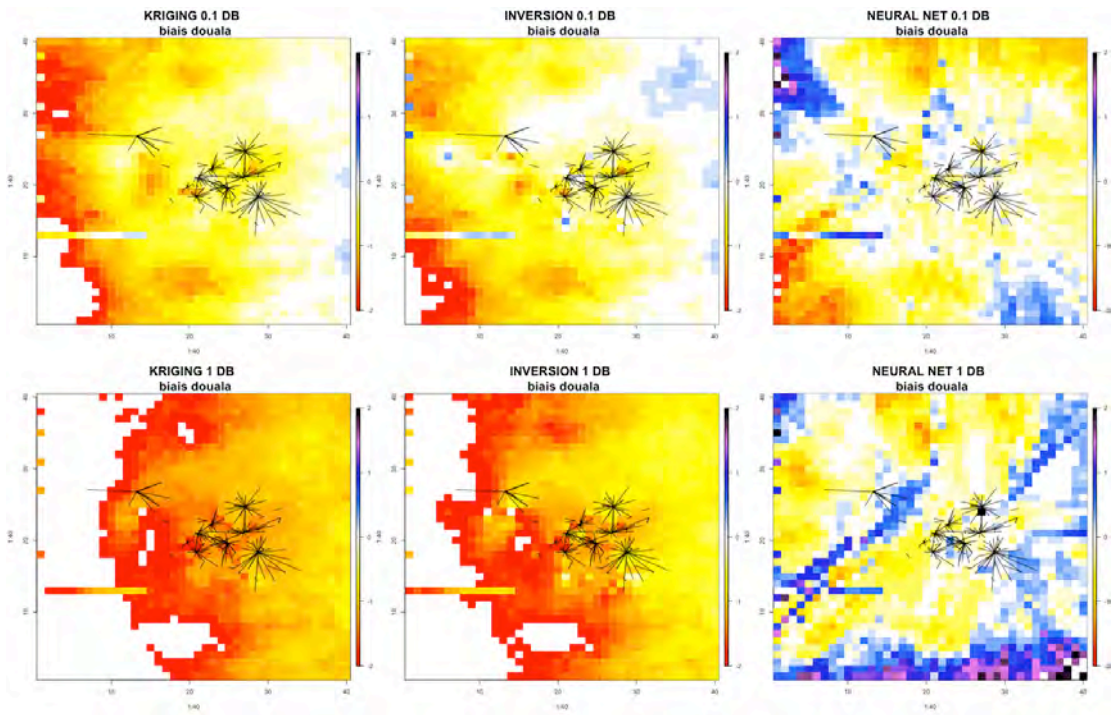


Figure A 16: Bias maps by method and attenuation quantification for Douala CML network.

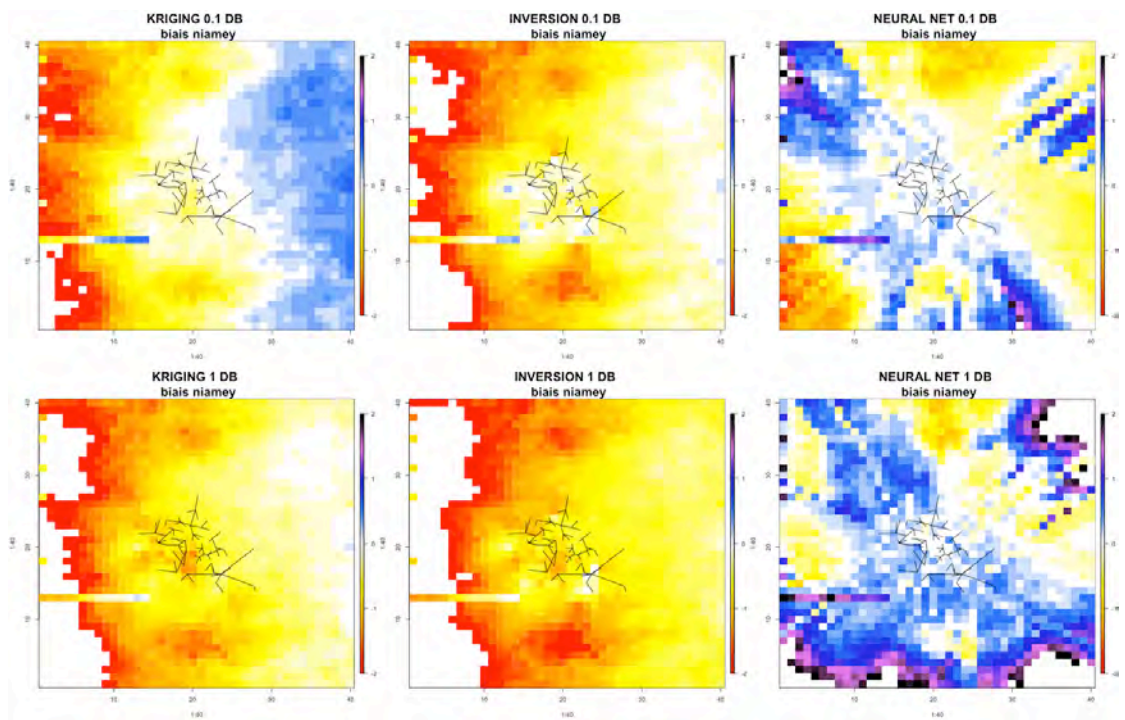


Figure A 17: Bias maps by method and attenuation quantification for Niamey CML network.

Appendix 6 : Additional figures of chapter 7

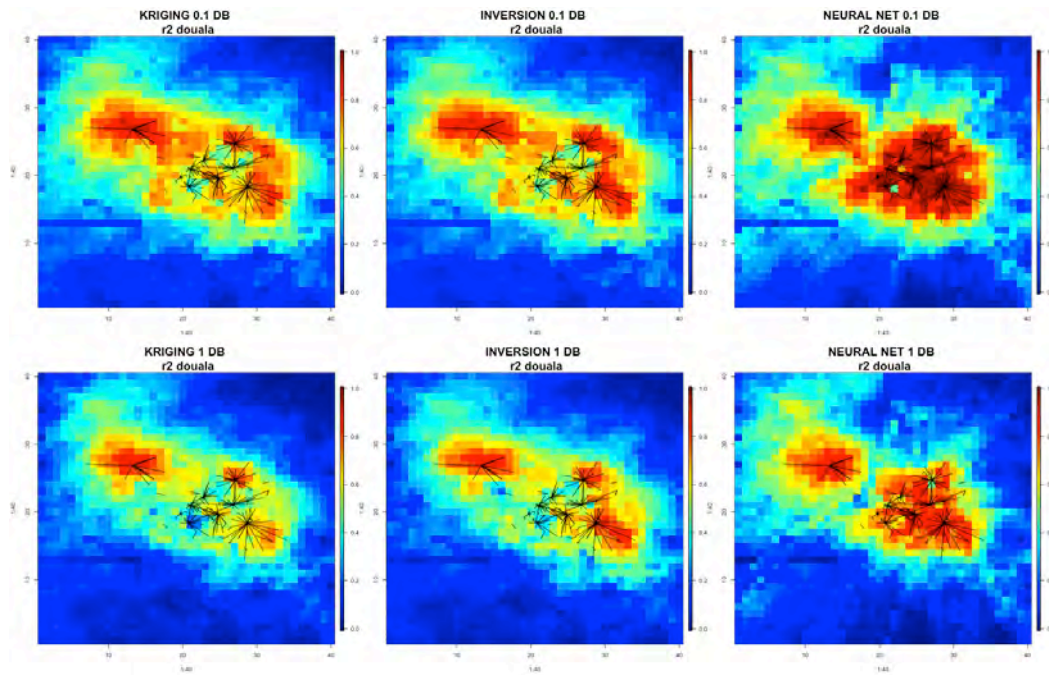


Figure A 18: R2 maps by method and attenuation quantification for Douala CML network.

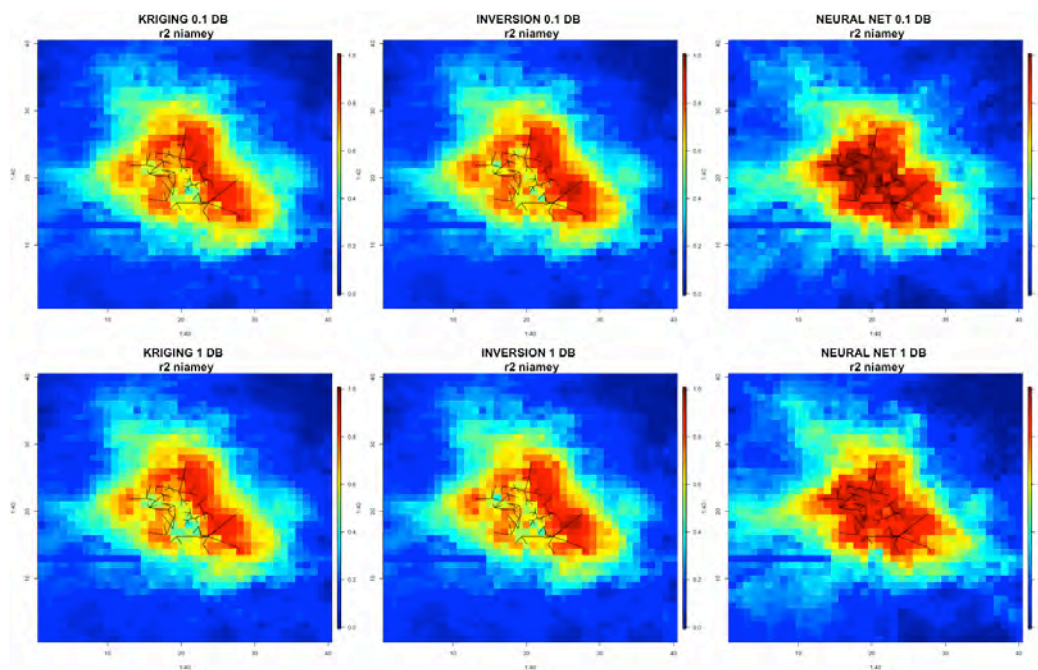


Figure A 19: R2 maps by method and attenuation quantification for Douala CML network.

Appendix 6 : Additional figures of chapter 7

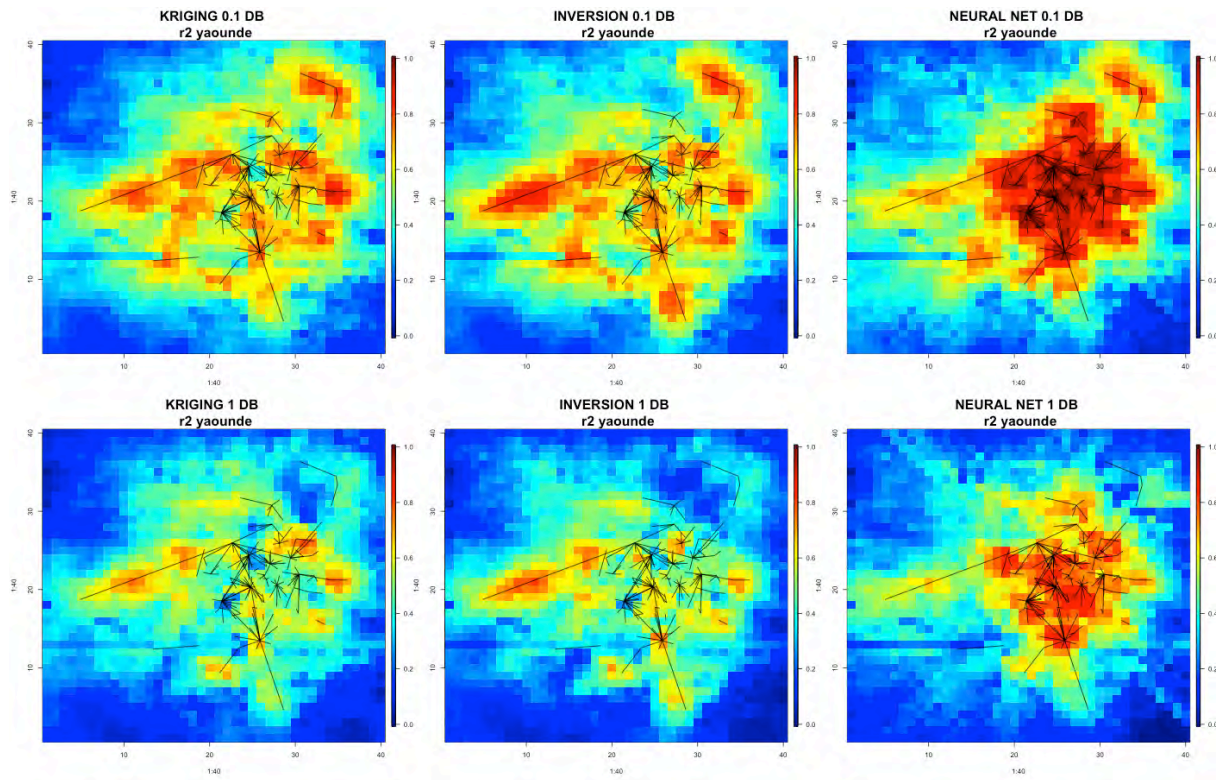


Figure A 20: R2 maps by method and attenuation quantification for Douala CML network.

BIBLIOGRAPHY

Alcoba, M., Marielle Gosset, M. Kacou, Frédéric Cazenave, and E. Fontaine
2016 Characterization of Hydrometeors in Sahelian Convective Systems with an X-Band Radar and Comparison with in Situ Measurements. Part II: A Simple Brightband Method to Infer the Density of Icy Hydrometeors. *Journal of Applied Meteorology and Climatology* 55(2): 251–263.

Anagnostou, Marios N., Emmanouil N. Anagnostou, Gianfranco Vulpiani, et al.
2008 Evaluation of X-Band Polarimetric-Radar Estimates of Drop-Size Distributions From Coincident S-Band Polarimetric Estimates and Measured Raindrop Spectra. *IEEE Transactions on Geoscience and Remote Sensing* 46(10): 3067–3075.

Andsager, Karen, Kenneth V. Beard, and Neil F. Laird
1999 Laboratory Measurements of Axis Ratios for Large Raindrops. *Journal of the Atmospheric Sciences* 56(15): 2673–2683.

Arnaud, Patrick, Jacques Lavabre, Catherine Fouchier, Stéphanie Diss, and Pierre Javelle
2011 Sensitivity of Hydrological Models to Uncertainty in Rainfall Input. *Hydrological Sciences Journal* 56(3): 397–410.

Atlas, David, and Carlton W. Ulbrich
1977 Path- and Area-Integrated Rainfall Measurement by Microwave Attenuation in the 1–3 Cm Band. *Journal of Applied Meteorology* 16(12): 1322–1331.

Atlas, David, Carlton W. Ulbrich, Frank D. Marks, Eyal Amitai, and Christopher R. Williams
1999 Systematic Variation of Drop Size and Radar-Rainfall Relations. *Journal of Geophysical Research: Atmospheres* 104(D6): 6155–6169.

Balme, Maud, Théo Vischel, Thierry Lebel, Christophe Peugeot, and Sylvie Galle
2006 Assessing the Water Balance in the Sahel: Impact of Small Scale Rainfall Variability on Runoff. *Journal of Hydrology* 331(1–2): 336–348.

Bibliography

- Barber, P., and C. Yeh
1975 Scattering of Electromagnetic Waves by Arbitrarily Shaped Dielectric Bodies. *Applied Optics* 14(12): 2864.
- Beard, Kenneth V., V.N. Bringi, and M. Thurai
2010 A New Understanding of Raindrop Shape. *Atmospheric Research* 97(4): 396–415.
- Bennartz, Ralf, and Grant W. Petty
2001 The Sensitivity of Microwave Remote Sensing Observations of Precipitation to Ice Particle Size Distributions. *Journal of Applied Meteorology* 40(3): 345–364.
- Bernard Fong, A.C.M. Fong, and G.Y. Hong
2005 On the Performance of Telemedicine System Using 17-GHz Orthogonally Polarized Microwave Links under the Influence of Heavy Rainfall. *IEEE Transactions on Information Technology in Biomedicine* 9(3): 424–429.
- Berne, A., and R. Uijlenhoet
2007 Path-Averaged Rainfall Estimation Using Microwave Links: Uncertainty Due to Spatial Rainfall Variability. *Geophysical Research Letters* 34(7). <http://doi.wiley.com/10.1029/2007GL029409>, accessed July 9, 2019.
- Bohren, Craig F., and Donald R. Huffman
2004 *Absorption and Scattering of Light by Small Particles*. Weinheim: Wiley-VCH.
- Boudevillain, Brice, and Hervé Andrieu
2003 Assessment of Vertically Integrated Liquid (VIL) Water Content Radar Measurement. *Journal of Atmospheric and Oceanic Technology* 20(6): 807–819.
- Brandes, Edward A., Guifu Zhang, and J. Vivekanandan
2004 Drop Size Distribution Retrieval with Polarimetric Radar: Model and Application. *Journal of Applied Meteorology* 43(3): 461–475.
- Bringi, V. N., Gwo-Jong Huang, V. Chandrasekar, and E. Gorgucci
2002 A Methodology for Estimating the Parameters of a Gamma Raindrop Size Distribution Model from Polarimetric Radar Data: Application to a Squall-Line Event from the TRMM/Brazil Campaign. *Journal of Atmospheric and Oceanic Technology* 19(5): 633–645.
- Bringi, V. N., and V. Chandrasekar
2001 *Polarimetric Doppler Weather Radar: Principles and Applications*. Cambridge university press.

Bibliography

- Bringi, V.N., T.D. Keenan, and V. Chandrasekar
2001 Correcting C-Band Radar Reflectivity and Differential Reflectivity Data for Rain Attenuation: A Self-Consistent Method with Constraints. *IEEE Transactions on Geoscience and Remote Sensing* 39(9): 1906–1915.
- Cao, Qing, Guifu Zhang, Edward Brandes, et al.
2008 Analysis of Video Disdrometer and Polarimetric Radar Data to Characterize Rain Microphysics in Oklahoma. *Journal of Applied Meteorology and Climatology* 47(8): 2238–2255.
- Cao, Qing, Guifu Zhang, Edward A. Brandes, and Terry J. Schuur
2010 Polarimetric Radar Rain Estimation through Retrieval of Drop Size Distribution Using a Bayesian Approach. *Journal of Applied Meteorology and Climatology* 49(5): 973–990.
- Carey, Lawrence D., Steven A. Rutledge, David A. Ahijevych, and Tom D. Keenan
2000 Correcting Propagation Effects in C-Band Polarimetric Radar Observations of Tropical Convection Using Differential Propagation Phase. *Journal of Applied Meteorology* 39(9): 1405–1433.
- Cazenave, Frédéric, Marielle Gosset, M Kacou, et al.
2016 Characterization of Hydrometeors in Sahelian Convective Systems with an X-Band Radar and Comparison with in Situ Measurements. Part I: Sensitivity of Polarimetric Radar Particle Identification Retrieval and Case Study Evaluation. *Journal of Applied Meteorology and Climatology* 55(2): 231–249.
- Chang, Wei-Yu, Jothiram Vivekanandan, and Tai-Chi Chen Wang
2014 Estimation of X-Band Polarimetric Radar Attenuation and Measurement Uncertainty Using a Variational Method. *Journal of Applied Meteorology and Climatology* 53(4): 1099–1119.
- Chen, Haonan, V. Chandrasekar, and Renzo Bechini
2017 An Improved Dual-Polarization Radar Rainfall Algorithm (DROPS2.0): Application in NASA IFloodS Field Campaign. *Journal of Hydrometeorology* 18(4): 917–937.
- Cherkassky, Dani, Jonatan Ostrometzky, and Hagit Messer
2014 Precipitation Classification Using Measurements From Commercial Microwave Links. *IEEE Transactions on Geoscience and Remote Sensing* 52(5): 2350–2356.
- Chwala, C., A. Gmeiner, W. Qiu, et al.
2012 Precipitation Observation Using Microwave Backhaul Links in the Alpine and Pre-Alpine Region of Southern Germany. *Hydrology and Earth System Sciences* 16(8): 2647–2661.

Bibliography

- Ciach, Grzegorz J.
2003 Local Random Errors in Tipping-Bucket Rain Gauge Measurements. *Journal of Atmospheric and Oceanic Technology* 20(5): 752–759.
- D’Amico, Michele, Andrea Manzoni, and Gian Leonardo Solazzi
2016 Use of Operational Microwave Link Measurements for the Tomographic Reconstruction of 2-D Maps of Accumulated Rainfall. *IEEE Geoscience and Remote Sensing Letters* 13(12): 1827–1831.
- Das, Saurabh, Animesh Maitra, and Ashish K. Shukla
2010 RAIN ATTENUATION MODELING IN THE 10-100 GHz FREQUENCY USING DROP SIZE DISTRIBUTIONS FOR DIFFERENT CLIMATIC ZONES IN TROPICAL INDIA. *Progress In Electromagnetics Research B* 25: 211–224.
- Delahaye, J.-Y., L. Barthès, P. Golé, J. Lavergnat, and J.P. Vinson
2006 A Dual-Beam Spectropluviometer Concept. *Journal of Hydrology* 328(1–2): 110–120.
- Delrieu, G., S. Caoudal, and J. D. Creutin
1997 Feasibility of Using Mountain Return for the Correction of Ground-Based X-Band Weather Radar Data. *Journal of Atmospheric and Oceanic Technology* 14(3): 368–385.
- Depraetere, Christian, Marielle Gosset, Stéphane Ploix, and Henri Laurent
2009 The Organization and Kinematics of Tropical Rainfall Systems Ground Tracked at Mesoscale with Gages: First Results from the Campaigns 1999–2006 on the Upper Ouémé Valley (Benin). *Journal of Hydrology* 375(1–2): 143–160.
- Doumounia, Ali, Marielle Gosset, Frederic Cazenave, Modeste Kacou, and François Zougmore
2014 Rainfall Monitoring Based on Microwave Links from Cellular Telecommunication Networks: First Results from a West African Test Bed: WIRELESS NETWORKS FOR RAINFALL IN AFRICA. *Geophysical Research Letters* 41(16): 6016–6022.
- Elshaikh, Zain Elabdin Omer, Md. Rafiqul Islam, Othman O. Khalifa, and Hany Essam Abd-El-Raouf
2009 MATHEMATICAL MODEL FOR THE PREDICTION OF MICROWAVE SIGNAL ATTENUATION DUE TO DUSTSTORM. *Progress In Electromagnetics Research M* 6: 139–153.
- Fabry, Frédéric
2015 *Radar Meteorology: Principles and Practice*. Cambridge, United Kingdom: Cambridge University Press.
- Fabry, Frédéric, and Wanda Szyrmer

Bibliography

- 1999 Modeling of the Melting Layer. Part II: Electromagnetic. *Journal of the Atmospheric Sciences* 56(20): 3593–3600.
- Fabry, Frederic, and Isztar Zawadzki
1995 Long-Term Radar Observations of the Melting Layer of Precipitation and Their Interpretation. *Journal of the Atmospheric Sciences* 52(7): 838–851.
- Fontaine, E., A. Schwarzenboeck, J. Delanoë, et al.
2014 Constraining Mass–Diameter Relations from Hydrometeor Images and Cloud Radar Reflectivities in Tropical Continental and Oceanic Convective Anvils. *Atmospheric Chemistry and Physics* 14(20): 11367–11392.
- Galle, S., M. Grippa, C. Peugeot, et al.
2018 AMMA-CATCH, a Critical Zone Observatory in West Africa Monitoring a Region in Transition. *Vadose Zone Journal* 17(1): 0.
- Goldshtein, O., H. Messer, and A. Zinevich
2009 Rain Rate Estimation Using Measurements From Commercial Telecommunications Links. *IEEE Transactions on Signal Processing* 57(4): 1616–1625.
- Gorgucci, Eugenio, Luca Baldini, and V. Chandrasekar
2006 What Is the Shape of a Raindrop? An Answer from Radar Measurements. *Journal of the Atmospheric Sciences* 63(11): 3033–3044.
- Gorgucci, Eugenio, V. Chandrasekar, and Luca Baldini
2009 Can a Unique Model Describe the Raindrop Shape–Size Relation? A Clue from Polarimetric Radar Measurements. *Journal of Atmospheric and Oceanic Technology* 26(9): 1829–1842.
- Gorgucci, Eugenio, V. Chandrasekar, V. N. Bringi, and Gianfranco Scarchilli
2002 Estimation of Raindrop Size Distribution Parameters from Polarimetric Radar Measurements. *Journal of the Atmospheric Sciences* 59(15): 2373–2384.
- Gorgucci, Eugenio, Gianfranco Scarchilli, V. Chandrasekar, and V. N. Bringi
2000 Measurement of Mean Raindrop Shape from Polarimetric Radar Observations. *Journal of the Atmospheric Sciences* 57(20): 3406–3413.
- 2001a Rainfall Estimation from Polarimetric Radar Measurements: Composite Algorithms Immune to Variability in Raindrop Shape–Size Relation. *Journal of Atmospheric and Oceanic Technology* 18(11): 1773–1786.
- 2001b Rainfall Estimation from Polarimetric Radar Measurements: Composite Algorithms Immune to Variability

Bibliography

in Raindrop Shape–Size Relation. *Journal of Atmospheric and Oceanic Technology* 18(11): 1773–1786.

Gosset, Marielle, Matias Alcoba, Remy Roca, Sophie Cloché, and Guillaume Urbani
2018 Evaluation of TAPEER Daily Estimates and Other GPM Era Products against Dense Gauge Networks in West Africa, Analyzing Ground Reference Uncertainty. *Quarterly Journal of the Royal Meteorological Society*.

Gosset, Marielle, Julien Viarre, Guillaume Quantin, and Matias Alcoba
2013 Evaluation of Several Rainfall Products Used for Hydrological Applications over West Africa Using Two High-Resolution Gauge Networks. *Quarterly Journal of the Royal Meteorological Society* 139(673): 923–940.

Gosset, Marielle, Eric-Pascal Zahiri, and Sounmaila Moumouni
2010a Rain Drop Size Distribution Variability and Impact on X-Band Polarimetric Radar Retrieval: Results from the AMMA Campaign in Benin. *Quarterly Journal of the Royal Meteorological Society* 136(S1): 243–256.

2010b Rain Drop Size Distribution Variability and Impact on X-Band Polarimetric Radar Retrieval: Results from the AMMA Campaign in Benin. *Quarterly Journal of the Royal Meteorological Society* 136(S1): 243–256.

Gou, Yabin, Haonan Chen, and Jiafeng Zheng
2019 An Improved Self-Consistent Approach to Attenuation Correction for C-Band Polarimetric Radar Measurements and Its Impact on Quantitative Precipitation Estimation. *Atmospheric Research* 226: 32–48.

Gourley, Jonathan J., Pierre Tabary, and Jacques Parent du Chatelet
2007 Empirical Estimation of Attenuation from Differential Propagation Phase Measurements at C Band. *Journal of Applied Meteorology and Climatology* 46(3): 306–317.

Guillot, Gilles, and Thierry Lebel
1999 Disaggregation of Sahelian Mesoscale Convective System Rain Fields: Further Developments and Validation. *Journal of Geophysical Research: Atmospheres* 104(D24): 31533–31551.

Guilloteau, Clément, Rémy Roca, and Marielle Gosset
2016 A Multiscale Evaluation of the Detection Capabilities of High-Resolution Satellite Precipitation Products in West Africa. *Journal of Hydrometeorology* 17(7): 2041–2059.

Hachani, Sahar, Brice Boudevillain, Guy Delrieu, and Zoubeida Bargaoui
2017 Drop Size Distribution Climatology in Cévennes-Vivarais Region, France. *Atmosphere* 8(12): 233.

Haykin, Simon
1994 *Neural Networks: A Comprehensive Foundation*. New York : Toronto : New York: Macmillan ; Maxwell

Bibliography

Macmillan Canada ; Maxwell Macmillan International.

Houze, Robert A.
2004 Mesoscale Convective Systems. *Reviews of Geophysics* 42(4).
<http://doi.wiley.com/10.1029/2004RG000150>, accessed July 4, 2019.

Hubbert, J., and V. N. Bringi
1995 An Iterative Filtering Technique for the Analysis of Copolar Differential Phase and Dual-Frequency Radar Measurements. *Journal of Atmospheric and Oceanic Technology* 12(3): 643–648.

Illingworth, Anthony J., and T. Mark Blackman
2002 The Need to Represent Raindrop Size Spectra as Normalized Gamma Distributions for the Interpretation of Polarization Radar Observations. *Journal of Applied Meteorology* 41(3): 286–297.

Islam, Tanvir, Miguel A. Rico-Ramirez, and Dawei Han
2012 Tree-Based Genetic Programming Approach to Infer Microphysical Parameters of the DSDs from the Polarization Diversity Measurements. *Computers & Geosciences* 48: 20–30.

Kacou, Modeste Huberson Ahiba
2014 Analyse Des Précipitations En Zone Sahélienne à Partir d'un Radar Bande X Polarimétrique. PhD Thesis, Université de Toulouse, Université Toulouse III-Paul Sabatier; Université

Kalogiros, John, Marios N. Anagnostou, Emmanouil N. Anagnostou, et al.
2014 Evaluation of a New Polarimetric Algorithm for Rain-Path Attenuation Correction of X-Band Radar Observations Against Disdrometer. *IEEE Transactions on Geoscience and Remote Sensing* 52(2): 1369–1380.

Kharadly, M.M.Z., and R. Ross
2001 Effect of Wet Antenna Attenuation on Propagation Data Statistics. *IEEE Transactions on Antennas and Propagation* 49(8): 1183–1191.

Kidd, Chris, Andreas Becker, George J. Huffman, et al.
2017 So, How Much of the Earth's Surface Is Covered by Rain Gauges? *Bulletin of the American Meteorological Society* 98(1): 69–78.

Kim, Dong-Soon, Masayuki Maki, and Dong-In Lee
2008 Correction of X-Band Radar Reflectivity and Differential Reflectivity for Rain Attenuation Using Differential Phase. *Atmospheric Research* 90(1): 1–9.

Bibliography

Kim, D-S., M. Maki, and D-I. Lee
2010 Retrieval of Three-Dimensional Raindrop Size Distribution Using X-Band Polarimetric Radar Data. *Journal of Atmospheric and Oceanic Technology* 27(8): 1265–1285.

Kirstetter, Pierre-Emmanuel, Hervé Andrieu, Brice Boudevillain, and Guy Delrieu
2013 A Physically Based Identification of Vertical Profiles of Reflectivity from Volume Scan Radar Data. *Journal of Applied Meteorology and Climatology* 52(7): 1645–1663.

Kirstetter, Pierre-Emmanuel, Nicolas Viltard, and Marielle Gosset
2013 An Error Model for Instantaneous Satellite Rainfall Estimates: Evaluation of BRAIN-TMI over West Africa. *Quarterly Journal of the Royal Meteorological Society* 139(673): 894–911.

Klaassen, Wim
1988 Radar Observations and Simulation of the Melting Layer of Precipitation. *Journal of the Atmospheric Sciences* 45(24): 3741–3753.

Koffi, A.K., M. Gosset, E.-P. Zahiri, et al.
2014 Evaluation of X-Band Polarimetric Radar Estimation of Rainfall and Rain Drop Size Distribution Parameters in West Africa. *Atmospheric Research* 143: 438–461.

Kumar, Lakshmi Sutha, Yee Hui Lee, and Jin Teong Ong
2010 Truncated Gamma Drop Size Distribution Models for Rain Attenuation in Singapore. *IEEE Transactions on Antennas and Propagation* 58(4): 1325–1335.

Kummerow, C., W.S. Olson, and L. Giglio
1996 A Simplified Scheme for Obtaining Precipitation and Vertical Hydrometeor Profiles from Passive Microwave Sensors. *IEEE Transactions on Geoscience and Remote Sensing* 34(5): 1213–1232.

Lebel, T., D. J. Parker, C. Flamant, et al.
2010 The AMMA Field Campaigns: Multiscale and Multidisciplinary Observations in the West African Region. *Quarterly Journal of the Royal Meteorological Society* 136(S1): 8–33.

Lee, Choong Ke, Gyu Won Lee, Isztar Zawadzki, and Kyung-Eak Kim
2009 A Preliminary Analysis of Spatial Variability of Raindrop Size Distributions during Stratiform Rain Events. *Journal of Applied Meteorology and Climatology* 48(2): 270–283.

Lee, Gyu Won, and Isztar Zawadzki

Bibliography

- 2005 Variability of Drop Size Distributions: Time-Scale Dependence of the Variability and Its Effects on Rain Estimation. *Journal of Applied Meteorology* 44(2): 241–255.
- Lee, Gyu Won, Isztar Zawadzki, Wanda Szyrmer, Daniel Sempere-Torres, and Remko Uijlenhoet
2004 A General Approach to Double-Moment Normalization of Drop Size Distributions. *Journal of Applied Meteorology* 43(2): 264–281.
- Leijnse, H., R. Uijlenhoet, and J. N. M. Stricker
2007 Rainfall Measurement Using Radio Links from Cellular Communication Networks: RAPID COMMUNICATION. *Water Resources Research* 43(3). <http://doi.wiley.com/10.1029/2006WR005631>, accessed July 4, 2019.
- Leijnse, H., R. Uijlenhoet, and J.N.M. Stricker
2008 Microwave Link Rainfall Estimation: Effects of Link Length and Frequency, Temporal Sampling, Power Resolution, and Wet Antenna Attenuation. *Advances in Water Resources* 31(11): 1481–1493.
- Leijnse, Hidde, Remko Uijlenhoet, and Alexis Berne
2010 Errors and Uncertainties in Microwave Link Rainfall Estimation Explored Using Drop Size Measurements and High-Resolution Radar Data. *Journal of Hydrometeorology* 11(6): 1330–1344.
- Liebe, Hans J., George A. Hufford, and Takeshi Manabe
1991 A Model for the Complex Permittivity of Water at Frequencies below 1 THz. *International Journal of Infrared and Millimeter Waves* 12(7): 659–675.
- Liebe, HJ, GA Hufford, and MG Cotton
1993 Propagation Modeling of Moist Air and Suspended Water/Ice Particles at Frequencies below 1000 GHz. *In AGARD, Atmospheric Propagation Effects Through Natural and Man-Made Obscurants for Visible to MM-Wave Radiation* 11 p (SEE N94-30495 08-32).
- Liu, Hongping, and V. Chandrasekar
2000 Classification of Hydrometeors Based on Polarimetric Radar Measurements: Development of Fuzzy Logic and Neuro-Fuzzy Systems, and In Situ Verification. *Journal of Atmospheric and Oceanic Technology* 17(2): 140–164.
- Lorenz, Christof, and Harald Kunstmann
2012 The Hydrological Cycle in Three State-of-the-Art Reanalyses: Intercomparison and Performance Analysis. *Journal of Hydrometeorology* 13(5): 1397–1420.
- Marshall, J. S., and W. K. Palmer

Bibliography

- 1948 THE DISTRIBUTION OF RAINDROPS WITH SIZE. *Journal of Meteorology* 5(4): 165–166.
- Matrosov, Sergey Y., Kurt A. Clark, Brooks E. Martner, and Ali Tokay
2002 X-Band Polarimetric Radar Measurements of Rainfall. *Journal of Applied Meteorology* 41(9): 941–952.
- Matrosov, Sergey Y., David E. Kingsmill, Brooks E. Martner, and F. Martin Ralph
2005 The Utility of X-Band Polarimetric Radar for Quantitative Estimates of Rainfall Parameters. *Journal of Hydrometeorology* 6(3): 248–262.
- Menke, William
2018 *Geophysical Data Analysis: Discrete Inverse Theory*. Fourth edition. Amsterdam London Cambridge, MA: Elsevier/Academic Press.
- Messer, H.
2006 Environmental Monitoring by Wireless Communication Networks. *Science* 312(5774): 713–713.
- Mie, Gustav
1908 Beiträge zur Optik trüber Medien, speziell kolloidaler Metallösungen. *Annalen der Physik* 330(3): 377–445.
- Minda, Haruya, and Kenji Nakamura
2005 High Temporal Resolution Path-Average Rain Gauge with 50-GHz Band Microwave. *Journal of Atmospheric and Oceanic Technology* 22(2): 165–179.
- Mishchenko, Michael I., Larry D. Travis, and Daniel W. Mackowski
1996 T-Matrix Computations of Light Scattering by Nonspherical Particles: A Review. *Journal of Quantitative Spectroscopy and Radiative Transfer* 55(5): 535–575.
- Moumouni, Soumaila
2009 *Analyse Des Distributions Granulométriques Des Pluies Au Bénin : Caractéristiques Globales, Variabilité et Application à La Mesure Radar*.
- Moumouni, Soumaila, Marielle Gosset, and Etienne Houngrinou
2008 Main Features of Rain Drop Size Distributions Observed in Benin, West Africa, with Optical Disdrometers. *Geophysical Research Letters* 35(23). <http://doi.wiley.com/10.1029/2008GL035755>, accessed May 16, 2018.
- Olsen, R., D. Rogers, and D. Hodge

Bibliography

- 1978 The AR²B²Relation in the Calculation of Rain Attenuation. *IEEE Transactions on Antennas and Propagation* 26(2): 318–329.
- Ostrometzky, Jonatan, and Hagit Messer
2014 Accumulated Rainfall Estimation Using Maximum Attenuation of Microwave Radio Signal. *In* 2014 IEEE 8th Sensor Array and Multichannel Signal Processing Workshop (SAM) Pp. 193–196. A Coruna, Spain: IEEE. <http://ieeexplore.ieee.org/document/6882373/>, accessed July 4, 2019.
- 2018 On the Information in Extreme Measurements for Parameter Estimation. ArXiv:1809.08662 [Cs, Eess, Math]. <http://arxiv.org/abs/1809.08662>, accessed July 4, 2019.
- Overeem, A., H. Leijnse, and R. Uijlenhoet
2011 Measuring Urban Rainfall Using Microwave Links from Commercial Cellular Communication Networks: MEASURING URBAN RAINFALL USING MICROWAVE LINKS. *Water Resources Research* 47(12). <http://doi.wiley.com/10.1029/2010WR010350>, accessed September 10, 2018.
- Overeem, Aart, Hidde Leijnse, and Remko Uijlenhoet
2013 Country-Wide Rainfall Maps from Cellular Communication Networks. *Proceedings of the National Academy of Sciences* 110(8): 2741–2745.
- Panthou, G., T. Vischel, and T. Lebel
2014 Recent Trends in the Regime of Extreme Rainfall in the Central Sahel: RECENT TRENDS OF EXTREME RAINFALL IN THE WEST AFRICAN SAHEL. *International Journal of Climatology* 34(15): 3998–4006.
- Park, S. G., Masayuki Maki, K. Iwanami, V. N. Bringi, and V. Chandrasekar
2005 Correction of Radar Reflectivity and Differential Reflectivity for Rain Attenuation at X Band. Part II: Evaluation and Application. *Journal of Atmospheric and Oceanic Technology* 22(11): 1633–1655.
- Pruppacher, H. R., and K. V. Beard
1970 A Wind Tunnel Investigation of the Internal Circulation and Shape of Water Drops Falling at Terminal Velocity in Air. *Quarterly Journal of the Royal Meteorological Society* 96(408): 247–256.
- Rahim, S. K. A., A. Y. Abdulrahman, T. A. Rahman, and M. R. Ul Islam
2012 Measurement of Wet Antenna Losses on 26 GHz Terrestrial Microwave Link in Malaysia. *Wireless Personal Communications* 64(2): 225–231.
- Raupach, Timothy H., and Alexis Berne
2017 Retrieval of the Raindrop Size Distribution from Polarimetric Radar Data Using Double-Moment Normalisation. *Atmospheric Measurement Techniques* 10(7): 2573–2594.

Bibliography

- Ray, Peter S.
1972 Broadband Complex Refractive Indices of Ice and Water. *Applied Optics* 11(8): 1836.
- Rayitsfeld, Asaf, Rana Samuels, Artem Zinevich, Uri Hadar, and Pinhas Alpert
2012 Comparison of Two Methodologies for Long Term Rainfall Monitoring Using a Commercial Microwave Communication System. *Atmospheric Research* 104–105: 119–127.
- Reller, Christoph, Hans-Andrea Loeliger, and Juan Pablo Marín Díaz
N.d. A Model for Quasi-Periodic Signals with Application to Rain Estimation From Microwave Link Gain: 5.
- Rincon, R.F., S.W. Bidwell, A.R. Jameson, and O.W. Thiele
1996 A Multi-Frequency, Dual-Polarization, Microwave Link for Rainfall Estimation. *In* IGARSS '96. 1996 International Geoscience and Remote Sensing Symposium Pp. 402–404. Lincoln, NE, USA: IEEE. <http://ieeexplore.ieee.org/document/516354/>, accessed July 9, 2019.
- Roca, R., J. Aublanc, P. Chambon, T. Fiolleau, and N. Viltard
2014 Robust Observational Quantification of the Contribution of Mesoscale Convective Systems to Rainfall in the Tropics. *Journal of Climate* 27(13): 4952–4958.
- Roca, Romy, H  ne Brogniez, Philippe Chambon, et al.
2015 The Megha-Tropiques Mission: A Review after Three Years in Orbit. *Frontiers in Earth Science* 3. http://www.frontiersin.org/Atmospheric_Science/10.3389/feart.2015.00017/abstract, accessed July 4, 2019.
- Roy, Venkat, Shahzad Gishkori, and Geert Leus
2014 Spatial Rainfall Mapping from Path-Averaged Rainfall Measurements Exploiting Sparsity. *In* Signal and Information Processing (GlobalSIP), 2014 IEEE Global Conference On Pp. 321–325. IEEE.
- van het Schip, T. I., A. Overeem, H. Leijnse, et al.
2017 Rainfall Measurement Using Cell Phone Links: Classification of Wet and Dry Periods Using Geostationary Satellites. *Hydrological Sciences Journal* 62(9): 1343–1353.
- Schleiss, Marc, and Alexis Berne
2010 Identification of Dry and Rainy Periods Using Telecommunication Microwave Links. *IEEE Geoscience and Remote Sensing Letters* 7(3): 611–615.
- Schleiss, Marc, J  rg Rieckermann, and Alexis Berne

Bibliography

- 2013 Quantification and Modeling of Wet-Antenna Attenuation for Commercial Microwave Links. *IEEE Geoscience and Remote Sensing Letters* 10(5): 1195–1199.
- Semplak, R. 1970 The Influence of Heavy Rainfall on Attenuation at 18.5 and 30.9 GHz. *IEEE Transactions on Antennas and Propagation* 18(4): 507–511.
- Semplak, R. A., and R. H. Turrin 1969 Some Measurements of Attenuation by Rainfall at 18.5 GHz*. *Bell System Technical Journal* 48(6): 1767–1787.
- Shi, Zhao, Haonan Chen, Venkatachalam Chandrasekar, and Jianxin He 2017 Deployment and Performance of an X-Band Dual-Polarization Radar during the Southern China Monsoon Rainfall Experiment. *Atmosphere* 9(1): 4.
- Steiner, Matthias, James A. Smith, and Remko Uijlenhoet 2004 A Microphysical Interpretation of Radar Reflectivity–Rain Rate Relationships. *Journal of the Atmospheric Sciences* 61(10): 1114–1131.
- Szakáll, Miklós, Subir K. Mitra, Karoline Diehl, and Stephan Borrmann 2010 Shapes and Oscillations of Falling Raindrops — A Review. *Atmospheric Research* 97(4): 416–425.
- Tabary, Pierre, Abdel-Amin Boumahmoud, Hervé Andrieu, et al. 2011 Evaluation of Two “Integrated” Polarimetric Quantitative Precipitation Estimation (QPE) Algorithms at C-Band. *Journal of Hydrology* 405(3–4): 248–260.
- Tarantola, Albert 2005 *Inverse Problem Theory and Methods for Model Parameter Estimation*, vol.89. *siam*.
- Tarantola, Albert, and Bernard Valette 1982 Generalized Nonlinear Inverse Problems Solved Using the Least Squares Criterion. *Reviews of Geophysics* 20(2): 219.
- Tat-Soon Yee, Pang-Shyan Kooi, Mook-Seng Leong, and Le-Wei Li 2001 Tropical Raindrop Size Distribution for the Prediction of Rain Attenuation of Microwaves in the 10-40 GHz Band. *IEEE Transactions on Antennas and Propagation* 49(1): 80–83.

Bibliography

- Testud, Jacques, Erwan Le Bouar, Estelle Obligis, and Mustapha Ali-Mehenni
2000 The Rain Profiling Algorithm Applied to Polarimetric Weather Radar. *Journal of Atmospheric and Oceanic Technology* 17(3): 332–356.
- Testud, Jacques, Stéphane Oury, Robert A. Black, Paul Amayenc, and Xiankang Dou
2001 The Concept of “Normalized” Distribution to Describe Raindrop Spectra: A Tool for Cloud Physics and Cloud Remote Sensing. *Journal of Applied Meteorology* 40(6): 1118–1140.
- Thurai, M., V. N. Bringi, M. Szakáll, et al.
2009 Drop Shapes and Axis Ratio Distributions: Comparison between 2D Video Disdrometer and Wind-Tunnel Measurements. *Journal of Atmospheric and Oceanic Technology* 26(7): 1427–1432.
- Tokay, Ali, and Kenneth V. Beard
1996 A Field Study of Raindrop Oscillations. Part I: Observation of Size Spectra and Evaluation of Oscillation Causes. *Journal of Applied Meteorology* 35(10): 1671–1687.
- Tokay, Ali, and David A. Short
1996 Evidence from Tropical Raindrop Spectra of the Origin of Rain from Stratiform versus Convective Clouds. *Journal of Applied Meteorology* 35(3): 355–371.
- Torres, Daniel Sempere, Josep M. Porrà, and Jean-Dominique Creutin
1994 A General Formulation for Raindrop Size Distribution. *Journal of Applied Meteorology* 33(12): 1494–1502.
- Uijlenhoet, Remko, Matthias Steiner, and James A. Smith
2003 Variability of Raindrop Size Distributions in a Squall Line and Implications for Radar Rainfall Estimation. *Journal of Hydrometeorology* 4(1): 43–61.
- Upton, G.J.G., A.R. Holt, R.J. Cummings, A.R. Rahimi, and J.W.F. Goddard
2005 Microwave Links: The Future for Urban Rainfall Measurement? *Atmospheric Research* 77(1–4): 300–312.
- Vivekanandan, J., W. M. Adams, and V. N. Bringi
1991 Rigorous Approach to Polarimetric Radar Modeling of Hydrometeor Orientation Distributions. *Journal of Applied Meteorology* 30(8): 1053–1063.
- Vivekanandan, J., Guifu Zhang, and Edward Brandes
2004 Polarimetric Radar Estimators Based on a Constrained Gamma Drop Size Distribution Model. *Journal of Applied Meteorology* 43(2): 217–230.

Bibliography

- Waldvogel, A.
1974 The N_0 Jump of Raindrop Spectra. *Journal of the Atmospheric Sciences* 31(4): 1067–1078.
- Wang, Z., Marc Schleiss, J. Jaffrain, A. Berne, and J. Rieckermann
2012 Using Markov Switching Models to Infer Dry and Rainy Periods from Telecommunication Microwave Link Signals. *Atmospheric Measurement Techniques* 5(7): 1847–1859.
- Waterman, P. C.
1971 Symmetry, Unitarity, and Geometry in Electromagnetic Scattering. *Physical Review D* 3(4): 825–839.
- Waterman, P.C.
1965 Matrix Formulation of Electromagnetic Scattering. *Proceedings of the IEEE* 53(8): 805–812.
- Wen, Guang, Haonan Chen, Guifu Zhang, and Jiming Sun
2018 An Inverse Model for Raindrop Size Distribution Retrieval with Polarimetric Variables. *Remote Sensing* 10(8): 1179.
- Xiao-Ying Dong, Hsing-Yi Chen, and Dong-Hui Guo
2011 Microwave and Millimeter-Wave Attenuation in Sand and Dust Storms. *IEEE Antennas and Wireless Propagation Letters* 10: 469–471.
- Yoshikawa, Eiichi, V. Chandrasekar, and Tomoo Ushio
2014 Raindrop Size Distribution (DSD) Retrieval for X-Band Dual-Polarization Radar. *Journal of Atmospheric and Oceanic Technology* 31(2): 387–403.
- Zawadzki, I., W. Szyrmer, C. Bell, and F. Fabry
2005 Modeling of the Melting Layer. Part III: The Density Effect. *Journal of the Atmospheric Sciences* 62(10): 3705–3723.
- Zhang, Guifu, J Vivekanandan, and Edward Brandes
N.d. A Method For Estimating Rain Rate And Drop Size Distribution From Polarimetric Radar Measurements:
4.
- Zinevich, A., H. Messer, and P. Alpert
2010 Prediction of Rainfall Intensity Measurement Errors Using Commercial Microwave Communication Links. *Atmospheric Measurement Techniques* 3(5): 1385–1402.

Bibliography

Zinevich, Artem, Pinhas Alpert, and Hagit Messer
2008 Estimation of Rainfall Fields Using Commercial Microwave Communication Networks of Variable Density. *Advances in Water Resources* 31(11): 1470–1480.

Zohidov, Bahtiyor, Hervé Andrieu, Myriam Servières, and Nicolas Normand
2014 Rainfall Retrieval in Urban Areas Using Commercial Microwave Links from Mobile Networks: A Modelling Feasibility Study. *In EGU General Assembly Conference Abstracts*.